UC Berkeley
UC Berkeley Electronic Theses and Dissertations

Title
Isovalent Anion Substitution in Ga-Mn-pnictide Ferromagnetic Semiconductors

Permalink
https://escholarship.org/uc/item/5s75p7kq

Author
Stone, Peter

Publication Date
2010

Peer reviewed|Thesis/dissertation

eScholarship.org Powered by the California Digital Library
University of California

Isovalent Anion Substitution in Ga-Mn-pnictide Ferromagnetic Semiconductors

By

Peter Robert Stone

A dissertation submitted in partial satisfaction of the

requirements for the degree of

Doctor of Philosophy

in

Engineering – Materials Science and Engineering

in the

Graduate Division

of the

University of California, Berkeley

Committee in charge:

Professor Oscar D. Dubon, Chair
Professor Yuri Suzuki
Professor Joseph Orenstein

Spring 2010

Isovalent Anion Substitution in Ga-Mn-pnictide Ferromagnetic Semiconductors

Copyright 2010

By

Peter Robert Stone

Abstract

Isovalent Anion Substitution in Ga-Mn-pnictide Ferromagnetic Semiconductors

By

Peter Robert Stone

Doctor of Philosophy in Engineering- Materials Science and Engineering

University of California, Berkeley

Professor Oscar D. Dubon, Chair

While remarkable progress has been made towards understanding the properties of Mn-doped GaAs, the fundamental nature of carrier-mediated ferromagnetism in Mn-doped III-V semiconductors remains unclear. The research described in this dissertation focuses on the synthesis of novel ferromagnetic semiconductor alloys using ion implantation and pulsed-laser melting to investigate how changing the host from GaAs to another semiconductor affects ferromagnetism and transport. Using the $Ga_{1-x}Mn_xAs$ system as a reference, the chemistry of the anion sublattice is manipulated by performing *isovalent anion substitution* in which either the entire anion sublattice is changed from As to another Group V element (e.g. P) or the As sublattice is dilutely alloyed with isovalent P or N. By choosing isovalent elements of shorter atomic radius the interplay of carrier localization (determined by the Mn acceptor level in the host semiconductor) and exchange strength (determined by the energetic alignment of the Mn $3d$ and anion p states) can be explored.

It will be shown that changing the host semiconductor from GaAs to GaP leads to significant localization of ferromagnetism-mediating holes. Nonetheless, robust carrier-mediated ferromagnetism is observed in $Ga_{1-x}Mn_xP$ as determined by combined of ion-channeling, SQUID magnetometry, magnetotransport, X-ray magnetic circular dichroism, and magnetic anisotropy experiments. This finding indicates that hole localization does not destroy the carrier-mediated ferromagnetic phase, though T_C is generally lower in localized systems. Ternary semiconductor hosts are also explored with particular attention paid to the $Ga_{1-x}Mn_xAs_{1-y}P_y$ system that has attracted considerable theoretical attention as a system in which it is predicted that carrier delocalization and exchange strength are simultaneously maximized. However, this research indicates that T_C is *not* enhanced by dilute P alloying into $Ga_{1-x}Mn_xAs$, which is attributed to the scattering of ferromagnetism-mediating holes by the alloy disorder introduced onto the anion sublattice. Finally, the magnetic anisotropy of $Ga_{1-x}Mn_xP$ is explored in detail and found to be substantially similar to that observed in other $III_{1-x}Mn_xV$ materials. Collectively this work demonstrates the importance of considering effects of hole localization for predictions of ferromagnetism and transport in $III_{1-x}Mn_xV$ materials.

Dedication

To my parents for giving me every chance to succeed and always believing in me.

To Agnieszka for her unwavering emotional support and keeping me focused on the important things in life.

Table of Contents

List of Figures

List of Tables

Acknowledgements

This completion of this work would not have been possible without the assistance of numerous people:

Prof. Oscar Dubón – for giving me the opportunity to work on this project and for providing invaluable guidance. Oscar has demonstrated to me through his actions that he holds the mental and physical wellbeing of his students above all else. I can only hope to one day pay the favor forward through similar treatment of students or employees of my own.

Jeffrey W. Beeman – for entrusting me with the responsibilities as ion implanter operator. The knowledge accumulated through working on this instrument supersedes what can be learned in any classroom. His general knowledge of experimental design and procedure saved me countless hours in the lab.

Prof. Michael Scarpulla – For mentoring me for my first year of graduate school and getting me started on the right foot.

Dr. Kin Man Yu – for expert ion channeling measurements and analysis.

Dr. Ian Sharp – for numerous time-consuming ion implantation runs early in my tenure and for eventually teaching me the art (not science) of implantation.

Prof. Eugene Haller – for use of facilities and experimental guidance.

Dr. Christoph Bihler, Lukas Dreher, Michael Kraus, and Prof. Martin Brandt at the Walter Schottky Institut in Garching, Germany– for ferromagnetic resonance measurements and modeling and for inviting me to visit in the Spring of 2008.

Dubón group members past and present – Michael Scarpulla, Jeremy Robinson, Kirstin Alberi, Rouin Farshchi, Rajesh Chopdekar, Amanda Velazquez, Joe Wofford, Doug Detert, Alejandro Levander, Grant Buchowicz, Alex Luce, Sam Tardif, Cesario Julaton, and Thomas Winkler – for stimulating and entertaining group meetings and seminars. Special thanks to Joe for expertly fulfilling the role of distracting officemate when required.

Bill Hansen – for his encyclopedic knowledge of semiconductor science and technology

Prof. Yuri Suzuki and Prof. Joe Orenstein – for reading this dissertation.

Prof. Eugene Haller, Prof. Yuri Suzuki, Prof. Daryl Chrzan, and Tsu-Jae King – for serving on my qualifying exam committee.

Dr. Kirstin Alberi and Dr. Wladek Walukiewicz – for providing theory with which to explain some of my experimental results and for teaching me about band anticrossing interactions.

David Hom – for expert knowledge of the Berkeley and Department of Energy bureaucracies. Building 2 and the EMAT program would not run nearly as smoothly without all of your hard work.

Sam Tardif and Cesario Julaton – for helping me assemble and program the magnetotransport measurement system.

Dr. Rajesh Chopdekar, Dr. Kirstin Alberi, Dr. Becca Jones, Nate Miller, Robert Broesler, Jodi Iwata, Virat Mehta, and Franklin Wong – for experimental assistance

Prof. Yuri Suzuki and her group members – for maintaining the SQUID.

Tom Mates and Yumin Gao – for SIMS measurmements

Dr. Elke Arenholz, and Dr. Marco Liberati for experimental assistance at ALS Beamline 4.0.2 where XAS and XMCD measurements were performed.

I would also like to acknowledge the American Society for Engineering Education and the Office of Naval Research for the financial assistance provided by my National Defense

Science and Engineering Graduate Fellowship and the National Science Foundation for fellowship assistance. This work is supported by the Director, Office of Science, Office of Basic Energy Sciences, Division of Materials Sciences and Engineering, of the U.S. Department of Energy under Contract No. DE-AC02-05CH11231.

1. Introduction

1.1. Spintronics: Motivation and Overview

Devices for the processing and storage of information have traditionally exploited either the electronic charge or spin. Transistors for information processing are based on the manipulation of electronic charge. Figure 1 (a) shows a schematic representation of an n^+-p-n^+ metal-oxide-semiconductor field-effect transistor (MOSFET). If a voltage is applied between the source and drain terminals the current that flows between the two regions is controlled by the gate voltage, V_G. If V_G=0 then very little current can flow from the source to the drain, since the material separating the two is p-type and will not support the transfer of electrons from source to drain. For V_G>0 the band structure of the semiconductor is modified in the vicinity of the metal-oxide-semiconductor junction; holes in the p-type semiconductor are depleted by the bias. For large enough V_G, referred to as the threshold voltage (V_T) a channel near the oxide-semiconductor interface will be inverted to n-type and current can flow from source to drain through the n-type channel. Therefore, the MOSFET is in an "ON" state for $V_G \geq V_T$ while it is "OFF" for $V_G < V_T$. The MOSFET takes advantage of the dynamic control of charge carrier populations by electrical gating, which is one of the attractive properties of *semiconducting* materials for electronics.

The spin of the electron has primarily entered modern devices in the field of nonvolatile information storage. Figure 1(b) shows a simplified representation of a magnetic recording medium. The orientation of the magnetization within a bit is determined by the electronic spin state. Information is written by applying small magnetic fields in the vicinity of a bit, which sets the orientation of the magnetization. The relative orientation of successful bits encodes the binary information on the recording medium. For the data storage to be nonvolatile, the magnetic recording media must be *ferromagnetic* such that the information is retained by the magnetic track once the external field is removed.

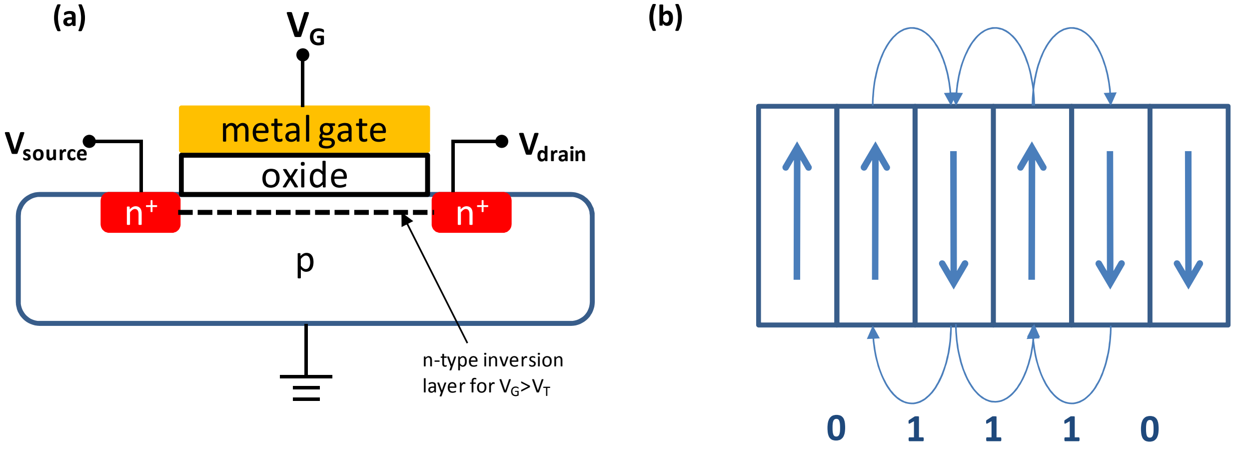

Figure 1: (a) Cross-section of a basic *n-p-n* MOSFET. (b) Schematic of a perpendicular magnetic recording medium. Arrows represent the orientation of the magnetic domains comprising a single bit. A "0" occurs when there is no change in the orientation of the magnetization between bits, while a "1" occurs when the orientation flips direction.

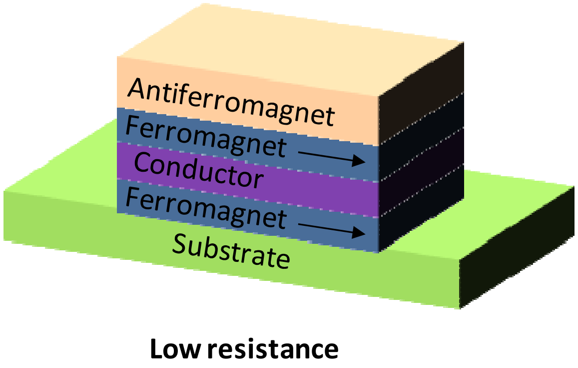

Figure 2: Basic structure of a spin valve for low and high resistance states.

Unlike the previous two examples, *spintronic* devices aim to exploit the spin and charge degrees of freedom in a strongly coupled manner. Simultaneous control of the spin and charge of the electron would open the door to a host of new device architectures. One simple example is the combination of logic and data storage in a single device **[1]**. Moreover, spintronic devices are proposed to have the potential advantages of increased integration densities and processing speeds and decreased power consumption when compared to current electronic devices **[2]**.

One of the first demonstrated spintronic devices was the spin valve shown in Figure 2. The spin valve is based on the giant magnetoresistance (GMR) effect **[3, 4]**, which is observed in multilayer structures of alternating ferromagnetic and nonferromagnetic layers. The resistance of the structure is lowest when the ferromagnetic layers are parallel and highest when they are anti-aligned. GMR is observed in device geometries with either current in-plane (CIP) or current perpendicular to the plane (CPP), but the effect is more pronounced for the CPP configuration **[5]**. In a spin valve geometry the GMR effect can be used as a magnetic field sensor. The orientation of the magnetization of one ferromagnetic layer is pinned by a combination of shape anisotropy (Section 5.1) and/or exchange biasing to an antiferromagnet. The magnetization of the other ferromagnetic layer is free to switch in the presence of an external magnetic field. A change in resistance of the spin valve thus signifies that the component of the magnetic field parallel to the magnetization direction has changed. The spin valve has found technological relevance as the readout mechanism of magnetic nonvolatile memory [*c.f.* Figure 1 (b)]. When the read head is passed over the storage medium a change in resistance registers a "1" since the fringing magnetic fields flip the orientation of the free ferromagnetic layer. Otherwise a "0" is read. The spin valve qualifies as a spintronic device because the electrical response of the circuit is influenced by a perturbation of the electronic spin state; the spin and charge degrees of freedom are intertwined.

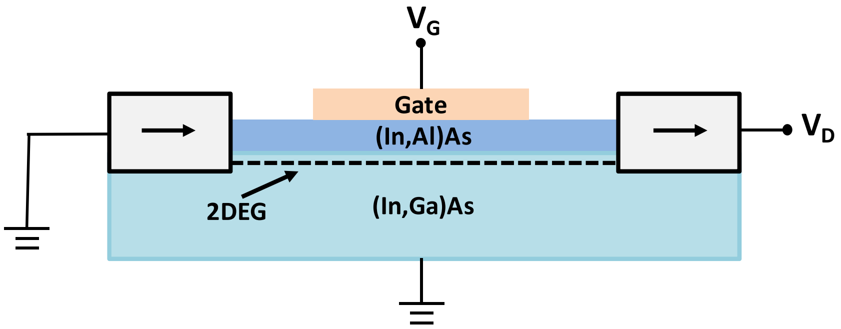

Figure 3: Schematic drawing of a spin field-effect transistor. After [8].

A closely related device to the spin valve is the magnetic tunnel junction (MTJ) in which the conductive metal spacer between ferromagnetic layers is replaced by an insulator, usually an oxide. The so-called tunneling magnetoresistance (TMR) can be much larger in the CPP geometry than the associated GMR effect **[6]**. As in the case for spin valves, MTJs have also found use as read heads for nonvolatile magnetic memory. Moreover, the MTJs themselves can serve as memory elements in magnetoresitive random access memory (MRAM) elements. In the MRAM configuration the "1"s and "0"s are coded as the high- and low-resistance states of the CPP-MTJ stack. The state of the memory element is set from the magnetic field from a current-carrying write wire. Advantages of MRAM over capacitor-based dynamic random access memory (DRAM) or flash are nonvolatile information storage, faster reading and writing times, and lower energy consumption during writing **[2]**. Both GMR read heads and MRAM have rapidly found relevance in the technology sector in the past two decades demonstrating the potential and promise of spintronic devices **[1]**.

Another goal of the field of spintronics is to integrate the spin degree of freedom to traditional charge-based semiconductor devices. A complete discussion of the spin-based analogues of traditional semiconductor devices is beyond the scope of this work. A review can be found elsewhere **[7]**. Perhaps the best known example of such a device is the spin field-effect transistor (spin-FET) that was first proposed by Datta and Das in 1990 **[8]**, which is illustrated in Figure 3. The ferromagnetic contact at the source serves as an injector of spin polarized carriers to a high mobility channel, which in the original proposal of Datta and Das is a two-dimensional electron gas (2DEG) that forms at the (In,Al)As/(In,Ga)As interface. A second ferromagnetic contact at the drain acts as a detector of spin-polarized carriers. The degree of spin polarization of the carriers is controlled by the gate voltage, which would determine the spin diffusion length. The electric field applied through the gate generates an effective magnetic field through relativistic transformation known as the Rashba field **[5]**, which decreases the spin relaxation time for spin-polarized carriers in the semiconductor base. The Rashba effect thus provides a means to execute spin transistor action by controlling the spin polarization of the current that reaches the drain contact.

An implicit assumption in the operation of the spin-FET illustrated in Figure 3 is that one can efficiently inject spin-polarized carriers from the ferromagnetic contact into the semiconductor. However, the injection of spin polarized carriers from a metallic contact into a semiconductor is fundamentally limited by the conductivity mismatch between the two materials. The conductivity mismatch problem has been approached theoretically by adaptation of the "two current" model originally used to describe electrical transport in ferromagnetic metals **[9]**. In the two current model it is assumed that the spin-conserving scattering events that determine the electrical resistivity are much more frequent than spin-flip scattering events. Thus, one can define parameters such as the conductivity, current density, diffusion length, *etc.* for each spin orientation that need not be equal if a spin-polarization is present, which is the case for a ferromagnet. The extension of the two current model to spin-injection from a ferromagnet to a normal material has been done by numerous groups **[5, 7, 10, 11]**. Here, the notation of Fert and Jaffrès is used **[12]**. For a perfect interface between the magnetic and normal materials the spin polarization at the interface is

$$\left(\frac{J_+ - J_-}{J}\right)_I = \frac{\beta r_F}{r_F + r_N} \tag{1}$$

where J_+ and J_- are the current densities of the spin up and spin down channels, J is the total current, β is the spin polarization of the ferromagnetic material (β=1 for a half metal, β=0 for a normal metal), and r_F (r_N) is the product of the resistivity, ρ, and spin diffusion length, L_{spin}, in the ferromagnetic (normal) material. For the case of a ferromagnetic metal/normal semiconductor interface, $r_F << r_N$ implying that the spin polarization transferred through the interface is vanishingly small (approximately β/r_N). This contrasts with the case where the normal material is a metal and r_F and r_N are of comparable magnitude, which allows for reasonable levels of spin injection (see, for example, Figure 1 of Ref. **[12]**). Ferromagnetic semiconductors, the materials class that is the main subject of this dissertation, provide one such route to overcome the impedance-match issue. If the ferromagnetic material is a semiconductor, then one can tune its properties such that $r_F \approx r_N$ thus allowing for efficient spin injection between the ferromagnetic and normal material.

For completeness it should be noted that alternate routes besides ferromagnetic semiconductors exist to overcome impedance mismatch. For example, if one introduces a tunneling barrier between the ferromagnetic and normal materials an additional interface resistance term must be added to Equation 1 **[12]**,

$$\left(\frac{J_+ - J_-}{J}\right)_I = \frac{\beta r_F + \gamma r_B}{r_F + r_N + r_B} \tag{2}$$

where r_B is related to the interfacial resistance and γ is the spin-selectivity of the tunnel barrier. Thus, by taking advantage of spin-dependent tunneling through a resistive barrier one can in principle obtain efficient spin injection provided $r_B >> r_F$.

1.2. Ferromagnetic Semiconductors: Basic Principals

Creating a material that is simultaneously semiconducting and ferromagnetic would not only solve the impedance mismatch problem discusses in Section 1.1 but would also allow dynamic control of both the charge and spin degrees of freedom of the electron. Such a material does not occur naturally. Traditional ferromagnetic materials such as Ni and Fe possess the desired spin polarization of carriers at the Fermi energy (E_F). However, these systems are strongly metallic and thus do not possess the desired tunable electronic properties provided by semiconductors. On the other hand, common semiconductors such as Si or GaAs are non-magnetic. Furthermore, their low Landé *g* factors imply that prohibitively large magnetic fields would be necessary to produce a large asymmetry in the spin-resolved density of states (DOS) **[13]**.

One strategy for obtaining a material that is both semiconducting and ferromagnetic is to replace a few percent of a semiconductor lattice with a magnetically active impurity, resulting in a so-called diluted magnetic semiconductor (DMS). DMSs are particularly attractive since they maintain the crystal structure of the host semiconductor, thus allowing for easy integration into the currently existing technological infrastructure. If a long-range exchange interaction spontaneously couples the impurity spins, then the material is said to be a ferromagnetic semiconductor (FS). The magnetic ions present in ferromagnetic semiconductors typically constitute only a few percent of the total atoms in a material. Accordingly, the exchange interaction between the magnetically active atoms is mediated by the spins of the charge carriers since the individual Mn moments are spatially too separated to communicate via direct exchange. As a result of this carrier-mediated exchange interaction there is a strong coupling between the spin and charge degrees of freedom of the electron in FSs, which gives rise to many novel effects (Section 1.4). This work will focus on one particularly well-studied subset of ferromagnetic semiconductors: Mn-doped III-V materials. However, there is currently active research into ferromagnetic semiconductors based on semiconducting oxides **[14]** as well as II-VI **[15]** and Group IV **[16]** materials.

1.3. Exchange Interactions in $III_{1-x}Mn_xV$ Ferromagnetic Semiconductors

Qualitatively, one can understand the indirect exchange mechanism operative in $III_{1-x}Mn_xV$ materials as follows. When Mn is introduced into an III-V semiconductor one possible location of its incorporation is onto a cation site. Mn atoms which are substitutional upon the Group III sublattice serve a twofold purpose. First, their 5 localized 3*d* electrons give rise to a local magnetic moment of 5 μ_B. Second, Mn, with an electronic structure of $[Ar]3d^5 4s^2$ has one fewer valence electron than the Group III element, which has electronic structure $[No](n-1)d^{10} ns^2 np^1$, where [No] represents the noble gas core electrons and *n* represents the principle quantum number of the valence shell. As a result, when Mn is incorporated substitutionally onto cation sites, it acts not only as a source of local magnetic moments but also as an acceptor. A *p-d* kinetic exchange mechanism between the holes provided by substitutional Mn acceptors and the local Mn magnetic moments gives rise to long range ferromagnetic order. The spin-polarized, magnetic state is stable if the lowering in energy of the system due to the exchange interaction is greater than the decrease in entropy associated with spin alignment **[17]**.

A qualitative picture of the *p-d* exchange mechanism between one spin-1/2 degenerate valence band and the Mn 3*d* states is presented in Figure 4. Due to Hund's rules, the 5 3*d* electrons of Mn have parallel spins, resulting in an energetic difference in 3*d* states of opposite spin. In Figure 4 it is (arbitrarily) assumed that the spin down *d*-level is deep in the valence band, while the spin up level is higher in energy. The mixing of the Mn 3*d* and anion *p* states of like spin (*p-d* hybridization) results in the spin-down Mn 3*d* states moving lower in energy while the spin-down anion *p* states near the top of the valence band move up in energy. Similarly, *p-d* hybridization moves the spin-up Mn 3*d* states up in energy relative to the spin-up valence band states. When electrons are excited from the (spin-split) valence band to the Mn acceptor levels more spin-down holes will be created than spin-up. The spin-polarized carriers thus have a net spin-down moment. The total Mn magnetic moment is due to the spin-down 3*d* electrons. Due to the negative charge of the electron, the moment vector points opposite to the angular momentum, and the Mn moments are spin *up*. Therefore, the *p-d* exchange interaction leads to antiferromagnetic coupling between valence-band holes and Mn spins. The Mn moments themselves are ferromagnetically coupled to one another through mutual interaction with the spin-polarized holes. It must be stressed that this simple example of the *p-d* exchange mechanism is for illustrative purposes only. In actuality the spin degeneracy of all three valence bands in GaAs are split by the *p-d* exchange interaction and the states are perturbed by the influence of the Mn acceptor levels as well. Furthermore, there is considerable controversy over whether or not E_F lies in the valence band (as pictured in Figure 4) or in a detached impurity band derived from the Mn acceptor states. This point will be discussed further in Section 1.5.

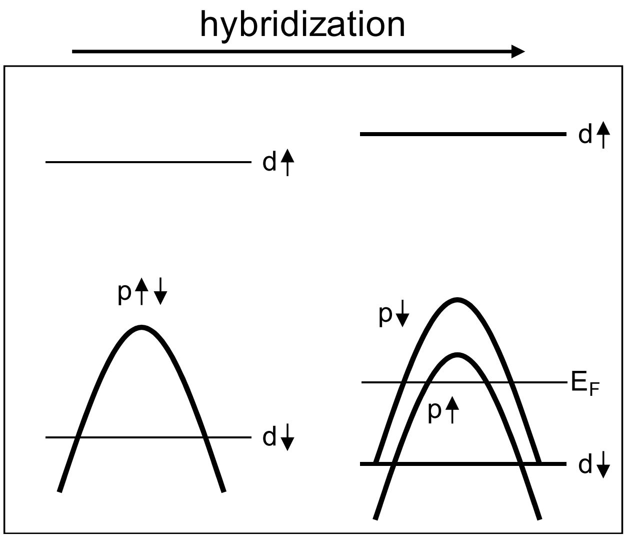

Figure 4: Illustration of the *p-d* exchange interaction in III$_{1-x}$Mn$_x$V materials according to a valence band model. Image modeled after Ref. [18].

The *p-d* exchange interaction also can give rise to short range antiferromagnetic coupling between substitutional Mn spins due to superexchange. This superexchange interaction is mediated by the spin polarization of *occupied* electronic states in contrast to the kinetic-exchange interaction described above in Figure 4, which is mediated by the spin polarization of the carrier liquid **[19]**. Superexchange arises when local moments are separated by a non-magnetic atom. An electron can be transferred from the non-magnetic (in this case Group V) atom to the unoccupied 3*d* orbitals of the localized Mn moment. In turn, the transferred electron can interact via direct exchange with the other 3*d* electrons on the localized moment. The nonmagnetic atom is thereby polarized by its interaction with all of its magnetic neighbors in the tetrahedral crystal field environment of the III-V semiconductor. When a Mn-Group V-Mn trimer exists locally in the material the two direct exchange interactions give rise to antiferromagnetic coupling between the Mn moments **[18]**. Antiferromagnetic coupling due to superexchange may limit the ferromagnetic Curie temperature (T_C) in heavily doped magnetic semiconductors as the probability of finding Mn-Group V-Mn complexes increases. On the other hand, Mn moments in close proximity to one another can also form bound magnetic polarons with localized holes, which are likely to be found near substitutional Mn due to their dual function as sources of magnetic moments and charge carriers. The mutual antiferromagnetic interaction of the Mn moments with the hole causes ferromagnetic coupling of Mn within the polarons. Thus, the effect of antiferromagnetic superexchange in materials where compensation is low may be limited in III$_{1-x}$Mn$_x$V materials **[19]**.

Another possible source for antiferromagnetic exchange interaction comes from Mn atoms that occupy the tetrahedral interstitial sides of the zincblende lattice. These interstitial Mn atoms (Mn$_I$) do not participate in the *p-d* exchange interaction. Instead, they form complexes with substitutional Mn atoms in which the magnetic moment of the Mn$_I$ aligns antiferromagnetically with a substitutional Mn moment **[20]**. Furthermore, since its two valence electrons do not participate in valence bonding, Mn$_I$ is a double electron donor. Thus, each Mn$_I$ effectively eliminates one Mn spin and two mediating holes. Interstitial Mn is commonly found in III$_{1-x}$Mn$_x$V materials grown by low-temperature molecular beam epitaxy (LT-MBE). The effect of Mn_I can be minimized through proper post-growth annealing of LT-MBE grown samples, which eliminates a large fraction of the Mn_I defects (Section 2.1) **[21]**.

1.4. Ferromagnetic Semiconductors as Spintronic Materials

The carrier-mediated nature of the exchange interaction in ferromagnetic semiconductors gives rise to numerous novel properties that can potentially be exploited for spintronic applications. The ability of ferromagnetic semiconductors to overcome the impedance mismatch problem that has impeded the development of spin-FETs and related devices has already been discussed in Section 1.1. Ferromagnetic semiconductors also possess the advantage that the charge carriers responsible for generating an electrical current are themselves involved in the exchange interaction. Hence, there exists a natural spin polarization of the current even in the absence of an applied magnetic field.

By utilizing techniques from the semiconductor industry designed to dynamically modulate the carrier concentration it is possible to control the degree of magnetic ordering in a ferromagnetic semiconductor. For example, holes can be accumulated or depleted from a FS by electrical gating, which alters T_C. By working in an appropriate T and p regime, gating can drive the system from a ferromagnetic to paramagnetic state **[22, 23]**. Electrical current pulses have been shown to be able to reorient magnetic domains and drive domain-wall motion in $Ga_{1-x}Mn_xAs$ **[24]**. The magnetic ordering can also be controlled by illumination with circularly polarized photons, which preferentially excite charge carriers according to their spin state **[25, 26]**. Optical and electrical control of the magnetic anisotropy and magnetization reversal processes has also been demonstrated in $Ga_{1-x}Mn_xAs$ **[27]**.

These unique effects are observed in ferromagnetic III-V semiconductors only below T_C, which is still well below room temperature, thus hindering the development of useful devices out of these materials. To understand the factors that control T_C and strategies for potentially boosting T_C to values that would allow for the integration of these materials into mainstream technology, the details of ferromagnetic exchange in $III_{1-x}Mn_xV$ materials must be explored in more detail. This is the subject of the following two sections.

1.5. Theoretical Overview of $III_{1-x}Mn_xV$ Materials

An overview of several theoretical models developed to explain carrier-mediated ferromagnetism is given in this section, which focuses on the mean-field, valence band theory adapted from Zener's kinetic-exchange model. This model was shown to be consistent with results in the $Ga_{1-x}Mn_xAs$ system by the authors of Ref. **[13]** and has developed into arguably the most widely utilized theoretical approach for studying $III_{1-x}Mn_xV$ FSs. Other computational and theoretical methods have been applied to $III_{1-x}Mn_xV$ materials including first principles calculations, and tight binding approaches **[28]** as well as polaronic models **[29]**. A detailed review of the theory of $III_{1-x}Mn_xV$ materials can be found in Ref. **[18]**. Currently none of the theoretical approaches are able to capture successfully all of the physics that have been observed experimentally; the detailed, microscopic description of ferromagnetism is still an area of considerable controversy. Likely the true mechanisms responsible for the properties of Mn-doped III-V materials lie intermediate to the extremes represented by the various models and theoretical constructs. In general, the advantages of a fully microscopic approach have increasing importance for more localized acceptors, and, hence, shorter Mn-Mn interactions, while the mean-field approaches are better suited for systems with more shallow Mn acceptors in which interactions are longer range **[18]**.

1.5.1 *Effective k·p Hamiltonian Approaches*

The band structure of a semiconductor over the entire Brillouin zone can be extrapolated from the zone center energy gaps and optical matrix elements by ***k·p*** band structure calculations. The method is so-named since the use of periodic Bloch functions as the eigenfunctions in the single particle Schrodinger equation leads to a term in the Hamiltonian proportional to the dot product ***k·p***. The band dispersion is determined from the ***k·p*** Hamiltonian by first-order perturbation theory. Thus, this method best reproduces the band structure for small ***k*** since the perturbation terms are proportional to the magnitude of ***k***. To apply this method to magnetic semiconductors, the 6×6 ***k·p*** matrix describing the 6 T_2 symmetric valence bands is augmented by terms describing the perturbation of these valence bands by the *p-d* exchange interaction between the holes and Mn moments. The kinetic exchange interaction is described by the *p-d* exchange Hamiltonian, which within the virtual-crystal and molecular-field approximations is written as **[19, 30]**

$$H_{pd} = \beta \boldsymbol{s} \cdot \boldsymbol{M}(\boldsymbol{r})/g\mu_B \tag{3}$$

where ***s*** and ***M(r)*** are the orientations of the hole and Mn spins, respectively, *g* is the Landé factor of the electron, μ_B is the Bohr magneton, and β is the *p-d* exchange integral and quantifies the strength of the antiferromagnetic exchange interaction between the holes and Mn moments. Some theoretical formulations utilize the *p-d* exchange constant $J_{p\text{-}d}=N_0\beta$ in the Hamiltonian, which changes its functional form but not the relevant results **[18, 31]**. Equation 3 has been written as a 6×6 matrix in the Kohn-Luttinger basis by Dietl *et al.* **[19]**. This method is attractive since it contains no free parameters: β can be extracted from photoemission experiments **[32, 33]** and the valence band parameters for III-V semiconductors that enter the ***k·p*** Hamiltonian are well tabulated. Diagonalization of the *p-d* exchange-augmented ***k·p*** Hamiltonian yields the 6 spin-polarized valence bands of the ferromagnetic semiconductor. In combination with the partition function of the system, these eigenstates provide a basis for computing the carrier contribution of the free energy to the system, $F_C[\boldsymbol{M}]$, which depends on the magnetization orientation. The total free energy functional, *F* depends also on the part of the free energy due to the localized spins

$$F_S[M] = \int_0^M dM_0 H(M_0) \tag{4}$$

where $H(M_0)$ is written as an inverse Brillouin function (B_S) in the mean-field approximation

$$H(M_0) = B_S^{-1}\left(\frac{M_0}{g\mu_B S N_0 x}\right)\frac{k_B T}{g\mu_B S} \tag{5}$$

with xN_0 equal to the concentration of Mn, k_B the Boltzmann constant, and *S* equal to 5/2 for Mn in a $3d^5$ configuration. Minimization of *F* at a given *T, H,* and hole concentration yields the equilibrium orientation and magnitude of the magnetization. T_C can then be determined as the temperature at which $M \rightarrow 0$.

While the method described in the preceding paragraph provides the most accurate quantitative prediction of the Curie temperature, it must be performed numerically as it involves taking the determinant of a 6×6 matrix and evaluating the system's partition function. It is possible to derive an analytical expression for T_C from simple thermodynamic considerations. Near T_C $M\approx 0$, which allows one to expand the free energy in a Taylor series about $M=0$. Combined with the linearization of the Brillouin function in Equation 5, T_C can be written as a function of materials parameters and physical constants. Using the notation of Dietl *et al.* **[19]**

$$T_C = \frac{xN_0S(S+1)\beta^2 m_{eff}k_F}{12k_B\pi^2\hbar^2} \tag{6}$$

where m_{eff} is the valence band effective mass and k_F is the Fermi wavevector. The form of Equation 6 assumes that antiferromagnetic interactions are negligible and that the carrier states are strongly degenerate. These approximations should be valid for the high doping densities used to synthesize ferromagnetic semiconductors if compensation is not severe. Equation 6 does not require any detailed knowledge of either the parameters that enter into the *p-d* exchange or ***k·p*** Hamiltonians. It provides a useful method by which to estimate the dependence of T_C on important materials parameters such as doping (x), carrier concentration ($k_F \propto p^m$), and semiconductor host (N_0 and β) at least within the approximations made above.

1.5.2 *Applicability of the Effective k·p Approach*

One can identify two major assumptions about the character of the charge carriers implicit in the valence band, mean-field approach. First, the *p-d* exchange Hamiltonian assumes that each Mn or hole spin feels an effective field due to the collective action of all other Mn and hole spins. Localization and disorder effects, which are expected to be important in a strongly-correlated system with randomly distributed magnetic dopants, are not explicitly considered by this approach. Second, through the use of valence band parameters to describe the band dispersion, it is implicit that E_F lies within the valence band. This scenario may be plausible given the 10^{20}-10^{21} cm^{-3} level impurity concentrations typically found in $Ga_{1-x}Mn_xAs$. At these doping levels it is argued that the Mn impurity band and host valence bands are sufficiently broadened by screening and disorder effects to cause them to overlap and E_F to lie in delocalized states of predominantly valence band character **[34]**. These assumptions appear to be valid in highly-doped, metallic $Ga_{1-x}Mn_xAs$ thin films where the mean field models adequately describe experiment. Of particular note is the successful quantitative description of the variation of T_C with x and p **[18, 19, 31, 35]**, and the magnetic anisotropy (see also Section 5.3) **[17, 19, 36-38]**. On the other hand, this approach may not be explicitly valid in samples with lower Mn doping in which electrical transport is thermally activated and a sharp minimum in the density of states exists between the valence and impurity bands. Similarly, these approaches may not capture completely the behavior of materials in which the Mn acceptor level is deep in the band gap. The larger binding energy of the deep acceptors shifts the metal-insulator transition to higher doping levels. It will be shown in Chapter 3 that due to an acceptor level that is 4 times deeper than in $Ga_{1-x}Mn_xAs$, $Ga_{1-x}Mn_xP$ exhibits impurity-band physics for at least $x \leq 0.042$. Therefore, the prediction of materials properties in Mn-doped GaP, GaN, C, etc. through the extension of the ***k·p*** formalism is misguided as the Fermi energy does not lie in the valence band in these wide gap materials.

The valence band formalism has struggled, moreover, to explain several important experiments in $Ga_{1-x}Mn_xAs$ that seem to indicate that the Fermi energy does not reside in the valence band but instead in a separate unmerged Mn impurity band even at Mn concentrations where electrical transport is nominally metallic. Infrared absorption studies point towards the existence of an unmerged Mn impurity band and an effective mass of the mobile holes that is on the order of 10 times the free electron mass **[39]**. Electrical transport measurements show signatures of weak localization, which suggests that transport occurs in a narrow, localized band **[40]**. Magnetic circular dichroism (MCD) measurements imply that the carriers responsible for mediating ferromagnetic exchange are localized **[41]**. While these experiments have called into question some of the assumptions of the effective ***k·p***, valence band approach, theories based on impurity-band physics are much less well-developed, though there have been a few notable successes. An impurity-band picture based on multiband tight-binding calculations has recently been used to explain MCD measurements as well as the relationship between ferromagnetism and electrical transport in low-doped, insulating $Ga_{1-x}Mn_xAs$ **[42, 43]**. An impurity-band model based on band anticrossing theory has been used to explain the behavior of the hole effective mass, mobility, and thermopower in $Ga_{1-x}Mn_xAs$ **[44, 45]**.

1.6. Anion Substitution

From the preceding section it is clear that the fundamental nature of ferromagnetism throughout Mn-doped III-V semiconductors remains unclear. One significant contribution to this is materials growth; successful, reproducible synthesis routes for the carrier-mediated phases of several $III_{1-x}Mn_xV$ materials have yet to be identified. Combined experimental-theoretical studies have been nearly exclusively limited to the canonical $Ga_{1-x}Mn_xAs$ system and to a lesser extent $In_{1-x}Mn_xAs$ **[46-48]**, although some experimental results are also available in $Ga_{1-x}Mn_xSb$ **[49]** and $In_{1-x}Mn_xSb$ **[50]**. Systematic expansion of the range of experimentally accessible $III_{1-x}Mn_xV$ materials would provide a broader parameter space with which to test and refine current models. One can identify two general trends that occur when one changes the host semiconductor for Mn_{Ga} moments from GaAs to one with a wider band gap and shorter lattice constant. These trends are illustrated in Figure 5 for Ga-based III-V semiconductors, which are the subject of this dissertation. In comparison to GaAs the wider gap semiconductors GaP and GaN have band edges that are closer energetically to the Mn-derived 3*d* levels. Thus, there is increased mixing of Mn 3*d* and anion *p* states leading to an enhancement of *p-d* exchange– that is, β increases. On the other hand, as one moves up the group V column of the periodic table, the Mn acceptor level becomes much deeper in the forbidden gap. For example, at 400 meV above the valence band **[51]**, the Mn acceptor level is nearly four times deeper in the band gap of GaP than it is in GaAs where it is 110 meV above the valence band maximum **[52]**. As the acceptor level moves farther away from the valence band edge, the hole wavefunctions become increasingly localized, which decreases their efficacy at mediating exchange between the dilute Mn moments.

There are, therefore, two competing and intimately correlated effects that occur upon changing the composition of the semiconductor host: localization and exchange. Both of these effects are determined by the semiconductor host. Therefore, it is possible to systematically explore the interplay of localization and exchange by altering the composition of the host semiconductor. Here, this is accomplished by using the $Ga_{1-x}Mn_xAs$ system as a baseline and performing *isovalent anion substitution*[*]. This work explores two classes of isovalent anion substitution. The first, as was discussed above, is changing completely the anion sublattice of the semiconductor host from As to P. One can also perform *partial isovalent anion substitution* to examine the properties of Mn-doped ternary III-V hosts (e.g. $GaAs_{1-y}P_y$) and how ferromagnetic exchange and localization vary between the end point compounds. These are the subjects of Chapters 3 and 4, respectively.

---

[*] Of course a similar argument holes for the cation sublattice (e.g. moving from $Ga_{1-x}Mn_xAs$ to $Al_{1-x}Mn_xAs$) but due to constraints in the materials processing (Chapter 2) it proves more convenient to study isovalent anion substitution.

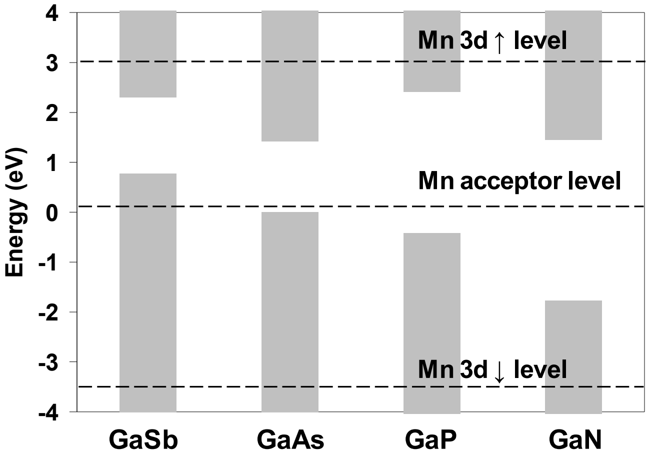

Figure 5: Valence and conduction band offsets for the Ga-V semiconductors. The Mn-derived energy levels are constant across the series due to the internal reference rule [53, 54].

In addition to addressing important fundamental questions regarding the interplay of exchange and localization effects, the synthesis of novel ferromagnetic semiconductor alloys is also highly relevant in the search for room temperature ferromagnetism in $\mathrm{III}_{1-x}\mathrm{Mn}_x\mathrm{V}$ materials. Currently the highest reported T_Cs for $\mathrm{Ga}_{1-x}\mathrm{Mn}_x\mathrm{As}$ are between 180-190 K, the highest reliable T_Cs reported for any $\mathrm{III}_{1-x}\mathrm{Mn}_x\mathrm{V}$ system **[55-57]**. While this is within 100 K of room temperature the T_C record has hardly changed during the period in which the research in this dissertation has been conducted; in 2005 the T_C record was already 173 K **[58]** indicating that progress towards room temperature ferromagnetism in $\mathrm{Ga}_{1-x}\mathrm{Mn}_x\mathrm{As}$ is proceeding at a very slow rate. The reasons for this slow progress are rooted in difficulties in substitutionally incorporating large quantities of Mn into the GaAs lattice **[57, 59-61]**. Calculations suggest that x=0.1-0.125 is necessary for room temperature ferromagnetism in $\mathrm{Ga}_{1-x}\mathrm{Mn}_x\mathrm{As}$ **[19, 31]**. It must be emphasized that this value of x is the *substitutional* Mn concentration and isn't the *nominal* or *total* Mn concentration quoted in many works.

There have also been efforts to increase T_C through increasing the concentration of holes by co-doping with an additional, non-magnetic impurity. However, calculations indicate that the dependence of T_C is weak for large p **[31]**. Large p is defined relative to the concentration of Mn moments (N_{Mn}) or, analogously, to the degree of compensation in the material. When $p/\mathrm{N}_{\mathrm{Mn}}$ is low (i.e. a highly compensated material) the authors of Ref. **[31]** find good agreement with the expected $T_C \sim xp^{1/3}$ trend. But for $p/\mathrm{N}_{\mathrm{Mn}} \geq 1$ (the regime of *additional* hole doping), the dependence of T_C on p becomes very weak. This indicates that while a critical concentration of carriers is necessary to effectively mediate ferromagnetic coupling, the prospects for *enhancement* of T_C through incorporation of holes in excess of those produced by the $\mathrm{Mn}_{\mathrm{Ga}}$ acceptors is limited.

With prospects for achieving room temperature ferromagnetism limited in $\mathrm{Ga}_{1-x}\mathrm{Mn}_x\mathrm{As}$, some have proposed utilizing wider gap semiconductor hosts with larger values of β. According to mean-field theory (Equation 6) this would result in a higher T_C for a given $\mathrm{Mn}_{\mathrm{Ga}}$ concentration, x. However, mean-field theory does not explicitly consider the increased localization associated with Mn acceptor states in the wider gap III-V hosts. It is, therefore, essential to synthesize materials such as $\mathrm{Ga}_{1-x}\mathrm{Mn}_x\mathrm{P}$ and $\mathrm{Ga}_{1-x}\mathrm{Mn}_x\mathrm{N}$ to assess the validity of the predicted increase in T_C by enhancement of the p-d exchange interaction in wider gap ferromagnetic semiconductors.

1.7. Organization of the Dissertation

This document is organized as follows. In Chapter 2 the growth procedures for $\mathrm{III}_{1-x}\mathrm{Mn}_x\mathrm{V}$ materials are discussed with emphasis placed on the combination of ion implantation and pulsed-laser melting (II-PLM), which has allowed for the synthesis of novel $\mathrm{III}_{1-x}\mathrm{Mn}_x\mathrm{V}$ ferromagnetic semiconductor alloys including $\mathrm{Ga}_{1-x}\mathrm{Mn}_x\mathrm{P}$ and $\mathrm{Ga}_{1-x}\mathrm{Mn}_x\mathrm{As}_{1-y}\mathrm{P}_y$. The structural, electronic, and magnetic properties of $\mathrm{Ga}_{1-x}\mathrm{Mn}_x\mathrm{P}$ formed by II-PLM are presented in Chapter 3. These experiments on $\mathrm{Ga}_{1-x}\mathrm{Mn}_x\mathrm{P}$ unambiguously demonstrate that ferromagnetism in $\mathrm{Ga}_{1-x}\mathrm{Mn}_x\mathrm{P}$ is mediated by carriers localized in a detached Mn impurity band. In Chapter 4 the synthesis of novel Mn-doped ternary semiconductors $\mathrm{Ga}_{1-x}\mathrm{Mn}_x\mathrm{As}_{1-y}\mathrm{N}_y$ and particularly $\mathrm{Ga}_{1-x}\mathrm{Mn}_x\mathrm{As}_{1-y}\mathrm{P}_y$ are discussed. The interplay of localization and exchange can be examined in these quaternary materials, which has led to important discoveries concerning the critical parameters governing electrical transport and T_C in Mn-doped III-V materials. Chapter 5 is devoted to the discussion of the magnetic anisotropy of Mn-doped III-V semiconductors. A complete discussion of the magnetic anisotropy of $\mathrm{Ga}_{1-x}\mathrm{Mn}_x\mathrm{P}$ and its dependence of epitaxial strain, and compensation is given. Finally, some concluding remarks and future perspectives are given in Chapter 6.

2. Materials Synthesis: Ion Implantation and Pulsed-Laser Melting

The occurrence of ferromagnetism in Mn-doped semiconductors requires incorporating a few percent Mn substitutionally onto the cation sublattice, which translates to substitutional Mn concentrations on the order of 10^{20}-10^{21} cm^{-3}. These concentrations exceed the equilibrium solubility of Mn in GaAs or GaP by at least an order of magnitude **[62, 63]**. Therefore, the synthesis of ferromagnetic semiconductors requires the use of non-equilibrium processing techniques. For the most part, the most reliable synthesis method has been low-temperature molecular beam epitaxy, which has been used to grow $Ga_{1-x}Mn_xAs$ **[64]**, $In_{1-x}Mn_xAs$ **[46]**, and several other Mn-doped semiconductors. However, some Mn-doped III-V materials have yet to be grown successfully by LT-MBE including $Ga_{1-x}Mn_xP$. This suggests the need for alternate synthesis routes for magnetic semiconductors that can augment the existing library of materials formed by LT-MBE. The successful synthesis of the carrier-mediated phase of $Ga_{1-x}Mn_xP$ by the combination of ion implantation and pulsed-laser melting (II-PLM) marked an important step in this direction (Chapter 3). The inherent flexibility of the II-PLM method has allowed for relatively easy extension into novel quaternary materials- e.g. $Ga_{1-x}Mn_xAs_{1-y}P_y$, $Ga_{1-x}Mn_xP_{1-y}N_y$, *etc.* (Chapters 4 and 5).

This chapter begins with a brief overview of LT-MBE processing of magnetic semiconductors in order to provide a baseline of the structural properties and defect chemistry associated with ferromagnetic semiconductors grown by this common method (Section 2.1). This is followed by a discussion of the II-PLM processing technique used to make the films in this work. A general overview of the II-PLM process is given in Section 2.2. More detailed discussion of the individual steps of and theory underlying the synthesis method are given in Sections 2.3-2.5. Finally a brief overview of the properties of $Ga_{1-x}Mn_xAs$ is given in Section 2.6. Comparison is made to $Ga_{1-x}Mn_xAs$ produced by LT-MBE in order to demonstrate the similarity of the bulk magnetic and electronic properties of the materials produced by these two methods.

2.1. Growth of $III_{1-x}Mn_xV$ Materials by Molecular Beam Epitaxy

The growth of GaAs and other III-V materials by MBE is usually performed at sufficiently high temperature to promote the necessary surface reactions and migration kinetics required to produce stoichiometric, single crystalline thin films **[65]**. Typical growth temperatures for GaAs range from about 400º-700º C **[66]**. The incorporation of large concentrations Mn into GaAs by MBE requires the use of much lower growth temperatures to avoid Mn-related phase segregation **[67]**. An inverse relationship exists between the concentration of Mn that can be incorporated into a film and growth temperature **[68]**. However, if the growth temperature is too low the growth mode changes from two-dimensional to three-dimensional due to insufficient surface mobility. A narrow temperature window exists wherein large quantities of Mn can be incorporated into GaAs while maintaining the requisite atomic mobilities required for two-dimensional layer-by-layer growth. The temperature window is approximately 180º -300º C **[67]** with the current state-of-the-art $Ga_{1-x}Mn_xAs$ films grown at ~200º C **[57]**.

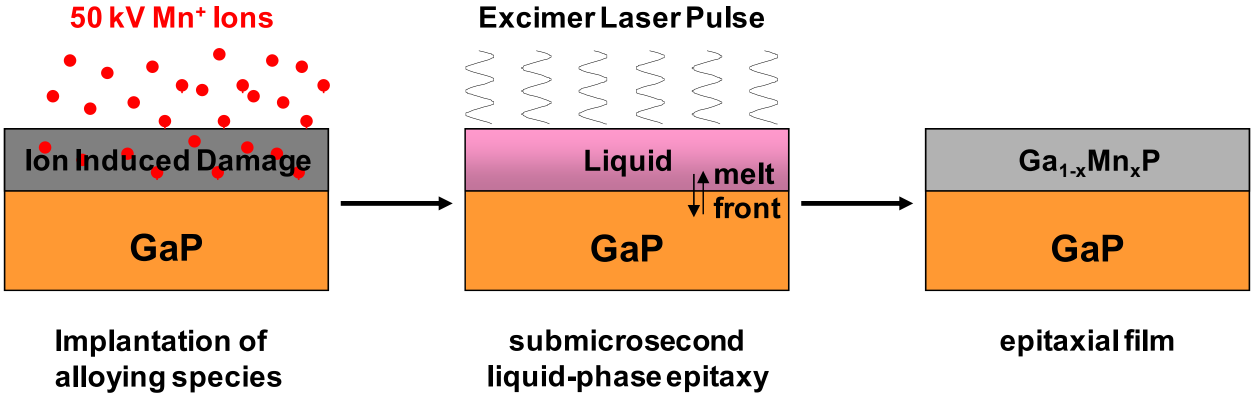

Figure 6: Schematic of the II-PLM process.

Low growth temperatures have important ramifications on the defect chemistry of the final $Ga_{1-x}Mn_xAs$ film. The formation of arsenic antisite (As_{Ga}) and Mn interstitial (Mn_I) defects is promoted by the low growth temperature. Both are undesirable as they are double donors and compensate the holes necessary to mediate ferromagnetic exchange. Furthermore, electrostatic interaction causes the Mn_I to migrate towards oppositely polarized Mn_{Ga} where an antiferromagnetic complex is formed with zero net moment **[20]**. Annealing at temperatures near the growth temperature increases the magnitude of both T_C and the conductivity of LT-MBE formed $Ga_{1-x}Mn_xAs$ **[69]**. This behavior was directly correlated to the removal of Mn_I upon annealing by ion beam studies **[70]** whereby the Mn_I outdiffuse to the surface of the film **[71]**. Arsenic antisites, on the other hand, cannot be removed after growth as they remain stable up to annealing temperatures and timescales known to produce Mn-containing second phases. Films formed by II-PLM have no Mn_I defects (Appendix A and Section 4.2.1). Therefore, the best comparison for II-PLM formed materials is provided by *annealed* LT-MBE grown films **[18, 72]**.

2.2. Overview of the II-PLM Process

The II-PLM process is illustrated in Figure 6 for the synthesis of $Ga_{1-x}Mn_xP$. Specific processing parameters used to produce the materials in this work are given in later chapters and the appendices. The first step, ion implantation, serves to introduce the Mn dopants into the material. In order to synthesize $Ga_{1-x}Mn_xP$, a GaP wafer is implanted with 50 kV Mn^+ ions to doses of 10^{15}-10^{16} cm^{-2}. Ion implantation is performed at an angle of 7º from normal incidence to avoid channeling. For the synthesis of $Ga_{1-x}Mn_xAs$, the GaP wafer is simply replaced with a GaAs wafer. If one desires to make a quaternary material, the fourth element is introduced during a second ion implantation step. After implantation the near-surface region is supersaturated with Mn and is amorphous due to the damage caused by the implantation of high-energy ions. In order to repair the damage as well as incorporate the Mn atoms substitutionally onto Ga sites, the sample is illuminated with a single pulse from a KrF (λ=248 nm) excimer laser with duration ~32 ns, FWHM 23 ns, and peak intensity at 16 ns. The laser beam is homogenized to ensure spatial uniformity of ±5% of the incident beam on the sample. The energy from the laser pulse melts the amorphous region down to the crystalline substrate. Resolidification then occurs in crystallographic registry with the underlying substrate. The standard laser energy fluences of 0.30 J/cm^2 and 0.44 J/cm^2 for GaAs- and GaP-based materials, respectively, are sufficiently large to melt the entire amorphous region and produce an epitaxial thin film (Sections 2.3 and 2.4) **[73]**.

Due to the short temporal duration of the laser pulse the heating and cooling processes are rapid. The large cooling rate results in solid-liquid interfacial velocities on the order of several meters per second (Section 2.4). The rapid movement of the interface does not allow sufficient time for the diffusion of atomic species to and from the interface, which is necessary for solidification at equilibrium stoichiometries. Thus, equilibrium solubility limits can be overcome via this kinetically-controlled "solute trapping" process (Section 2.5) **[74]**. After PLM, samples are then etched in concentrated HCl for to remove excess Mn from the surface that was present in Ga-rich droplets and in surface oxides **[75]**.

It should be emphasized that the II-PLM method is highly flexible, which makes it well-suited for the current study. Mn can be easily introduced to many semiconductors by ion implantation. By appropriately adjusting the laser energy for the different optical and thermal properties of the semiconductor hosts, one can synthesize numerous $III_{1-x}Mn_xV$ materials by II-PLM although group III-nitrides and AlP are likely exceptions to this rule since they do not have a stable liquid phase and are therefore poor candidates for PLM **[73]**. Quaternary materials are a simple extension through the implantation of a second species. However, positive results in the quaternary alloys have been achieved only in systems where the second implanted element incorporates on the group V (anion) sublattice. If both Mn and the other element (e.g. Be, Zn) prefer the group III (cation) sublattice, the other element will tend to incorporate preferentially to Mn due to the extremely low solubility and segregation coefficient of the latter. Therefore, the quaternary materials discussed in this work will focus on manipulating the composition of the anion sublattice through implantation of P^+, As^+, N^+, or S^+ into Mn^+-implanted GaAs and/or GaP.

2.3. Ion Implantation of Mn into III-V Semiconductors

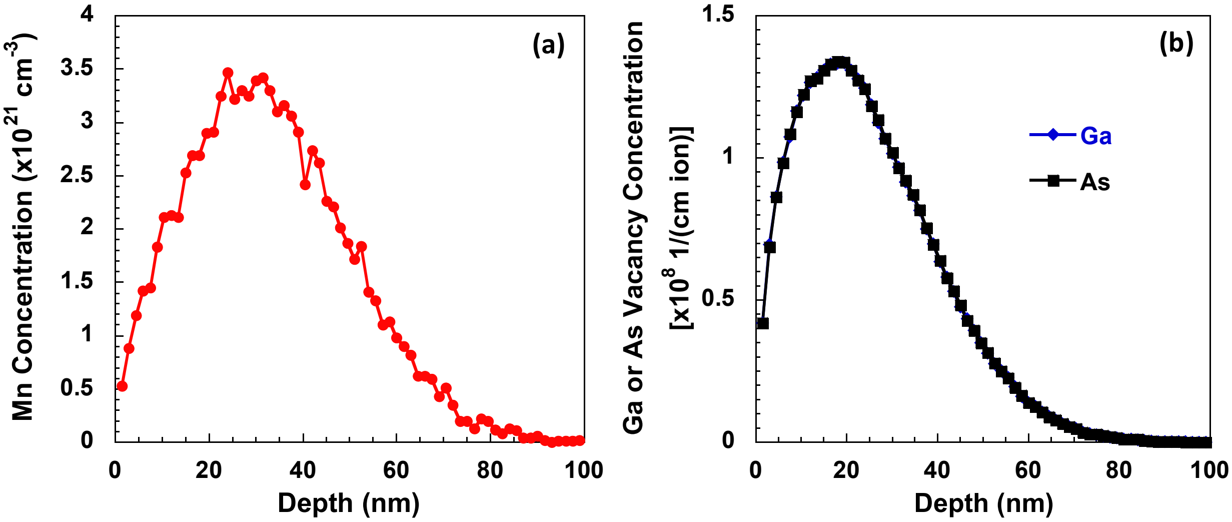

Figure 7: (a) Mn concentration profile after an implantation of $1.5x10^{16}$ 50 kV Mn^+/cm^2 into GaAs at an angle 7° offset from normal. (b) Distribution of vacancies throughout the film for generic Mn implantation into GaAs at 50 kV. The Ga and As curves are basically indistinguishable due to similar defect formation energies. To obtain the vacancy concentration for a specific implant, the ordinate axis should be scaled by the implant dose, which gives the proper units of cm^{-3}. Both panels are simulations done using the SRIM software package for 10,000 incident ions [76].

In ion implantation the semiconductor host is exposed to an ionized beam of the desired dopant species, which is rastered over the surface of the host material. The number of dopant atoms introduced to the system is determined by the integrated current of the beam. Higher currents and longer exposure times lead to higher final concentrations of dopant atoms. This external control of the doping concentration makes ion implantation particularly well-suited for applications in which large, non-equilibrium dopant concentrations are required; in principle only time and surface sputtering limit the final concentration of dopant atoms in the host. The figure of merit for ion implantation is the implanted dose, which is the number of ions per unit area that is incident on the substrate. There is no one-to-one correspondence between dose and concentration. Converting from dose to concentration requires knowing the depth and distribution of ions.

The final distribution of the dopant atoms in the host is determined by a combination of nuclear and electronic stopping of the ions by the substrate target, which dissipates the kinetic energy of the incident ion. For the energy scales and ion masses considered in this work nuclear stopping- that is a binary collision in which some of the energy of the incident ion is transmitted to a displaced host atom- is the dominant mechanism. Energy transfer to the substrate via electronic excitations is prominent only for higher energy implants of ions with low *Z*. The stopping process is statistical. Each ion undergoes a different series of nuclear collisions, which leads to a distribution of dopant atoms throughout the depth of the film that is nonuniform. A representative implantation profile is shown in Figure 7(a) for a 50 kV Mn^+ implantation into GaAs. The profile is a simulation using the Stopping Range of Ions in Matter (SRIM) package, which is a Monte Carlo simulation of implantation process **[76]**. For a 50 kV implant the peak in the Mn concentration occurs at a depth of ~25-35 nm.

One important consequence of ion implantation is that each implanted ion causes numerous damage events through nuclear collisions. SRIM simulations indicate that a 50 kV Mn^+ ion causes about 1000 atomic displacements in GaAs. Hence, the material will be highly damaged after implantation, and, for a sufficiently high implanted dose, will be completely amorphous. To see this more clearly the SRIM-simulated concentration of Ga and As vacancies throughout the film for a 50 kV Mn^+ implant are shown in Figure 7(b). The implant damage more or less tracks the implantation profile, though the peak is slightly closer to the surface. The units are such that multiplying the ordinate value by the implanted ion dose will yield the concentration of vacancies in units of cm^{-3}. For a typical implanted dose of $1.5x10^{16}$ cm^{-2}, the peak total vacancy concentration is on the order of 10^{24} cm^{-3}, which exceeds the atomic density of GaAs by about a factor of 20. It can be reasonably inferred from the simulations that the near-surface region is completely amorphous. Arbitrarily defining the amorphous phase as that concentration of vacancies which is equal to the atomic density of GaAs ($4.42x10^{22}$ cm^{-3}) allows one to place a lower bound on the thickness of the amorphous layer. This corresponds to 80 nm for an implant dose of $1.5x10^{16}$ Mn^+/cm^2 at 50 kV. All implant doses in this work are $\geq 10^{15}$ cm^{-2}, which is more than sufficient to create an amorphous surface layer.

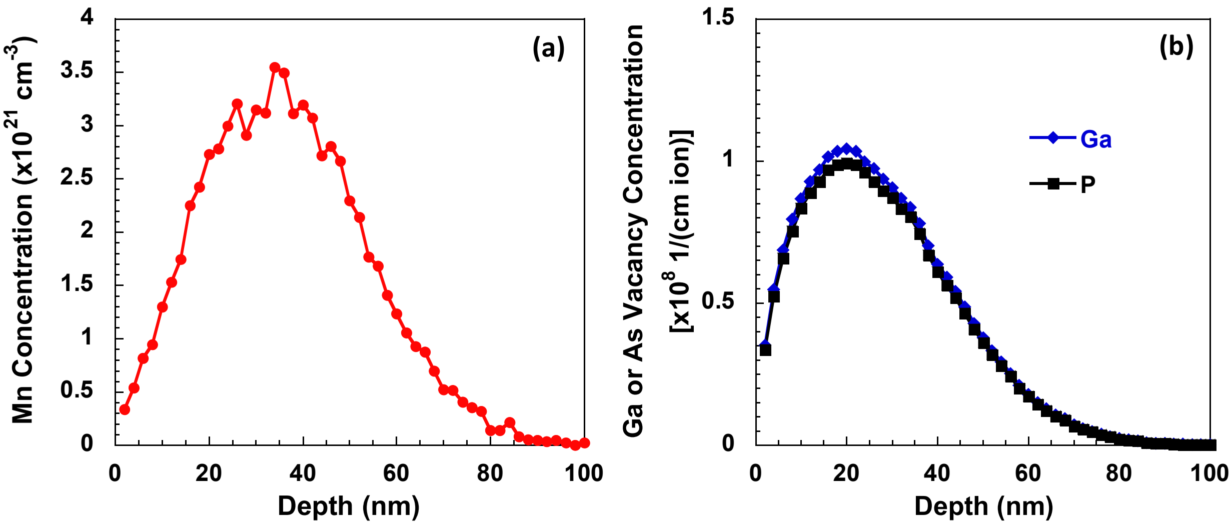

Figure 8: SRIM simulations of (a) Mn concentration, and (b) substrate vacancies for a 1.5x10^{16} 50 kV Mn^{+}/cm^2 implant into GaP at 7° off-normal incidence.

The transition from amorphous to crystalline material is not sharply defined. The defect concentration due to implantation damage decreases gradually with depth. Immediately following the amorphous layer is a highly defective crystalline region, which is referred to as the end-of-range damage. The concentration of point defects then smoothly varies towards its equilibrium value in the substrate as one moves deeper into the film. These characteristic length scales for ion implantation- namely, the amorphous depth and the extent of the end of range damage- factor into the quality of the film that is regrown during the subsequent pulsed-laser melting step. This point will be discussed further in Section 2.4.

For completeness Figure 8 shows the results of SRIM simulations for Mn^{+} implantation into GaP under the same conditions that were used for the simulations in Figure 7. The results are qualitatively similar to those in GaAs except that the peak in the total Mn concentration and vacancy distribution are slightly deeper in the film owing primarily to the lower mass density of GaP relative to GaAs.

In summary ion implantation provides a method for supersaturating a semiconductor with dopants in excess of their equilibrium solubility. For example, the peak concentration of Mn in GaAs shown in Figure 7(a) would represent x=0.11 in a $Ga_{1-x}Mn_xAs$ film if all of the Mn were directly incorporated substitutionally on Ga sites. Of course this is not the case since the implant process causes the layer to be amorphous. Thus, the goal of the following step is to repair the lattice damage while maintaining dopant supersaturation. The following sections briefly describe how pulsed-laser melting can achieve this goal.

2.4. Heating and Cooling of a Material During PLM

In general, the heating of an ion-implanted material by a laser pulse and the subsequent cooling process constitute a complex problem. To completely treat the problem requires knowledge of the thermal and optical properties of the sample as well as the temporal and spatial characteristics of the laser pulse. The problem is further complicated by phase changes, and additional latent heat terms must also be introduced. The thermal and optical properties are also different for the different phases. Moreover, the materials properties of the amorphous and liquid phases as a function of temperature are generally not well tabulated for many materials.

Even if these parameters are all known, the problem can only be solved numerically. A detailed numerical treatment of this problem is found elsewhere **[73, 77]**.

Here some general qualitative observations of the heating and cooling processes are made. If the energy of an individual photon in the laser pulse is greater than the band gap of the semiconductor then it can be assumed that the absorbed light intensity is instantaneously converted to heat. The incident photons are absorbed and excite bound electrons over the bandgap of the material while holes are formed in the valence band. Further free-carrier absorption by these excited photoelectrons can occur which raises their energy well above the conduction band minimum. This excess electronic energy is then converted to heat. The excited electrons quickly come into thermal equilibrium with one another and can be treated as a plasma phase. The hot carriers then heat the lattice by emitting phonons as they relax to lower energy states before eventually recombining. The emitted phonons are responsible for the lattice heating. The timescale for electron-lattice relaxations is on the order of 10^{-11}-10^{-12} seconds, which is essentially instantaneous for the timescales associated with laser heating by nanosecond pulses.

Once the surface has been melted, the remaining energy of the laser pulse drives the liquid-solid interface inward. For a given pulse width duration, higher power pulses increase the volume of the sample that is melted. Once the laser pulse has ended and the source of heat removed from the system the molten volume resolidifies from the internal liquid solid interface towards the surface. The underlying solid material is used as a "template" for growth **[78]**. If low energy densities are used the melt depth may not exceed the amorphized depth of the implanted region. The resulting films are either amorphous or highly defective polycrystals since the template has no long range order. If the energy density is sufficiently high, the material is melted all the way down to the undamaged crystalline substrate. In this case the crystal quality is very high. Intermediate energies melt down to the end of implantation range damage and result in films of intermediate quality. These qualitative observations underscore the importance of considering the characteristic length scales of both ion implantation and laser processing **[73]**. In general it is best to work in a regime where the implantation range and melt depth are approximately the same, which allows for the greatest flexibility in determining the final properties of the film.

The velocity of the liquid-solid interface during resolidification can be estimated by considering the conservation of heat **[77, 79]**. As the interface moves towards the sample surface the latent heat of fusion (ΔH_m) that is liberated must be conducted away from the interface through the substrate. The heat balance is expressed as

$$\Delta H_m \rho v = \left(\frac{\partial T}{\partial z}\right)_i \tag{7}$$

where $(\partial T/\partial z)_i$ is the temperature gradient in the solid immediately behind the interface, v is the velocity of the interface, and ρ is the mass density. Since the temperature of the material immediately adjacent to the interface is at the melting point (T_m) and the characteristic length scale for heat transfer is the thermal diffusion length

$$L_{th} = 2\sqrt{D_{th}\tau}, \tag{8}$$

the temperature gradient can be approximated as

$$\left(\frac{\partial T}{\partial z}\right)_i = \frac{T_m}{2\sqrt{D_{th}\tau}}. \tag{9}$$

Table 1: Thermal properties of several semiconductors near their melting point as well as the calculated interfacial velocity according to Equation 10.

Material	κ [W cm^{-1}K^{-1}]	ΔH_m [J/g]	ρ [g/cm^3]	C_p [J g^{-1} K^{-1}]	T_m [K]	v [m/s]
GaP	0.1$^{(a)}$	1200$^{(b)}$	4.14	0.5$^{(c)}$	1749	4.5
GaAs	0.1$^{(d)}$	728$^{(d)}$	5.32	0.4$^{(d)}$	1511	5.0
Si	0.2$^{(e)}$	1790$^{(f)}$	2.33	1.0$^{(g)}$	1687	7.8

$^{(a)}$Ref. **[80]**; $^{(b)}$Ref. **[81]**; $^{(c)}$Estimated from Ref. **[82]**; $^{(d)}$Ref. **[83]**; $^{(e)}$Ref. **[84]**; $^{(f)}$Ref. **[77]**; $^{(g)}$Ref. **[85]**

In Equations 8 and 9 τ is the temporal pulse duration of the laser, $D_{th}=\kappa/\rho C_p$ is the thermal diffusivity, κ is the thermal conductivity, and C_p is the heat capacity of the material. Combining Equations 7 and 9, the velocity of the interface is

$$v = \frac{\sqrt{\kappa C_p}}{\Delta H_m \sqrt{\rho}} \frac{T_m}{2\sqrt{\tau}} \tag{10}$$

where the thermal diffusivity term has been expanded to emphasize the dependence of the interfacial velocity of the thermal and structural parameters of the material. To obtain the most accurate estimate of the interfacial velocity, Equation 10 should be evaluated using the thermal properties of the solid near its melting point, which are listed in Table 1 for GaP, GaAs, and Si. For the KrF excimer laser in this study (τ=32 ns) the interfacial velocities are on the order of meters per second.

2.5. Solute Trapping

The large velocity of the solid-liquid interface during regrowth is the primary factor that allows for the incorporation of dopants in excess of their equilibrium solubility. If the interface were moving at near-zero velocity, then the growing solid would incorporate the alloying species according to equilibrium thermodynamics. In general the concentration of a solute in the solid and liquid phases is different and characterized by the equilibrium segregation coefficient

$$k_0 = \frac{C_s}{C_l} \tag{11}$$

where C_s and C_l and the equilibrium concentrations of the solute in the host solid and liquid phases respectively. There will be a discontinuity in the concentration of impurity at the liquid-solid interface as shown in Figure 9 (a), which arbitrarily assumes that $k_o = 1/3$. As solidification occurs, solute is rejected at the interface since $k_0 < 1$. To maintain impurity concentration C_l in the liquid near the interface, the excess impurity atoms must diffuse away, which takes some finite amount of time.

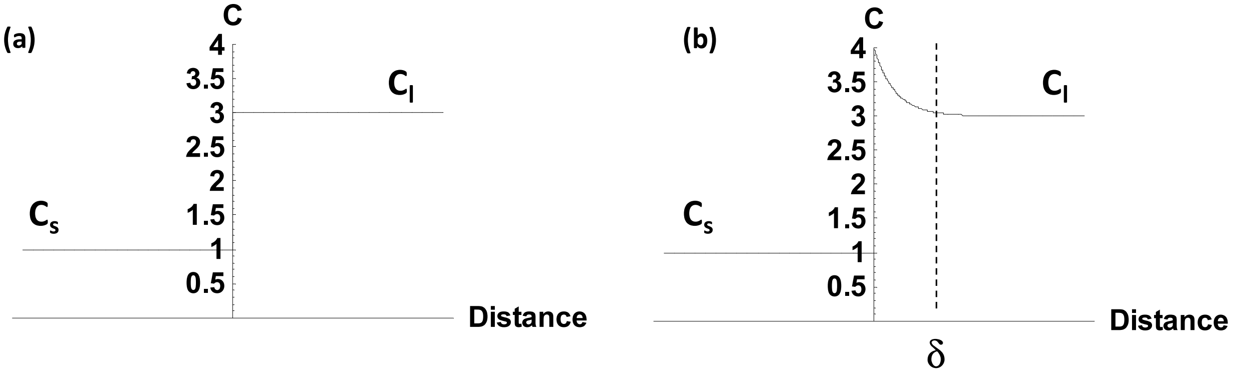

Figure 9: Impurity concentration near a moving solid-liquid interface for (a) zero interfacial velocity, and (b) finite growth rate.

A more realistic picture of the advancing solid-liquid interface is given in Figure 9 (b). There is some characteristic distance, δ, over which the liquid is locally out of equilibrium since the interface is moving faster than impurities can diffuse away from it. The appropriate figure of merit of the degree of dopant segregation is no longer the equilibrium segregation coefficient but the *effective* segregation coefficient *k'*. According to simplified Burton-Prim Slichter theory *k'* is related to the equilibrium segregation coefficient, k_o, by**[86]**

$$k' = \left[1 + \left(\frac{1}{k_0} - 1\right) exp\left(-\frac{v\delta}{D}\right)\right]^{-1} \tag{12}$$

where *D* is the solute diffusivity through the stagnant layer which is usually intermediate to the values of the diffusivity of the solute in the solid and liquid phases **[87]**. Some general conclusions about impurity segregation can be drawn from Equation 12. As the magnitude of the triple $v\delta / D$ increases, the exponential function tends to zero and *k*' tends to 1, which represents a supersaturation of solute in the solid phase. This process is known as solute trapping. For example, as the width of the stagnant layer, δ, increases, so does *k*' since the impurity atoms must diffuse over a longer distance. Similarly *k*' increases as *D* decreases since slowly diffusing impurity atoms require a longer time to leave the stagnant layer. These are primarily materials properties and generally cannot be significantly affected by altering the processing parameters. What can be controlled through processing, however, is the interfacial velocity. As $v \rightarrow \infty$, $k' \rightarrow 1$ demonstrating that high liquid-solid interfacial velocities enhance substitutional incorporation of dopants.

2.6. $Ga_{1-x}Mn_xAs$ Grown by II-PLM

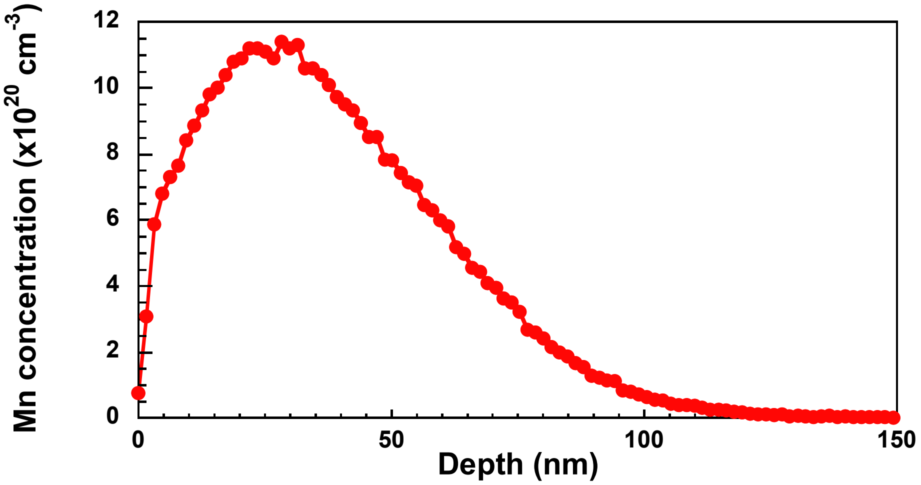

Figure 10: Measured total Mn concentration as a function of depth for a GaAs film implanted with $1.5\text{x}10^{16}$ Mn^+/cm^2 at 50 kV and laser melted using a 0.3 J/cm^2 pulse from a KrF laser. The sample was etched in concentration HCl for 20 minutes after PLM to remove Ga-rich surface phases as well as Mn-related oxide species.

Figure 10 shows the total Mn concentration profile in a typical $Ga_{1-x}Mn_xAs$ film formed by II-PLM. A maximum Mn concentration in the film of $>10^{21}$ cm^{-3} is observed and Mn concentrations of over 10^{20} cm^{-3} exist for ~100 nm. From ion beam analysis (Appendix A), it was determined that 80% of the Mn atoms reside in substitutional positions. These two observations demonstrate that the II-PLM method is capable of overcoming the 10^{18}-10^{19} cm^{-3} maximum equilibrium solubility limit of Mn in GaAs by one to two orders of magnitude. The total concentration of Mn in the film after PLM is about a factor of 2 or 3 less than was present in the as-implanted state (compare Figure 7 and Figure 10). This implies that the factor limiting Mn incorporation is not the concentration of implanted ions, but the redistribution of Mn in the growing solid during PLM. The "missing" Mn atoms were likely segregated to the surface during PLM and subsequently removed by the post-PLM etching step or ablated during PLM. Hence, while the experimental setup is sufficient to exceed solubility limits of Mn in GaAs, there is still room for improving *k*' by optimizing the PLM parameters and driving the liquid-solid interface to even higher velocities.

Similar results hold for Mn in GaP (see Appendices A and B). Further information about the synthesis of $Ga_{1-x}Mn_xP$ and $Ga_{1-x}Mn_xAs$ by II-PLM can be found elsewhere **[73, 75, 88-90]**.

In order to demonstrate the viability of II-PLM as a reliable method for synthesizing ferromagnetic semiconductors, it is necessary to confirm that the properties of films produced by II-PLM are similar to more well-established LT-MBE counterparts. This step is particularly important since, unlike typical LT-MBE films, $Ga_{1-x}Mn_xAs$ formed by II-PLM has a non-uniform concentration of Mn throughout the film thickness. Measurements of several important properties of $Ga_{1-x}Mn_xAs$ synthesized by II-PLM are shown in Figure 11. Figure 11(a) shows that the films are clearly ferromagnetic with a sharp ferromagnetic to paramagnetic transition occurring at approximately 100 K. The temperature dependence of the electrical resistivity [Figure 11(b)] shows the characteristic lineshape observed in $Ga_{1-x}Mn_xAs$ grown by LT-MBE with critical behavior observed near $T=T_C$. Further discussion of the electrical transport behavior of $Ga_{1-x}Mn_xAs$ can be found in Section 4.3. The Hall resistance [Figure 11(c)] shows a strong anomalous component that tracks the out-of-plane field-dependent magnetization profile indicating that the mobile charge carriers are participating in ferromagnetic exchange **[90]**. Finally, Figure 11(d) shows the relation between T_C and x for $Ga_{1-x}Mn_xAs$ produced by both LT-MBE and II-PLM. When x is defined for II-PLM films as the peak substitutional Mn concentration, it is observed that both LT-MBE and II-PLM films fall along the same approximately linear relationship expected for carrier mediated ferromagnetism. Hence, the static electronic and magnetic properties of $Ga_{1-x}Mn_xAs$ are substantially similar to films produced by LT-MBE. The effects of the alternate II-PLM processing method can be excluded as being responsible for any differences observed in the behavior of the novel ferromagnetic semiconductor alloys presented in Chapters 3 through 5.

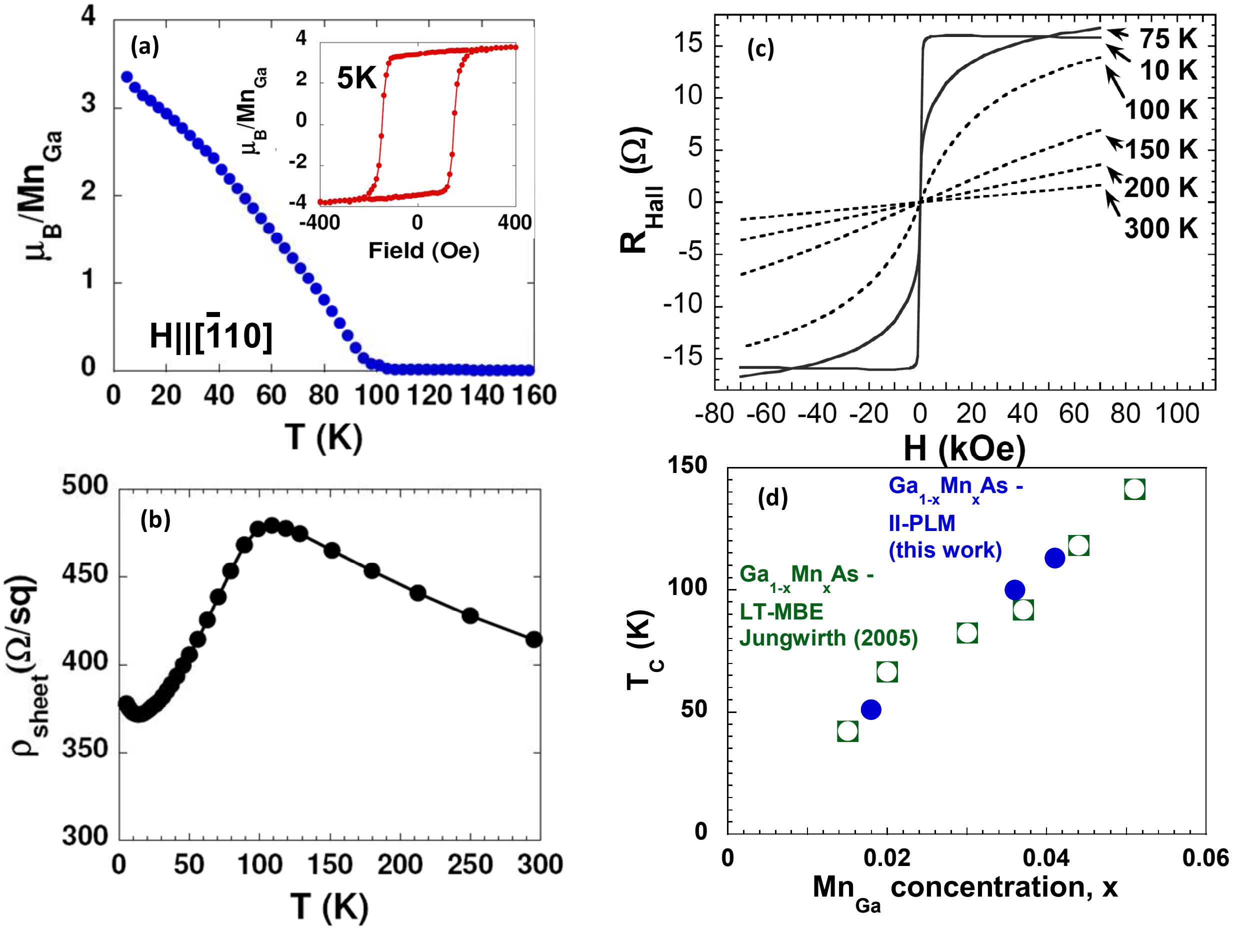

Figure 11: (a) Magnetization as a function of temperature and field (inset) for $Ga_{1-x}Mn_xAs$. The temperature dependent measurement was performed at μ_0H=5 mT. (b) Temperature dependence of the sheet resistivity for the same material. (c) Field dependence of the Hall resistance at various temperatures. After [90]. Films in panels (a), (b), and (c) have $x\approx0.04$. Relationship between T_C and x for $Ga_{1-x}Mn_xAs$ produced by II-PLM and LT-MBE. LT-MBE data from Ref. [31].

3. Complete Anion Substitution: $Ga_{1-x}Mn_xP$

3.1. Introduction

Early reports of ferromagnetism in Mn-doped GaP focused largely on polycrystalline materials grown by molecular beam epitaxy and/or ion implantation followed by rapid thermal annealing **[91-93]**. These studies were initially quite exciting as ferromagnetic behavior persisted up to room temperature (300 K) suggesting that the GaP semiconductor host provided a more robust environment for ferromagnetism than GaAs or InAs. However, insufficient evidence was given to establish that the magnetic behavior of the samples was *carrier-mediated*. Characterization focused mostly of SQUID magnetometry measurements, which can only distinguish the total magnetic moment of the sample and gives no insight as to its origin. Little to no connection was made between the magnetic and electrical transport characteristics of the materials. The authors never clearly established that the Mn dopants were substitutionally incorporated onto the Ga sublattice as required for carrier-mediated ferromagnetism according to the standard models (Section 1.5). Moreover, the processing temperatures used in these studies are inconsistent with the formation of a metastable state in which the Mn reside predominantly on Ga sites. The MBE growth temperature of the Mn-doped semiconductor was 600° C **[92]**. This growth temperature is known in $Ga_{1-x}Mn_xAs$ to result in phase segregation of MnAs **[67]**. For ion-implanted films the implantation step was done at 350° C followed by a post-implantation anneal at 700 ° -1000 ° C for 5 minutes **[94]**. These processing temperatures are above the activation threshold for removal of Mn from Ga sites, which occurs for heat treatments above 300° C **[95]**. It is unlikely that the observed magnetic behavior in these studies is due to carrier-mediated exchange among Mn_{Ga} moments. A more plausible explanation is that the observed magnetic properties are due to Mn-rich second phases such as MnP or $Ga_{1-x}Mn_x$-type compounds. The combination of Mn^+ ion implantation and heat treatment at 600°-920° C for 0.083-20 min is known to give rise to submicron-sized $Ga_{1-x}Mn_x$ ferromagnets **[96]**. Furthermore, MnP has a T_C of ~291 K **[97]** while several $Ga_{1-x}Mn_x$ phases with above 300 K T_C are known to exist (for example Mn_7Ga_3 has T_C=470 K **[98]**), which may explain the observations of room temperature ferromagnetism in Refs. **[91-94]**. The hypothesis of ferromagnetism due to second phases is further supported by the fact that the films in question are polycrystalline thereby containing grain boundaries which can serve as nucleation sites for second phases **[73]**.

More recently it was demonstrated that II-PLM is a viable growth method that can produce epitaxial $Ga_{1-x}Mn_xP$ thin films **[73, 99]**. Ion-channeling analysis and transmission electron microscopy (TEM) of II-PLM-formed $Ga_{1-x}Mn_xP$ revealed that the films are single crystalline, epitaxial and have the majority of Mn atoms incorporated substitutionally on Ga sites **[88]**. Electrical and optical studies of $Ga_{1-x}Mn_xP$ indicated that the carriers responsible for mediating ferromagnetic exchange are *localized* in a Mn-derived *impurity-band* that remains unmerged with the GaP valence band for $x \leq 0.042$. Nonetheless, ferromagnetic behavior was observed in $Ga_{1-x}Mn_xP$ although T_C is lower in $Ga_{1-x}Mn_xP$ than $Ga_{1-x}Mn_xAs$ for a given x due to the more strongly localized carriers in the former.

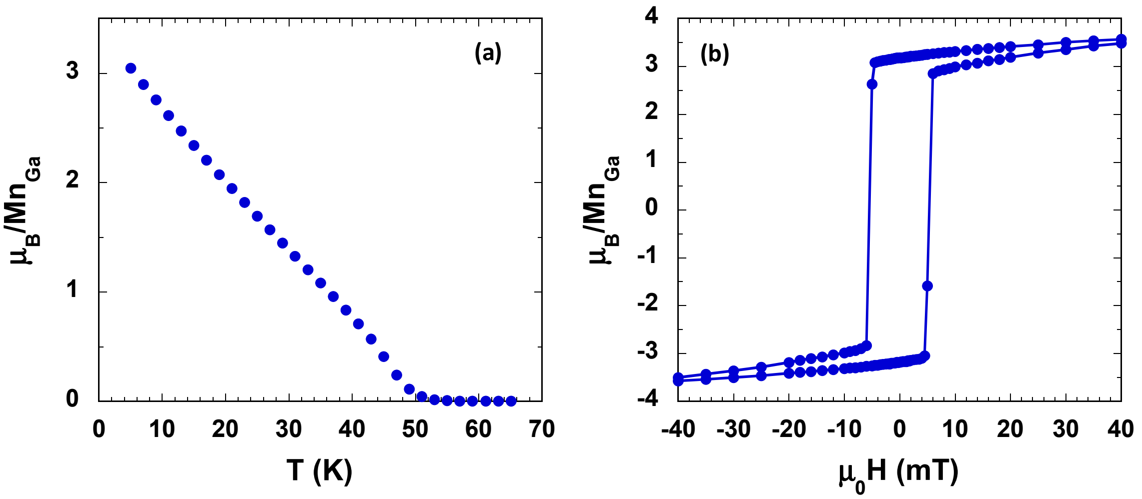

Figure 12: (a) Zero-field cooled thermomagnetic curve for $Ga_{0.962}Mn_{0.038}P$ measured in an applied field μ_0H=1 mT. (b) Field-dependence of the magnetization for the same sample at T=5 K. The applied field was parallel to the in-plane [0-11] direction in both measurements.

This chapter focuses on the current author's own contributions to the understanding of $Ga_{1-x}Mn_xP$ films produced by II-PLM. These studies have provided further proof that ferromagnetism in $Ga_{1-x}Mn_xP$ synthesized by II-PLM is carrier-mediated. The characterization of a series of $Ga_{1-x}Mn_xP$ films with varying Mn concentration ($0.0042 \leq x \leq 0.042$), as well as different levels of intentional compensation by S donors is presented in Section 3.2. Magnetometry measurements of these samples show the proper T_C scaling with x and p. Section 3.3 details X-ray absorption and magnetic circular dichroism spectroscopy measurements of $Ga_{1-x}Mn_xP$. These synchrotron techniques probe directly the Mn atoms responsible for ferromagnetic exchange. The Mn X-ray absorption and circular dichroism lineshapes show spectroscopic signatures of the high-spin $3d^5$ configuration identical to that observed in $Ga_{1-x}Mn_xAs$. Section 3.4 gives a brief overview of the onset of ferromagnetism of $Ga_{1-x}Mn_xP$ as a function of Mn doping. This is followed by a discussion of the collective evidence that demonstrates that ferromagnetism in $Ga_{1-x}Mn_xP$ is *carrier-mediated* in Section 3.5. The evidence for carrier-mediated ferromagnetism includes an extensive magnetic anisotropy study of $Ga_{1-x}Mn_xP$ and its alloys that is given its own chapter later in this dissertation (Chapter 5). Finally, $Ga_{1-x}Mn_xP$ is compared to other $III_{1-x}Mn_xV$ systems in Section 3.6, which is followed by a summary of the chapter (Section 3.7). Several important early studies of $Ga_{1-x}Mn_xP$ that were done by my Dubón Group colleagues are presented as appendices. A discussion of the ion-beam techniques used to probe the lattice location of Mn atoms as well as the methods used to determine the overall thin film composition are given in Appendix A. Details of the electrical and optical measurements which were crucial to establishing the localized, impurity-band nature of the charge carriers responsible for ferromagnetic exchange are presented in Appendix B. Appendix B also contains information regarding the synthesis parameters and structural properties of the $Ga_{1-x}Mn_xP$ films discussed in this chapter.

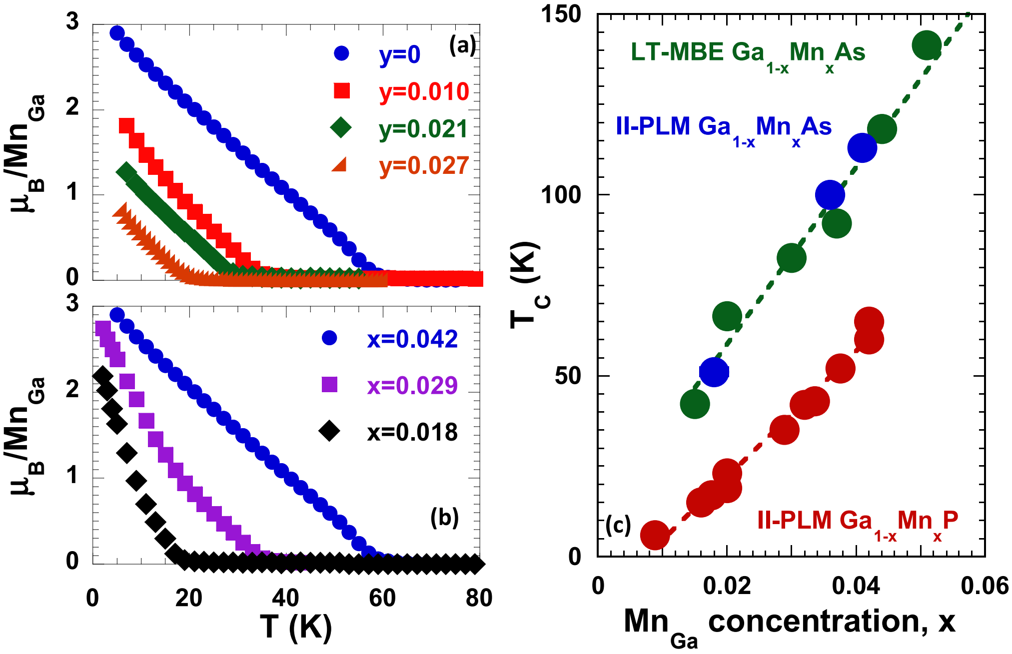

Figure 13: Temperature-dependence of the magnetization as a function of (a) x (after [31]]) and (b) p (after [40]). Data were taken with the applied field $\mu_0 H$=5 mT parallel to an in-plane <110> direction. Samples in panel (b) have x=0.041 except for y=0 which has x=0.042. (c) T_C as a function of x for II-PLM grown $Ga_{1-x}Mn_xP$ and $Ga_{1-x}Mn_xAs$ as well as LT-MBE grown $Ga_{1-x}Mn_xAs$. The dashed lines are linear fits to the data. II-PLM data from [31] and [83]. LT-MBE data from Ref. [74].

3.2. Magnetic Properties of $Ga_{1-x}Mn_xP$

Despite the localized nature of the charge carriers in $Ga_{1-x}Mn_xP$ long range ferromagnetic interactions are observed. Figure 12 (a) shows the temperature dependence of the magnetization for a $Ga_{1-x}Mn_xP$ sample with x=0.038. The data were measured in an applied field $\mu_0 H$=1mT parallel to $\left[0\bar{1}1\right]$ after zero-field cooling. The $\left[0\bar{1}1\right]$ direction is the magnetic easy axis for this sample (Section 5.5). A clear and distinct rise in the magnetization is observed at T_C=50 K. The field-dependence of the magnetization for the same sample exhibits hysteresis and is shown in Figure 12 (b). Hysteresis persists until $T \approx T_C$ at which point is disappears, which is consistent with ferromagnetic behavior (not shown). At fields of greater than 1 T, the magnetic moment saturates to a value of ~3.6 μ_B/Mn_{Ga} at this low temperature limit, which is on the same order as the 4-4.5 μ_B/Mn_{Ga} observed in the carrier-mediated phase of $Ga_{1-x}Mn_xAs$ **[20]**.

Figure 13 (a) shows the effect of intentional compensation of holes by incorporation of S donors onto the anion sublattice on T_C for constant Mn_{Ga} concentration. The quaternary $Ga_{1-x}Mn_xP_{1-y}S_y$ alloys were synthesized by implantation of S^+ ions into Mn-implanted GaP prior to PLM. Further details of the synthesis procedure can be found in Section 5.7.1 and references **[100]** and **[101]** . As expected for carrier-mediated ferromagnetism T_C decreases monotonically with increasing y due to compensation of the ferromagnetism-mediating holes by S donors. A parallel trend has been observed in $Ga_{1-x}Mn_xP$ co-doped with Te **[99]**. Figure 13 (b) shows thermomagnetic curves for several $Ga_{1-x}Mn_xP$ samples with different Mn_{Ga} concentration x. The ferromagnetic Curie temperature of $Ga_{1-x}Mn_xP$ is proportional to x providing further evidence of carrier-mediated ferromagnetism.

Figure 13 (c) compares the dependence of T_C with x for $Ga_{1-x}Mn_xAs$ and $Ga_{1-x}Mn_xP$. For a given value of x, the T_C of a $Ga_{1-x}Mn_xP$ thin film is lower than its arsenide counterpart. This behavior is attributed to the decreased efficacy of localized carriers at mediated ferromagnetic exchange between the Mn_{Ga} moments. The dependence of T_C on x is substantially similar in these two materials suggesting that similar mechanisms are responsible for ferromagnetic exchange in the two materials despite the differences in carrier localization. Indeed, both sets of data are well described by linear trends, though other fits (e.g. $x^{4/3}$) also reasonably describe the $Ga_{1-x}Mn_xP$ data over this dilute range of x. Linear extrapolation of the $Ga_{1-x}Mn_xP$ data to room temperature implies that x~0.18 is required for room temperature ferromagnetism in this system. The data for both II-PLM-formed and LT-MBE-formed $Ga_{1-x}Mn_xAs$ follow the same linear trend indicating that II-PLM processing of materials has little influence on T_C (Section 2.6).

3.3. X-ray Magnetic Circular Dichroism (XMCD) in $Ga_{1-x}Mn_xP$

XMCD provides a means for probing directly the element or elements responsible for ferromagnetism in a material. The element-specific magnetic information is obtained through measuring resonant photon absorption in which either the initial or final states are at least partially responsible for a material's magnetic moment. In the context of $III_{1-x}Mn_xV$ ferromagnetic semiconductors, one probes $2p \rightarrow 3d$ excitations (i.e. the L_3 and L_2 absorption edges), which provides information about the spin polarized $3d$ density of states at E_F. A more detailed description of the theory underlying XMCD is found in Appendix D. XMCD provides supplementary information to that provided from the aforementioned traditional bulk characterization techniques (e.g. SQUID magnetometry). As an X-ray absorption spectroscopy it is *element-specific*. Therefore, XMCD can unambiguously verify that Mn is, indeed, the source of ferromagnetism in these materials. Furthermore, examination of the XMCD spectral lineshape provides information about the local bonding and electronic structure around each magnetically active, Mn_{Ga} atom **[102]**.

3.3.1 *Experimental*

Room temperature X-ray absorption spectroscopy (XAS) was performed at beamline 8.0 at the Advanced Light Source (ALS). Low-temperature XAS and XMCD measurements were carried out between 13 and 52 K in the vector magnetometer endstation at beamline 4.0.2 at the ALS in applied fields of up to ±0.54 T **[103]**. Data were collected with 90% circular polarization of the incident X-rays. The field and beam were oriented 30º from the sample normal towards a <011> in-plane direction. The dichroism signal was produced by fixing the circular polarization of the incident photons and reversing the sample's magnetization axis. This is equivalent to holding the sample magnetization constant and reversing the circular polarization of the photons (Appendix D).

Data were collected both total electron yield (TEY) and total fluorescence yield (TFY) modes. These detection methods provide complementary information as TEY is very surface sensitive while TFY can probe depths on the order of a few tens of nanometers **[104]**. To facilitate TEY data collection samples were mounted on a Cu rod using doubled-sided adhesive conductive carbon tape. Silver paste was applied around the perimeter of the sample to improve electrical contact. In some measurements a small Indium contact was soldered to the sample to mitigate surface charging. The samples were surrounded by a gold mesh that is kept at a positive bias, which serves as a collector for the photoemitted electrons for TEY data acquisition.

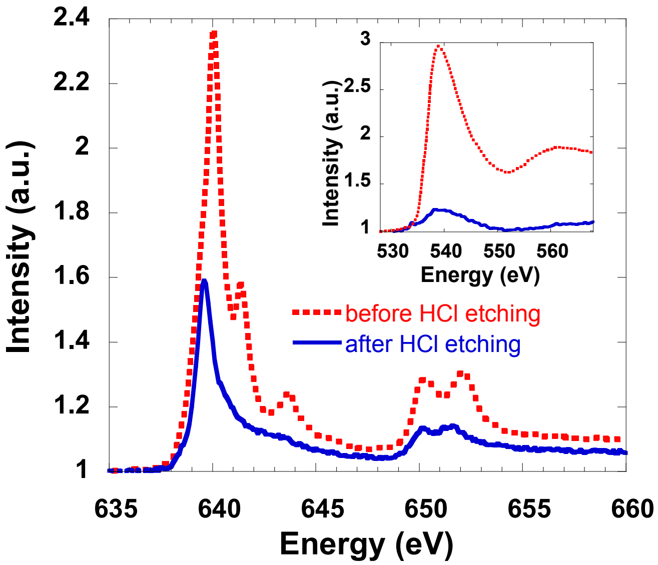

Figure 14: Room temperature XAS spectra before and after etching in HCl for 24 hrs for a $Ga_{0.958}Mn_{0.042}P$ at the Mn $L_{3,2}$ edge (main) and oxygen K edge (inset).

3.3.2 *Room Temperature X-ray Absorption Spectroscopy (XAS)*

Early XMCD experiments on $Ga_{1-x}Mn_xAs$ were obscured by the presence of native oxide phases on the surface of the thin films **[105, 106]**. This led to the observation of a so-called "magnetization deficit" in the XMCD measurements in which it appeared less than 15% of the Mn atoms were involved in ferromagnetic exchange within the film. These issues were resolved through a simple HCl etch immediately before measurements were taken **[107]**. TEM analysis revealed that the HCl etch removes an MnO phase that was present at the surface. Upon removal of this oxide, there was a distinct change in the X-ray absorption lineshape which was consistent with Mn in the GaAs lattice as opposed to Mn in a surface oxide.

Similar precautions were therefore taken before commencing XMCD studies of $Ga_{1-x}Mn_xP$ in order to minimize the effect of surface oxide phases. The main panel of Figure 14 presents room temperature XAS data at the Mn $L_{3,2}$ edge taken in total electron yield (TEY) mode from a sample having x=0.042 before and after etching with HCl for 24 hours. The pre-edge absorption intensities have been normalized to unity and the main Mn^{2+} absorption peak in the unetched sample has been calibrated to fall at an energy of 640.0 eV. The spectrum before HCl etching shows multiple sharp peaks characteristic of the unhybridized atomic Mn d^5 absorption spectrum, which is similar to that observed in MnO **[102, 107]**. The atomic multiplets and higher energy peaks disappear after etching, resulting in the smoother Mn absorption spectrum characteristic of the orbital mixing between Mn_{Ga} d states and phosphorus p states. Furthermore, the L_3 absorption peak shifts to a lower energy by approximately 0.5 eV, which is characteristic of the spectral change from atomic to hybridized Mn **[102, 107]**.

Corresponding effects can be seen at the oxygen K-edge, as demonstrated in the inset to Figure 14. After etching, the signal from oxygen is reduced by an order of magnitude demonstrating the removal of a majority of surface oxide phases. A very small residual oxygen signal is still observed perhaps due to brief exposure of the sample to air after etching. The strong spectral shifts observed at the Mn $L_{3,2}$ edge indicates that the Mn atoms that we are probing via X-ray absorption are predominantly incorporated substitutionally into the GaP lattice. Therefore, the following XAS and XMCD signals obtained at low temperature arise primarily from Mn in the GaP matrix and not from surface oxide phases.

3.3.3 *XMCD Spectra of $Ga_{1-x}Mn_xP$*

Figure 15(a) presents Mn $L_{3,2}$ TEY XAS spectra taken at 17 K with the field and photon helicity parallel (I^+) and antiparallel (I^-) for $Ga_{0.966}Mn_{0.034}P$. The XMCD spectrum is also shown. Linear backgrounds fit to the pre-edge region were subtracted from the raw data, and the data were normalized to the main L_3 peak. Strong XMCD is present at both the L_3 and L_2 edges indicating strong magnetization of Mn and a large spin polarization of states derived from Mn *d* levels at E_F. Very similar XMCD spectra were obtained for all of the samples with different compositions as shown in Figure 15(b). These spectra were all measured in a field of 0.5 T at a temperature of 17 K. Successive spectra are offset from each other by 0.2 arbitrary units for clarity. This behavior is similar to that observed in $Ga_{1-x}Mn_xAs$ in which the XMCD lineshape is not altered by the Mn concentration **[20]**.

The existence of a large Mn XMCD asymmetry at large magnetic fields does not itself imply ferromagnetism. In large fields even paramagnetic moments would show a dichroism due to the field-induced Zeeman splitting. Therefore, measurements were performed to determine the remanent XMCD signal. The sequence of steps to produce a remanent XMCD spectrum is as follows:

1. Apply a large, positive magnetic field greater than the sample's coercive field. In this case a field of 400 mT was used. Measure the intensity (I_1).
2. Reduce the field to zero. Measure the intensity (I_2).
3. Apply a large, negative magnetic field symmetric to that in step 1. Measure the intensity (I_3).
4. Reduce the field to zero. Measure the intensity (I_4).

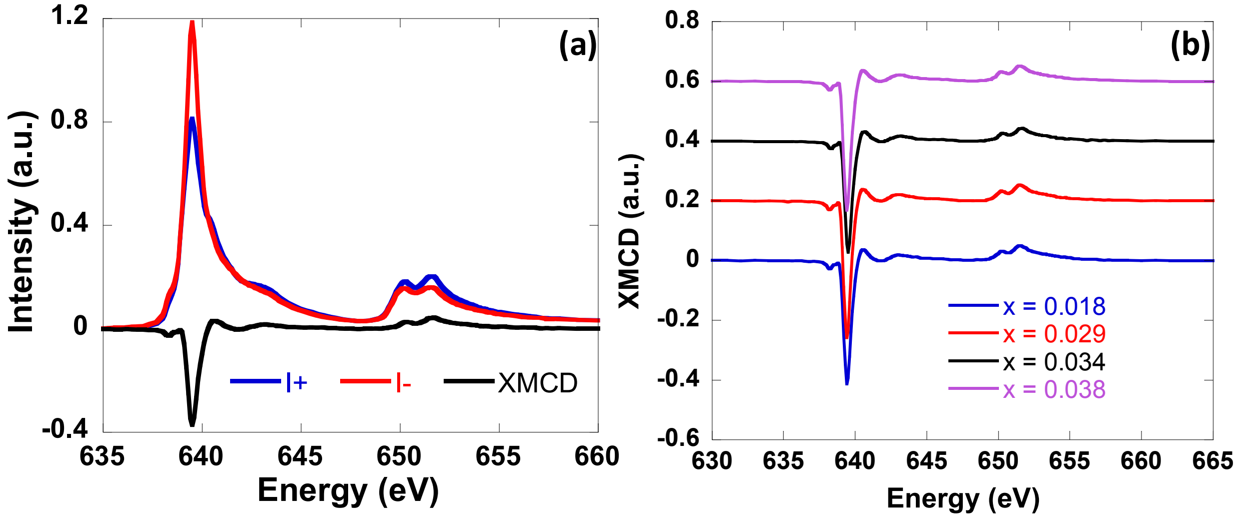

Figure 15: (a) Mn $L_{3,2}$ TEY XAS spectra for magnetization and helicity parallel (I^+) and antiparallel (I^-) as well as the difference (XMCD) spectrum for a $Ga_{0.966}Mn_{0.034}P$ measured at 17 K. (b) Mn $L_{3,2}$ XMCD spectra for $Ga_{1-x}Mn_xP$ samples with different Mn_{Ga} concentration. Successive spectra have been offset by 0.2 for clarity. Data were measured in an applied field of 0.5 T at a temperature of 17 K.

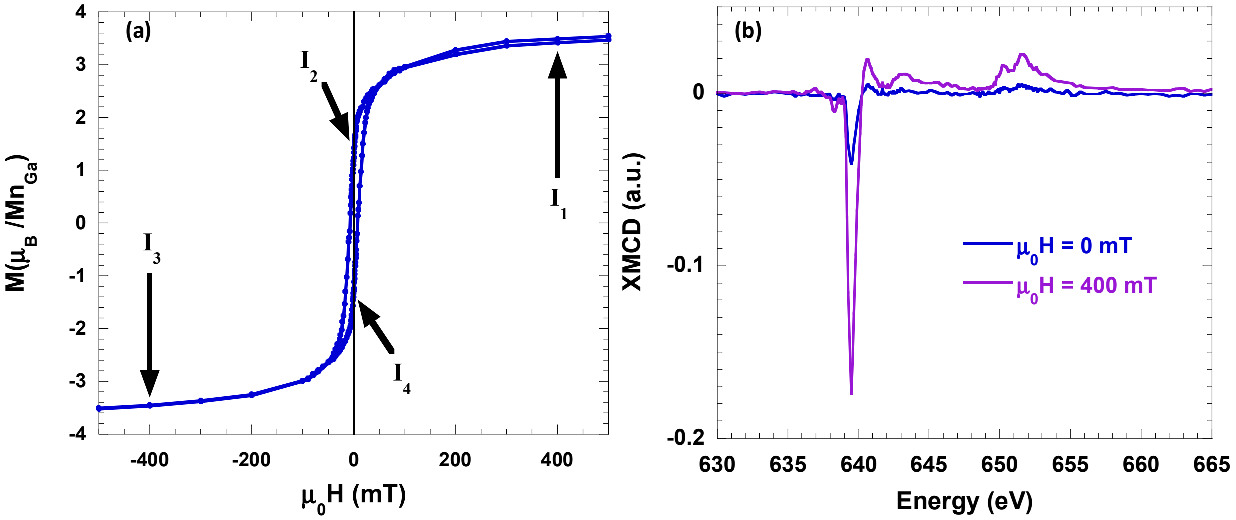

Figure 16: (a) Field-dependence of the magnetization for a $Ga_{0.966}Mn_{0.034}P_{1-y}N_y$ sample with $y \approx 0.004$ measured at T=5K with the field oriented normal to the plane of the film. (b) XMCD spectra of the same sample measured with an applied field of 400 mT and at remanence. The XMCD data were taken at 13 K.

The points in the hysteresis loop at which the intensities are measured according to this sequence are illustrated in Figure 16 (a) for a $Ga_{0.966}Mn_{0.034}P$ sample that has been alloying with N. The nitrogen content of the anion sublattice was approximately 0.4%. The N alloying reduces the lattice constant of the film, which causes the magnetic easy axis to rotate out of the plane of the film (Sections 5.3 and 5.6). This step was necessary for remanent measurements since the experimental geometry is such that the out-of-plane component of the magnetization is probed by the XMCD measurement. $Ga_{1-x}Mn_xP$, which has an in-plane easy axis does not show a remanent moment in the out-of-plane geometry [see Figure 45 (a)]. From the measurement sequence the XMCD spectra is determined at both 400 mT (I_1-I_3) and at 0 mT (I_2-I_4). These XMCD spectra are shown in Figure 16 (b) and were measured at a temperature of 13 K. The sample clearly shows remanent XMCD, which indicates that the Mn moments are *ferromagnetically* coupled. Quantitative comparison is hindered by the different measurement temperatures used for the two measurements shown in Figure 16. However, the remanent XMCD intensity is greatly reduced relative to the near-saturation value measured at 400 mT in qualitative agreement with the field-dependent magnetization measurements.

3.3.4 *Comparison of Electron Yield and Fluorescence Yield Results*

Figure 17 displays Mn $L_{3,2}$ XMCD spectra collected in both the total fluorescence yield and total electron yield modes for a $Ga_{1-x}Mn_xP$ film with x=0.034. The ratio of the intensity of the L_3 peak to the L_2 peak is smaller in the TFY measurement than the TEY measurement. This is likely due to saturation effects associated with TFY data collection that can lead to suppression of high intensity peaks when the film thickness is on the order of the photon escape depth from the sample **[104]**. TEY, on the other hand, is less sensitive to saturation effects since the electron escape depth is usually less than the X-ray penetration depth **[108]**. While the relative peak intensities are different in TEY and TFY measurements the overall features of the two spectra are quite similar, though the signal-to-noise ratio is significantly worse in the TFY spectrum. The maximum value of the XMCD is larger at both the L_3 and L_2 edges for the TFY spectrum. This is in contrast to behavior in XMCD spectra measured for LT-MBE grown $Ga_{1-x}Mn_xAs$ in

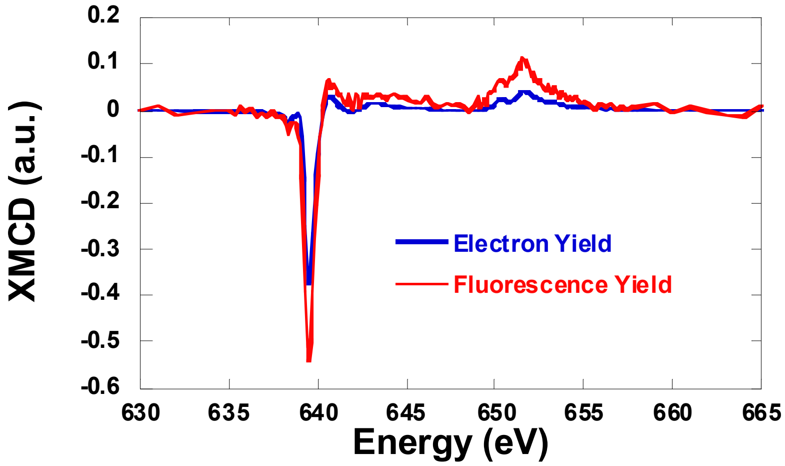

Figure 17: Comparison of Mn $L_{3,2}$ XMCD spectra as obtained in total electron yield and total fluorescence yield mode for $Ga_{0.966}Mn_{0.034}P$.

which the TEY and TFY spectra are nearly identical **[20]**. The difference in behavior of II-PLM $Ga_{1-x}Mn_xP$ can be understood in terms of the different processes used to make the materials. Recall from Section 3.3.1 that TEY probes primarily the near surface region while TFY probes much deeper into the sample. LT-MBE grown films have a uniform Mn distribution through the depth of the film. Thus, there should be little difference in the XMCD signal whether the probe depth is a few nanometers (TEY) or tens of nanometers (TFY). However, the II-PLM films have a non-uniform Mn distribution with the peak Mn concentration generally occurring between 20 and 30 nm from the surface (Figure 58). The locally lower Mn concentration in the first few nanometers of the film implies that the magnetic coupling is weaker in this region of the film, which gives rise to a smaller effective magnetic moment and, therefore, a smaller measured XMCD signal. Thus, TFY is a better probe of the bulk properties of the film, although absolute quantitative analysis may be hindered by saturation effects.

The maximum XMCD asymmetry at the Mn L_3 absorption edge measured at 17 K and a field of 0.5 T is plotted as a function of x in Figure 18. Here the asymmetry is defined as the quotient of the XMCD intensity to the average XAS intensity $[2(I^+-I^-)/(I^++I^-)]$. Some authors

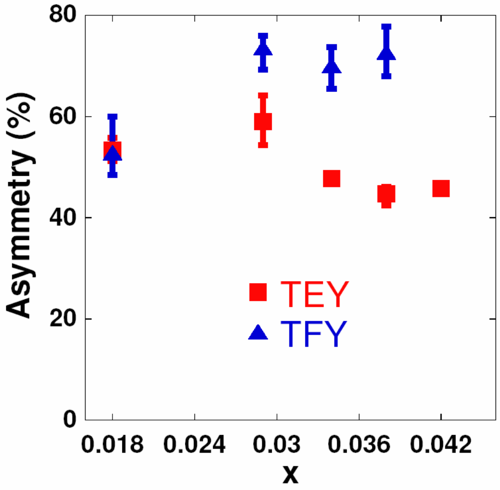

Figure 18: TEY and TFY asymmetry at the Mn L_3 peak versus x. The raw XMCD data have been corrected for non-unity X-ray polarization and incident angle by multiplying by 1.283.

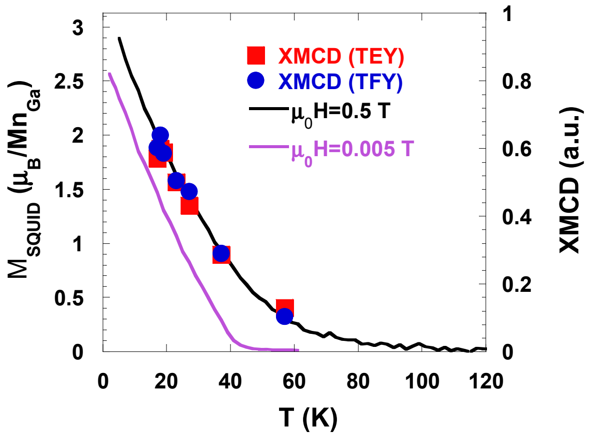

Figure 19: Temperature dependence of magnetization (M_{SQUID}) measured at fields of 0.5 and 0.005 T and normalized XMCD signals from TEY (squares) and TFY (circles) taken at 0.5 T for $Ga_{0.966}Mn_{0.034}P$.

divide by the sum of the I^+ and I^- XAS signals and care must be taken when comparing results from different studies to avoid being off by a factor of 2. The asymmetry is corrected for the grazing angle of incidence and degree of circular polarization of the photons. For the experimental setup at Beamline 4.0.2, the photon beam is incident at 30º off normal with a degree of circular polarization of 90 %, which leads to a normalization factor of $(1/cos(30))(1/0.9) \sim 1.283$. The error bars in Figure 18 account for both the observed spread in experimental measurements as well as any uncertainties in background removal during data processing. The TFY asymmetry is generally larger than that measured by TEY as discussed above. The only exception is for $Ga_{0.982}Mn_{0.018}P$. This is attributed to the significantly more uniform Mn concentration profile for samples with low x **[73]**. The TFY asymmetry value saturates at 0.70±0.04 in all samples except for the one having x=0.018. This is primarily because the T_C of 18 K of this film is very close to the measurement temperature, and thus its magnetic order is disrupted by thermal fluctuations. The near-constant value of the TFY XMCD asymmetry at the higher compositions suggests that at the measurement field and temperature the magnetization per Mn and spin polarization in the hole density of states is nearly constant **[20]** although this effect could, in principle, be an artifact of signal saturation **[104, 108, 109]**.

3.3.5 *Comparison of XMCD to Bulk Magnetometry*

Figure 19 compares the film magnetization measured by SQUID magnetometry, M_{SQUID}, and normalized XMCD TEY and TFY signals as a function of temperature for $Ga_{0.966}Mn_{0.034}P$. The magnetization data obtained with a measuring field of 50 Oe yield a film T_C of 43± 2K. In a measuring field of 5 kOe, corresponding to the measuring field with which XMCD spectra were taken, sample magnetization (dashed line) persists at temperatures above T_C. This explains the stronger than expected spin polarization above T_C when the sample in nominally paramagnetic as well as the observation of a strong XMCD signal at T=17 K in the sample with x=0.018 and T_C=18 K. The identical temperature dependencies of magnetization and XMCD demonstrate that the SQUID magnetometry and XMCD signal originate from the same magnetic phase.

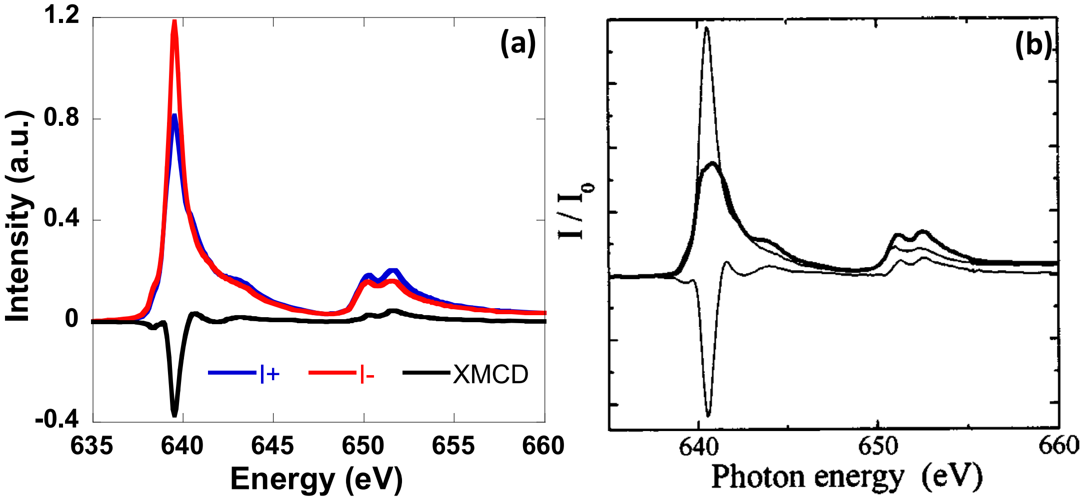

Figure 20: TEY XAS and XMCD spectra for (a) $Ga_{0.966}Mn_{0.034}P$ at 17 K and 5 kOe and (b) $Ga_{0.933}Mn_{0.067}As$ at 15 K and 6 kOe. Data in panel (b) reproduced from [107].

3.3.6 *Comparison of the XMCD of $Ga_{1-x}Mn_xP$ to Other $Ga_{1-x}Mn_xV$ Materials*

Figure 20 compares the XAS and XMCD spectra for the $Ga_{0.966}Mn_{0.034}P$ grown by II-PLM from this work to LT-MBE grown $Ga_{0.933}Mn_{0.067}As$ as measured by TEY. The spectra were measured at similar temperatures and magnetic fields. The XAS and XMCD lineshapes are nearly identical. The only major difference is that the Mn L_3 and L_2 peaks occur at slightly different energies. However, this is not a materials effect and is likely due to calibration.

The similarity between the XAS and XMCD lineshapes for $Ga_{1-x}Mn_xP$ and those reported for $Ga_{1-x}Mn_xAs$ is remarkable. Because XAS and XMCD lineshapes are strongly influenced by the hybridization of the Mn *d* orbitals with the neighboring anion *p* orbitals, this suggests that the bonding and *p-d* exchange between Mn_{Ga} and As or P in dilute alloys are substantially similar. This experimentally confirms electronic structure calculations, which generally show very similar densities of states near E_F for $Ga_{1-x}Mn_xAs$ and $Ga_{1-x}Mn_xP$ **[110]**.

The similarity of the XMCD lineshapes also sheds some light on the electronic configuration of Mn in GaP. When Mn is substitutionally incorporated into the zincblende lattice, it requires one extra electron to complete its bonding. In GaAs:Mn the consensus view is that the electron comes from the valence band, which results in a weakly localized hole. This results in a quasi-hydrogenic d^5+bound hole ground state for which the hole states are composed primarily of As *p* states, which form the valence band. In GaN:Mn the acceptor level is mid-gap. Therefore, one of the Mn *d* electrons is used to complete the bonding, resulting in Mn d^4 configuration and a hole with dominant *d* character **[111]**. For the $Ga_{1-x}Mn_xP$ alloy, the hole states at E_F are expected to have more localized Mn *d* character than for $Ga_{1-x}Mn_xAs$ but still contain substantial phosphorus *p* character, leading to a stronger tendency for a non-zero, spin-polarized density of states separated by a gap from the valence band. Electronic structure calculations show a very small difference in energy between the d^4 and d^5 configurations **[112]**. In fact, conflicting results have been reported with a nearly equal split between reports of d^4 and d^5 configurations.

These XMCD measurements suggest that in this dilute alloy limit (i.e. for 1.8-4.2% Mn_{Ga}) the Mn acceptor is predominantly d^5 in character due to the similarity in lineshapes between the $Ga_{1-x}Mn_xP$ and $Ga_{1-x}Mn_xAs$ in which the Mn electronic configuration has been well-established. A transition to a d^4 configuration in going from a GaAs to GaP host would be accompanied by a change in the overall XMCD lineshape **[102]**. For parameters which reproduce the XMCD lineshapes in $Ga_{1-x}Mn_xP$, as well as the LT-MBE grown $Ga_{1-x}Mn_xAs$ **[20, 107]**, there is a significant difference in the pre- and post- absorption edge fine structure between the d^4 and d^5 configurations at the L_3 and L_2 edges (see Figure 1 in Ref. **[102]**). This interpretation is supported by XMCD measurements of $Ga_{1-x}Mn_xN$ at the Mn *K* edge, which indicate that the Mn_{Ga} are in a d^4 charge state **[113]**. In parallel, the *L* edge XMCD and XAS spectra associated with bulk, substitutional Mn in GaN exhibit a marked difference in XMCD lineshape as well as an energy shift when compared to materials in the d^5 configuration **[114]**.

3.4. Onset of Ferromagnetism in $Ga_{1-x}Mn_xP$

Figure 21 shows *M(H)* curves for $Ga_{1-x}Mn_xP$ samples with x=0.0042 and x=0.0088. The sample with x=0.0042 exhibits no spontaneous magnetization when the applied field is parallel to either in-plane <011> orientation or the film normal [100] at T=2 K. Since no remanence or hysteresis is observed in any of the measurements, it can be concluded that the sample with x=0.0042 is not ferromagnetic at T=2 K. The sample with x=0.0088 clearly shows hysteresis and magnetic remanance at T=2 K, and ferromagnetic behavior persists to 5 K implying that $T_C \approx 5$-6 K for this sample. The onset of ferromagnetism occurs in $Ga_{1-x}Mn_xP$ for $0.0042 \leq x \leq 0.0088$.

A recent study on lightly doped, insulating $Ga_{1-x}Mn_xAs$ correlated the onset of ferromagnetism to the magnitude of the activation energy for hopping transport **[42]**. The authors of Ref. **[42]** used Mott variable-range hopping (VRH) theory to analyze electrical transport data since T_C and hopping energies were mostly insensitive to the estimated hole concentration **[115]**. It was determined that the hopping energy at T_C was the primary factor determining whether or not a sample had ferromagnetic order. A current study is ongoing to determine whether similar critical behavior is present in $Ga_{1-x}Mn_xP$.

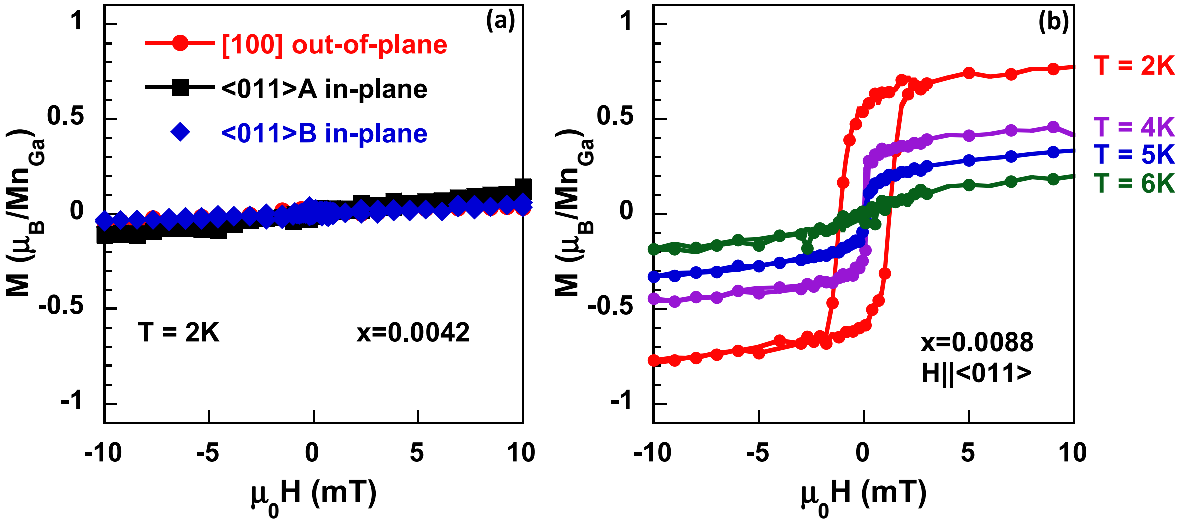

Figure 21: (a) Field dependence of the magnetization for a $Ga_{1-x}Mn_xP$ sample with x=0.0042 and the field applied parallel to three principal orthogonal directions. <011>A and <011>B refer to the two distinct in-plane <011>-type directions, but the polarity was not explicitly determined. (b) Field dependence of the magnetization for x=0.0088 at various temperatures and H||<011>.

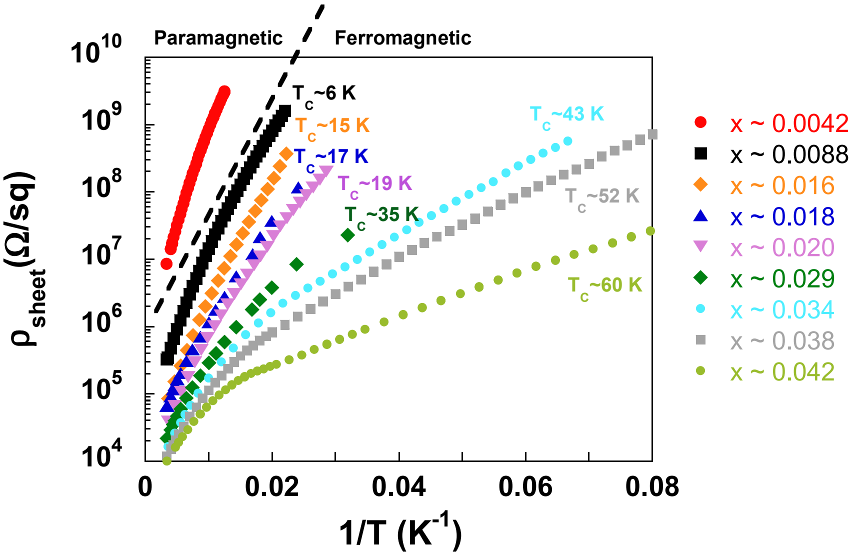

Figure 22: The temperature dependence of the sheet resistivity is shown for $Ga_{1-x}Mn_xP$ samples with x varying by a factor of 10. The T_C for each sample as well as the ferromagnetic to paramagnetic transition is indicated.

3.5. Establishment of the Carrier-Mediated Phase of $Ga_{1-x}Mn_xP$

While there are no standardized minimum requirements for the establishment of carrier-mediated ferromagnetism in a material, it is generally accepted that one must demonstrate the interconnection of the magnetic, electrical, and optical properties of the material. As was discussed in Section 3.1, previous studies of $Ga_{1-x}Mn_xP$ have fallen short of establishing the carrier-mediated nature of exchange interactions by focusing almost exclusively on bulk magnetometry studies. Here, structural, magnetic, electrical, and optical measurements have been presented which indicate that ferromagnetism in $Ga_{1-x}Mn_xP$ is unambiguously carrier-mediated. The large majority of the Mn atoms sits substitutionally on the cation sublattice in GaP (Appendix A). No evidence of second phase precipitates is found in X-ray diffraction (Appendix B), transmission electron microscopy (Ref. **[73]**), or magnetic measurements (Section 3.2). T_C is proportional to the concentration of Mn_{Ga} moments and holes (Section 3.2). In parallel, changes are observed in the electrical transport as is illustrated in Figure 22. There is a direct correlation between the resistivity of $Ga_{1-x}Mn_xP$ and robustness of magnetic ordering that persists over an order of magnitude of Mn doping. Further evidence of carrier-mediated ferromagnetism in $Ga_{1-x}Mn_xP$ comes from similarities of this materials system to $Ga_{1-x}Mn_xAs$. The similarity of the XAS and XMCD spectral lineshapes indicates that the hybridization between the Mn d and anion p orbitals and local environment are similar in the two systems. This result, along with the similar dependence of T_C on x [Figure 13 (c)], magnetotransport characteristics (Ref. **[99]**), and control of the magnetic anisotropy by epitaxial strain and carrier-concentration (Section 5.5-5.7), suggests that similar carrier-mediated ferromagnetic exchange mechanisms are operative in the two materials systems.

3.6. Comparison of $Ga_{1-x}Mn_xP$ to Other $III_{1-x}Mn_xV$ Materials

Perhaps the most important conclusion that can be drawn for the collective work in $Ga_{1-x}Mn_xP$ is the importance of localization in determining the properties of $III_{1-x}Mn_xV$ ferromagnetic

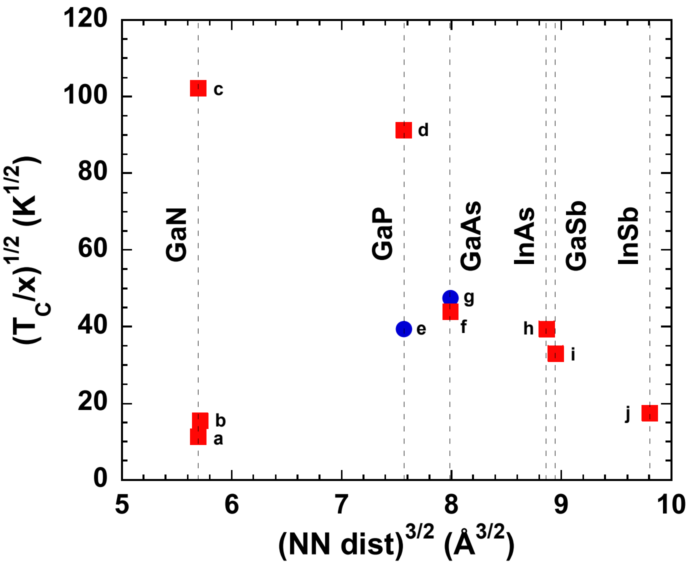

Figure 23: Scaling plot for the T_C of multiple $III_{1\text{-}x}Mn_xV$ ferromagnetic semiconductors with nearest neighbor cation distance. The ordinate value would be strictly proportional to $J_{p\text{-}d}$ for systems with no compensation and negligible localization. Blue circles refer to II-PLM samples discussed in this work, while red squares are taken from the literature. Plot courtesy of Prof. Michael Scarpulla. References: a= [113] (wurtzite), b= [116] (zincblende), c= [117], d= [93], e= [99], f= [57], g= [90], h= [26], i= [49] using x=0.023 and T_C=25 K to exclude phase-separated samples, j= [50].

semiconductors. The expected increase in the *p-d* exchange constant ($(J_{p\text{-}d}=|N_0\beta|)$ with decreasing lattice constant was discussed previously in Section 1.6. This has been expected to increase the effective coupling between different Mn ions ($J_{\text{Mn-Mn}}$) through their hole-mediated interaction leading to higher T_C. However, localization of holes lessens the interaction between a hole associated with a specific Mn ion and other Mn ions in the crystal. Thus, in systems with more strongly localized holes as a result of strong Coloumb interactions or disorder, the effective coupling $J_{\text{Mn-Mn}}$ through a mediating hole can be smaller. The balance between $J_{p\text{-}d}$ and spatial localization determines $J_{\text{Mn-Mn}}$ and therefore, T_C.

Localization effects are not explicitly considered in the mean field theory of carrier-mediated ferromagnetism. Instead, only scaling with *p-d* exchange strength is considered (*c.f.* Equation 6)

$$T_C \propto x N_0 \beta^2 \tag{13}$$

where N_0 is proportional to a^{-3}. Based on Equation 13 a plot of $(T_C/x)^{1/2}$ vs. $a_o^{3/2}$ will be proportional to $J_{p\text{-}d}$ for mean-field systems **[19]**. This simple analysis ignores the effect of compensation which is always present in real samples. Here only the highest T_C samples reported for different materials with $0<x<0.1$ are considered, which should represent the highest x, lowest compensation samples achieved over this range of compositions. Figure 23 illustrates the dependence of $(T_C/x)^{1/2}$ on nearest neighbor distance for the record highest T_C samples of a variety of $III_{1\text{-}x}Mn_xV$ ferromagnetic semiconductors **[26, 31, 49, 50, 90, 99, 113, 116, 117]**. The expected increasing trend in the $J_{p\text{-}d}$ parameter $(T_C/x)^{1/2}$ with decreasing nearest neighbor distance is seen for InSb, GaSb, InAs, and GaAs hosts. The striking break in this trend is seen for $Ga_{1\text{-}x}Mn_xP$ and the low-T_C $Ga_{1\text{-}x}Mn_xN$ data where $(T_C/x)^{1/2}$ begins to *decrease* with decreasing nearest neighbor distance, while the scaling for larger-lattice-constant materials would suggest that it should continue to increase. We interpret this as the effect of localization, which negates the fundamental assumption of the mean field treatment that holes interact with each Mn in the crystal. The relevant parameter to consider is not $J_{p\text{-}d}$ but instead $J_{\mathrm{Mn\text{-}Mn}}$ which depends on the details of the semiconductor band structure and impurity energy levels that determine the degree of hybridization and carrier localization in the system.

For illustrative comparison, data are included for two notable reports of high-T_C Mn-doped GaP (data point d **[93]**) and GaN (data point c **[117]**) in which the ferromagnetism was not shown conclusively to originate from a dilute, random, hole-mediated ferromagnetic phase. The data from these reports are clearly above the trend of increasing $J_{p\text{-}d}$ established in the larger lattice constant materials. The work on II-PLM formed $\mathrm{Ga}_{1\text{-}x}\mathrm{Mn}_x\mathrm{P}$ presented herein is consistent with well-substantiated data from both zincblende and wurtzite $\mathrm{Ga}_{1\text{-}x}\mathrm{Mn}_x\mathrm{N}$ demonstrating T_Cs in the 5-15 K range **[113, 116]**, indicating that the low T_C results in $\mathrm{Ga}_{1\text{-}x}\mathrm{Mn}_x\mathrm{N}$ are more consistent with the hole-mediated dilute ferromagnetic phase akin to that observed in $\mathrm{In}_{1\text{-}x}\mathrm{Mn}_x\mathrm{Sb}$, $\mathrm{Ga}_{1\text{-}x}\mathrm{Mn}_x\mathrm{Sb}$, $\mathrm{In}_{1\text{-}x}\mathrm{Mn}_x\mathrm{As}$, $\mathrm{Ga}_{1\text{-}x}\mathrm{Mn}_x\mathrm{As}$, and $\mathrm{Ga}_{1\text{-}x}\mathrm{Mn}_x\mathrm{P}$.

3.7. Summary

$\mathrm{Ga}_{1\text{-}x}\mathrm{Mn}_x\mathrm{P}$ is a novel ferromagnetic semiconductor alloy in which ferromagnetism is mediated by holes that are localized in a detached Mn-derived impurity band for $x \leq 0.042$. The unique, optical, electrical, and magnetic properties of this materials system make it an important medium for exploring the interplay of carrier localization, band structure and ferromagnetic exchange. $\mathrm{Ga}_{1\text{-}x}\mathrm{Mn}_x\mathrm{P}$ thin films exhibit all of the hallmarks of carrier-mediated exchange that are present in the canonical $\mathrm{Ga}_{1\text{-}x}\mathrm{Mn}_x\mathrm{As}$ system, where the character of the mediating holes is still unclear. The ferromagnetic Curie temperature in $\mathrm{Ga}_{1\text{-}x}\mathrm{Mn}_x\mathrm{P}$ is linear in x with a slope close to that for $\mathrm{Ga}_{1\text{-}x}\mathrm{Mn}_x\mathrm{As}$. $L_{3,2}$ XMCD spectra provide unambiguous evidence that the origins of ferromagnetism in $\mathrm{Ga}_{1\text{-}x}\mathrm{Mn}_x\mathrm{P}$ are due to $\mathrm{Mn}_{\mathrm{Ga}}$ acceptors which have a local electronic environment identical (within experimental resolution) to that of $\mathrm{Mn}_{\mathrm{Ga}}$ $\mathrm{Ga}_{1\text{-}x}\mathrm{Mn}_x\mathrm{As}$.

The similar nature of the $\mathrm{Mn}_{\mathrm{Ga}}$ acceptor and holes suggest that ferromagnetism in $\mathrm{III}_{1\text{-}x}\mathrm{Mn}_x\mathrm{V}$ varies continuously as exchange strength and carrier localization are adjusted through compositional tuning of the semiconductor host. Hence, one would expect a single unifying theory to be able to quantitatively describe and predict the properties of many $\mathrm{III}_{1\text{-}x}\mathrm{Mn}_x\mathrm{V}$ materials. Mean field models which are adequate at describing numerous materials properties in $\mathrm{Ga}_{1\text{-}x}\mathrm{Mn}_x\mathrm{As}$ must, therefore, be revisited as their assumption of itinerant holes which can be well-described using semiconductor valence band parameters is inconsistent with observation of impurity band ferromagnetism in $\mathrm{Ga}_{1\text{-}x}\mathrm{Mn}_x\mathrm{P}$. Polaronic models in which localized holes polarize a cloud of Mn spins are more consistent with the results of $\mathrm{Ga}_{1\text{-}x}\mathrm{Mn}_x\mathrm{P}$; however their predictive power is only qualitative, and applicability may not be appropriate for highly-doped, metallic $\mathrm{Ga}_{1\text{-}x}\mathrm{Mn}_x\mathrm{As}$ **[29]**. Clearly more theoretical and experimental advances are needed in order to elucidate the fundamental effect of anion substitution on ferromagnetic exchange. Integration of localization parameters into models of ferromagnetic exchange is crucial for improving their quantitative accuracy and predictive power.

4. Partial Anion Substitution: $Ga_{1-x}Mn_xAs_{1-y}P_y$ and $Ga_{1-x}Mn_xAs_{1-y}N_y$

4.1. Introduction

The optimal semiconductor host for Mn moments is the one that simultaneously optimizes the two competing effects of carrier localization and *p-d* exchange strength. Empirically, it can be inferred that among binary III-V semiconductors GaAs seems to lie at this optimal point (see Figure 23). Nonetheless, record T_Cs have remained well below room temperature even in this materials system. Increasing the magnitude of *p-d* exchange by tailoring the composition of the host semiconductor is a proposed, though relatively unexplored, route by which to raise T_C **[54, 118]**. It has been proposed that dilute alloying of GaAs with GaP may yield a host in which the itinerancy of the mediating holes is maintained while *p-d* exchange is enhanced due to the shorter average Mn-anion bond length **[118]**. First principles calculations have, in fact, predicted an enhancement of T_C by a factor of 1.5 due to this effect **[54]**. It should be noted that the calculations in Ref. **[54]** overestimate T_C in $Ga_{1-x}Mn_xP$ by about a factor of 3 since they do not explicitly consider the strongly localized wavefunctions of Mn-doped GaP. Nonetheless, the predictions on the quaternary $Ga_{1-x}Mn_xAs_{1-y}P_y$ system are expected to be accurate as long as the assumption of itinerant carrier-mediated ferromagnetism is still applicable.

In this chapter the synthesis and magneto-electronic properties of Mn-doped $GaAs_{1-y}P_y$ and $GaAs_{1-y}N_y$ ferromagnetic semiconductors are discussed. Emphasis is placed on dilutely alloyed As-rich materials- i.e. $GaAs_{1-y}P_y$ and $GaAs_{1-y}N_y$ with $y<0.04$- since the dilute, As-rich quaternary materials have garnered the most theoretical interest as materials with potential for higher T_C. Even in this dilute limit the incorporation of P and N into $Ga_{1-x}Mn_xAs$ results in a strong *decrease* in T_C with increasing y (Section 4.5). Concurrent to the decrease in magnetic ordering, a metal-insulator transition as a function of y is observed in both quaternary materials even as the Mn_{Ga} concentration is held constant (Sections 4.2 and 4.3). The alloy-induced metal-insulator transition is understood within the context of a simple impurity-band picture where increased scattering of holes by alloy disorder drives the system to an insulating phase (Section 4.4). Finally, a summary and perspective for future prospects in Mn-doped quaternary systems are presented in Sections 4.6 through 4.8.

4.2. Materials Synthesis and Structural Properties

$Ga_{1-x}Mn_xAs$ was synthesized by implantation of 1.5×10^{16} cm^{-2} 50 keV Mn^+ ions into semi-insulating GaAs followed by irradiation with a single pulse from a KrF (λ=248 nm) excimer laser at a fluence of 0.3 J/cm^2. Quaternary alloys were synthesized by further implantation of P^+ or N^+ ions into the Mn^+-implanted GaAs prior to PLM. The P^+ implant parameters were doses in the range of 1×10^{15}-1×10^{16} cm^{-2} at 35 kV while the N^+ implant doses ranged from 1×10^{15} to 5×10^{15} cm^{-2} at 33 kV. All implants were intentionally performed at 7° offset to prevent channeling. Films were etched for 20 minutes in concentrated HCl to remove surface oxide layers **[107]**. Mn and P concentrations and substitutional fractions were determined by the combination of secondary ion mass spectrometry (SIMS) and ion beam analysis (Sections 4.2.1 and 4.2.2) **[75, 119]**. Weak N fluorescence prevented the determination of the N lattice location and concentration in $Ga_{1-x}Mn_xAs_{1-y}N_y$ by PIXE. Instead the active nitrogen content y of $Ga_{1-x}Mn_xAs_{1-y}N_y$ films was determined by photomodulated reflectance (PR) spectroscopy of $GaAs_{1-y}N_y$ films that were prepared under identical implant and laser conditions

[120, 121]. Nitrogen implant doses of 1.0, 2.5, and 5.0×10^{15} cm^{-2} correspond to y values 0.004, 0.010 and 0.014 respectively.

4.2.1 *Ion Beam Analysis of $Ga_{1-x}Mn_xAs_{1-y}P_y$*

Figure 24 shows PIXE spectra around the P K_α emission energy for a $Ga_{1-x}Mn_xAs_{1-y}P_y$ sample that had an implant dose of 1.0x10^{16} P^+/cm^2 as well as a Mn^+ implant dose of 1.5x10^{16} cm^{-2}. Details of the ion beam analysis techniques are found in Appendix A. These implant conditions produce a film with y=0.031 after PLM. The PIXE intensity is reduced significantly for the two channeled orientations relative to the random orientation. In fact, the channeled PIXE intensity for both <110> and <111> orientations is essentially zero. This signifies to within the noise and resolution of the measurement that all P atoms are commensurate in the lattice. This eliminates the possibility of P clusters or P-containing incoherent precipitates as a possible site of P incorporation in $Ga_{1-x}Mn_xAs_{1-y}P_y$ since such inclusions would result in some PIXE counts in the channeled geometry due to their random distribution relative to the semiconductor lattice. The negligible channeled PIXE counts also rule out the incorporation of P atoms as interstitials since both the tetrahedral and hexagonal interstitial sites in the zincblende lattice are visible in the <110> channel. Therefore, the fraction of substitutional P is nearly 1 since the P $\chi_{\min}$ is nearly zero. However, it should be noted that the ion-beam measurements cannot directly exclude the possibility of P antisites (P incorporated on the Ga sublattice) since those too would be shadowed in both the <110> and <111> orientations although energetically this is highly unlikely. Similar PIXE spectra were observed for P K_α radiation in all $Ga_{1-x}Mn_xAs_{1-y}P_y$ samples indicating that the P f_{sub} is nearly 1 for all $Ga_{1-x}Mn_xAs_{1-y}P_y$ samples presented in this work.

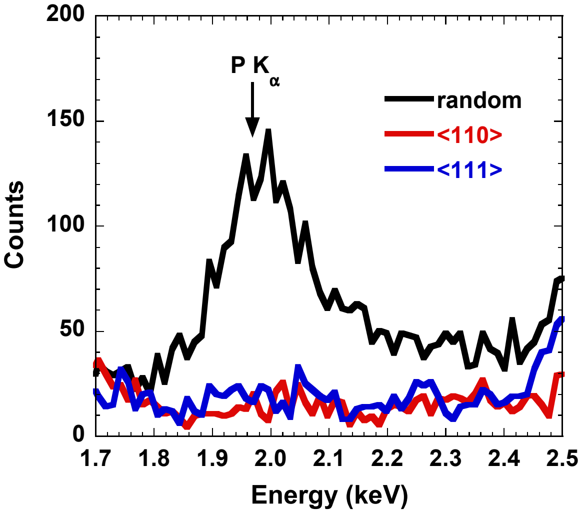

Figure 24: PIXE spectra of a $Ga_{1-x}Mn_xAs_{1-y}P_y$ with y=0.031 taken around the P K_α emission line with the α particle ion beam aligned parallel to <110>, <111> and random directions.

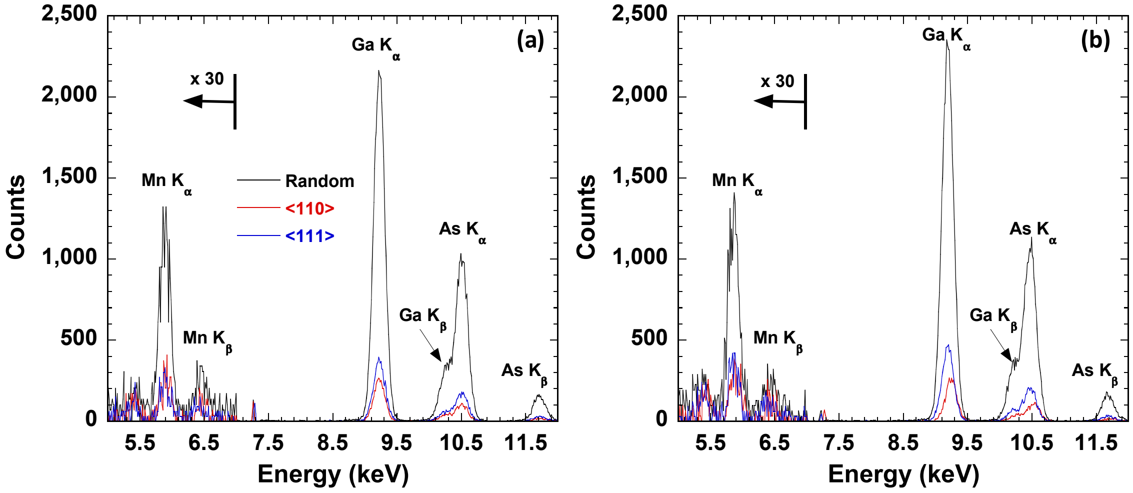

Figure 25: PIXE spectra for (a) Ga$_{1-x}$Mn$_x$As and (b) Ga$_{1-x}$Mn$_x$As$_{1-y}$P$_y$. The sample in panel (b) is the same for which the phosphorous PIXE results were presented in Figure 24. Data below 7 keV have been multiplied by 30 in order to be seen on the same scale as the Ga and As signals which dominate the measurement due to substrate effects.

Figure 25 shows PIXE spectra including the Mn, Ga, and As emission lines for Ga$_{1-x}$Mn$_x$As$_{1-y}$P$_y$ samples with y=0 and y=0.031. Comparison of the two sets of data indicates that the co-implantation of P into Mn-implanted GaAs does not have a significant effect on the substitutional fraction of the Mn in the film after PLM. Both samples show identical PIXE yields for <110> and <111> channeled measurements, which demonstrates that P alloying does not induce the formation of Mn$_\text{I}$. Moreover, the ratio of the channeled to random PIXE signals is unaltered by changing y implying that χ_{min} is constant. Indeed, integrating over the Mn K_α emission peak results in χ_{Mn}=0.23±.02 for both y=0 and y=0.031. Figure 26 shows the channeling RBS spectra for the same two samples for which PIXE data is shown in Figure 25. The RBS spectra are dominated by backscattering off of As and Ga atoms, which combine to produce a strong increase in the backscattered yield at ~1550 keV (see Table 9). The channeled RBS spectra are quite similar over the range of energies corresponding to the Ga$_{1-x}$Mn$_x$As$_{1-y}$P$_y$ thin films indicating that both films are of similar crystalline quality. Quantitatively, both films have χ_{GaAs}=0.06±0.01. This value is within a factor of two of the theoretical minimum χ_{min} of ~0.02-0.05, which signifies that both films are of high quality. Combining the c-RBS and PIXE data results in f_{sub}≈0.82 for the Mn atoms in Ga$_{1-x}$Mn$_x$As$_{1-y}$P$_y$ with y=0 and y=0.031, which shows that alloying with P has little effect on the Mn f_{sub}.

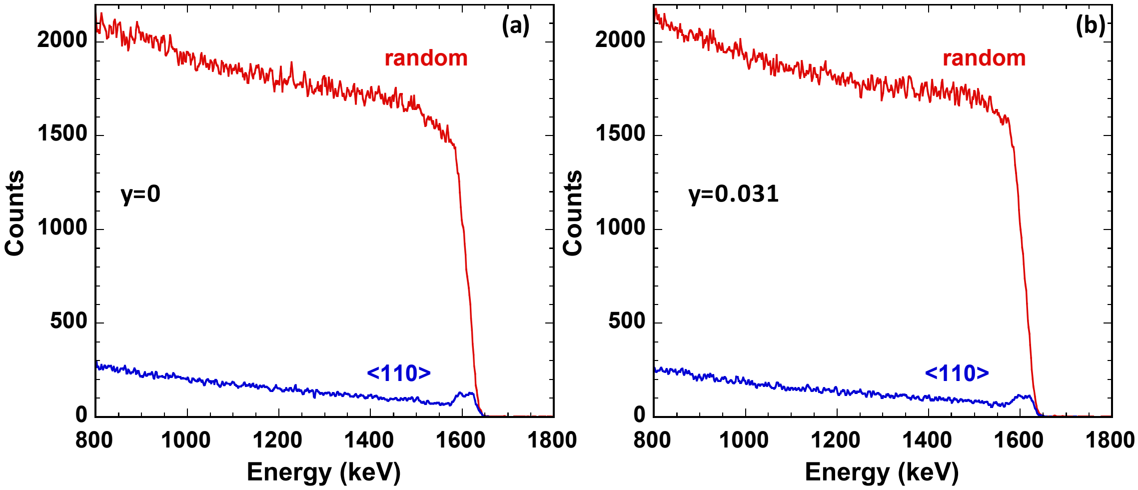

Figure 26: RBS spectra for $Ga_{1-x}Mn_xAs_{1-y}P_y$ samples with y=0 and y=0.031 for random and <110>-channeled orientations of the ion beam.

The retained dose of Mn is determined by comparing the magnitude of the PIXE intensities of the Mn and substrate signals. Here, the Ga K_α signal is used as the substrate reference signal since it is strong and easily resolved. The similar height ratios of the Ga K_α and Mn K_α PIXE peaks in films with y=0 and y=0.031 implies that the Mn retained dose is similar in the two materials. Quantitatively, one compares the total integrated intensities corresponding to Ga K_α and Mn K_α X-ray emission. Doing so it was found that Mn K_α/Ga $K_\alpha \approx 0.018$ for both y=0 and y=0.031 in agreement with the general observations above. To obtain the actual retained dose the Mn K_α/Ga K_α ratio is compared to that of a Mn-implanted GaAs standard for which the total dose is known. The implant standard analysis revealed that the Mn K_α/Ga K_α ratio of 0.018 corresponds to a Mn retained dose of 7.2×10^{15} cm^{-2}.

The structural and compositional parameters of a series of $Ga_{1-x}Mn_xAs_{1-y}P_y$ samples are shown in Table 2. Those parameters that were determined by ion beam analysis are in the leftmost eight columns of the table. The sample series as a whole bears out the trends discussed above, namely:

1. The Mn substitutional fraction and retained dose are not significantly affected by P+ co-implantation. The scatter in values of for both parameter is less than 10% which is about the resolution of ion beam measurements.
2. The concentration of interstitial Mn is negligible for all samples.
3. The P atoms are nearly completely substitutional. The concentration of interstitial P is negligible.
4. The overall sample quality (parameterized by χ_{GaAs}) is not significantly different between samples. Thus scattering by growth-related defects will not be that different between the materials.

These effects can be excluded when discussing the origins of the electrical and magnetic behavior in $Ga_{1-x}Mn_xAs_{1-y}P_y$ in Sections 4.3 through 4.5.

Table 2: Structural and compositional parameters of $Ga_{1-x}Mn_xAs_{1-y}P_y$ as determined by the combination of ion beam analysis and secondary ion mass spectrometry. All samples listed in this table were PLMed with a nominal laser fluence of 0.3 J/cm^2.

Mn implant dose [cm^{-2}]	P implant dose [cm^{-2}]	χ_{Mn}	χ_{GaAs}	Mn f_{sub}	P f_{sub}	Mn retained dose [cm^{-2}]	P retained dose [cm^{-2}]	x	y
1.5x10^{16}	0	0.22	0.05	0.82	----	7.2x10^{15}	----	0.046	0
1.5x10^{16}	1.0x10^{15}	0.26	0.06	0.80	>0.9*	7.7x10^{15}	6x10^{14*}	0.045	0.004
1.5x10^{16}	2.5x10^{15}	0.21	0.04	0.82	>0.9	7.7x10^{15}	1.4x10^{15}	0.047	0.009
1.5x10^{16}	5.0x10^{15}	0.19	0.04	0.84	>0.9	7.7x10^{15}	3.0x10^{15}	0.045	0.016
1.5x10^{16}	7.5x10^{15}	0.24	0.05	0.80	>0.9	7.2x10^{15}	4.9x10^{15}	0.046	0.024
1.5x10^{16}	1.0.x10^{16}	0.21	0.04	0.82	>0.9	7.2x10^{15}	6.7x10^{15}	0.046	0.031

*Estimated by average P retained fraction for other samples (~60%) due to weak P PIXE signal at low P concentrations.

4.2.2 *Secondary Ion Mass Spectrometry*

While ion beam analysis indicates that the Mn retained dose and substitutional fraction are unaffected by P alloying in $Ga_{1-x}Mn_xAs_{1-y}P_y$, it cannot definitively determine whether or not x is the same for all films. Thus, SIMS measurements were performed in order to obtain depth-dependent Mn and P concentration profiles for all films. A summary of the SIMS measurements is shown in Figure 27. The SIMS measurements show that the Mn distribution throughout the thickness of the film is also not strongly affected by P alloying [Figure 27 (a)]. Therefore, since the distribution, retained dose, and substitutional fraction of Mn are similar, all $Ga_{1-x}Mn_xAs_{1-y}P_y$ samples have similar x. The values of x for all samples are shown in the penultimate column of Table 2. The P concentration profiles for selected $Ga_{1-x}Mn_xAs_{1-y}P_y$ samples are shown in Figure 27 (b). The values for y were calculated in a similar manner by taking the maximum in the P concentration profiles and multiplying by the P f_{sub}. The values of y are shown in the last column of Table 2.

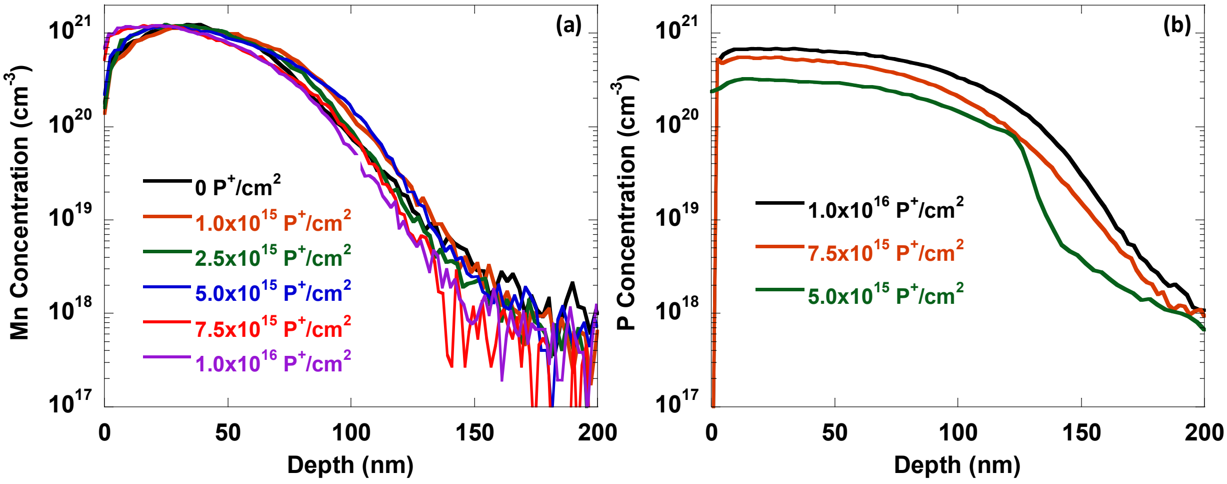

Figure 27: Secondary ion mass spectrometry profiles for (a) Mn and (b) P for $Ga_{1-x}Mn_xAs_{1-y}P_y$. Profiles are labeled by the implanted phosphorus dose. All materials had the same nominal Mn$^+$ implant dose of 1.5x10^{16} cm^{-2}.

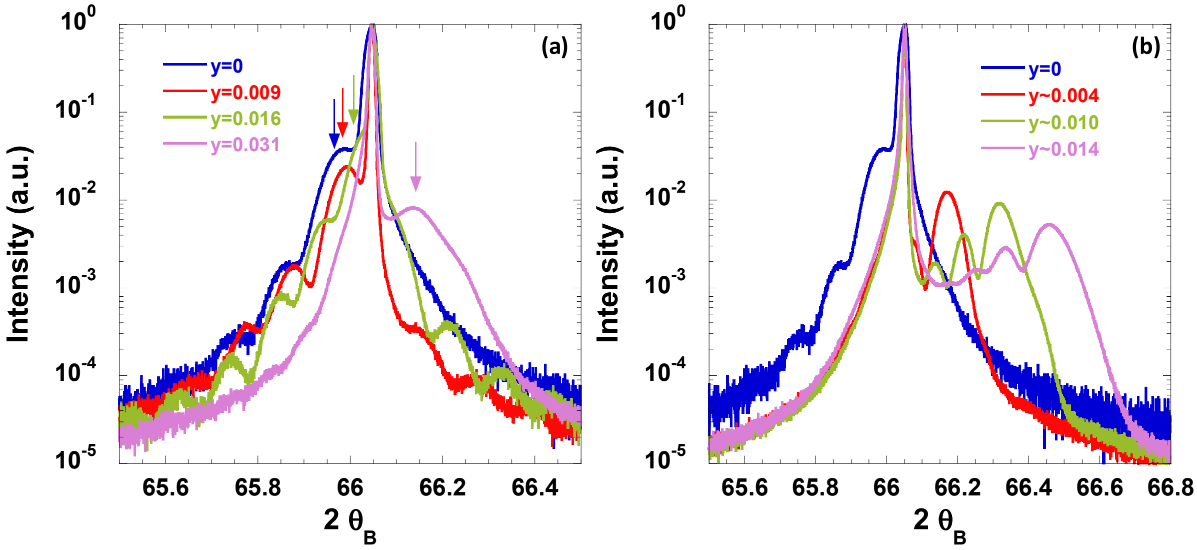

Figure 28: X-ray diffraction profiles around the GaAs (400) reflection for (a) $Ga_{1-x}Mn_xAs_{1-y}P_y$ and (b) $Ga_{1-x}Mn_xAs_{1-y}N_y$. Arrows in panel (a) emphasize the main features associated with X-ray diffraction from the $Ga_{1-x}Mn_xAs_{1-y}P_y$ film.

4.2.3 *X-ray diffraction*

Figure 28 (a) displays X-ray diffraction results from a series of $Ga_{0.954}Mn_{0.046}As_{1-y}P_y$ samples. The incorporation of the slightly smaller P atoms in place of As results in a contraction of the lattice, which is illustrated by the shift of the film peak to higher angle. While the film with y=0.016 is still under slight compressive strain substitution of 3.1% P atoms on the As sublattice gives rise to a film under tensile strain. In addition to substantiating the other structural measurements, the change in the strain state with P alloying has important connotations for magnetometry measurements. As will be discussed in more detail in Chapter 5 the magnetic easy axis of Mn-doped III-V semiconductors depends on the strain state of the film. In-plane easy axes are observed for samples in compressive strain while out-of-plane easy axes are found in materials under tensile strain. Hence, the strain state of the films determines the proper orientation for measuring the temperature-dependence of the magnetization (Section 4.5) in order to accurately determine T_C. It is important to probe both in-plane and out-of-plane components of the magnetization over the compositional range $0.016 \leq y \leq 0.031$ where the easy axis is transitioning from in-plane to out-of-plane. The transition from compressive to tensile strain occurs at much lower alloying levels in $Ga_{1-x}Mn_xAs_{1-y}N_y$ as is illustrated in Figure 28 (b). The behavior is expected as the atomic radius of nitrogen is significantly smaller than that of both As and P, which leads to a change in the sign of the strain state of the film at lower alloying levels.

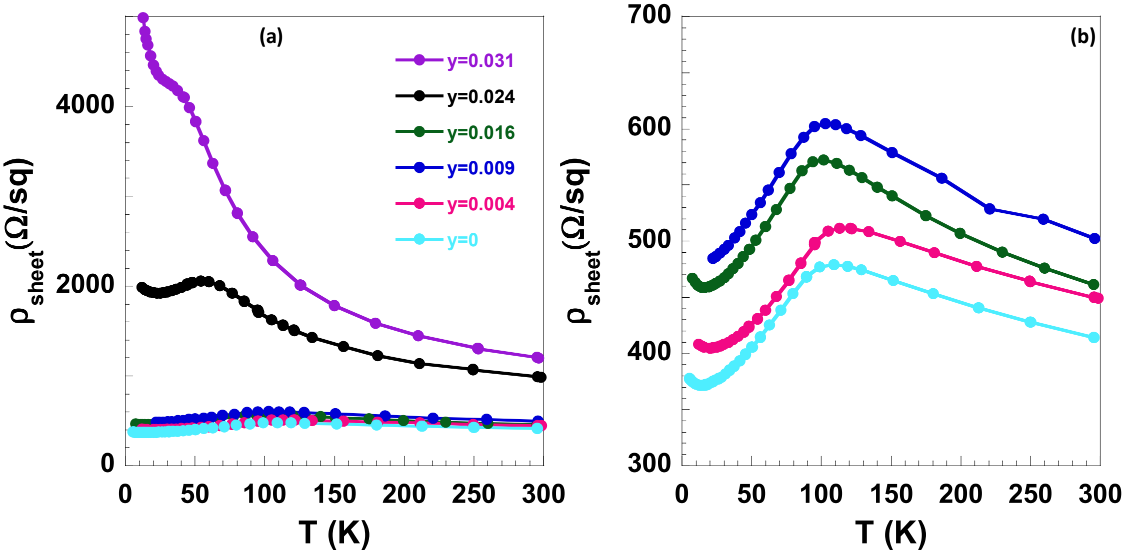

Figure 29: (a) ρ_{sheet} as a function of temperature for $Ga_{0.954}Mn_{0.046}As_{1-y}P_y$. A magnification of the low resistivity range is shown in panel (b) to emphasize the lineshape of the metallic samples. Color scheme is the same as in panel (a).

4.3. Electrical Transport in $Ga_{1-x}Mn_xAs_{1-y}P_y$

The temperature dependence of the sheet resistivity for a series of $Ga_{0.954}Mn_{0.046}As_{1-y}P_y$ samples is shown in Figure 29 (a). The sample with no phosphorous exhibits transport behavior typical of $Ga_{1-x}Mn_xAs$ films synthesized by both LT-MBE and II-PLM with x=0.046. The resistivity shows critical behavior at $T=T_C$ due to the onset of magnetic ordering; the resistivity increases (decreases) with decreasing temperature on the paramagnetic (ferromagnetic) side of T_C due to correlated (uncorrelated) spin fluctuations **[56]**. Recently it has been shown that in very uniform LT-MBE grown samples the critical behavior manifests itself as a singularity in $d\rho/dT$, which results in a kink in the $\rho(T)$ curve **[56]**. The non-uniformity of the Mn concentration throughout the depth of II-PLM formed $Ga_{1-x}Mn_xAs$ precludes the observation of such critical behavior. Different layers of the film may exhibit different effective transition temperatures depending on their Mn content. Thus, even though the transport behavior of II-PLM $Ga_{1-x}Mn_xAs$ is dominated by the region of the film with maximum Mn_{Ga} concentration **[90]**, the critical behavior is likely broadened by contributions from regions of the film with lower x. Disorder and nonuniformity also manifest themselves in many LT-MBE grown $Ga_{1-x}Mn_xAs$ samples in which $\rho(T)$ shows a "peak" or "shoulder" at T_C **[67]**. The temperature dependence of ρ_{sheet} observed in the sample with y=0 is therefore quite reasonable given these considerations. This type of lineshape will be used as the working definition of a "metallic" resistivity profile.

$Ga_{0.954}Mn_{0.046}As_{1-y}P_y$ samples with $y \leq 0.016$ all show metallic lineshapes which are qualitatively similar to the sample with y=0. In general the alloyed materials tend to show an increase in the resistivity with increasing y although the sample with y=0.016 seems to break this trend, which is likely due to minor sample-to-sample variation in x or crystalline quality that can result from fluctuations of the laser power during materials processing and therefore influence the magnitude of the resistivity. As y continues to increase a metal-insulator transition (MIT) is observed, which is qualitatively similar to the doping-induced MIT in $Ga_{1-x}Mn_xAs$ **[122]**. The sample with y=0.024 is identified as an insulating phase in that its resistivity increases

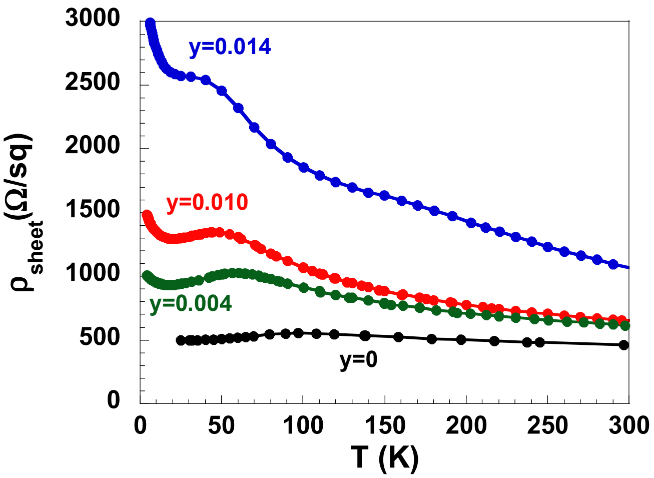

Figure 30: ρ_{sheet} as a function of temperature for $Ga_{1-x}Mn_xAs_{1-y}N_y$. Thin films with y=0, y=0.004, and y=0.010 have x=0.037 while the film with y=0.014 has x=0.046 and should be compared to the $Ga_{1-x}Mn_xAs$ reference sample in Figure 29.

exponentially at low temperature as $T \rightarrow 0$. This in contrast to the behavior of the metallic samples where the low temperature increase is non-exponential and tends towards a constant value in low temperature (mK) resistivity measurements **[40]**. The exponential behavior of the resistivity is even more pronounced in the sample with y=0.031 where the thermally-activated nature of the transport is more apparent. Using these standard definitions for the metallic and insulating phases of $Ga_{1-x}Mn_xAs$ the critical value of y (y_{crit}) must be between 0.016 and 0.024 for x=0.046. An MIT is also observed when $Ga_{1-x}Mn_xAs$ is alloyed with N as shown in Figure 30 (b) with $y_{crit} < 0.004$. The stoichiometrically similar alloys $Ga_{0.954}Mn_{0.046}As_{0.984}P_{0.016}$ and $Ga_{0.954}Mn_{0.046}As_{0.986}N_{0.014}$ show vastly different transport behavior. While alloying of the As sublattice with 1.4% nitrogen is sufficient to induce the MIT, the holes in the parallel phosphorus-alloyed sample remain itinerant. Hence, substitution of N for As in $Ga_{1-x}Mn_xAs$ has a much stronger effect on electrical transport than P. It should be emphasized that in both alloys these MITs are driven by the incorporation of *isovalent* species while the Mn_{Ga} doping concentration is held at a constant value. Additionally, the electrical behavior of these $Ga_{1-x}Mn_xAs_{1-y}N_y$ samples is similar to those reported for LT-MBE-grown films**[123-125]**.

4.4. A Simple Model for the MIT in $Ga_{1-x}Mn_xAs_{1-y}P_y$ and $Ga_{1-x}Mn_xAs_{1-y}N_y$

In this section a simple band structure argument that is consistent with the composition at which the MIT occurs in $Ga_{1-x}Mn_xAs_{1-y}P_y$ and $Ga_{1-x}Mn_xAs_{1-y}N_y$ is outlined. The electrical transport measurements that were presented in Section 4.3 are inconsistent with the valence band Zener model (Section 1.5). According to valence band models the change in electrical transport from insulating to metallic in $Ga_{1-x}Mn_xAs$ is essentially a Mott transition. Thus, the doping-induced (x dependent) metal-insulator transition (MIT) occurs when the broadened impurity band eventually merges with the valence band **[34]**. Experimentally this is typically observed around $x \approx 0.01$-0.02. In the context of the valence band model the effect of alloying $Ga_{1-x}Mn_xAs$ with P or N would be to shift the Mn acceptor level slightly deeper in the band gap as the valence band is shifted downwards (Figure 5). Within the virtual crystal approximation (VCA) the incorporation of 1% P or N into the anion sublattice of GaAs should shift the valence bands by ~4 and 20 meV respectively **[44]**. The slight increase in Mn acceptor binding energy with a few percent alloying is unlikely to induce a Mott-type MIT in $Ga_{0.954}Mn_{0.046}As$ since this system is well beyond the critical Mn density required for the merging of the valence and impurity bands.

Instead an impurity band picture that focuses on the effect of alloying on the mobility of the charge carriers is used to explain the alloy-induced MIT in $Ga_{1-x}Mn_xAs_{1-y}P_y$. One of the principal features that differentiates the character of impurity band or valence band holes is the effective mass. The effective mass of a hole residing in a narrow impurity band is much greater than that of a quasi-hydrogenic hole in the valence band. As will be shown below (Equation 16), the effect of alloying on mobility goes as the inverse square of the effective mass of the charge carrier. Thus, the effect of alloy disorder on electrical transport is significantly greater for impurity band systems. In the following it will be demonstrated that the reduction of the mobility of impurity band holes by alloy disorder is consistent with experimental findings for the onset of the MIT in $Ga_{1-x}Mn_xAs_{1-y}P_y$ and $Ga_{1-x}Mn_xAs_{1-y}N_y$. The notion of alloy disorder limited transport is inconsistent with the valence band picture as calculations using the effective mass of holes in the GaAs valence band show that alloying has a negligible effect on the magnitude of the resistivity **[44]**.

In this work it is proposed that an impurity band arises due to a valence band anticrossing (VBAC) interaction between the Mn impurity states and host valence band states. A band anticrossing interaction has been used previously to account for the sign and magnitude of the exchange energy in another transition metal-doped III-V semiconductor, $Ga_{1-x}Fe_xN$ **[126]**. The development of the VBAC theory and its application to magnetic semiconductors was primarily the work of Drs. Kirstin Alberi and Władysław Walukiewicz at Lawrence Berkeley National Laboratory. Here, the application of the VBAC model to metal-insulator transitions in $III_{1-x}Mn_xV$ materials is briefly outlined. A more rigorous discussion of the VBAC model and anticrossing in general is found in Refs.**[44, 127, 128]**. Alteration of the GaAs valence band edges by either P or N is treated according to the virtual crystal approximation (VCA). The VCA approximation is well justified in these dilute ternary alloys as deviation from the linear dependence of the valence band location on composition is negligible. The anticrossing interaction is treated according to the **k·p** formalism in which the standard 6×6 Kohn-Luttinger matrix expressing the VCA-corrected valence band structure of the $GaAs_{1-y}P_y$ (or $GaAs_{1-y}N_y$) host is augmented with the six wavefunctions of the localized Mn *p*-states resulting in a 12×12 Hamiltonian matrix. The band anticrossing interaction leaves the 6×6 Kohn-Luttinger matrix unperturbed. The addition of the interaction terms between localized impurity states and extended band states results in two types of additional terms to the Hamiltonian matrix. The diagonal terms are the self-energy of the Mn impurity state, E_{Mn}. The second type of term arises between host and impurity states of like symmetry and can be shown to be equal to $Cx^{1/2}$ where C is a coupling parameter that describes the strength of the anticrossing interaction and x is the impurity concentration. C must be determined empirically. For the case of Mn-doped GaAs the magnitude of C was determined by fitting the compositional dependence of the bandgap and is equal to 0.39 eV **[44]**.

Accepting the existence of a Mn impurity band, one can now discuss transport of holes through such a band. Transport within an impurity band can be either metallic or insulating in nature depending on the relative magnitude of the impurity band width, W, and the lifetime broadening of the hole energies, δE. For $W>\delta E$ the scattering of holes is such that metallic transport is possible while for $W<\delta E$ transport occurs primarily by hopping conduction. More explicitly one can write for the lifetime broadening based on the time-energy uncertainty relation

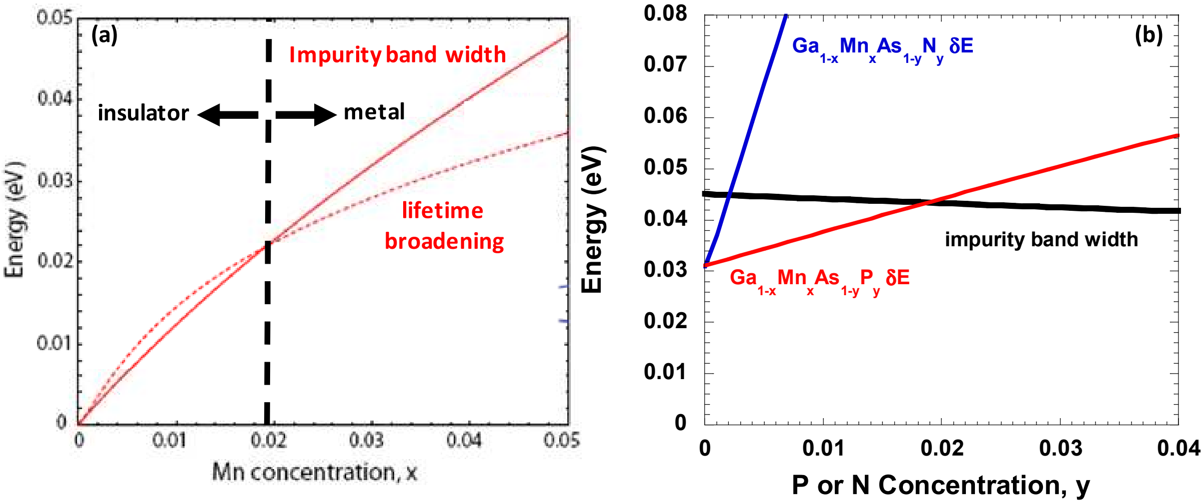

Figure 31: (a) Mn impurity-band width and lifetime broadening of the hole energies as a function of $\mathbf{Mn_{Ga}}$ doping in $\mathbf{Ga_{1-x}Mn_xAs}$. Plot adapted from Ref. [44] and courtesy of K. Alberi. (b) Mn impurity band width and lifetime broadening of the hole energies for $\mathbf{Ga_{0.954}Mn_{0.046}As_{1-y}P_y}$ (red) and $\mathbf{Ga_{0.954}Mn_{0.046}As_{1-y}N_y}$ (blue) as a function of anion sublattice composition.

$$\delta E = \frac{\hbar e}{\mu m_{eff}} \tag{14}$$

where m_{eff} is the hole effective mass and μ is the hole mobility. The effective mass in Equation 14 is determined from the VBAC-calculated impurity band dispersion by the relation

$$m_{eff} = \frac{\hbar k}{\partial E/\partial k} \tag{15}$$

which is evaluated at the Fermi wavevector, k_F. For $Ga_{1-x}Mn_xAs$ the effective mass is assumed to be limited primarily by ionized impurity scattering. Under such assumptions the anomalously low values for the hole mobility in $Ga_{1-x}Mn_xAs$ relative to GaAs doped with hydrogenic acceptors could be explained by the VBAC theory **[44]**. When this form for the mobility is substituted into Equation 14, it is possible to explain the onset of the metal-insulator transition as is illustrated in Figure 31 (a). The VBAC calculations suggest that the MIT should occur at $x\approx0.018$ in $Ga_{1-x}Mn_xAs$, which is in reasonable agreement with the range $0.01\leq x\leq0.02$ typically seen experimentally.

Following this protocol the alloy-induced MIT in Mn-doped $GaAs_{1-y}P_y$ and $GaAs_{1-y}N_y$ is addressed. Now the mobility is limited by a second significant mechanism: alloy disorder. The effect of alloy disorder is treated using a standard formula applicable to extended impurity band states**[129]**,

$$\mu_{AD} = \frac{h^3 e}{8\pi^2 m_{eff}^2 k_F |V_{AD}|^2 \Omega (1-y) y}. \tag{16}$$

In Equation 16, Ω is the unit cell volume. V_{AD} is the alloy disorder potential- i.e. the matrix element of the potential difference between the actual potential for the sites that are occupied by either As or P (N) and the average, composition-weighted (VCA) potential, which should be evaluated using the wave functions of the Mn band. For transport within an impurity band V_{AD} is taken to be the offset of the impurity band edges of the appropriate $Ga_{1-x}Mn_x$-pnictide endpoint compounds**[130]**, which is estimated from experimentally-determined valence band offsets and

Mn acceptor level positions. Figure 31 (b) shows the impurity band-width along with δE calculated for $Ga_{0.954}Mn_{0.046}As_{1-y}P_y$ as a function of y for V_{AD} = 0.21 eV. According to these calculations, the MIT should occur at approximately y = 0.018 in $Ga_{0.954}Mn_{0.046}As_{1-y}P_y$, which is in good agreement with experiment (*c.f.* Figure 29). While the Mn impurity band-width decreases slightly with y, the driving force behind the MIT is the strong increase of δE due to alloy disorder scattering. Estimation of the critical value of y might be improved by including the effects of state broadening by Mn, which would decrease the mobility and thus shift the calculated MIT to slightly lower y.

Unlike the case of $Ga_{1-x}Mn_xAs_{1-y}P_y$, the exact value for V_{AD} in $Ga_{1-x}Mn_xAs_{1-y}N_y$ is unknown since valence band offsets between GaAs and zincblende (ZB) GaN are not known. Given that $V_{AD}\approx 0.7$ eV for wurtzite (WZ) GaN and that the bandgap of ZB GaN is 0.23 eV smaller than that WZ GaN, V_{AD} should be between 0.47 and 0.7 eV depending on the exact positions of the band offsets. For V_{AD}=0.7 eV, the MIT is calculated to occur for y=0.0025 as is shown in Figure 31. Choosing smaller values of V_{AD} (i.e., introducing a valence band offset between ZB GaN and GaAs) shifts the calculated value of the MIT towards y = 0.004, which is in better agreement with experiment. This simple model reproduces and describes well the experimentally observed trend in the MIT in $Ga_{1-x}Mn_xAs_{1-y}P_y$ and $Ga_{1-x}Mn_xAs_{1-y}N_y$, namely, that significantly less N than P is necessary to induce a metal-insulator transition. The agreement of this model with our experimental data lends further support to the picture of impurity band ferromagnetism in $Ga_{1-x}Mn_xAs$ even when x is high as 4.6%**[39, 40, 131]**.

4.5. Magnetic properties of $Ga_{1-x}Mn_xAs_{1-y}P_y$ and $Ga_{1-x}Mn_xAs_{1-y}N_y$

The scattering of holes by alloy disorder has a profound effect on T_C. Figure 32 (a) shows thermomagnetic profiles for selected $Ga_{0.954}Mn_{0.046}As_{1-y}P_y$ films. Measurements were performed with the 50 Oe field applied parallel to either the in-plane $[0\bar{1}1]$ direction or the out-of-plane [100] direction; the addition of P to $Ga_{1-x}Mn_xAs$ films on a GaAs substrate results in a tensile-strain-induced rotation of the easy axis from in-plane to out-of-plane**[132]**. Details of the magnetic anisotropy of $Ga_{1-x}Mn_xAs_{1-y}P_y$ are presented in Section 5.4. The films with y=0 and y=0.009 have $[0\bar{1}1]$ easy axes while the easy axis for films with $y\geq 0.024$ is perpendicular to the film. T_C was determined by extrapolation of the steepest portion of the thermomagnetic curve corresponding to a sample's easy axis to zero magnetization resulting in an uncertainty of 2-3 K. Increasing the P concentration of the film causes a clear decrease in T_C for the entire series of samples as shown in Figure 32 (b). This trend is in agreement with theoretical calculations which show the importance of maximizing the hole mean free path ($l=\hbar k_f\mu/e$) to achieve the highest possible T_C for a given x**[133]**. Isovalent anion substitution results in a decrease in l since μ decreases as holes are scattered by an increasingly disordered potential landscape, thus lowering T_C. Indeed, T_C drops by nearly a factor of 2 from $Ga_{0.954}Mn_{0.046}As$ to $Ga_{0.954}Mn_{0.046}As_{0.969}P_{0.031}$— to a value below that observed in $Ga_{0.954}Mn_{0.046}P$—with the substitution of only 3.1% of As atoms with P. In $Ga_{1-x}Mn_xAs_{1-y}N_y$ T_C falls from ~100 K to 60 K for y=0.010 (not shown).

Alloy disorder scattering has a strong effect on the magnitude of the saturation moment as well. Prior to the onset of the MIT, alloying the As sublattice with P decreases T_C without changing the saturation moment of 4.2±0.2 μ_B/Mn_{Ga} as shown in Figure 32 (c). A transition from the metallic to insulating state results in a reduction of the saturation moment to ~3 μ_B/Mn_{Ga} for y=0.031 despite the fact that the concentration of substitutional Mn remains the same. The random distributions of P (substituting As) and Mn_{Ga} lead to regions in the film

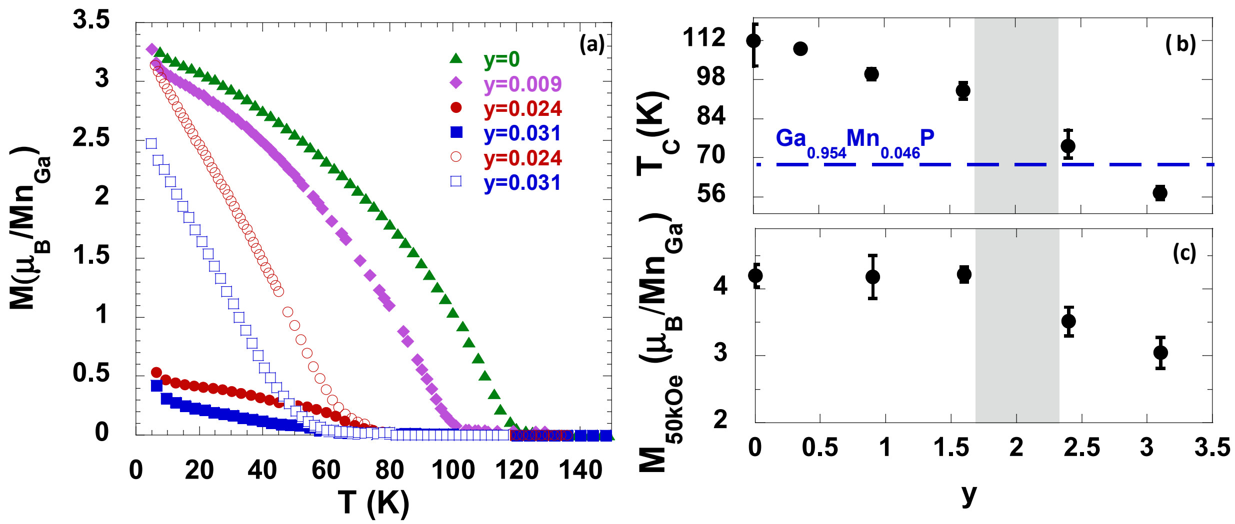

Figure 32: (a) Magnetization as a function of temperature for selected $Ga_{0.954}Mn_{0.046}As_{1-y}P_y$ films. Filled symbols correspond to data collected with the applied field parallel to an in-plane [011] direction. Open symbols show data collected with the applied field parallel to the [100] direction for films with out-of-plane easy axes, thus allowing for more accurate comparison of T_C. (b) Dependence of T_C on y for $Ga_{0.954}Mn_{0.046}As_{1-y}P_y$ for small y. The dashed grey line represents the T_C of $Ga_{0.954}Mn_{0.046}P$ indicating where the data points must eventually converge for y = 1 and is extrapolated from Figure 13. (c) Dependence of the saturation magnetization as measured in a field of 50 kOe as a function of y. The grey shaded regions of panels (b) and (c) represent the range of y in which the MIT occurs.

where stronger hole scattering by alloy disorder decouples locally Mn_{Ga} moments from the global ferromagnetic exchange. Hence, when $y>y_{crit}$ T_C is depressed further due to a decrease in the concentration of ferromagnetically active Mn_{Ga} moments.

The trends in magnetic and electrical properties discussed in this and the preceding sections have also been observed in other sets of $Ga_{1-x}Mn_xAs_{1-y}P_y$ thin films synthesized by II-PLM. Some data for these samples are given in Appendix E.

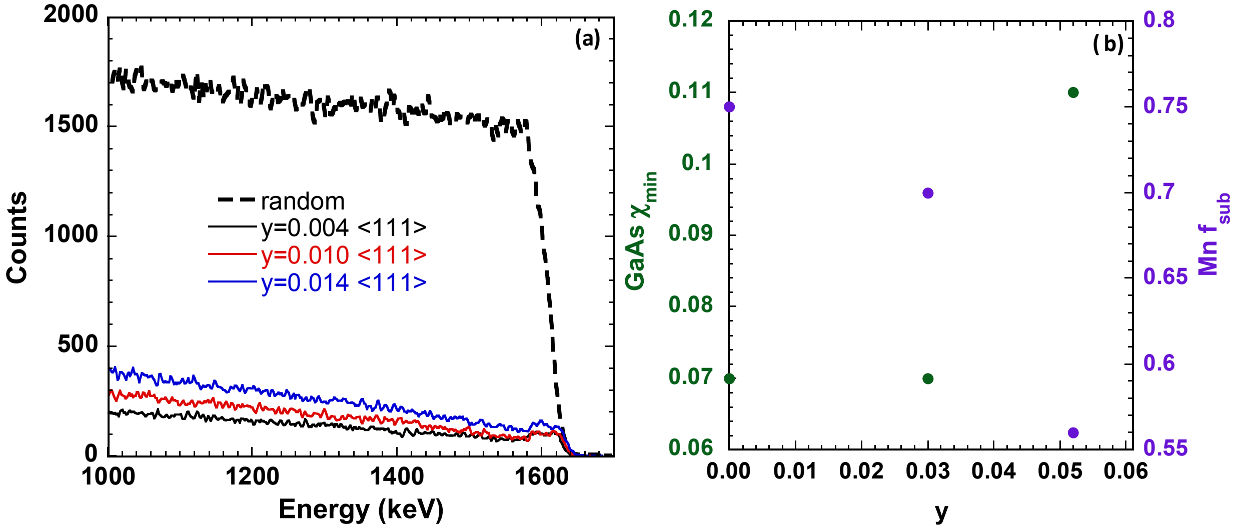

Figure 33: (a) RBS spectra for $Ga_{1-x}Mn_xAs_{1-y}N_y$ samples for random and <111>-channeled orientations of the ion beam. (b) Relationship between GaAs χ_{min}, Mn f_{sub} and P content for $Ga_{0.96}Mn_{0.04}As_{1-y}P_y$.

4.6. Limitations of II-PLM on the Study of Quaternary Ferromagnetic Semiconductors

The internal growth interface inherent to II-PLM makes this processing method incompatible with the use of buffer layers between the thin film and underlying substrate. Therefore, thin films based on GaAs must be grown on GaAs, thin films based on GaP must be grown on GaP, *etc.* This processing limitation places limits on the amount of an alloying species that can be incorporated into the material without compromising crystal quality due to the accommodation of the lattice mismatch between film and substrate. For the situation of Mn substituting for Ga, the difference in atomic radii is quite small, and high-quality films (here defined by having $\chi_{min}<0.1$) can be achieved for x up to 0.046. On the other hand, the quaternary materials that have been discussed in this chapter are already approaching critical lattice misfits due to the size mismatch between N or P and As.

Figure 33 (a) shows the RBS spectra for $Ga_{1-x}Mn_xAs_{1-y}N_y$ samples with various N concentrations. As y increases the backscattered intensity from the <111> channel monotonically increases relative to the random backscattered intensity. The value of χ_{min} increases from 0.05 to 0.09 as y increases from 0.004 to 0.014. In parallel, the full-width at half maximum (FWHM) of the X-ray diffraction peaks of the $Ga_{1-x}Mn_xAs_{1-y}N_y$ film increases with increasing y [Figure 28(b)]. These observations indicate that the defect levels in the $Ga_{1-x}Mn_xAs_{1-y}N_y$ film increases with N alloying, which is attributed to the accommodation of the lattice misfit of the $Ga_{1-x}Mn_xAs_{1-y}N_y$ film.

Figure 33 (b) shows the effect of P alloying on the GaAs χ_{min} and Mn f_{sub} for $Ga_{0.96}Mn_{0.04}As_{1-y}P_y$. For $y>0.05$ a sharp increase in χ_{min} is observed, which indicates a degradation of the crystalline quality of the thin film. Along with the poorer quality film, the Mn f_{sub} is also diminished. Once this structural regime is reached the usefulness of the materials is lessened in two ways. First, the increased defect levels will obviously affect resistivity measurements through increased scattering, which makes it difficult to directly assess the role of alloy scattering on the electrical properties. Second, since the Mn f_{sub} is affected, it is not possible to easily produce films with constant x by keeping the Mn implantation and laser processing conditions unchanged (*c.f.* Table 2). In this regime x will scale with y, which makes studies requiring nearly constant x difficult to accomplish.

One possible route to overcome processing limitations due to lattice misfit is to implant the Mn directly into a $GaAs_{1-y}P_y$ film. Then, the regrowth would occur using the $GaAs_{1-y}P_y$ as a template and misfit would only be due to Mn-related defects. The limiting factor here is the growth of single crystalline $GaAs_{1-y}P_y$ thin films with large P concentrations by MBE. Preliminary attempts to grow $Ga_{1-x}Mn_xAs_{1-y}P_y$ with larger y by this method have been unsuccessful mainly owing to the high defect levels in the initial $GaAs_{1-y}P_y$ film.

4.7. Comparison to Other Studies of $Ga_{1-x}Mn_xAs_{1-y}P_y$

After the commencement of this work several other groups have since produced $Ga_{1-x}Mn_xAs_{1-y}P_y$ by LT-MBE. Qualitatively, the trends observed in this work were observed in preliminary studies of $Ga_{1-x}Mn_xAs_{1-y}P_y$ grown by LT-MBE; namely, T_C decreases and alloying induces a MIT and increase in resistivity **[134, 135]**. In both of these studies, however, the onset of the MIT was found to occur at a larger value of y, which may be due to the films examined in these studies having a higher Mn_{Ga} concentration, x.

More recently, it was argued that T_C and conductivity are only weakly influenced by P alloying in $Ga_{0.93}Mn_{0.07}As_{1-y}P_y$ with $y\leq0.088$ **[136]**. No MIT was observed over this compositional range, which the authors claim is in contradiction to the results presented in this dissertation. However, the accuracy of the alloy compositions presented in Ref. **[136]** (as well as Ref. **[134]**) must be questioned as they were determined only by indirect methods. For example, the P concentration of each film was determined by applying Vegard's law to $GaAs_{1-y}P_y$ thin films grown in the absence of Mn, which assumes that the addition of a Mn flux to the LT-MBE growth conditions does not affect P incorporation or growth mode. Moreover, the electrical resistivity varies unsystematically by over a factor of 3 in these $Ga_{1-x}Mn_xAs_{1-y}P_y$ films, which suggests that the Mn incorporation and/or film quality is influenced by the presence of P during growth. Clearly, this must affect the interpretation of the electrical and magnetic measurements.

Recently presented data in the same series of samples in Ref. **[136]** shows that an MIT occurs for $y \approx 0.1$ **[137]**. Upon moving from metallic to localized electronic transport, both T_C and the saturation moment decrease **[137]**. The principal difference between Ref. **[136]** and the work presented herein is the that in the former the critical anion sublattice composition at which the MIT occurs is larger by a factor of ~3. Given the uncertainty in alloy composition (both in x and y) as well as the fact that the former study focused on films that were nominally more heavily doped, the differences between the two studies are not as significant as they appear at first sight. In this respect the behavior of LT-MBE grown $Ga_{1-x}Mn_xAs_{1-y}P_y$ is rather similar to II-PLM formed $Ga_{1-x}Mn_xAs_{1-y}P_y$; an alloy-induced MIT occurs which results in sharp decreases in T_C and the saturation moment. These observations underscore the need for careful and systematic determination of the structural properties of $Ga_{1-x}Mn_xAs_{1-y}P_y$ films (Section 4.2) in order to allow for accurate comparison of their electronic and magnetic properties.

4.8. Summary

This chapter has explored the effect of dilute anion sublattice alloying on the structural, electronic, and magnetic properties of Mn-doped III-V semiconductors. The principle finding of this chapter is that the conductivity and T_C of $Ga_{1-x}Mn_xAs$ *decrease* strongly upon dilute alloying (<4%) with either P or N. In both cases a transition from metallic to insulating electrical behavior is observed with $0.016 \leq y_{crit} \leq 0.024$ for $Ga_{0.954}Mn_{0.046}As_{1-y}P_y$ and $y_{crit} < 0.004$ in $Ga_{0.954}Mn_{0.046}Mn_{1-y}N_y$. The observation of an MIT at such small alloying levels is consistent with a band structure in which impurity-band holes are increasingly scattered by the potential fluctuations due to alloy disorder. This work further demonstrates the complex parameter space which determines T_C in ferromagnetic semiconductors. In addition to the Mn_{Ga} and hole concentrations, the mean free path, which depends strongly on local disorder, plays an important role in determining the robustness of ferromagnetic exchange.

The dependence of T_C on anion sublattice composition determined in this work is in contradiction with calculations based on mean-field theory that predict an enhancement of the T_C of $Ga_{1-x}Mn_xAs$ with P alloying due to an enhanced *p-d* exchange interaction **[54]**. Such calculations do not explicitly consider localization effects and therefore would not capture the effect of alloy disorder scattering. This further emphasizes the importance of integrating localization and disorder effects into theoretical predictions of the magnetic properties (particularly T_C) of ferromagnetic semiconductors.

5. The Magnetic Anisotropy of $Ga_{1-x}Mn_xP$ and Related Alloys

5.1. Introduction to Magnetic Anisotropy

The internal energy of a ferromagnetic material depends on the orientation of the magnetization relative to its coordinate axes**[138]**. As a result, the magnetic properties of a sample will depend on the direction on which they are measured, which is referred to as magnetic anisotropy**[139]**. Before exploring the origins of the magnetic anisotropy in magnetic materials, it is useful to review some basic definitions. The anisotropy energy refers to the contribution to the total energy of the system that is due to the orientation of the magnetization vector. The magnetic easy axis refers to the direction of the spontaneous magnetization that occurs at a minimum in the anisotropy energy landscape. Put another way it refers to the orientation that the magnetization vector takes in the absence of an applied magnetic field; since there is no Zeeman term for H=0, the anisotropy energy alone determines the orientation of the magnetization. Similarly a magnetic hard axis, refers to a maximum in the energy landscape. In order to orient the magnetization parallel to a hard axis an external field must be applied to overcome the anisotropy energy, which is known as the anisotropy field.

Some origins of the magnetic anisotropy in general ferromagnetic materials are now discussed. For contributions to the magnetic anisotropy specific to ferromagnetic semiconductors refer to Section 5.3. The magnetocrystalline anisotropy energy refers to the energy difference between samples magnetized along easy and hard directions **[139]**. While not completely understood from first principles the origin of the magnetocrystalline anisotropy is believed to be due to the coupling of the spin and orbital angular momenta. A simple illustration of the origin of the magnetocrystalline anisotropy is shown in Figure 34. The discussion follows that given by Spaldin **[139]**. The left side of the figure shows the minimum energy configuration of the atomic orbitals (represented schematically by green diffuse ovals). The coupling of the spin and orbital angular momenta is such that the spin wants to point up. Suppose now that one wishes to orient the spin vector such that it points to the right. This motion is resisted since the orbital angular momentum is coupled to the lattice. In the final, higher energy state (right side of Figure 34) the orbital components no longer have favorable overlap with one another or the lattice. The magnitude of the magnetocrystalline anisotropy scales with the strength of the spin-orbit interaction. Since the spin-orbit interaction scales as Z^4, the magnetocrystalline anisotropy is most pronounced in materials with heavy magnetic elements. Similarly, if the total orbital angular momentum is zero, then no magnetocrystalline anisotropy is expected to first order since there is no orbital angular momentum for the spins to couple to.

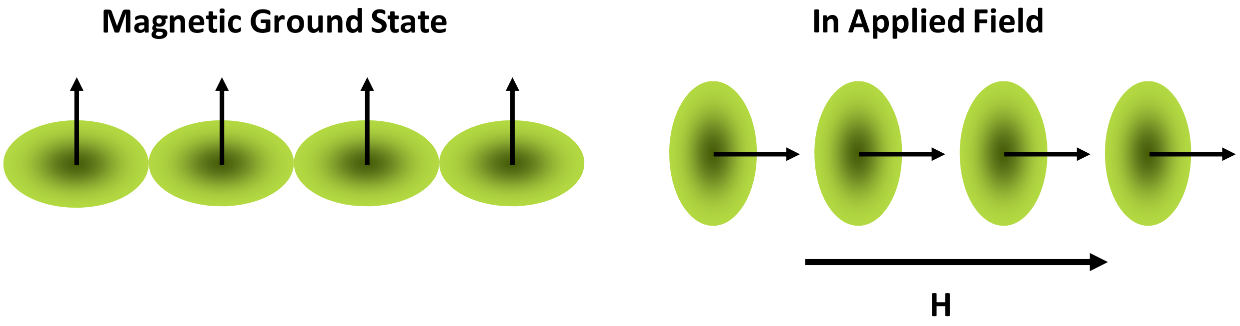

Figure 34: Schematic illustration of magnetocrystalline anisotropy arising from spin-orbit coupling. An applied field of magnitude *H* is needed to orient the spins along the magnetically hard direction. Illustration modeled after [140].

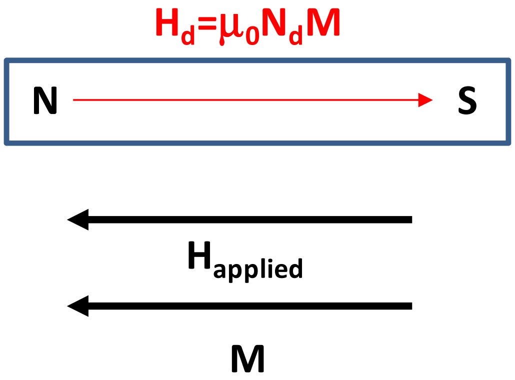

Figure 35: Illustration of the demagnetization field in a bar magnet.

Since the orbital angular momentum is strongly tied to the crystal lattice, it is not surprising that the symmetry of the magnetocrystalline anisotropy is the same as the crystal structure. The anisotropy energies for magnetocrystalline anisotropy are generally expressed as series of trigonometric functions which reflect the symmetry of the underlying lattice. For example a crystal of cobalt has hexagonal symmetry. The magnetic easy axis in such a material is the *c* axis while orientations in the basal plane are magnetically hard **[138]**. Following Chikazumi, the free energy is expanded in terms of $\sin^2\phi$ where ϕ defines the angle between the *c* axis and the magnetization vector:

$$E = K_{u1}\sin^2\phi + K_{u2}\sin^4\phi + \cdots \tag{17}$$

where K_{u1} and K_{u2} are the first and second order anisotropy constants. Higher order terms may be added as needed, but usually the first term K_{u1} is sufficient to describe the anisotropy. For materials of cubic symmetry the free energy is written as a polynomial series of the directional cosines α_1, α_2, α_3 between the magnetization vector and the cube edges. The series is simplified by making a few observations. All terms containing odd powers of α_i must vanish since the energy should be invariant under the transformation $\alpha_i \rightarrow -\alpha_i$. Second, not all of the directional cosines are independent of one another; in a cubic system the relation $\alpha_1^2+\alpha_2^2+\alpha_3^2=1$ holds. Using these relations the energy is written as

$$E = K_{C1}(\alpha_1^2\alpha_2^2 + \alpha_2^2\alpha_3^2 + \alpha_1^2\alpha_3^2) + K_{C2}(\alpha_1^2\alpha_2^2\alpha_3^2) \tag{18}$$

where K_{C1} and K_{C2} are now the first and second order cubic anisotropy constants. The sign of K_{C1} determines which crystallographic axes are magnetically easy.

Magnetic anisotropy can also arise due to the shape of a material. The origin of the shape anisotropy is the demagnetization field, which is depicted in Figure 35. When an external magnetic field is applied as shown in Figure 35, the magnetic moment will rotate such as to align the magnetization vector with the applied field. For the bar magnet shown in Figure 35 this results in the north pole on the left and south pole on the right. By definition magnetic field lines are drawn from the north pole to the south pole. Therefore the effective field within the material is reduced by an amount H_d referred to as the demagnetization field. The demagnetization field is a function of the sample magnetization

$$H_d = \mu_0 N_d M \tag{19}$$

where N_d is the demagnetization factor. The demagnetization factors can be solved exactly only for a few high-symmetry geometries such as spheres, infinite planes, and ellipsoids. For example, a sphere has $N_x=N_y=N_z=1/3$ where N_x, N_y, and N_z are the components of the demagnetization factor parallel to the three Cartesian axes. For a thin film with surface normal parallel to the z-axis, we have that N_z=1 and N_x=N_y=0. Therefore, it is harder to magnetize a thin-film sample for $H||z$ than for $H||x$ or $H||y$ due to shape anisotropy.

5.2. Experimental Determination of the Magnetic Anisotropy

5.2.1 *Magnetic Resonance*

The starting point for discussing magnetic resonance is the gyromagnetic effect, which refers to the generation of angular momentum by the magnetization of a ferromagnetic body **[138]**. Consider a magnetic moment with angular momentum **L** that is placed in an external magnetic field **H** as is illustrated in Figure 36. The magnetic field **H** causes a torque $\boldsymbol{\tau}$=d**L**/dt=$\mu_0 MH\sin\theta$ which changes the angular momentum. At any moment in time, d**L** is orthogonal to both **H** and **L** giving rise to the characteristic precessional motion traced out by the dashed line in Figure 36. Since dϕ=d**L**/(**L** sinθ), the precession frequency Ω=dϕ/dt is

$$\Omega = \frac{dL}{dt}\frac{1}{L\,sin\theta} = \frac{\mu_0 MH}{L}. \tag{20}$$

Defining gyromagnetic ratio as

$$\gamma = M/L \tag{21}$$

which connects a particles angular momentum and magnetic moment, the precessional frequency is

$$\Omega = \upsilon\gamma H. \tag{22}$$

The gyromagnetic ratio is defined as

$$\gamma = \frac{ge}{2m} = 8.782x10^{10} \cdot g\ [A \cdot \frac{s}{kg}] \tag{23}$$

where m is the rest mass of the electron, e is the elementary charge, and g is the Landé g-factor, which is equal to 1 for angular momentum derived from orbital motion and 2 for spin. Equation 23 is given in SI units as indicated in the square brackets. Electromagnetic radiation applied perpendicular to **H** can excite this precession into resonance provided that the frequency f of the incident radiation is matched to the precessional frequency Ω. Therefore, we arrive at the resonance condition

$$f = \frac{c}{\lambda} = \frac{\Omega}{2\pi} = \frac{ge\mu_0 H}{4\pi m} \tag{24}$$

which is satisfied for λ=1.1 cm and g=2 by an applied field of 1 T.

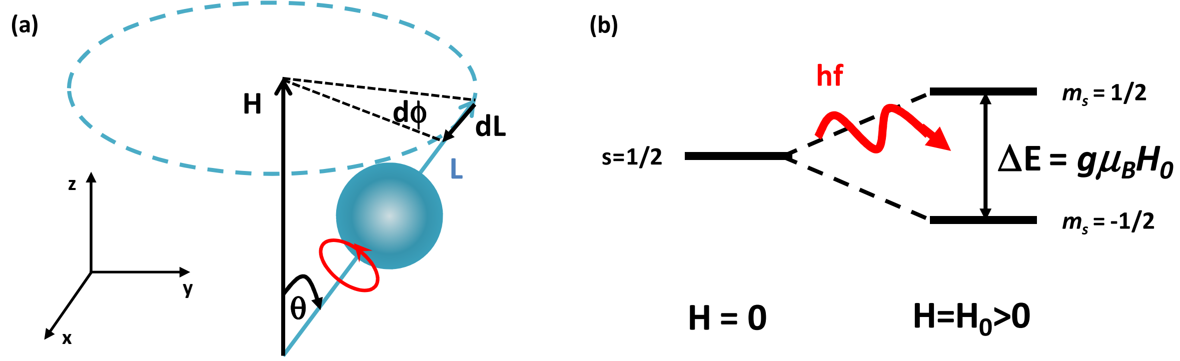

Figure 36: (a) Illustration of the precessional motion of a magnetic moment of angular momentum L in a magnetic field H. The frequency of precession Ω=dϕ/dt is given by νH. (b) Energy level splitting by the Zeeman effect for a spin-1/2 state.

One can also arrive at the condition for magnetic resonance by considering simple energy arguments. When an electron with s=1/2 is placed in a magnetic field H=H_0 the energy level Zeeman splits with a gap equal to $g\mu_B H_0$ [Figure 36 (b)]. Therefore, photons of frequency f= $g\mu_B H_0/h$ are resonantly absorbed. Recognizing that the Bohr magneton is defined as $eh/4\pi m$, one arrives at Equation 24.

The position of the magnetic resonance line depends strongly on a material's magnetic anisotropy. Consider a magnetic moment that is subject to a uniaxial anisotropy. The anisotropy energy can be written as

$$E = K_{u1}\sin^2\alpha \approx K_{u1}\alpha^2 \tag{25}$$

where K_{u1}>0 and α is the angle between the magnetization vector and the easy axis. The effect of the uniaxial magnetic anisotropy can be thought of as producing a fictitious magnetic anisotropy field H_a, the effect of which is to drive the alignment of magnetic moments along the easy axis. Therefore, the pseudo Zeeman energy of this field is

$$E = -\mu_0\vec{M}\cdot\overrightarrow{H_a} = -\mu_0 M H_a\cos\alpha \approx \frac{1}{2}\mu_0 M H_a\alpha^2. \tag{26}$$

Comparing Equations 25 and 26 the effective anisotropy field is defined as

$$\mu_0 H_a = \frac{2K_{u1}}{M}. \tag{27}$$

The anisotropy field alters the resonance condition since the frequency of precession will be determined by the combined effect of the applied magnetic field and the anisotropy field

$$\Omega = \mu_0\gamma(H + H_a) = 2\pi f. \tag{28}$$

Typically magnetic resonance experiments are performed by holding the frequency of the incident radiation constant and scanning the magnitude of the magnetic field through the resonance condition. Therefore, the applied field at which the resonance occurs is altered

$$\mu_0 H_{res} = \frac{\Omega}{\gamma} - \mu_0 H_a = \frac{4\pi m f}{ge} - \frac{2K_{u1}}{M}. \tag{29}$$

Since K_{u1}>0 for an easy axis in this example, the applied field at which resonance is observed for a given frequency is smaller than if no anisotropy were present (i.e. K_{u1}=0). Likewise if we were measuring a magnetically hard direction (K_{u1}>0 according to this convention), it requires a larger applied magnetic field it excite resonance. The resonance experiments performed in this work were performed at f=9.26 GHz resulting in $\mu_0 H_{res}$≈331 mT for moments exhibiting zero anisotropy with g≈2.0, which is a useful reference point for the anisotropy fields.

The situation in ferromagnetic materials is significantly more complicated than the simple examples discussed above. The magnetic field $\boldsymbol{H}$ that drives the precession motion is replaced by an effective field, which is the sum of the applied field, anisotropy fields, and the exchange field which couples the individual magnetic moments. Furthermore, the lattice dampens the motion of the magnetic moments around the field direction, which has so far not been considered. The full motion of the magnetic moments in a ferromagnetic material can be described by the Landau-Lifschitz-Gilbert equation

$$\frac{\partial\boldsymbol{M}}{\partial t} = -\gamma\boldsymbol{M}\times\left(\mu_0\boldsymbol{H_{eff}}\right) + \frac{\tilde{G}}{\upsilon M_{sat}^2}\boldsymbol{M}\times\frac{\partial\boldsymbol{M}}{\partial t} \tag{30}$$

where $\tilde{G}$ is the Gilbert damping parameter and M_{sat} is the value of the saturation magnetization. The first term in Equation 30 is the torque exerted on the magnetic moments by the effective field on the magnetic moment and is identical to that derived in the first paragraph of this section where $\boldsymbol{H}$ has been replaced by the effective field $\boldsymbol{H_{eff}}$. The second term describes the effect of energy losses on the trajectory of the magnetic moment, which relaxes towards the direction of

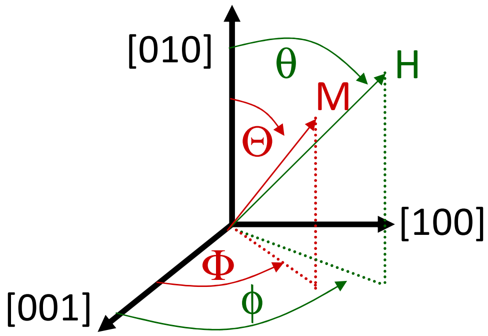

Figure 37: Coordinate system used for FMR calculations. The orientation of the magnetization is described by capital letters, while the applied field is described by lowercase letters. The [100] direction is normal to the thin film plane.

the applied field (the vector $\boldsymbol{M} \times \partial\boldsymbol{M}/\partial t$ that describes the direction of the damping force is always orthogonal to both $\boldsymbol{H}_{eff}$ and $\boldsymbol{M}$; see Figure 36).

While Equation 30 describes the complete time-dependent motion of the magnetic moment during a resonance experiment, it can be quite difficult to use in modeling experimental results. A more convenient approach is derived from applying Lagrange's equations of motion to a classical top in a potential field, F. In this formalism the resonance condition is written as

$$\left(\frac{\omega}{\gamma}\right)^2 = \frac{1}{M_{sat}^2 \sin^2\Theta}\left[\left(\frac{\delta^2 F}{\delta\Phi^2}\right)\left(\frac{\delta^2 F}{\delta\Theta^2}\right) - \left(\frac{\delta}{\delta\Phi}\frac{\delta}{\delta\Theta}F\right)^2\right]_{\substack{\Theta=\Theta_0\\ \Phi=\Phi_0}} \tag{31}$$

with the angles Θ and Φ describing the orientation of the magnetization vector relative to the crystallographic axes according to the coordinate system defined in Figure 37. The angles Θ_0 and Φ_0 denote the equilibrium orientation of the magnetization. The free energy F contains contributions from the Zeeman, and anisotropy energies

$$\begin{aligned} F(\Theta, \Phi, \theta, \phi, H) = -\mu_0 MH(&\sin\theta \sin\phi \sin\Theta \sin\Phi + \cos\Theta \cos\theta \\ &+ \sin\Theta \sin\theta \cos\Phi \cos\phi) + F_{anisotropy}(\Theta, \Phi, \{\mathrm{K}\}) \end{aligned} \tag{32}$$

where the anisotropy energy contains information about demagnetization, strain and magnetocrystalline effects. The specific form of the anisotropy energy will be written in the following section once the specific contributions to the magnetocrystalline anisotropy of III$_{1-x}$Mn$_x$V materials have been discussed. The Equations 31 and 32 along with the condition for equilibrium for the magnetization

$$\left.\frac{\delta F}{\delta\Theta}\right|_{\Theta=\Theta_0} = \left.\frac{\delta F}{\delta\Phi}\right|_{\Phi=\Phi_0} = 0 \tag{33}$$

form a set of three equations in three unknowns, Θ, Φ, and H. Therefore, for a specific magnetic field orientation relative to the sample's crystallographic axes one can calculate the equilibrium orientation of the magnetization $\{\Theta_0, \Phi_0\}$, and the resonance field H_{res} for a specific set of anisotropy constants.

To determine the anisotropy parameters from the free energy approach, one measures the dependence of the magnetic resonance field as a function of the orientation of the applied magnetic field– i.e. by rotating θ and ϕ. The data are compared to calculations of the position of the resonance field according to Equations 31-33. The set of anisotropy constants enter as fitting parameters; the anisotropy constants are iteratively adjusted until the measured angular dependence of the FMR is reproduced by the model.

It should be noted that the free energy model does not capture the complete set of information described by Equation 30. In essence Equation 31 considers only the driving term of Equation 30. While this is sufficient to determine the field at which magnetic resonance is observed for a specific frequency, information related to energy losses and the interaction of the precessing magnetic moments with the lattice is lost. Descriptions of the FMR line width and spin wave excitations are not possible using the free energy approach. The former requires modeling the entire absorption lineshape (not just the position of the resonance) while the latter produces additional resonances at fields less than the collective mode (Section 5.5). Both of these features are not captured by Equation 31. Nonetheless, the free energy approach provides a straightforward method by which to determine the anisotropy parameters of a material, which is the main focus of this chapter.

5.2.2 *SQUID Magnetometry*

The magnetic anisotropy can also be determined by measuring the field and/or temperature dependence of the magnetization in a SQUID magnetometer. This can be understood by considering the interplay of the Zeeman and anisotropy energies, which is considered here by the simple two-dimensional example in Figure 38. Let the magnetization be confined to the x-y plane. The magnetization and magnetic field vectors make angles α and β with the y axis, respectively, as illustrated in Figure 38. For this simple example the magnetic anisotropy will consist of a single uniaxial term. The energy of such a system is

$$F = K_u \sin^2 \beta - MH(\sin \alpha \sin \beta + \cos \alpha \cos \beta) \tag{34}$$

where the first term describes the anisotropy energy and the second term the Zeeman energy. Taking $K_u>0$, Eq. 34 implies that the y-axis is the magnetic easy axis. Figure 38(b) and Figure 38(c) show the energy of the systems as a function of the orientation of the magnetization for the applied field parallel to the easy axis (α=0°) and hard axis (α=90°) respectively. For these calculations it was assumed that M=10 kA/m and K_u=300 J/m^3. For the case of $\boldsymbol{H} \parallel y$ the free energy curves have minima at β=0° for $H\geq 0$ mT. Recalling that one are measuring the projection of the magnetization along the direction of the applied magnetic field, this implies that we will measure a large, positive signal for the α=0° geometry. The situation for α=90° is much different. At the highest field the Zeeman energy dominates and the minimum in the free energy contour occurs near β=90°, which again implies a large, positive signal. However, as the magnitude of the applied magnetic field is reduced, the anisotropy energy begins to dominate. Since y is the easy direction, the minimum shifts towards β=0°, thereby reducing the measured magnetic moment by a factor of Cos(90°-β) relative to the value measured at the same field for α=0°. At zero applied field the Zeeman energy vanishes thereby causing the minimum to occur precisely at β=0° and causing zero remanent magnetization to be measured in the α=90° alignment. As such the remanent moment provides a measure of the angle between the easy axis and the orientation of the applied magnetic field; one can triangulate the orientation of the magnetic easy axis by measuring *M(H)* for the principle crystallographic directions.

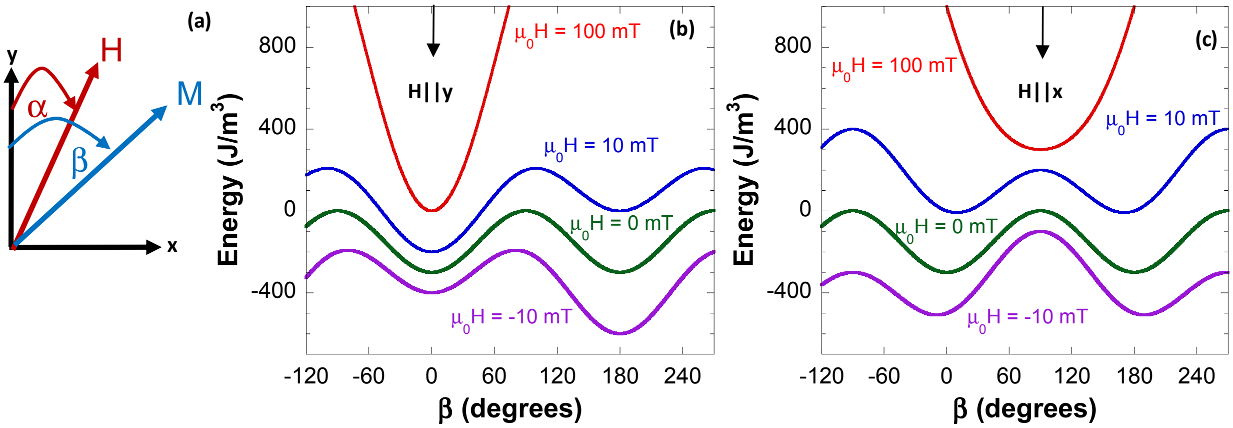

Figure 38: Example of the measurement geometry and determination of the magnetic anisotropy for a traditional magnetometry experiment. Panel (a) defines the two dimensional coordinate system used in the example. The *y*-direction is assumed to be the magnetic easy axis. Panel (b) displays free energy contours for the case where the magnetic field is parallel to the *y*-axis (α=0°). The energy minima always occur for β=0°/180° in accordance with Eq. 34. In panel (c) the field is applied parallel to the *x*-axis (α=90°).

The situation is, of course, more complicated in actual materials systems where there are numerous contributions to the magnetic anisotropy, as well as magnetic domains, materials defects, temperature effects, *etc.* Such effects were not considered in the simple example, where single domain behavior and T=0 K were assumed in order to calculate the free energy curves. As a result the remanent moment, even for the magnetic easy axis, is diminished relative to its saturation value, an effect not captured above where M is always the same value for the magnetic easy axis. However, the basic principles derived from Equation 34 are still applicable. The moment at remanence is reduced for non-easy axes by an amount proportional to the cosine of the angle between the easy axis and the magnetic field vector, and the lineshape of the *M(H)* curves will differ for easy and hard axes.

5.3. Magnetic Anisotropy in $III_{1-x}Mn_xV$ Materials

Based purely on the symmetry of the zincblende lattice, one would expect the magnetic anisotropy of $Ga_{1-x}Mn_xAs$ and other Mn-doped cubic III-V semiconductors to be dominated by cubic terms **[141]**. This would indeed be true for free-standing $III_{1-x}Mn_xV$ materials, and one could describe this cubic magnetocrystalline anisotropy by K_{C1}, and K_{C2} (see Equation 18). However, this is not done in practice because Mn-doped III-V materials are nearly exclusively grown as pseudomorphic, epitaxial thin films, which lowers the symmetry of the system from cubic to tetragonal. Instead, it is conventional in the field of magnetic semiconductors to use anisotropy parameters associated with tetragonal symmetry. Cubic anisotropy in the plane of the film and perpendicular to the plane are described by $K_{C1}^{||}$ and $K_{C1}^{\perp}$, respectively, which should only be equal when the system is of cubic symmetry. The sign of the cubic anisotropy terms determines whether the <100> or <110> crystallographic axes are magnetically easy. The strain along the growth direction also gives rise to a perpendicular uniaxial magnetic anisotropy term K_u^{100} in addition to the cubic terms. The sign and magnitude of K_u^{100} are tied to the strain state of the film. In both $In_{1-x}Mn_xAs$ **[47, 142]** and $Ga_{1-x}Mn_xAs$ **[143, 144]** the magnetic easy axis tends to lie in (perpendicular to) the thin film plane for compressive (tensile) epitaxial strain. However, some exceptions to this rule have been found in $Ga_{1-x}Mn_xAs$ with very low carrier concentration where a perpendicular easy axis can be found in material under compressive strain **[145]**.

Finally there is an additional component to the magnetic anisotropy that is unexpected on the grounds of symmetry: the in-plane <011>-type directions are magnetically inequivalent, which is parameterized by K_u^{011}. While this is by far the weakest contribution to the magnetic anisotropy, it is found in both $Ga_{1-x}Mn_xAs$ **[38, 143, 146-148]** and $In_{1-x}Mn_xAs$ **[142]** suggesting that it is a general property of $III_{1-x}Mn_xV$ systems. The origin of in-plane uniaxial anisotropy remains unclear and will be discussed in more detail in the following section. In $Ga_{1-x}Mn_xAs$ the magnitude and sign of K_u^{011} have been correlated to the carrier concentration of the material **[38]**.

The interplay of the cubic and uniaxial anisotropies can give rise to several unique behaviors. In $Ga_{1-x}Mn_xAs$ both positive and negative $K_{C1}^{||}$ have been observed meaning that in some samples <001> axes are magnetically preferred **[141, 143]** while in others <011>-type easy axes are observed **[56, 57]**. The underlying mechanism responsible for this behavior is not understood, nor can it be explained by common theoretical approaches **[17, 19]**. In $Ga_{1-x}Mn_xAs$ the uniaxial anisotropy favors <011>-type directions with either $[0\bar{1}1]$ or [011] as the easy axis depending on the sign of K_u^{011}. In general, uniaxial anisotropy fields scale with M^2 while cubic anisotropy fields scale with M^4 **[141]**. Therefore, when the temperature is low and the magnetization is large the cubic anisotropy dominates. Then, for samples with positive $K_{C1}^{||}$, the easy axis is parallel to one of the in-plane <001> directions at low temperatures. As the temperature increases and the magnetization decreases, a transition occurs whereby the uniaxial anisotropy is more significant than the cubic anisotropy. Since the uniaxial anisotropy field favors a non-<001> direction, there is a temperature at which the easy axis reorients spontaneously from <001> to either $[0\bar{1}1]$ or [011] **[149]**. On the other hand, in $In_{1-x}Mn_xAs$ as well as $Ga_{1-x}Mn_xAs$ films with negative $K_{C1}^{||}$ the cubic anisotropy field seems to always favor <011>-type easy axes in the plane of the film**[150]**. In this case, no temperature-induced reorientation of the easy axis is observed. The interplay of the cubic and uniaxial anisotropy fields leads to a complicated free energy landscape, particularly when the two are of similar magnitude. This can lead to multistep spin switching processes during magnetization reversal and the development of double hysteresis loops. In low-doped $Ga_{1-x}Mn_xAs$ double hysteresis loops were observed for out-of-plane magnetization reversal when the out-of-plane anisotropy fields were of similar magnitude **[151]**. It will be shown below that similar behavior is observed in $Ga_{1-x}Mn_xP$ for in-plane magnetization reversal (Section 5.7).

Having identified the principle components of the magnetic anisotropy in epitaxially-strained $III_{1-x}Mn_xV$ materials it is possible to rewrite the total anisotropy energy in Equation 32. The anisotropy energy is

$$\begin{aligned} F_{anisotropy}(\Theta, \Phi) &\\ &= K_{eff}^{100} \sin^2\Theta \sin^2\Phi \\ &\quad - \frac{1}{2} K_{C1}^{\perp} \sin^4\Theta \sin^4\Phi - \frac{1}{2} K_{C1}^{||} (\cos^4\Theta + \sin^4\Theta \cos^4\Phi) \\ &\quad + \frac{1}{2} \mathrm{K}_{\mathrm{u}}^{011} (\cos\Theta + \sin\Theta \cos\Phi)^2 \end{aligned} \tag{35}$$

and depends only on the orientation of the magnetization vector according to the coordinate system in Figure 37. The anisotropy constant K_{eff}^{100} combines the effect of the out-of-plane uniaxial anisotropy, K_{u}^{100}, due to epitaxial strain and the shape anisotropy, which have the same angular dependence. In the absence of strain (that is, the system relaxes to its cubic structure), Equation 35 simplifies since K_{u}^{100}=0 and $K_{C1}^{\perp}$=$K_{C1}^{||}$. In this case K_{eff}^{100} is exclusively due to the shape anisotropy and the second and third terms of Equation 35 are the first-order cubic magnetocrystalline anisotropy energy

$$-\frac{1}{2}K_{C1}(\sin^4\Theta\sin^4\Phi+\cos^4\Theta+\sin^4\Theta\cos^4\Phi)=-\frac{1}{2}K_{C1}(\alpha_1^4+\alpha_2^4+\alpha_3^4). \tag{36}$$

The right-hand side of Equation 36 is equivalent to the leading terms of Equation 18 by the addition theorem for directional cosines

$$\alpha_1^4+\alpha_2^4+\alpha_3^4=1-2(\alpha_1^2\alpha_2^2+\alpha_2^2\alpha_3^2+\alpha_1^2\alpha_3^2). \tag{37}$$

Therefore, the effects of strain on the magnetic anisotropy enter the theoretical framework in multiple locations. The cubic anisotropy parameters used in the rest of this chapter should not be interpreted as the magnetocrystalline anisotropy parameters as both contain a contribution from strain. It should be noted that it is possible to derive an alternate form of the free energy for tetragonally-distorted epitaxial thin films in which the anisotropy is written in terms of a single cubic magnetocrystalline anisotropy parameter and a second order perpendicular uniaxial parameter related to strain **[119]**.

It may seem surprising that the magnetic properties of Mn-doped III-V semiconductors show such a strong dependence on crystal orientation since the $\mathrm{Mn_{Ga}}$ moments are incorporated in a high-spin Mn^{2+} electronic state; all five 3*d* orbitals contain one electron and the total angular momentum of the system is 0, implying that magnetocrystalline anisotropy due to first order spin-orbit effects should be extremely weak. Indeed, the anisotropy fields due to single ion spin-orbit effects derived from electron-spin magnetic resonance experiments of Mn in GaAs are orders of magnitude too small to account for the magnitude of the magnetic anisotropy fields observed in $\mathrm{Ga}_{1-x}\mathrm{Mn}_x\mathrm{As}$ **[146, 152]**. Furthermore, shape anisotropy effects also cannot explain the magnetic anisotropy in $\mathrm{Ga}_{1-x}\mathrm{Mn}_x\mathrm{As}$. The effect of the demagnetization field would always induce the magnetization to lie in the plane of the film, which is inconsistent with the behavior of films in tensile strain. Even for compressively strained films demagnetization effects alone are generally too weak (owing to the dilute nature of the magnetic impurities) to explain the magnitude of the magnetic anisotropy. Assuming an atomic moment of $4.5\mu_B/\mathrm{Mn_{Ga}}$, the saturation magnetization of $\mathrm{Ga_{0.95}Mn_{0.05}As}$ is only 46 kA/m. Thin films of such a material exhibit a demagnetization field $\mu_0 M_{sat}$ of only 58 mT– for comparison a thin film of Fe despite having a smaller moment per atom of 2.2 μ_B/Fe **[139]** has a demagnetization field of 2.18 T. Since perpendicular uniaxial anisotropy fields of over 350 mT have been determined from FMR measurements**[143]**, there must be other contributions to the magnetic anisotropy than those considered so far.

What makes the magnetic anisotropy different in $\mathrm{III}_{1-x}\mathrm{Mn}_x\mathrm{V}$ materials from typical ferromagnets is the carrier-mediated nature of ferromagnetic exchange. The holes introduced by $\mathrm{Mn_{Ga}}$ acceptors strongly influence the magnetic anisotropy through their *p-d* exchange interaction with the localized $\mathrm{Mn_{Ga}}$ moments, which causes the total energy of the Mn-hole system to depend on the orientation of the magnetization vector. To date, theoretical understanding of the hole-dependent magnetic anisotropy in $\mathrm{III}_{1-x}\mathrm{Mn}_x\mathrm{V}$ materials has focused on valence band models (Section 1.5). In these models biaxial strain terms are added to the *p-d* exchange enhanced **k·p** Hamiltonian. The effect of epitaxial strain is to cause the spin-split light and heavy hole bands to shift relative to one another, which changes the character of the hole states at E_F. Since heavy hole and light hole states interact differently with the magnetic moments via the *p-d* exchange Hamiltonian, the total energy of the system for a given orientation of the magnetization depends both on the epitaxial strain and the orientation of the magnetization. The evolution of the perpendicular magnetic anisotropy with strain has been both qualitatively and quantitatively reproduced by this method in $Ga_{1-x}Mn_xAs$ **[19, 35, 37]**. The dependence of the sign and magnitude of K_u^{011} on the hole concentration has also been successfully accounted for by the valence band models **[38]**. However such agreement requires the assumption of a trigonal distortion of the lattice, which to the author's knowledge has never been directly correlated by experiment to in-plane uniaxial anisotropy in $Ga_{1-x}Mn_xAs$.

The ability to describe the orientation of the easy axis as a function of doping, carrier concentration, and strain is one of the principal successes of the valence band theories of carrier-mediated ferromagnetism. This has taken on even greater significance in recent years as an increasing body of evidence has developed suggesting that the holes in the canonical $Ga_{1-x}Mn_xAs$ system reside not in the valence band, but in a Mn-derived impurity band**[39, 40, 42-44, 153]**. The goal of the subsequent sections is to examine the magnetic anisotropy in a ferromagnetic semiconductor where it has been conclusively established that ferromagnetism is mediated by holes localized within a Mn impurity band- i.e. $Ga_{1-x}Mn_xP$ (Chapter 3). The discovery that the magnetic anisotropy of $Ga_{1-x}Mn_xP$ exhibits all of the hallmarks associated with $Ga_{1-x}Mn_xAs$ provides more compelling evidence that II-PLM $Ga_{1-x}Mn_xP$ is the carrier-mediated phase of the material. Furthermore, the similar anisotropies in the two material systems have important implications to magnetic semiconductors in general; models of ferromagnetism must be able to account for the fact that localized, impurity-band carriers are capable of producing mediating anisotropic exchange interactions.

5.4. Magnetic Anisotropy in Materials Formed by II-PLM

Nearly every study on the magnetic anisotropy of Mn-doped III-V semiconductors has been performed on materials grown by LT-MBE. The magnetic anisotropy studies in this work were all performed on samples grown by II-PLM. Therefore, before considering the magnetic anisotropy of $Ga_{1-x}Mn_xP$ and its alloys, it is worthwhile to compare and contrast the magnetic anisotropy in materials grown by different techniques in order to determine what effect, if any, the different growth technique has on the magnetic anisotropy. There have been only two detailed studies of the magnetic anisotropy of II-PLM-formed $Ga_{1-x}Mn_xAs$. Cho *et al.* performed a comparative study of II-PLM formed and LT-MBE formed $Ga_{1-x}Mn_xAs$/GaAs films **[154]**. Zhou *et al.* made a detailed study of the magnetic anisotropy of II-PLM formed $Ga_{1-x}Mn_xAs$ grown on (100) (110) and (311) oriented substrates **[155]**. Collectively these works determined that the magnetic anisotropy of materials formed by II-PLM and LT-MBE is quite similar. The magnetic anisotropy fields have the same sign and follow the same symmetry regardless of growth method. As mentioned in Section 5.3, this includes the presence of the in-plane uniaxial anisotropy between <011>-type directions. Based on work on $Ga_{1-x}Mn_xAs$, it was postulated that cubic symmetry of the (100) surface was lowered by surface reconstructions that occur during MBE growth **[147]**. The reconstructions were proposed to be seeded at the $Ga_{1-x}Mn_xAs$/GaAs interface and replicated in successive layers as growth continued **[148]**. However, uniaxial in-plane anisotropy is also observed in $Ga_{1-x}Mn_xAs$ grown by II-PLM, which is a form of liquid phase epitaxy **[154]**. The presence of this uniaxial component to the magnetic anisotropy in films grown by both II-PLM and LT-MBE indicates that the symmetry breaking mechanism responsible for the appearance of the uniaxial component to the magnetic anisotropy is not related to solid/vacuum surface reconstructions **[143, 148]** as such reconstructions are unlikely to take place along the advancing liquid-solid interface during PLM. Therefore, the <011> in-plane uniaxial anisotropy is likely an intrinsic materials property.

Some caution must be expressed when attempting a quantitative comparison of the magnetic anisotropy between materials. Quantitative differences may exist in the magnitude of the anisotropy fields for materials formed by different techniques. Cho *et al.* found that the magnitude of the out-of-plane uniaxial anisotropy field $2K_{\mathrm{eff}}^{100}/M$ is significantly smaller in materials grown by II-PLM than LT-MBE **[154]**. In parallel it was determined by X-ray diffraction that the sample grown by II-PLM was under significantly less compressive strain than its LT-MBE counterpart, which is reasonable given that the sign and magnitude of $2K_{\mathrm{eff}}^{100}/M$ are correlated to the strain state of the material (Section 5.3). The reasons for the difference in strain state are two-fold. First, the II-PLM formed material studied in **[154]** has about a factor of two less Mn than the LT-MBE formed film that was studied. Second, the LT-MBE formed film was *unannealed* and therefore contained a significant concentration of lattice-expanding Mn interstitials (Sections 1.3 and 2.1). Therefore, it is not so surprising that quantitative differences in the strain-related component of $2K_{\mathrm{eff}}^{100}/M$ were found. On the other hand, Zhou *et al.* found much better quantitative agreement between films grown by the two different methods. Ideally, comparison of II-PLM formed materials should be made to materials grown by LT-MBE that have been *annealed*. These cautionary remarks also apply to any comparison between nominally identical samples that differ only in their post-growth annealing schedule. The annealing process is known to change the strain, hole concentration, and active $\mathrm{Mn_{Ga}}$ concentration through the outdiffusion of $\mathrm{Mn_I}$. All three effects may change the anisotropy parameters.

The strain-engineering of the magnetic easy axis has also been demonstrated in II-PLM-formed $\mathrm{Ga}_{1-x}\mathrm{Mn}_x\mathrm{As}$ **[132]**. Historically the strain state of $\mathrm{Ga}_{1-x}\mathrm{Mn}_x\mathrm{As}$ thin films was controlled by changing the lattice constant of the buffer layer upon which the thin film was grown. Compressively-strained films were simply grown on GaAs; the slightly larger Mn atoms expand the lattice when substituting for Ga. Additionally, further compressive strain can result from $\mathrm{Mn_I}$ in LT-MBE films that have not been properly annealed. Films under tensile strain with out-of-plane easy axis were produced by growing on an (In,Ga)As buffer layer, which has a larger lattice constant than $\mathrm{Ga}_{1-x}\mathrm{Mn}_x\mathrm{As}$ **[143, 144]**. When growing materials by II-PLM, it is not possible to use buffer layers to tune the epitaxial strain. Since the growth interface is internal in II-PLM (as opposed to external in MBE which allows for multilayer vertical growth) the substrate for II-PLM formed thin films is always the starting wafer (see Chapter 2 and Section 4.6). Thus, while it is straightforward to produce compressively-strained $\mathrm{Ga}_{1-x}\mathrm{Mn}_x\mathrm{As}$ thin films, obtaining material in tensile strain requires an alternate approach.

Since the lattice constant of the substrate cannot be changed and the use of buffer layers is not feasible, the only method to produce II-PLM $\mathrm{Ga}_{1-x}\mathrm{Mn}_x\mathrm{As}$ in tensile strain is to further manipulate the composition of the film such that its lattice constant is shorter than that of GaAs. One method by which to accomplish this is to replace a few percent of the As atoms with a smaller radius anion such as phosphorus, which compensates the compressive strain induced by $\mathrm{Mn_{Ga}}$ atoms. For $\mathrm{Ga}_{1-x}\mathrm{Mn}_x\mathrm{As}_{1-y}\mathrm{P}_y$ grown on GaAs, the presence of a few percent $\mathrm{P_{As}}$ sites on the anion sublattice is sufficient to reverse the strain state of the film, which is demonstrated in Figure 39(b). The growth conditions for these films can be found elsewhere **[132]**. The film with $x \approx 0.04$ is characterized by the main GaAs substrate peak at $\omega = 33.02°$ and a broad shoulder at $\omega < 33.02°$ corresponding to the $\mathrm{Ga}_{1-x}\mathrm{Mn}_x\mathrm{As}$ film. A shoulder is observed instead of a peak due to the vertically inhomogeneous distribution of Mn throughout the depth of the film, which is characteristic of films produced by II-PLM at this Mn concentration (Appendix C). Addition of

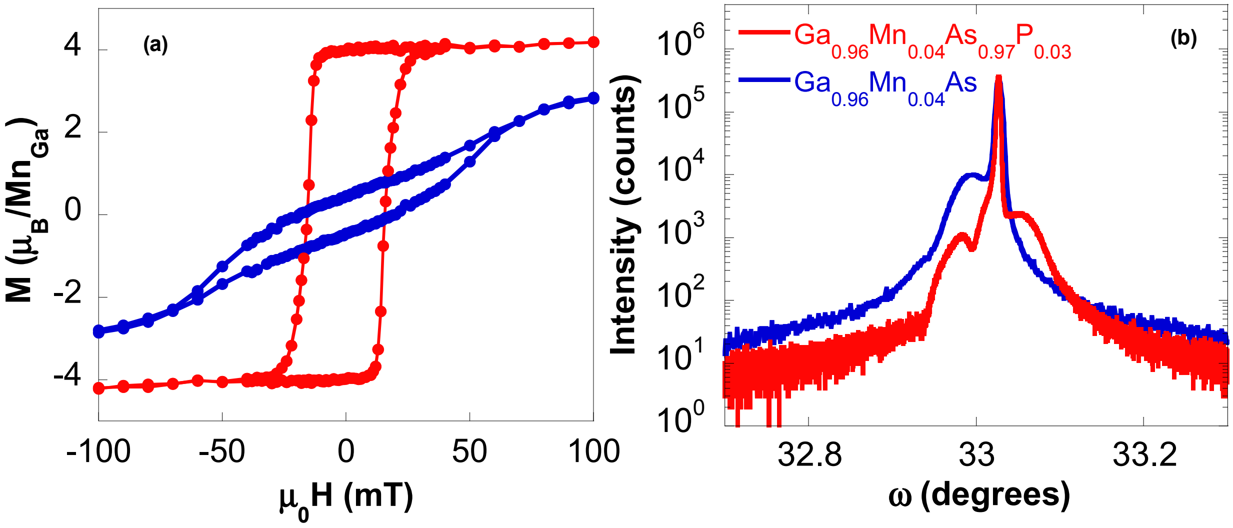

Figure 39: (a) Magnetization as a function of field for the same samples at *T*=5K with the applied magnetic field normal to the thin film plane. (b) X-ray rocking curves about the (400) reflection of $Ga_{0.964}Mn_{0.04}As$ (blue) and $Ga_{0.962}Mn_{0.04}As_{0.972}P_{0.028}$ (red).

only 3% P_{As} into the anion sublattice causes a significant change in the diffraction profile. The low angle feature decreases in intensity by an order of magnitude while a new, strong feature appears at $\omega > 33.02°$ indicating that the film has a lattice constant less than that of GaAs. The Mn and P atoms have slightly different concentration profiles. Therefore, there exists a region of the $Ga_{0.962}Mn_{0.04}As_{0.97}P_{0.03}$ film that is in compressive strain even though a majority of the film is under tension, which explains the multiple non-substrate features present in this film's rocking curve.

The change in the film's strain state has a clear effect on the perpendicular magnetic anisotropy. This is illustrated in Figure 39(a), which shows the field dependence of the magnetization for the same two samples that were shown in Figure 39(b). The hysteresis loops were measured with the applied field normal to the film plane at *T*=5K. It is obvious from these measurements that changing the strain state of $Ga_{1-x}Mn_xAs_{1-y}P_y$ from compressive to tensile by isovalent anion substitution causes a reorientation of the magnetic easy axis from in-plane to out-of-plane.

To summarize this brief but important section, the magnetic anisotropy of $Ga_{1-x}Mn_xAs$ films formed by II-PLM is substantially similar to films of the same material grown by LT-MBE. This applies to films grown in both compressive and tensile strain. Therefore, reasonable comparisons are possible between II-PLM formed of $Ga_{1-x}Mn_xP$ and LT-MBE formed $Ga_{1-x}Mn_xAs$ as the qualitative effect of growth technique on the magnetic anisotropy is minimal. However, care must be taken when making quantitative comparisons between materials due to the sensitivity of the magnetic anisotropy parameters on x, p, and ε.

5.5. The Magnetic Anisotropy of $Ga_{1-x}Mn_xP$

The contributions to the magnetic anisotropy of $Ga_{1-x}Mn_xP$ grown in compressive strain were studied in depth by Bihler *et al.*[**119**]. Figure 40 shows the dependence of the ferromagnetic resonance field on crystallographic orientation for a $Ga_{1-x}Mn_xP$ sample with x=0.042. For the out-of-plane rotation, the resonance field is at a maximum when H||[100] and minimized for the in-plane orientation of the magnetic field. This indicates the presence of a

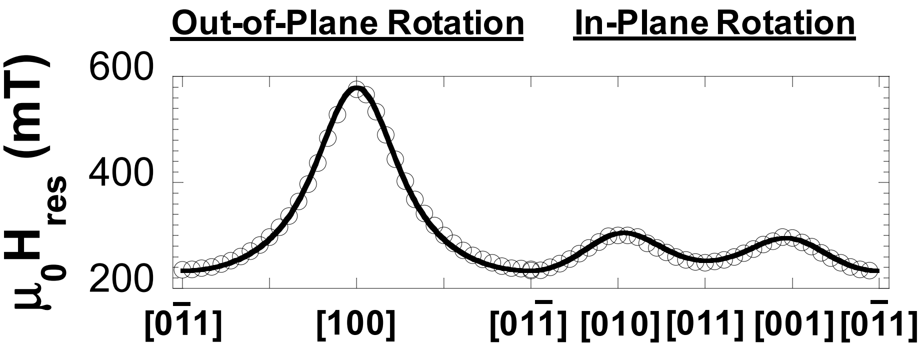

Figure 40: Angular dependence of the ferromagnetic resonance field for $Ga_{0.958}Mn_{0.042}P$ for rotations about the [011] axis (out-of-plane rotation) and [100] axis (in-plane rotation). Data were collected at T=5K and $\omega/2\pi$= 9.3 GHz. Open circles represent experimental data while the solid line is a fit according to the model described in the text. After [119].

large uniaxial anisotropy field normal to the film plane. The in-plane rotation exhibits local minima for H||<011> and local maxima for H||<001> due a cubic term; however the four fold symmetry is broken by an additional uniaxial term that breaks the degeneracy between <011>-type directions. The $[0\bar{1}1]$ direction is magnetically easier than [011]. This in-plane uniaxial component to the magnetic anisotropy seems general to $III_{1-x}Mn_xV$ systems as it is also observed in $In_{1-x}Mn_xAs$ **[150]** and $Ga_{1-x}Mn_xAs$ **[38, 145, 156]**.

The magnetic anisotropy fields were determined by simulating the FMR data according to the model outlined in Section 5.2.1. The total free energy used in the simulation was

$$\begin{aligned} F = -MH(&\sin\Theta\sin\Phi\sin\theta\sin\phi + \cos\Theta\cos\theta + \sin\Theta\cos\Phi\sin\theta\cos\phi) \\ &+ K_{eff}^{100}\sin^2\Theta\sin^2\Phi \\ &- \frac{1}{2}K_{C1}^{\perp}\sin^4\Theta\sin^4\Phi - \frac{1}{2}K_{C1}^{\parallel}(\cos^4\Theta + \sin^4\Theta\cos^4\Phi) \\ &+ \frac{1}{2}K_{u}^{011}(\cos\Theta + \sin\Theta\cos\Phi)^2 \end{aligned} \tag{38}$$

where the anisotropy parameters have been defined in Section 5.3 and the angles in Figure 37. The results of the FMR simulation are shown as the solid line in Figure 40. The data are well described by the range of anisotropy fields given in Table 3. The magnetic anisotropy of $Ga_{1-x}Mn_xP$ grown in compressive strain is dominated by the out-of-plane terms, which induce the easy axis to lie in the plane of the film. Based on the saturated magnetic moment measured by SQUID magnetometry, it is possible to estimate the demagnetization field that contributes to K_{eff}^{100}. It should be noted that there is some intricacy to this process. All of the terms that enter Equation 38 are volumetric. Since the Mn distribution in II-PLM formed materials is not homogeneous throughout the depth of the film (Appendices A and B and Section 4.2.2), one cannot simply divide the total magnetic moment measured in SQUID by the sample volume. Instead the magnetization corresponding to the region of the film with highest Mn concentration is estimated as follows. The magnetic moment per substitutional Mn is

$$m_{Mn} = \frac{m_{tot}}{D_{Mn,retained}Af_{sub}}. \tag{39}$$

In Equation 39 m_{Mn} is the moment per Mn_{Ga}, m_{tot} is the total magnetic moment measured by the magnetometer, $D_{Mn,retained}$ is the Mn retained dose, A is the sample area and f_{sub} the Mn substitutional fraction. The total magnetization M is approximately

$$M = m_{Mn}x[Ga] \tag{40}$$

Table 3: Range of anisotropy fields at T=5 K for $Ga_{0.958}Mn_{0.042}P$ grown on GaP determined by simulation of FMR experiments. After [119].

$2K_{eff}^{100}/M$ (mT)	$2K_{C1}^{\perp}/M$ (mT)	$2K_{C1}^{\parallel}/M$ (mT)	$2K_{u}^{011}/M$ (mT)
160-190	-100-(-60)	-40-(-30)	0-12

where [Ga] is the Ga sublattice density and is 2.47×10^{22} cm^{-3} for GaP at room temperature. This approach is equivalent to defining an effective film thickness $t_{eff}=x[\mathrm{Ga}]/(D_{Mn,retained}\,f_{sub})$ for the II-PLM formed materials, which, since the area of the sample can be measured, allows for calculation of the magnetic moment per unit volume. For the $Ga_{0.958}Mn_{0.042}P$ sample M=37 kA/m according to Equations 39 and 40. The demagnetization field μ_0M is therefore ~ 50 mT and constitutes only a small fraction of $2K_{eff}^{100}/M$. The remainder of $2K_{eff}^{100}/M$ must be due to strain-related anisotropy owing to the tetragonal distortion of the $Ga_{1-x}Mn_xP$ film **[143, 157, 158]**. The negative sign of the in-plane cubic anisotropy field indicates that the <011> directions are magnetically preferred over <001>, which is reminiscent of results in $In_{1-x}Mn_xAs$ **[142]**. Finally the small in-plane uniaxial anisotropy field $2K_{u}^{011}/M$ reflects the broken symmetry between <011> in-plane directions. Its negative value indicates that $[0\bar{1}1]$ is the magnetic easy direction in the plane of the film. As the temperature increases the position of the resonance field tends towards and eventually reaches $\mu_0H_{res}\approx331$ mT, which is the expected field at which paramagnetic Mn^{2+} moments with $g\approx2.0$ would exhibit resonance (Section 5.2.1). All anisotropy fields decrease and eventually tend to zero at T_C.

Changing the concentration of Mn_{Ga} has an effect on the magnetic anisotropy of $Ga_{1-x}Mn_xP$ **[159]**. While the FMR rotations exhibit the same symmetry as discussed above for x=0.042, the magnetic anisotropy fields differ quantitatively. The principal difference is that the value of $2K_{eff}^{100}/M$ scales with Mn doping. There are two reasons for this observation. First, the demagnetization field scales with the value of the magnetization. If the moment per substitutional Mn is constant then a sample's magnetization and demagnetization field must increase with Mn doping (*c.f.* Equations 39 and 40). Second, increasing the Mn concentration will increase the strain in the film. This augments the tetragonal distortion of the film, thus increasing the strain-related contribution to $2K_{eff}^{100}/M$.

The resonance fields plotted in Figure 40 were those due to the so-called collective mode. For out-of-plane orientations of the magnetic field, spin-wave resonances were also visible and appear at lower fields than the collective mode (see for example Figure 1 of Ref. **[119]**). In the collective mode all of the moments precess in phase with one another, which is essentially a spin wave with wavevector k=0. Higher order modes with finite k are also possible provided the allowed values of k meet the boundary conditions imposed by sample geometry. For magnetic semiconductor thin films the appropriate boundary conditions are that the magnetization is pinned at M=0 at both the film surface and film-substrate interface. For the geometry where the magnetic field is applied perpendicular to the thin film the problem therefore becomes analogous to the quantum mechanical particle in a box where the wavefunction is replaced by the magnetization vector and the potential by the magnetic field. In parallel to the particle in a box, the spacing of the spin wave eigenenergies is representative of the shape of the potential well. For example for a parabolic magnetic field distribution the energies of the spin wave modes j scale as j^1 while a triangular distribution results in a $j^{2/3}$ energy spacing. A homogenous film with a rectangular magnetic field profile would show j^2 mode spacing. Experiments on $Ga_{0.958}Mn_{0.042}P$ showed spin waves resonances only up to index j=2 and T=15 K, which limited

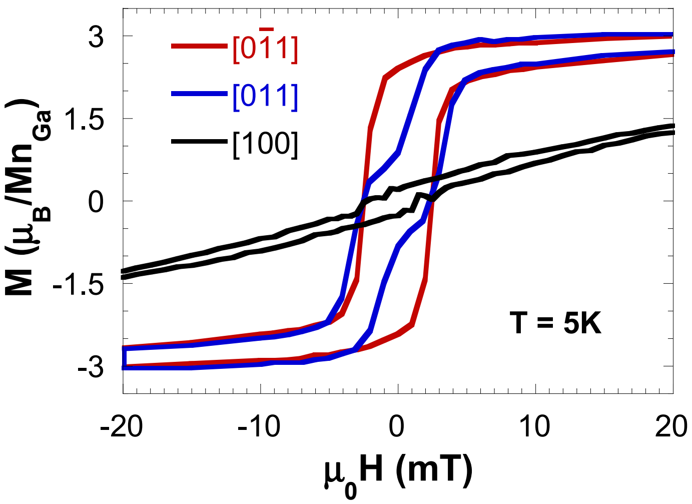

Figure 41: Magnetization as a function of applied magnetic field for $Ga_{0.958}Mn_{0.042}P$ grown on GaP for three different crystal orientations. Data are courtesy of Christoph Bihler.

quantitative analysis in the current case. Based on these resonance fields the mode spacing exponent is estimated to be around 0.8 indicative of an inhomogeneous magnetization profile perpendicular to the growth direction, which is in lineshape somewhere between parabolic and triangular. This behavior is in reasonable agreement with Mn concentration profiles observed by SIMS; however deviations from the homogeneous case have been observed in $Ga_{1-x}Mn_xAs$ films with depth dependent carrier concentrations **[160]**.

The strong and complex magnetic anisotropy in $Ga_{1-x}Mn_xP$ causes the magnetization reversal process to depend strongly on crystallographic orientation. *M(H)* curves for $Ga_{0.958}Mn_{0.042}P$ are shown in Figure 41 for three different crystallographic orientations. When the applied field is normal to the film plane, the *M(H)* curve shows no remenance as expected for a hard axis. It is clear that the $\left[0\bar{1}1\right]$ is the easy axis; it exhibits the largest remenant magnetization and the most square hysteresis loop. The small uniaxial in-plane anisotropy field has a strong effect on magnetization reversal. The $Ga_{0.958}Mn_{0.042}P$ sample shows a "kinked" hysteresis loop when the field is applied parallel to [011]. The kinked hysteresis loop is the result of a multistep spin switching process whereby magnetization reversal occurs by a combination of coherent rotation and noncoherent spin switching, which will be discussed in greater detail in Section 5.7.5. Overall, the *M(H)* curves are in agreement with FMR results. The experimental *M(H)* curves can be reasonably reproduced by Equation 38 using a model described in the following sections and Appendix F **[119]**.

5.6. Strain-Engineered Easy Axis in $Ga_{1-x}Mn_xP_{1-y}N_y$

5.6.1 *Introduction*

In this section, a direct connection is established between the magnetic easy axis in Mn-doped GaP and epitaxial strain by a combined ferromagnetic resonance, X-ray diffraction and SQUID magnetometry study. The magnetic easy axis of $Ga_{1-x}Mn_xP$ is gradually rotated from the in-plane $\left[0\bar{1}1\right]$ direction towards the film normal [100] through alloying with isovalent N which changes the strain state of the film from compressive to tensile. For a nearly lattice-matched film the strain-related component to the out-of-plane uniaxial anisotropy field is close to zero. Both in-plane and out-of-plane magnetization reversal processes are explored by a simple model that considers the combination of coherent spin rotation and noncoherent spin switching. The results are used to estimate domain wall sizes and energetics, which have yet to be directly measured in this materials system.

5.6.2 *Materials Synthesis and Structural Properties*

$Ga_{1-x}Mn_xP$ was synthesized by implantation of 50 keV Mn^+ into (100)-oriented GaP ([100] is the crystallographic direction normal to the film plane) to a dose of $1.5x10^{16}$ cm^{-2} followed by irradiation with a single pulse from a KrF (λ=248 nm) excimer laser at a fluence of 0.44±0.05 J/cm^2. Quaternary alloys were synthesized by co-implanting the Mn-implanted GaP with 33 keV N^+ to doses ranging from 1.0 to 5.0 $x10^{15}$ cm^{-2} prior to PLM.

The value of x for the reference, nitrogen free sample was determined by the dependence of T_C on x which has been carefully established (Section 3.2). The reference sample's T_C of 44 K indicates that $x\approx0.034$. All samples had similar Mn retained doses and substitutional fractions of 7.3×10^{15} cm^{-2} and 0.77 respectively as determined by ion beam analysis (Appendix A) suggesting that x is the same for all samples. The N content with the highest N^+ implant dose was determined by measuring its lattice constant by X-ray diffraction and then applying Vegard's Law. The values of y estimated by the work in the $Ga_{1-x}Mn_xAs_{1-y}N_y$ system and are shown in Table 4. The exact value of y is not crucial in this work; the magnetic anisotropy is controlled by the epitaxial strain, which is determined below.

Reciprocal space maps around the (511) reflection of GaP are shown in Figure 42 for all $Ga_{0.966}Mn_{0.034}P_{1-y}N_y$ samples. The measurements were performed on a Panalytical brand X'Pert PRO Difrractometer using Cu K_α radiation (λ=1.5405 Å) with line focusing. The sample with y=0 shows significant intensity in a diffuse region at smaller perpendicular reciprocal lattice vector ($q_\perp$) than the substrate, which is attributed to the compressively-strained $Ga_{1-x}Mn_xP$ thin film. Again, a shoulder is observed instead of a distinct peak due to the non-uniform vertical Mn concentration profile inherent to II-PLM formed materials at these doping levels, which leads to significant broadening of the diffraction peak. The replacement of only 1.0% of the P atoms in the anion sublattice with Mn causes the strain state of the film to shift from compressive to tensile. The significantly smaller N atoms easily reverse the strain state of the film to the point where the film peak can be resolved, although significant broadening still exists due to vertical inhomogeneity. A residual feature at $q_\perp$ below the substrate peak still exists due to imperfect overlap of the Mn and N profiles (Section 5.4). Increasing y from 1.0% to 1.4% causes the film peak to shift to even larger $q_\perp$ implying that the film is under increased tensile strain. The film with 0.4% N alloying is nearly lattice-matched; there is very little intensity outside of the main substrate peak.

Table 4: Relationship between N^+ implant dose, anion sublattice composition (y), lattice constant (a) and perpendicular strain ($\varepsilon_\perp$) for $Ga_{0.966}Mn_{0.034}P_{1-y}N_y$.

Implanted N^+ Dose (cm^{-2})	Approximate y	a (Å)	$\varepsilon_\perp$ (%)
$0.0x10^{15}$	0	5.4519±0.0012	0.0220±0.0189
$1.0x10^{15}$	0.004	5.4480±0.0012	-0.0404±0.0202
$2.5x10^{15}$	0.010	5.4456±0.0020	-0.0808±0.0331
$5.0x10^{15}$	0.014	5.4396±0.0024	-0.182±0.0442

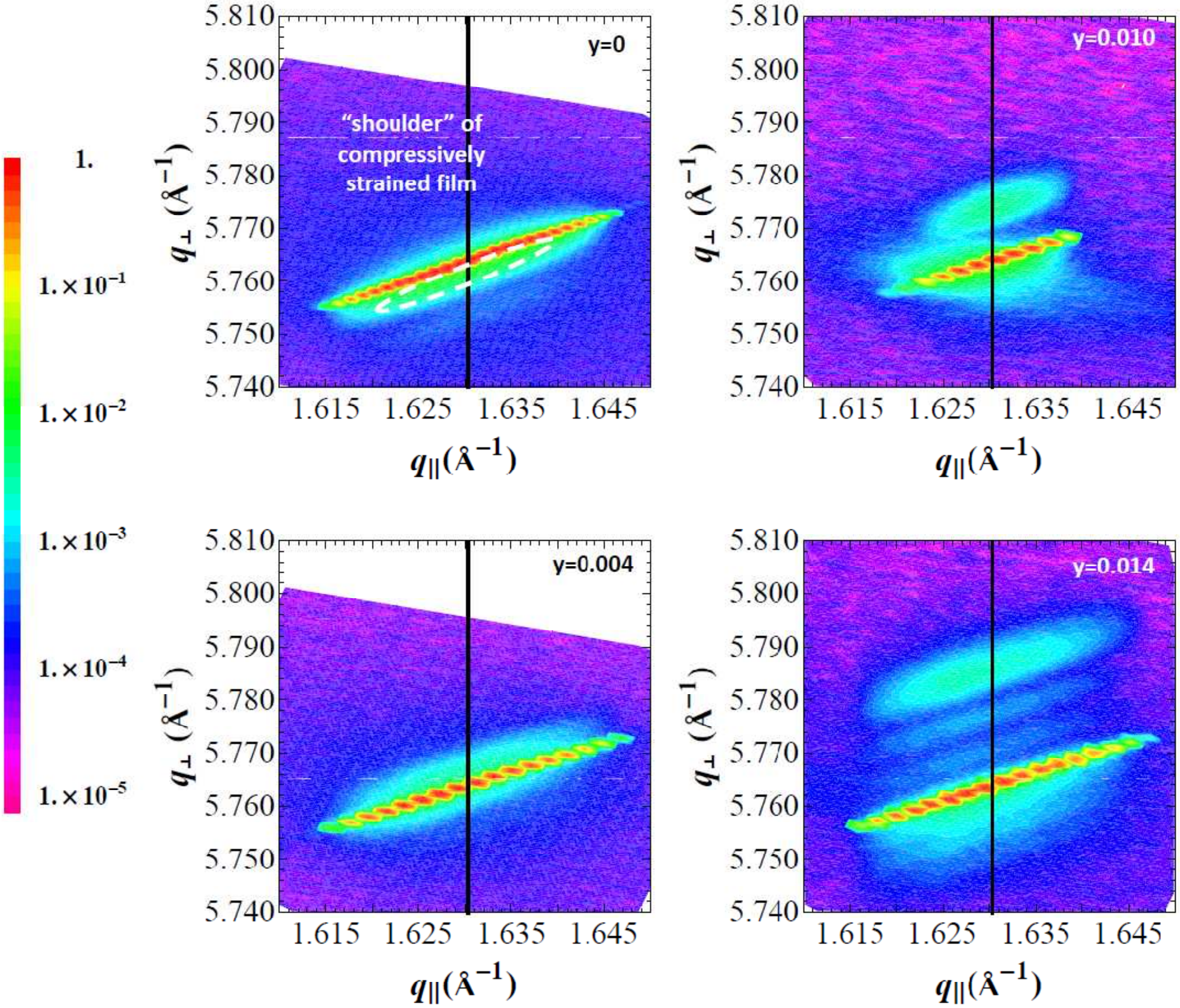

Figure 42: Reciprocal space maps around the GaP (511) peak for four $Ga_{0.966}Mn_{0.034}P_{1-y}N_y$ samples. Measurements were taken using Cu $K_{\alpha 1}$ radiation, λ=1.5405 Å with line focusing of the X-rays. The solid line at $q_{||}=2^{1/2}\times 2\pi/5.4505$ Å =1.6303 Å^{-1} indicates the in-plane projection of the scattering vector corresponding to pseudomorphic films.

Even though peak broadening hinders quantitative analysis of the reciprocal space maps, it is still possible to extract information regarding the in-plane ($a_{||}$) and out-of-plane ($a_{\perp}$) film lattice constants from the data shown in Figure 42. For the films with y=0.010 and y=0.014, the analysis is rather straightforward since the film peak can be separated from the substrate peak. The values of $q_{||}$ and $q_{\perp}$ are the center of the film peak are used to determine $a_{||}$ and $a_{\perp}$. Errors are determined from the full-width at half maximum (FWHM) contour. For the films with y=0 and y=0.004 it is assumed that $a_{||}=a_{\mathrm{GaP}}$=5.4505 Å. The fact that the films with y=0.010 and y=0.014 are pseudomorphic yet under considerably more strain justifies this assumption. The individual ω-2θ scans comprising the reciprocal lattice map were fit using the two peak model described in Appendix C in which the film is described by a Gaussian distribution **[161]**. The mean value of $a_{\perp}$ was taken as the mean of the Gaussian film fit, and errors are once again quoted as the FWHM. For all films the relaxed lattice constant a was determined by

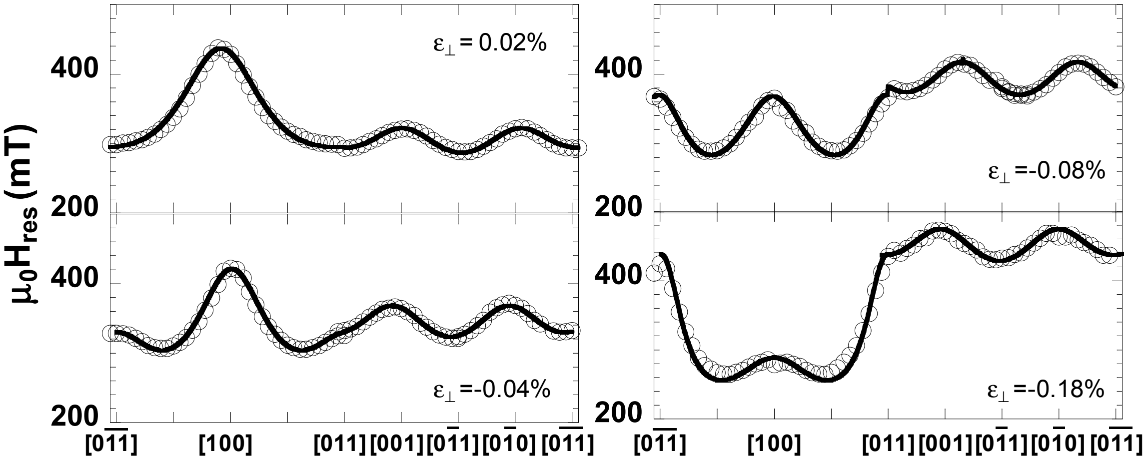

Figure 43: Angular dependence of the ferromagnetic resonance field at T=5 K for $Ga_{0.966}Mn_{0.034}P_{1-y}N_y$ as a function of $\varepsilon_\perp$. Data courtesy of Lukas Dreher.

$$a = \frac{a_\perp + 2a_{||}\nu - a_\perp\nu}{1+\nu}. \tag{41}$$

It was assumed that dilute alloying with Mn or N did not alter Poisson's ratio, ν=0.31 **[162]**. Finally the strain along the growth direction

$$\varepsilon_\perp = (a_\perp - a)/a \tag{42}$$

was calculated. The calculated values of a and $\varepsilon_\perp$ are listed in Table 4 for the various N concentrations. The quantitative analysis of the X-ray diffraction measurements reflect the trends discussed qualitatively above, particularly the change in the strain state with N alloying.

5.6.3 *Ferromagnetic Resonance Spectroscopy*

Figure 43 shows the dependence of the ferromagnetic resonance field on rotations about the$[0\bar{1}1]$ axis and [100] axis. The in-plane rotations are all qualitatively similar regardless of the strain in the film. Local minima occur for H||<011> and local maxima for H||<001>. The behavior of the out-of-plane rotations about the $[0\bar{1}1]$ axis show a strong dependence on $\varepsilon_\perp$. For the film under compressive strain the $\mu_0 H_{res}$ is at a maximum for field orientations normal to the film plane indicating that the magnetic easy axis is in the plane of the film. As the strain in the film changes to tensile the global maximum in $\mu_0 H_{res}$ observed when H||[100] becomes less pronounced. By $\varepsilon_\perp$=-0.08% the global maximum has shifted to the plane of the film. In parallel the global minimum shifts towards [100] revealing that the magnetic easy axis is shifted out-of-plane as the lattice constant of the film is decreased although the easy axis is still not parallel to [100] at $\varepsilon_\perp$=-0.18%

Table 5: Cubic and uniaxial magnetic anisotropy fields determined from FMR for $Ga_{0.966}Mn_{0.034}P_{1-y}N_y$

$\varepsilon_\perp$ (%)	$2K_{eff}^{100}/M$ (mT)	$2K_{C1}^{\perp}/M$ (mT)	$2K_{C1}^{\parallel}/M$ (mT)	$2K_{u}^{011}/M$ (mT)
0.0220±0.0189	78±3	-26±3	-24±3	5±1
-0.0404±0.0202	4±3	-84±3	-34±3	4±1
-0.0808±0.0331	-80±3	-116±3	-38±3	3±1
-0.182±0.0442	-172±3	-124±3	-40±3	4±1

The solid lines in Figure 43 are the results of FMR simulations according to the free energy model discussed in Sections 5.2.1 and 5.5 using the parameters listed in Table 5. The small uniaxial anisotropy field $2K_{eff}^{100}/M$ is positive for all samples. This, along with the negative sign of $2K_{C1}^{||}/M$ indicates that $[0\bar{1}1]$ is the in-plane easy axis for all samples. The out-of-plane anisotropy fields are much more dependent on film strain and dominate the magnetic anisotropy of the $Ga_{1-x}Mn_xP_{1-y}N_y$ system. In particular the effective uniaxial anisotropy field $2K_{eff}^{100}/M$ is strongly linked to both the sign and magnitude of $\varepsilon_\perp$. The linear dependence of $2K_{eff}^{100}/M$ on $\varepsilon_\perp$ is emphasized in Figure 44. In $Ga_{1-x}Mn_xAs$ a linear relationship between $2K_{eff}^{100}/M$ and $\varepsilon_\perp$ is observed for both compressive and tensile strains up to 0.4%, which suggests a common origin to this effect in the two materials systems **[37]**. However, this linear behavior in $Ga_{1-x}Mn_xAs$ has been shown to be consistent with the standard valence band theory of magnetic anisotropy in $III_{1-x}Mn_xV$ ferromagnetic semiconductors **[19, 37]**, which is unlikely to apply to the $Ga_{1-x}Mn_xP_{1-y}N_y$ samples studied here. The linear regression crosses the ordinate axis at $2K_{eff}^{100}/M \approx 46$ mT. High field ($1\ T \leq |\mu_0 H| \leq 5\ T$) SQUID magnetometry measurements indicate that the saturation magnetization M_{sat}=26.1±2.1 kA/m, which implies a demagnetization field $\mu_0 M_{sat}$ of 32.8±2.6 mT, which accounts for a significant portion of $2K_{eff}^{100}/M$ at $\varepsilon_\perp=0$. Within the rather large error bar of the strain measurements, it is likely that $2K_{eff}^{100}/M = \mu_0 M_{sat}$ at $\varepsilon_\perp=0$, which would be expected if the strain-related contribution to $2K_{eff}^{100}/M$ was determined entirely by tetragonal distortion. Therefore, for a nearly lattice-matched film the component of $2K_{eff}^{100}/M$ related to epitaxial strain is close to zero for $Ga_{1-x}Mn_xP$.

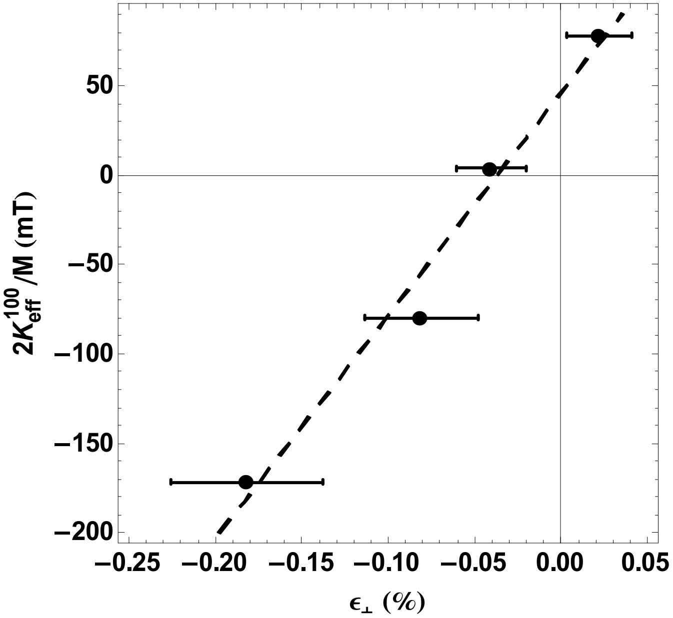

Figure 44: Relationship between $2K_{eff}^{100}/M$ and $\varepsilon_\perp$ for $Ga_{1-x}Mn_xP_{1-y}N_y$. The dashed line is a linear fit to the mean data points, which intercepts the ordinate axis at $2K_{eff}^{100}/M \approx 46$ mT.

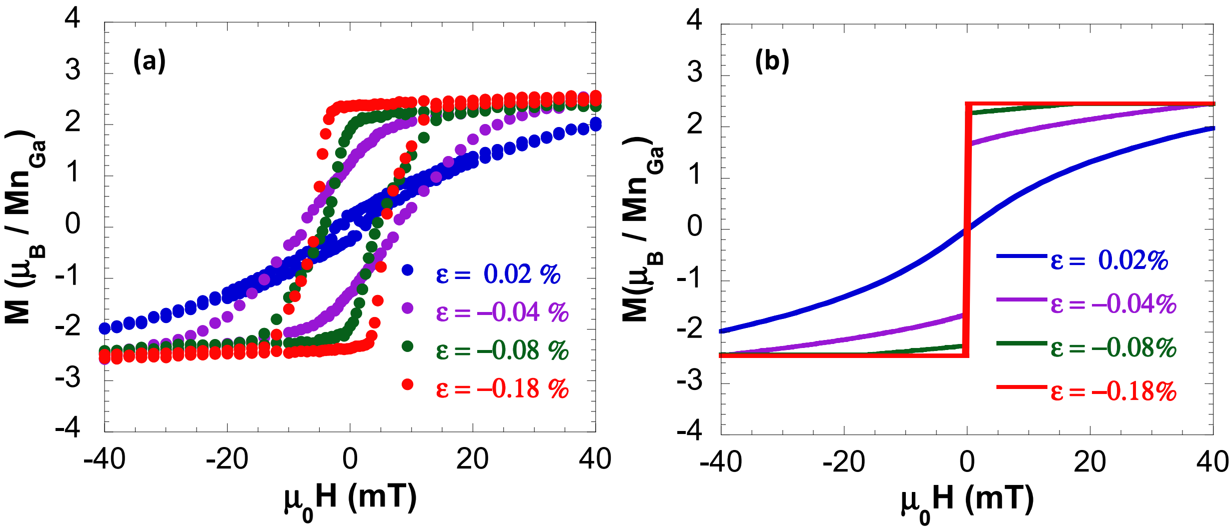

Figure 45: (a) Magnetization as a function of applied magnetic field for *H*||[100]. (b) Simulations of *M(H)* curves according to the model described in Appendix F. The anisotropy fields {$2K_{eff}^{100}/M$, $2K_{C1}^{\perp}/M$, $2K_{C1}^{||}/M$, $2K_{u}^{011}/M$} used in the simulation were {60 mT, -64 mT, -52 mT, 5 mT } for $\varepsilon_{\perp}$=0.02%, {-18 mT, -60 mT, -40 mT, 4 mT } for $\varepsilon_{\perp}$=-0.04%, {-84 mT, -98 mT, -40 mT, 3 mT } for $\varepsilon_{\perp}$=-0.08%, and {-222 mT, -164 mT, -40 mT, 4 mT } for $\varepsilon_{\perp}$=-0.18%

5.6.4 *Field Dependence of the Magnetization*

Measured *M(H)* curves for *H*||[100] and *T*=5 K are shown in Figure 45(a). The sample in compressive strain shows no remanance; the magnetic easy axis is perpendicular to the field direction (in the sample plane). As the strain state of the film changes from compressive to tensile the remanent magnetization increases as the magnetic easy axis rotates from $\left[0\bar{1}1\right]$ towards [100]. At the same time the line shape of the *M(H)* curves change and hysteresis is observed. All of these observations are characteristic of gradually changing the magnetic easy axis from in-plane to out-of-plane.

To gain further insight into the magnetization reversal processes in $Ga_{1-x}Mn_xP_{1-y}N_y$ the in-plane and out-of-plane *M(H)* curves have been simulated using a free energy approach. Details of the calculations are found in Appendix F. Briefly, the calculations are performed by inputting the values for the anisotropy fields determined from FMR, which allows for the free energy to be calculated as a function of the magnetization for a given magnetic field. A free parameter ΔE can be used to account for the energy required to nucleate and grow domains that gives rise to hysteresis during the magnetization reversal process. The values of ΔE are chosen such that the measured fields at which noncoherent spin switches occur are reproduced by the simulation. Simulations of the out-of-plane *M(H)* curves are found in Figure 45(b). In these simulations the effects of hysteresis have been neglected for simplicity and clarity; the effect of energy losses and irreversible processes will be considered below. The key features of the experimental hysteresis loops, namely the increase in the remanent magnetization with increasing tensile strain and the general change in lineshape of the *M(H)* curves, are captured by the simulations. The specific values of the anisotropy fields that were used to generate the *M(H)* simulations are listed in the caption to Figure 45. In general, the anisotropy fields used to fit the *M(H)* data and the FMR data agree with one another to within a factor of two. This level of agreement is quite reasonable given the simplicity of the magnetization reversal simulations. Additionally, we

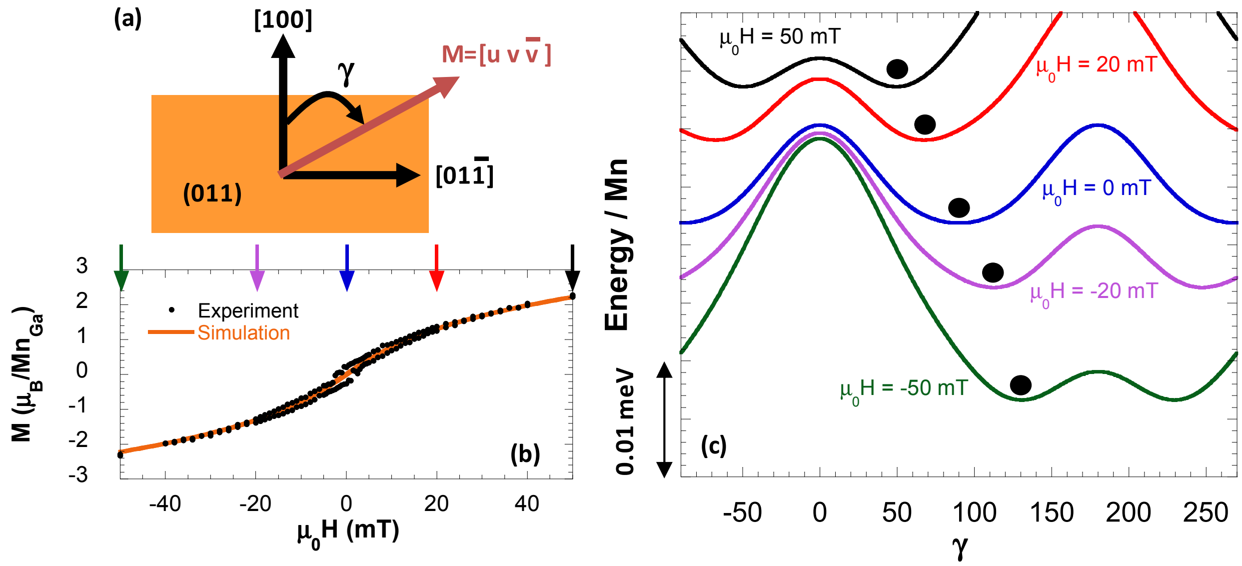

Figure 46: (a) Definition of the angle γ which describes the orientation of the magnetization in the (011) plane. (b) Comparison of experimental and simulated *M(H)* curves for the sample with $\varepsilon_{\perp}$=0.02%. The anisotropy parameters used in the simulations are the same as those in Figure 45. (c) *F(γ)* contours for specific values of the applied magnetic field. The colored arrows in panel (b) refer to the contours in (c). The solid black circles denote energy minima are determined the orientation of the magnetization vector. Multiple minima present in panel (c) are related by symmetry and do not affect the results of the calculations.

observe spin wave resonances in FMR experiments on $Ga_{1-x}Mn_xP_{1-y}N_y$. Spin wave excitations were briefly discussed in the previous section. Although a complete treatment of spin wave excitations is again limited by the observation of only two higher order modes it is worth noting a few effects of spin wave excitations on the quantitative analysis of FMR experiments. The anisotropy parameters listed in Table 5 were determined by analyzing the angular-dependence of the fundamental mode. According to the previously discussed model whereby the spin wave excitations are treated in parallel to the particle in a potential well the presence of spin waves can cause an underestimation of the resonance field corresponding to the collective mode **[163]**. This may explain some of the discrepancy between the anisotropy parameters determined from the FMR and SQUID simulations. Regardless, the anisotropy fields determined from *M(H)* calculations further emphasize that the sign and magnitude of $2K_{eff}^{100}/M$ are primarily determined by the epitaxial strain of the film.

The simulations indicate that the magnetization vector is always of the form $[u\bar{v}v]$ during the reversal process when the field is applied normal to the film. This behavior is understood as follows. As the magnitude of the magnetic field is reduced, the Zeeman energy decreases. Since none of the samples have an easy axis parallel to [100] eventually the anisotropy energy will cause the magnetization to bend towards the sample plane. The lowest energy path is that towards the in-plane easy axis, which is $\left[0\bar{1}1\right]$. Therefore, reversal occurs in the (011) plane, which is common to both [100] and $\left[0\bar{1}1\right]$ directions. To aid in the visualization of the magnetization reversal process it is therefore useful to write the magnetization in terms of a single angle in the (011) plane. The angle, γ, is measured from [100] towards $\left[0\bar{1}1\right]$ in the (011) plane [Figure 46 (a)]. In this coordinate system the free energy simplifies to

$$F(\gamma) = -MH\cos\gamma + K_{eff}^{100}\cos^2\gamma - \frac{K_{C1}^{\perp}}{2}\cos^4\gamma - \frac{K_{C1}^{\parallel}}{4}\sin^4\gamma\,. \tag{43}$$

when H||[100]. Simulations for H||[100] are shown in Figure 46 for the compressively strained film ($\varepsilon_\perp$=0.02%) alongside selected $F(\gamma)$ contours. The free energy minimum shifts gradually through γ=90° demonstrating that the magnetization process is completely reversible and occurs by coherent rotation of the moments. At $\mu_0 H$=0 mT the minimum occurs at precisely γ=90° resulting in a projection of the magnetization vector on the field direction of zero in agreement with the negligible remanent magnetization observed in experiment.

The magnetization reversal process is markedly different for films under tensile strain. Experimental and calculated $M(H)$ curves for the film with $\varepsilon_\perp$=-0.18% are shown in Figure 47. In this case as the field is lowered from a large positive value towards zero, the magnetization stays pinned near γ=0° since the magnetic anisotropy energy induces the magnetization to lie close to [100] at zero field. Since the minimum does not gradually shift past γ=90°, the only mechanism whereby the magnetization can change sign is by noncoherent switching. The noncoherent switch occurs when the energy gained by switching from the local minimum in $F(\gamma)$

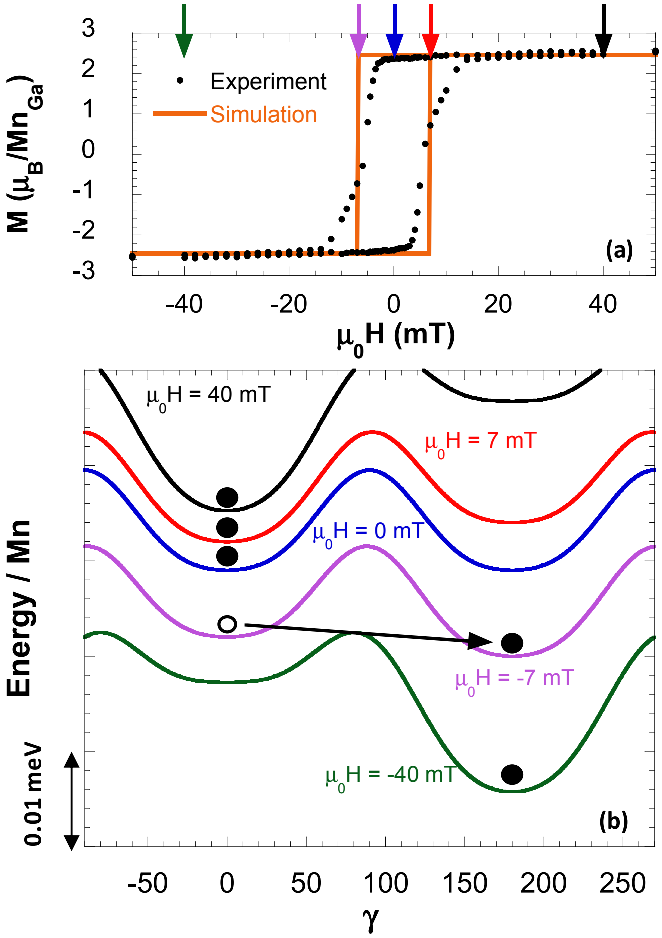

Figure 47: (a) Comparison of experimental and simulated $M(H)$ curves for the sample with $\varepsilon_\perp$=0.02%. The anisotropy parameters used in the simulations are the same as those in Figure 45. (b) $F(\gamma)$ contours for specific values of the applied magnetic field. Solid black circles again denote energy minima. Open symbols and arrows represent noncoherent spin switching from one magnetization orientation to another which occurs at the specified field.

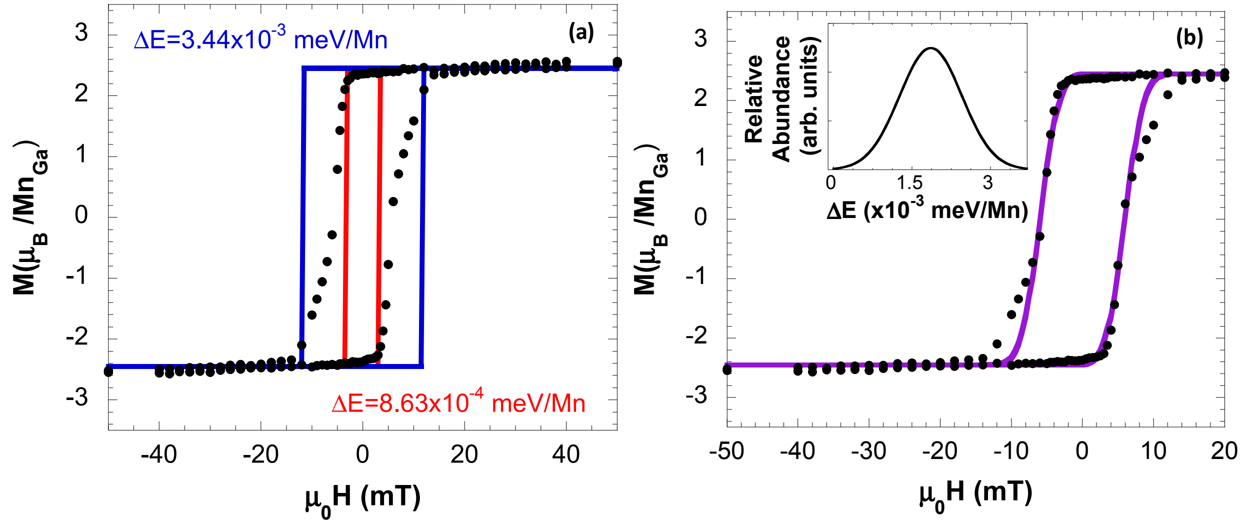

Figure 48: (a) Simulations of the *M(H)* curves (solid lines) for the sample with $\varepsilon_\perp$=-0.18% using a single value for *ΔE*. Experimental data points are shown by the black solid symbols. The two simulated curves place upper and lower bounds for the value of *ΔE* according to the single-valued model. (b) Comparison of experimental (symbols) and simulated (solid line) *M(H)* curves for the same sample using a Gaussian distribution of *ΔE*. The Gaussian distribution is centered at *ΔE*=1.9x10^{-3} meV/Mn with σ=0.60x10^{-3} meV/Mn and is shown in the inset.

to the global minimum is sufficient to account for the energy necessary for domain nucleation and growth, ΔE^{100}. For the simulation shown in Figure 47, it was assumed that ΔE^{100}= 2.01x10^{-3} meV/Mn which causes the noncoherent spin flips to occur at ±7 mT in reasonable agreement with the experiment.

It is readily apparent that the *M(H)* simulations predict much sharper spin switches than are observed experimentally. One reason for this disagreement is that the simulations account only for hysteretic effects caused by noncoherent spin switching and neglect other processes, particularly the pinning and depinning of domain walls by defects during magnetization reversal. Furthermore, the model assumes that the material is completely homogeneous and well-described by single-valued parameters for both the magnetic anisotropy (set of K) and the hysteretic processes (ΔE). Nonuniform distribution of the Mn moments and materials defects can result in local fluctuations in the magnetization and carrier concentration which can affect both the magnetic anisotropy and reversal process **[164]**, thus giving rise to differences in the experimental and calculated hysteresis loops. In regards to the single-valued model, error bars can be placed on the value of ΔE^{100} by "bounding" the hysteresis loop as is done in Figure 48 (a). Based on these results the approximate range of ΔE^{100} is $0.863\text{x}10^{-3} \leq \Delta E^{100} \leq 3.44\text{x}10^{-3}$ meV/Mn for the energy required for domain nucleation and growth for the sample with $\varepsilon_\perp$=-0.18%. The model can also be improved by taking into account that the anisotropy parameters are not single-valued, and have a distribution of values related to the inhomogeneity in the sample. Kim *et al*. have demonstrated that local fluctuations give rise to a broad distribution of domain pinning fields ($\Delta E/M$) in annealed, LT-MBE grown $Ga_{1-x}Mn_xAs$ thin films, which is well described by a broad Gaussian distribution **[164]**. The simulated *M(H)* curve shown in Figure 48 (b) follows this approach and shows must better agreement with experiment indicating that local fluctuations in x, p, and/or defect concentrations have a significant effect on the magnetic anisotropy and magnetization reversal. The Gaussian distribution of ΔE centered around 1.9x10^{-}

^{3} meV/Mn with a standard deviation of 6.0x10^{-4} meV/Mn. Further details regarding computation of *M(H)* curves for distributions of *ΔE* are found in Appendix F.

5.6.5 *Domain Parameters and Materials Trends*

As was indicated in Section 5.4, quantitative comparison of the magnetic anisotropy of materials grown by II-PLM and LT-MBE is not straightforward. It is noted here as a point of reference that Liu *et al.* found that $\Delta E^{100} \approx 5.5\text{x}10^{-3}$ meV/Mn in $Ga_{0.98}Mn_{0.02}As$ thin films with out-of-plane easy axis using a similar approach **[165]**. This value is of similar magnitude to the values reported here for $Ga_{1-x}Mn_xP_{1-y}N_y$. However, direct comparison is limited since the $Ga_{1-x}Mn_xP_{1-y}N_y$ film with $\varepsilon_\perp$=-0.18% has nearly a factor of 2 larger x and its easy axis is not completely out-of-plane.

With knowledge of the *ΔE,* it is possible to estimate the Bloch domain wall energy per unit area according to the standard approach**[165, 166]**

$$\sigma_w = 2\pi\sqrt{\frac{\Delta E S^2 J}{d}} \tag{44}$$

where J is the exchange energy, $d=ax^{-1/3}$ is the average spacing between Mn atoms and *ΔE* is determined from simulation. In Equation 44 *ΔE* takes the units of J/m^3. The conversion for *ΔE* from meV/Mn to J/m^3 is

$$\Delta E[J/m^3] = \Delta E[meV/Mn] \cdot 3.95 \times 10^6 \cdot x \tag{45}$$

Following Refs. **[165]** and **[21]**, it is assumed that $J=3k_BT_C/2zS(S+1)$ where S=5/2 for Mn^{2+} ions and T_C = 35 K for the film with $\varepsilon_\perp$=-0.18 %. As pointed out in Ref. **[21]** the number of nearest-neighbor spins z is not well-defined for a system of random magnetic dopants in a zincblende lattice; so the range $4 \le z \le 12$ was used which introduces a source of error. Within these approximations we find that $0.013<\sigma_w<0.032$ erg/cm^2 ($1.31\text{x}10^{-5}<\sigma_w<3.17\text{x}10^{-5}$ J/m^2), which is close to the value of 0.027 erg/cm^2 reported for $Ga_{0.98}Mn_{0.02}As$ established by a similar method**[165]**. On the other hand, Gourdon *et al.* determined a much larger value of $\sigma_w \approx 0.2$ erg/cm^2 from domain theory for $Ga_{0.93}Mn_{0.07}As$ films in a state of tensile strain**[167]**. The range of domain parameters determined for $Ga_{1-x}Mn_xAs$ of different compositions underscores the need to compare materials of nearly identical x, p, and $\varepsilon_\perp$ since the magnetic anisotropy depends strongly on these quantities.

Finally an attempt is made to compare the magnitude of $2K_{eff}^{100}/M$ between $Ga_{1-x}Mn_xAs$ and $Ga_{1-x}Mn_xP$. Based on the results of Ref. **[164]**, $2K_{eff}^{100}/M \approx 30$ mT for $Ga_{0.976}Mn_{0.024}As$. While this value is significantly less than the 78 mT found in this work for $Ga_{0.966}Mn_{0.034}P$, one cannot discount the increase in $2K_{eff}^{100}/M$ with Mn doping as explaining some of this difference (Section 5.5). Thus, further studies are necessary in order to establish trends in the domain parameters between $Ga_{1-x}Mn_xAs$ and $Ga_{1-x}Mn_xP$.

5.6.6 *Summary*

In summary, this study has revealed a correlation between the perpendicular magnetic anisotropy and epitaxial strain in $Ga_{1-x}Mn_xP$. Substitution of N for P in the anion sublattice causes a contraction of the film lattice constant and induces the easy axis to lie perpendicular to the film plane. This behavior is reminiscent of the strain-dependent perpendicular magnetic anisotropy in $Ga_{1-x}Mn_xAs$, which suggests a common origin for the effect in the two materials despite differences in band structure and carrier localization.

The ability to strain-engineer the easy axis in $Ga_{1-x}Mn_xP_{1-y}N_y$ may open the door to new experiments that will increase our understanding of the material. An out-of-plane easy axis enhances contrast in techniques such as spatially-resolved magneto-optic Kerr effect (MOKE) microscopy, which has been used previously to image both the domain structure and domain dynamics during magnetization reversal**[168, 169]**. These measurements may also provide additional information about the magnetic anisotropy of $Ga_{1-x}Mn_xP$. The combination of spatially-resolved MOKE and micromagnetic theory provides a complementary approach by which to calculate domain parameters. In this way it is possible to check and refine the estimates made from the simple free energy analysis in the previous section. Furthermore, the micromagnetic theory approach allows for the determination of additional parameters that are inaccessible from the free energy model, including the spin stiffness constant, which has yet to be experimentally determined in $Ga_{1-x}Mn_xP$**[167]**.

5.7. Compensation-Dependent Magnetic Anisotropy in $Ga_{1-x}Mn_xP_{1-y}S_y$

5.7.1 *Introduction*

The effect of dilute alloying of the anion sublattice with S on the in-plane uniaxial magnetic anisotropy and magnetization reversal process in $Ga_{1-x}Mn_xP$ as measured by both FMR and SQUID magnetometry is presented. At T=5K, raising the S concentration increases the uniaxial magnetic anisotropy between in-plane <011> directions while decreasing the magnitude of the (negative) cubic anisotropy field. Simulation of the SQUID magnetometry indicates that the energy required for the nucleation and growth of domain walls decreases with increasing y. These combined effects have a marked influence on the shape of the field-dependent magnetization curves; while the $[0\bar{1}1]$ direction remains the easy axis in the plane of the film, the field dependence of the magnetization develops double hysteresis loops in the [011] direction as the S concentration increases similar to those observed for perpendicular magnetization reversal in lightly doped $Ga_{1-x}Mn_xAs$. The incidence of double hysteresis loops is explained with a simple model whereby magnetization reversal occurs by a combination of coherent spin rotation and noncoherent spin switching, which is consistent with both FMR and magnetometry experiments. The evolution of magnetic properties with S concentration is attributed to compensation of Mn acceptors by S donors, which results in a lowering of the concentration of holes that mediate ferromagnetism.

5.7.2 *Materials Synthesis*

$Ga_{1-x}Mn_xP$ was synthesized by implantation of 50 keV Mn^+ into (100)-oriented GaP to a dose of $1.5x10^{16}$ cm^{-2} followed by irradiation with a single pulse from a KrF (λ=248 nm) excimer laser at a fluence of 0.44±0.05 J/cm^2. Quaternary alloys were synthesized by co-implanting the Mn-implanted GaP with 60 keV S^+ to doses ranging from 2.5 to 7.3 $x10^{15}$ cm^{-2} prior to PLM. Selected compositional parameters for the samples used in this study are presented in Table 6. The substitutional Mn concentration was determined by the combination of secondary ion mass spectrometry (SIMS) and $^4He^+$ ion beam analysis**[75, 119]**. For samples used in this study the fraction of Mn atoms substituting for Ga was 80-88%, which is comparable to that observed in $Ga_{1-x}Mn_xAs$ thin films grown by LT-MBE **[31]**. It is important to reiterate

Table 6: Selected compositional parameters of $Ga_{1-x}Mn_xP_{1-y}S_y$ as determined by SIMS and ion beam analysis.

Mn^+ Implant Dose (cm^{-2})	x	S^+ Implant Dose (cm^{-2})	y
$1.5x10^{16}$	0.042	0	0
$1.5x10^{16}$	0.041	$2.5x10^{15}$	0.010±0.001
$1.5x10^{16}$	0.041	$5.0x10^{15}$	0.021±0.0015
$1.5x10^{16}$	0.041	$7.3x10^{15}$	0.027±0.002

here that the II-PLM process results in no interstitial Mn (Mn_I); the remainder of the Mn atoms is incommensurate with the lattice. Therefore, II-PLM films have no unintentional compensation due to Mn_I defects, allowing for more reliable control of the carrier concentration in this study. The S concentration as a function of depth was determined by SIMS. The peak substitutional sulfur concentration, y, was estimated by multiplying the peak in the S concentration by the typical substitutional fractions of dopants in GaP and GaAs after PLM, which ranges between 75% and 90% based on previous pulsed-laser melting studies of dopant incorporation into GaP and GaAs **[89, 99, 170]**. The parameter y refers to the concentration of *substitutional* sulfur. The fraction of S atoms that is *electrically active* was estimated from Hall effect measurements on $GaP_{0.979}S_{0.021}$ synthesized under identical conditions to the $Ga_{0.959}Mn_{0.041}P_{0.979}S_{0.021}$ film. Without Mn the carrier concentration can be measured because the anomalous Hall contribution to the Hall resistivity is absent. Comparison of the Hall effect, SIMS, and ion channeling data indicate that ~36% of substitutionally incorporated S atoms are electrically active. Ion channeling measurements on S-doped $Ga_{1-x}Mn_xAs$ show that there is no appreciable incorporation of S into interstitial sites. Given the similarities in processing between GaAs and GaP the formation of interstitial S defects can be precluded for the samples presented in this work.

DC magnetization measurements were performed using a SQUID magnetometer. FMR measurements were performed at $\omega/2\pi \approx 9.26$ GHz in an electron paramagnetic resonance (EPR) spectrometer using magnetic field modulation with the sample temperature controlled using a liquid-He flow cryostat. Differentiation of the in-plane <011> directions was accomplished by etching samples in H_3PO_4 at 180° C for 5 minutes, which produces asymmetric etch pits oriented in the $[0\bar{1}1]$ direction **[171, 172]**.

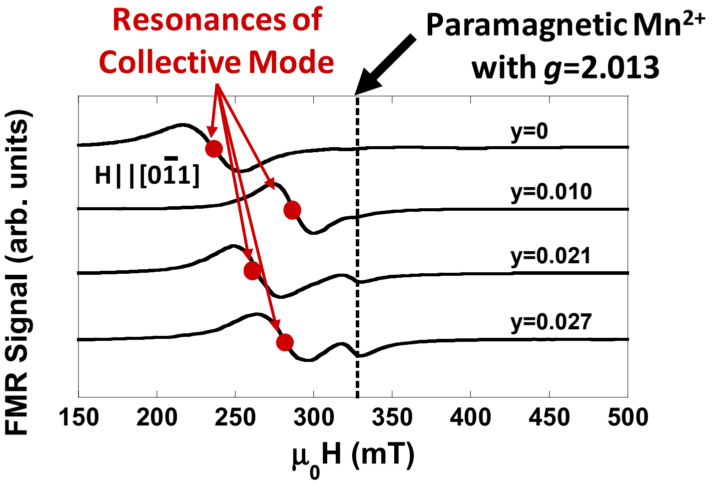

Figure 49: Field dependence of the ferromagnetic resonance for $Ga_{0.958}Mn_{0.042}P_{1-y}S_y$ with y=0, y=0.010, y=0.021, and y=0.027 taken with the field applied parallel to the in-plane $[0\bar{1}1]$ direction at T=5K.

5.7.3 *Ferromagnetic Resonance Spectroscopy*

The field dependence of the FMR intensity at T=5 K and $H\|[0\bar{1}1]$ is shown in Figure 49 for films with various S concentrations. The film with no sulfur shows a single, orientation-dependent resonance due to the collective mode of the ferromagnetically-coupled Mn moments. As y increases a second resonance appears in the FMR measurements at $\mu_0 H\approx330$ mT. This resonance shows only a very weak angular dependence. For $H\|[100]$ this resonance appears at $\mu_0 H$=330.3 mT which corresponds to a g-factor of 2.004. This value of the g-factor is identical to that observed for paramagnetic Mn^{2+} in GaP **[173]**. For $H\|[0\bar{1}1]$ or [011] the position of the resonance shifts to $\mu_o H_{res}$ ~ 328.8 mT (g=2.013). The 1.5 mT shift in the resonance position with crystallographic orientation is consistent with the hypothesis that the resonance is due to paramagnetic Mn^{2+} moments. A similar effective shift in the resonance field of ionized Mn acceptors in highly doped $Ga_{1-x}Mn_xAs$ has already been observed and attributed to low temperature demagnetization effects of Mn^{2+} ions **[174]**. The paramagnetic resonance at $\mu_0 H\approx330$ mT is unlikely to be caused by electrons at neutral S donors. The g-factor of the S donor resonance is g=1.998. Additionally the peak-to-peak line width of the S donor resonance is ~6 mT, which is about a factor of two lower than that observed here (Figure 49) **[175, 176]**. Therefore, the resonance at ~330 mT is attributed to paramagnetic Mn^{2+}.

As y increases, the magnitude of the paramagnetic Mn^{2+} resonance increases with respect to that of the collective mode. This observation suggests that as the concentration of S increases an increasing fraction of the Mn_{Ga} moments are decoupling from ferromagnetic exchange. Such behavior can be explained with the help of the SIMS profiles in Figure 50. As the S concentration increases, the inhomogeneous distribution of Mn and S throughout the film creates regions of the film where the sulfur concentration is greater than or equal to the Mn concentration. In these regions compensation due to S donors decreases the concentration of ferromagnetism-mediating holes to a point where long-range exchange is interrupted. As a result the Mn moments in such regions behave as paramagnets. For y up to 0.027, the region of the film with maximum Mn concentration still has a sufficient hole concentration support ferromagnetic exchange as evidenced by the T_C of 21K for $Ga_{0.959}Mn_{0.041}P_{0.973}S_{0.027}$ **[101, 177]**. Therefore, a magnetic resonance measurement at T= 5K detects two resonances: an orientation-dependent resonance due to the collective precession of ferromagnetically-coupled Mn moments, and another due to paramagnetic Mn moments. As y increases, the paramagnetic "tail" of the Mn distribution increases because the depth over which the sulfur concentration is sufficient to completely disrupt ferromagnetic exchanges increases. Consequently, the relative intensity of the paramagnetic resonance to the collective ferromagnetic resonance increases with increasing y.

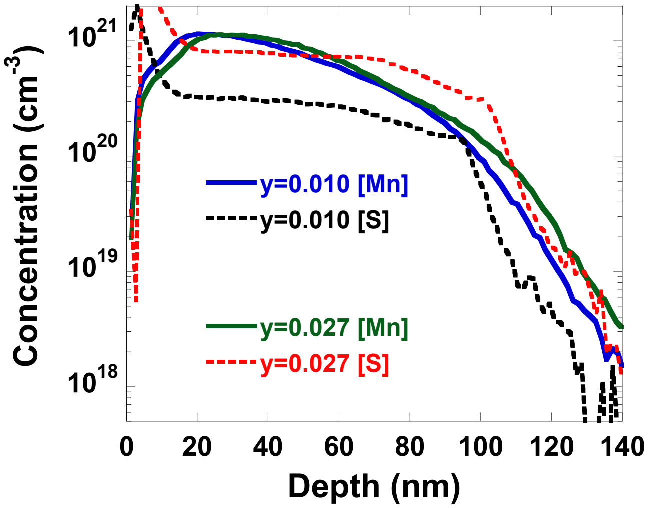

Figure 50: Mn (solid lines) and S (dashed lines) concentrations as a function of depth for samples with *y*=0.010 and *y*=0.027 as determined by secondary ion mass spectrometry. The near-surface peaks visible in the S profiles are measurement artifacts.

The decrease in the fraction of ferromagnetically coupled Mn atoms with increasing *y* is supported by SQUID magnetometry measurements. The magnetic moment at $\mu_0 H$=5T decreases monotonically from 3.5±0.2 μ_B/Mn$_{Ga}$ for *y*=0 to 1.9±0.2 μ_B/Mn$_{Ga}$ for *y*=0.027 since at this magnitude of the applied field the paramagnetic Mn spins are not yet completely aligned along the field direction. Further support for sulfur-induced compensation comes from the decrease of T$_C$ as well as the XMCD asymmetry with increasing *y* **[101, 177]**, and similarity to results obtained in Te co-doped $Ga_{1-x}Mn_xP$ **[99]**. In addition, the aforementioned Hall and ion channelling measurements demonstrate an electrical activation of ~36% of substitutional S donors in GaP:S synthesized by II-PLM.

Since this chapter is focused on magnetic anisotropy the remainder of the analysis will focus on the ferromagnetically-coupled collective mode. The dependence of the magnetic resonance field for in-plane orientations of the applied magnetic field is shown in Figure 51 as a function of *y*. As has already been discussed in Sections 5.5 and 5.6, the in-plane rotations

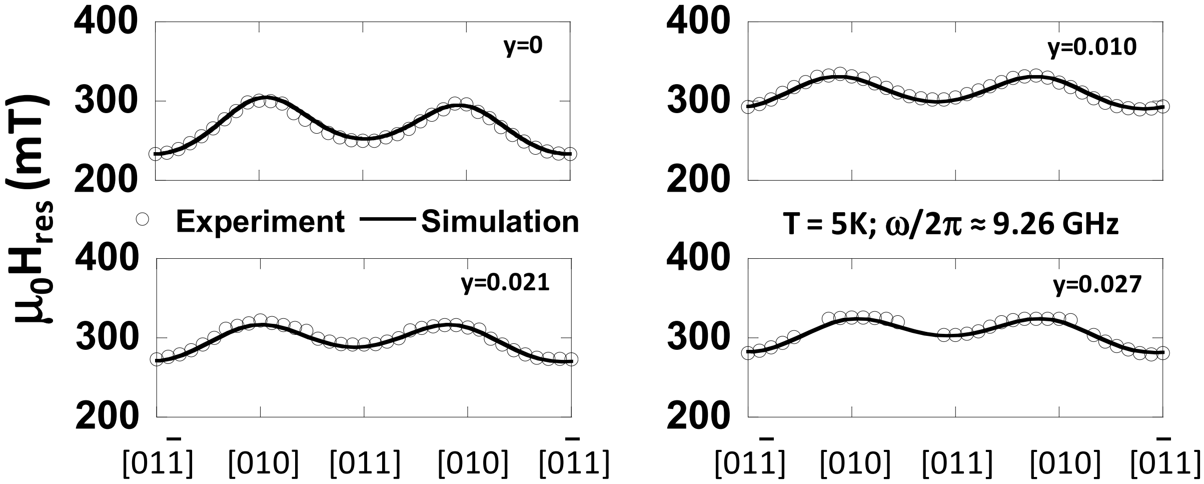

Figure 51: In-plane FMR rotations for $Ga_{1-x}Mn_xP_{1-y}S_y$. Open symbols refer to experimental data while the solid lines are simulations according to the model described Section 5.2.1.

exhibit minima when the field is parallel to <011> directions, and the four-fold symmetry is broken by the presence of an in-plane uniaxial component to the magnetic anisotropy in all samples.

Following the procedure outlined in Section 5.2.1, the anisotropy fields are determined from the angular dependence of the resonance field. The solid lines in Figure 51 show the results of the ferromagnetic resonance simulations, which were calculated using the range of anisotropy fields listed in Table 7. These simulations also agree with the out-of-plane FMR rotations as well for the same range of anisotropy fields (data not shown). The magnetic anisotropy is dominated by the out-of-plane cubic and uniaxial terms. The combined effect of the perpendicular anisotropy parameters is to confine the magnetization strongly to the film plane. These terms show a non-monotonic dependence with y, but in general are weaker in samples with sulfur. The origin of this behavior is not completely understood at this time and will not be further discussed in this work. The values of the out-of-plane anisotropy fields do, however, play a role in determining the absolute magnitude of the in-plane resonance fields shown in Figure 49 and Figure 51. Thus, the resonance field for $H\|[0\bar{1}1]$ occurs at a lower field for y=0 than for y=0.010, 0.021, or 0.027 due to the enhanced out-of-plane anisotropy in the former material. On the other hand, the *relative* difference in resonance fields for different in-plane magnetic field orientations within a given sample does not depend strongly on the out-of-plane anisotropy parameters, which makes it possible to compare the in-plane anisotropy between materials by considering in-plane rotations of the external magnetic field. For all y, $2K_{C1}^{\|}/M$ is negative and $2K_u^{011}/M$ is positive. The former results in the <011>-type directions being magnetically preferred over <001>-type directions while the latter determines that the in-plane easy axis is oriented parallel to $[0\bar{1}1]$ as opposed to [011]. Increasing the S content of the anion sublattice results in an enhancement of the in-plane uniaxial anisotropy between $[0\bar{1}1]$ and [011] directions; the [011] direction becomes progressively magnetically harder. This observation is consistent with the effect of carrier concentration on $2K_u^{011}/M$ in $Ga_{1-x}Mn_xAs$ where a rotation of the easy axis from $[0\bar{1}1]$ to [011] occurs as p increases **[38]**. In terms of anisotropy parameters $2K_u^{011}/M$ is negative is $Ga_{1-x}Mn_xAs$ with large p but changes sign and subsequently increases in (positive) magnitude as p decreases. In $Ga_{1-x}Mn_xP$ a similar trend is observed. The $Ga_{0.958}Mn_{0.042}P$ sample starts with small, positive $2K_u^{011}/M$. As compensation occurs and p is decreased, $2K_u^{011}/M$ remains positive and increases in magnitude. Presumably the synthesis of $Ga_{1-x}Mn_xP$ with even larger p would result in a change in sign of $2K_u^{011}/M$ in analogy to the behavior of $Ga_{1-x}Mn_xAs$.

Table 7: Cubic and uniaxial anisotropy fields of $Ga_{1-x}Mn_xP_{1-y}S_y$ as determined by FMR

y	$2K_u^{011}/M$ (mT)	$2K_{C1}^{\|}/M$ (mT)	$2K_{eff}^{100}/M$ (mT)	$2K_{C1}^{\perp}/M$ (mT)
0	5±1	-35±2	175±3	-80±3
0.010	8±1	-28±2	68±3	-40±3
0.021	10.5±1.5	-28±2	98±3	-50±3
0.027	12.5±2	-25±2	75±3	-40±3

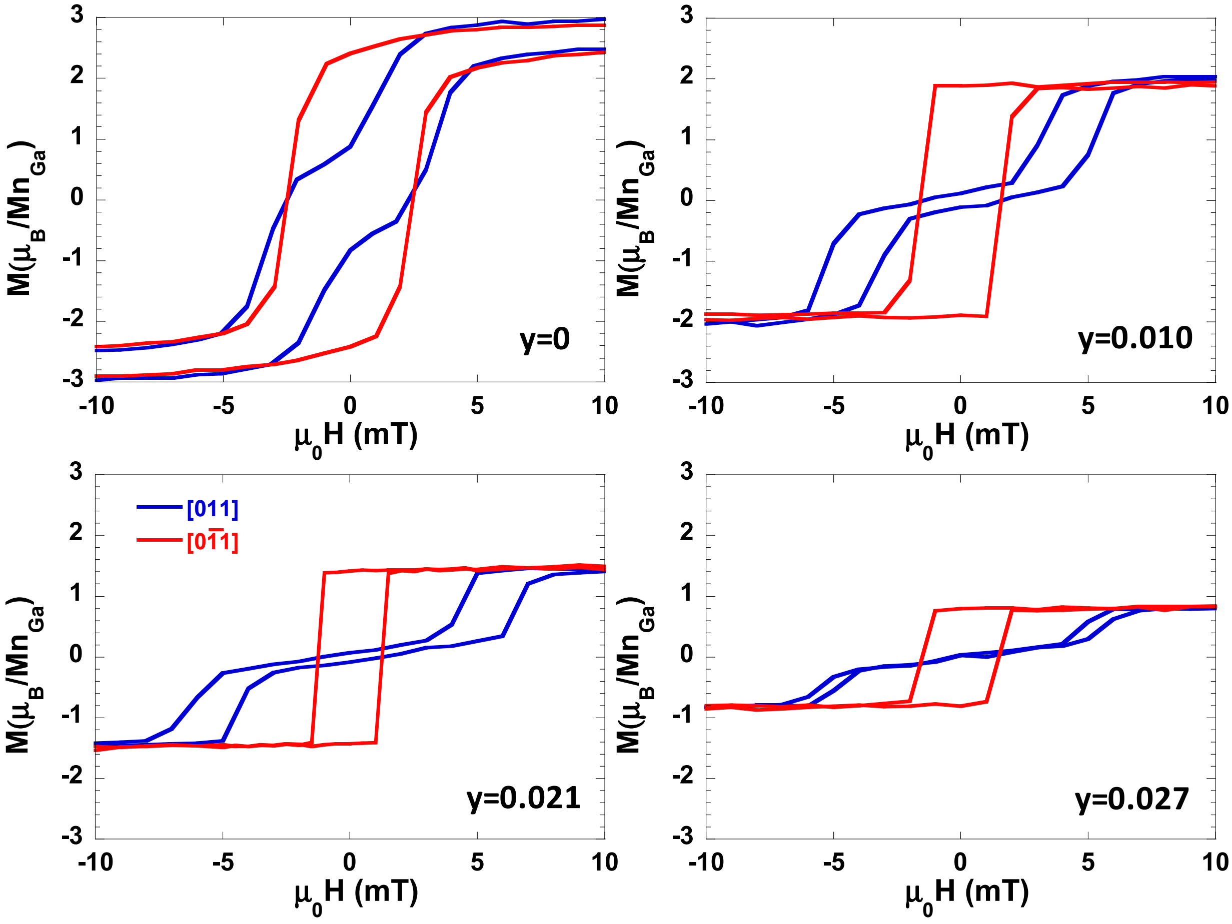

Figure 52: Field dependence of the magnetization for y=0, y=0.010, y=0.021, and y=0.027 for the two different in-plane <011> directions. Measurements were performed at T=5K after saturating the magnetic moment at $\mu_0 H$=5T.

5.7.4 *SQUID Magnetometry Measurements*

The effect of the changes in the in-plane magnetic anisotropy fields on the process by which in-plane magnetization reversal occurs will now be explored. Figure 52 shows the field dependence of the magnetization, $M(H)$, at T=5K for the applied external field oriented parallel to either the [011] or $\left[0\bar{1}1\right]$ as measured by SQUID magnetometry. All curves for $H \| \left[0\bar{1}1\right]$ show relatively small coercivities (less than 4 mT) and square-like hysteresis loops indicative of a magnetic easy axis. The remanent magnetization decreases as y increases. This is not a result of magnetic anisotropy but instead is due to the drop in the saturation moment with compensation (see above).

The magnetization reversal process for $H \| [011]$ is strongly influenced by the increase in the in-plane uniaxial anisotropy with S alloying. For y=0 the $M(H)$ curve exhibits a "kink" near H=0. As the sulfur concentration increases, the kinked lineshape changes into a "wasp-waisted" or "double" hysteresis loop. The incidence of both the kinked and double hysteresis loops is due to a multistep magnetization reversal mechanism that will be discussed in the detail in the following section. Double hysteresis loops have previously been observed in $Ga_{1-x}Mn_xAs$ for the case of *perpendicular* magnetization reversal when the Mn concentration was low (x≈1-2 %)

[151]. The existence of double hysteresis loops in $Ga_{1-x}Mn_xAs$ was attributed by Titova *et al.* to the complex nature of the free energy surface arising from uniaxial and cubic anisotropy terms that were of similar magnitude **[151]**. For $Ga_{1-x}Mn_xP_{1-y}S_y$, $3.5 \leq |K_{C1}^{||} / K_u^{011}| \leq 2$ for the wasp-wasited loops. In this regard, these results are consistent with this explanation.

5.7.5 *Modeling of Hysteresis Loops*

To further investigate the evolution of the *M(H)* lineshape with increasing compensation, the in-plane hysteresis loops were simulated according to the model described in Appendix F. For these calculations it was assumed that the both the magnetic field and magnetization vectors were confined to the film plane ($\Phi=\phi=0°$, or 180°). Within these assumptions the free energy takes on the more simple form,

$$F(\theta,\Theta) = -MH(\cos\Theta\cos\theta + \sin\Theta\sin\theta) - \frac{1}{2}K_{C1}^{||}(\cos^4\Theta + \sin^4\Theta) + \frac{1}{2}K_u^{011}(\cos\Theta + \sin\Theta)^2. \tag{46}$$

The assumption that $\Phi=0^{\circ}$ or 180° is reasonable given the compressive strain state of the $Ga_{1-x}Mn_xP_{1-y}S_y$ thin films on GaP, which induces the easy axis to lie in the film plane (Section 5.6). Therefore, when the magnetic field is applied in the plane of the film, both the Zeeman and anisotropy energies favor an in-plane orientation of the magnetic moment, which justifies the use of Equation 46. Since the magnetization is confined to the film plane, the reversal process depends only on the in-plane anisotropy parameters $K_{C1}^{||}$ and K_u^{011}. The simulated *M(H)* curve for *y*=0 and *H*||[011] is shown in Figure 53 (a) along with the calculated free energy curves as a function of the in-plane orientation of the magnetization vector Θ. When the magnetic field is large the equilibrium orientation of the magnetization vector is parallel to [011] (Θ=45°), due to the dominance of the Zeeman energy. As the magnitude of the magnetic field decreases a global minimum emerges near (Θ=45°) which is parallel to the in-plane easy axis $[01\bar{1}]$. The magnetization remains pinned in the minimum at Θ=45° until the energy gained by switching to the global minimum ΔE^{011} is sufficient to overcome the energy barrier to domain wall nucleation and growth (Appendix F). For a noncoherent spin switch occurring at μ_0H=-0.2 mT, ΔE^{011}=4.3x10^{-4} meV/Mn produces reasonable agreement with experiment. After the first noncoherent spin switch the magnetization vector rotates towards $[0\bar{1}\bar{1}]$; as the Zeeman energy increases with increasing magnitude of the (negative) magnetic field, the minimum of *F*(Θ) shifts away from Θ=-45°. Magnetization reversal proceeds by coherent rotation until another noncoherent spin flip occurs to the global minimum at Θ=-135°, which again requires overcoming an energy barrier of 4.3x10^{-4} meV/Mn. For *y*=0 the second switch occurs at μ_0H=-4.5 mT. Similar arguments hold for the opposite process. As the field is swept from negative to positive values, noncoherent switches occur at μ_0H=0.2 mT and 4.5 mT, thus completing the kinked hysteresis loop.

The magnetization reversal process occurs by the same two mechanisms in the sample with *y*=0.027 [Figure 53 (b)]. However, now the noncoherent spin switches are separated by a much larger magnetic field range in which magnetization reversal occurs by coherent rotation of the magnetic moment. Both the decreased width of each half of the double hysteresis loop as well as the higher field at which the center of each half of the double hysteresis loop occurs are

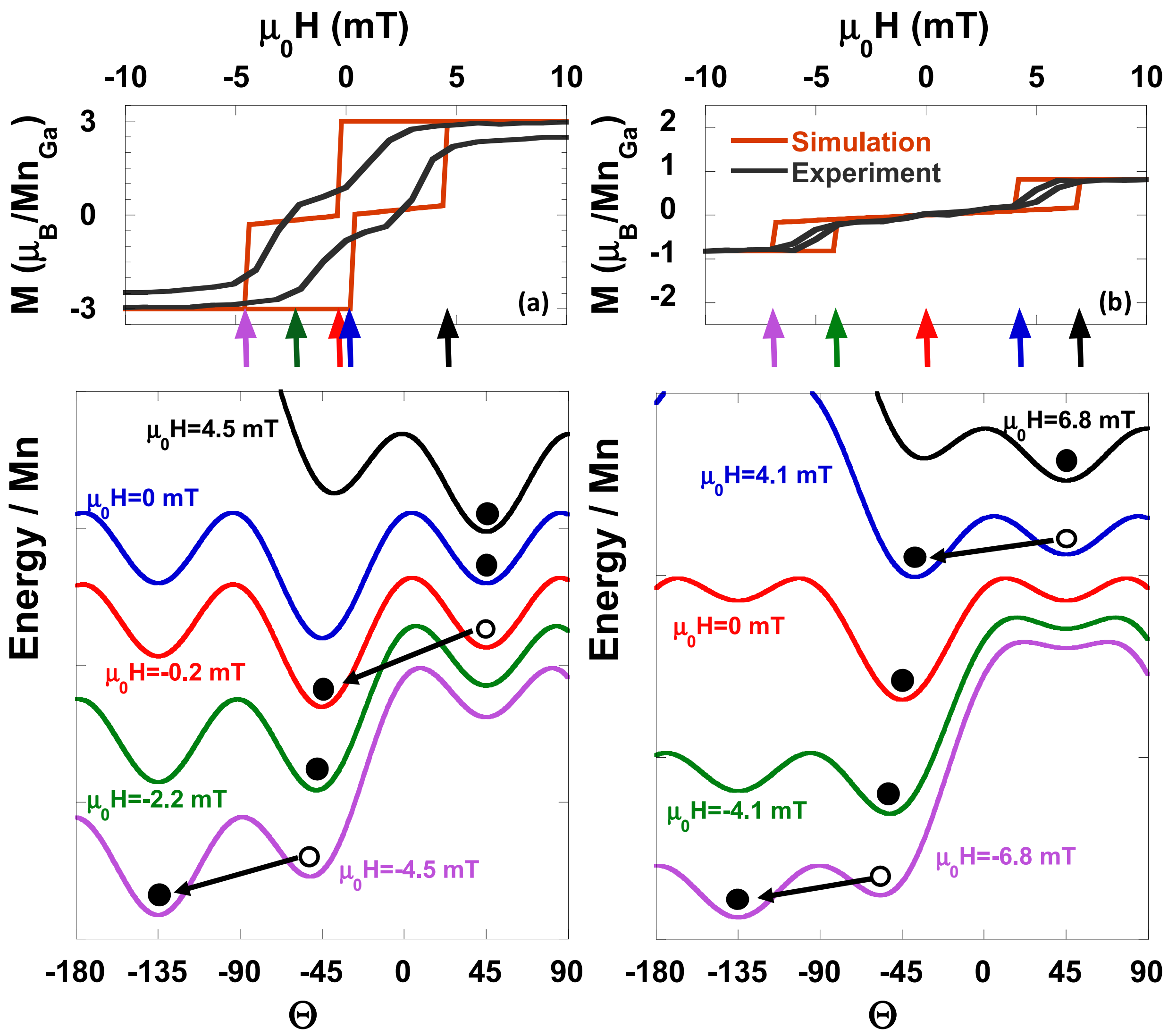

Figure 53: Comparison of simulated and experimental *M(H)* curves (top panels) and free energy contours at selected magnetic field strengths (bottom panels) for $Ga_{0.959}Mn_{0.041}P_{1-y}S_y$ films with (a) y=0 and (b) y=0.027. Filled symbols correspond to the orientation of the magnetic moment at a given field. Open symbols and arrows represent noncoherent spin switching from one magnetization orientation to another which occurs at the specified field.

captured by our simple model using a reduced value for ΔE^{011} of 6.2x10^{-5} meV/Mn and the in-plane anisotropy fields determined from FMR.

As a guide to further discussion of the SQUID simulations, Figure 54 indicates the effects of the key model parameters on the shape of the *M(H)* lineshape when $H\|[011]$. The fields at which the first and second noncoherent spin switches occur are defined as μ_0H_1 and μ_0H_2, respectively. Therefore, the "width" of each lobe of a double hysteresis loop is equal to ($\mu_0H_2-\mu_0H_1$) and determined predominately by the value of ΔE^{011}. The simulations tend to predict much sharper noncoherent switches than are observed in experiment as discussed in Section 5.6.4. Using the method presented in Section 5.6.4 and Figure 48(a) the range of ΔE^{011} for the single-valued model can be "bounded." The results of these calculations are displayed in

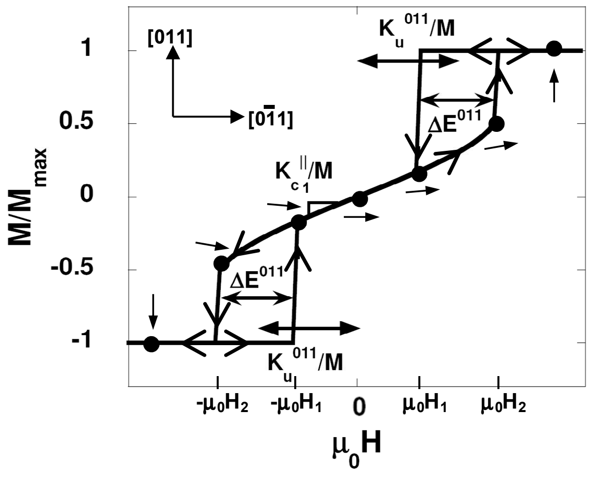

Figure 54: The effect of the in-plane anisotropy fields and *ΔE* on the shape of calculated *M(H)* curves for *H*||[011]. The orientation of the magnetic moment at magnetic fields specified by filled black circles is indicated by black arrows above or below the symbols with respect to the coordinate system included. The magnetic fields $\mu_0 H_1$ and $\mu_0 H_2$ correspond to those at which the first and second noncoherent spin flips occur. A positive magnetic field is defined as parallel to [011].

Table 8. Although the spread in values is rather large the general trend suggests that ΔE^{011} decreases with increasing *y*.

As mentioned in Section 5.6.4 the *M(H)* simulations can be improved by assuming that the parameter *ΔE* is not single valued but takes on instead a continuous distribution of values. Figure 55 shows the results of *M(H)* calculations where a Gaussian distribution **[164]** of ΔE^{011} with a mean of 1.2x10^{-4} meV/Mn and standard deviation of 4.9x10^{-5} meV/Mn are used. Clearly, the calculated *M*(*H*) loops agree much better with experiment when a distribution of ΔE^{011} is used. The similar distributions of domain wall energies between the annealed LT-MBE grown $Ga_{1-x}Mn_xAs$ and II-PLM formed $Ga_{1-x}Mn_xP_{1-y}S_y$ suggests that lateral inhomogeneity is inherent to materials grown by both processes and that the vertical inhomogeneity inherent to II-PLM processing does not produce additional spread in the domain wall energies.

Simulations of the *M(H)* profiles for all samples were performed using a Gaussian distribution in *ΔE*. The results of the calculations are summarized in Figure 55(c). For all *y* $\Delta E^{011} < \Delta E^{0\bar{1}1}$, which is reasonable considering that the former case requires nucleation of 90° domain walls while the latter involves 180° domain wall formation **[119]**. As *y* increases, both ΔE^{011} and $\Delta E^{0\bar{1}1}$ decrease. This indicates that magnetization reversal by noncoherent spin switching becomes easier as the carrier concentration is decreased– that is, it requires less energy. This trend is in agreement with that observed from the single-valued model calculations.

Table 8: ΔE^{011} as a function of *y* for $Ga_{1-x}Mn_xP_{1-y}S_y$ for single-valued *M(H)* simulations.

y	$\Delta E^{011}_{\min}$ (x10^{-4} meV/Mn)	$\Delta E^{011}_{\max}$ (x10^{-4} meV/Mn)
0	1.5	3.1
0.010	0.95	1.9
0.021	0.62	1.2
0.027	0.19	0.62

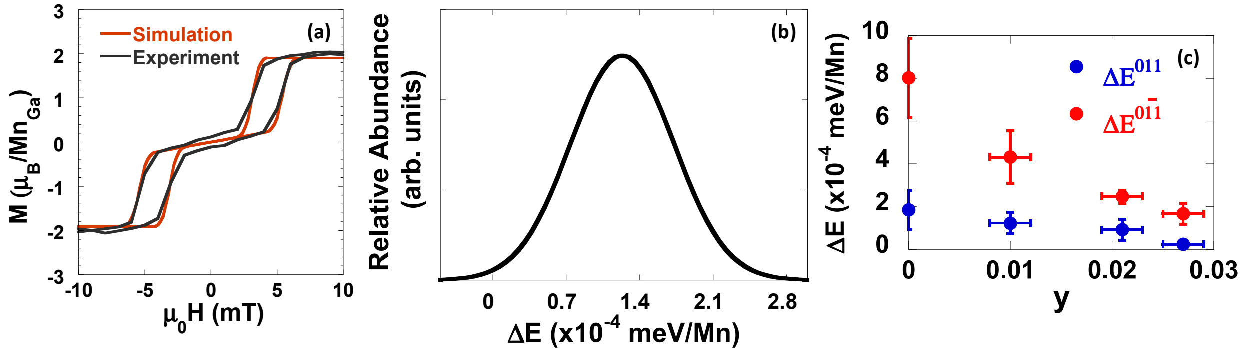

Figure 55: (a) Comparison of simulated and experimental hysteresis loops for *y*=0.010 in which ΔE^{011} is assumed to follow a Gaussian distribution with a mean of 1.2x10^{-4} meV/Mn and standard deviation of 4.9x10^{-5} meV/Mn. (b) Relative abundance of different ΔE^{011} according to the Gaussian distribution. (c) *ΔE* as a function of *y* for both in-plane <011> orientations. Symbols represent the mean value and the errors bars one standard deviation of *ΔE* within a Gaussian distribution.

Returning to Figure 54, the slope of the portion of the *M(H)* curve where magnetization reversal occurs by coherent rotation is principally determined by $K_{C1}^{||}$. A larger value of the anisotropy field $2K_{C1}^{||}/M$ implies that the energetic difference between <011> and <001> directions is increased. Thus, less rotation of the magnetization occurs per unit magnetic field since the Zeeman energy has less influence on the angular location of the free energy minimum. It should be noted that the experimental hysteresis loops would be better described by anisotropy fields ($2K_{C1}^{||}/M$) that are approximately a factor of two smaller than those determined from FMR experiments and therefore used in the simulations. This discrepancy may be due to the small total sample magnetization (~10^{-7} emu) that is measured by the SQUID magnetometer in the region of the *M(H)* curve where magnetization reversal is occurring by coherent rotation. On the other hand, the angular-dependence of the FMR is not subject to such limitations, which makes it better suited for the determination of the in-plane cubic anisotropy field than explicitly matching the slope of the measured and simulated field-dependent SQUID measurements. Furthermore, as was alluded to in Section 5.6.4, agreement within a factor of two of the anisotropy parameters determined by FMR and SQUID is quite reasonable as a result of the simple nature of the *M(H)* model. Given these collective limitations the level of agreement between *M(H)* experiments and calculations is adequate.

Each lobe of the double hysteresis loop is centered at roughly $\mu_0H=K_u^{011}/M$. Some deviation from this value occurs because of the in-plane cubic anisotropy, which causes the two noncoherent spin flips that bound the lobe to occur over different angles. In Figure 54 the noncoherent switch at μ_0H_1 occurs over a greater angle than that at μ_0H_2 since less coherent rotation has occurred at μ_0H_1 than μ_0H_2. Nevertheless, the deviation in lobe width from $\mu_0H=K_u^{011}/M$ is minor. As an example, for *y*=0.010 the simulated loop [Figure 55(a)] has lobes centered at μ_0H=4.1 mT while K_u^{011}/M=3.5 mT, a difference of about 20%. The effect becomes more pronounced as the magnitude of $2K_{C1}^{||}/M$ decreases. The increased slope of the quasi-linear portion of the *M(H)* curve enhances the angular disparity at fields μ_0H_1 than μ_0H_2 resulting in greater shifts in the lobe centers. All Ga$_{1-x}$Mn$_x$P$_{1-y}$S$_y$ samples analyzed here have similar values for $2K_{C1}^{||}/M$. Comparison of the location of the lobe centers between samples by the parameter K_u^{011}/M is, therefore, valid.

With these basic trends in mind the evolution of kinked hysteresis loops to double loops is easily understood in the context of the present model. For y=0.010, the hysteretic width of each lobe of the double hysteresis loop, $\mu_0H_2-\mu_0H_1$, is ~2 mT. The center of each lobe occurs at ~4.1 mT. Therefore, the field at which the first non-coherent spin flip occurs upon magnetization reversal is $-\mu_0H_1\approx$4.1 mT-$(\mu_0H_2-\mu_0H_1)/2\approx$3 mT. The two halves of the loop do not overlap and are connected to one another by a reversible linear region, resulting in the wasp-waisted lineshape. On the other hand, when y=0 the increase in ΔE^{011} causes each lobe to be much broader. At the same time the smaller value of the in-plane uniaxial anisotropy field causes the center of each lobe to occur at ~2.5 mT. Hence, $\mu_0H_1\approx0$ resulting in an effective overlap of the two lobes, which leads to the "kinked" lineshape. Increasing y from 0.010 to 0.027 causes further wasp-waisting of the hysteresis loops due to the combined increase of K_u^{011}/M and decrease in ΔE^{011}. As a result the proportion of magnetization reversal that occurs by coherent spin rotation increases with respect to noncoherent spin switching. By further increasing y, it is expected that magnetization reversal will eventually occur entirely by rotation of the magnetization vector as the uniaxial contribution to the in-plane magnetic anisotropy will start to dominate. The situation would be similar to that observed in Section 5.6.4 for perpendicular magnetization reversal in $Ga_{1-x}Mn_xP_{1-y}N_y$ where the compressively-strained films show completely reversible behavior due to the dominance of the uniaxial anisotropy in this geometry. Assessing this behavior in $Ga_{1-x}Mn_xP_{1-y}S_y$ may not be straightforward as increasing y will result in further lowering of T_C; the sample may become paramagnetic before $2K_u^{011}/M$ exceeds $2K_{C1}^{||}/M$.

5.7.6 *Summary*

The effect of dilutely alloying the anion sublattice of $Ga_{1-x}Mn_xP$ with S has been investigated by the combination of FMR spectroscopy and SQUID magnetometry. The in-plane uniaxial anisotropy field along [011], $2K_u^{011}/M$, can be controlled by adjusting the S concentration whereby the $[0\bar{1}1]$ axis is increasingly preferred as y increases. In parallel, the magnitude of the (negative) in-plane cubic anisotropy field, $2K_{C1}^{||}/M$, decreases as y increases. The combination of these two effects creates an intricate free energy landscape in which magnetization reversal occurs by a combination of coherent spin rotation and noncoherent spin switching, which produces either a kinked or wasp-waisted hysteresis loop when the applied field is parallel to [011]. The appearance of wasp-waisted loops as the sulfur concentration increases is also caused by a decrease in the barrier to domain nucleation ΔE^{011}, which causes a greater fraction of magnetization reversal to occur by coherent rotation as y increases. Indeed, for y=0.027 the field-dependence of the magnetization is nearly completely reversible, in contrast to the behavior observed at smaller values of y. The unique magnetization reversal behavior in $Ga_{1-x}Mn_xP_{1-y}S_y$ is, therefore, the consequence of a multifaceted interplay of anisotropy and thermodynamic parameters, each of which has its own unique compositional dependence.

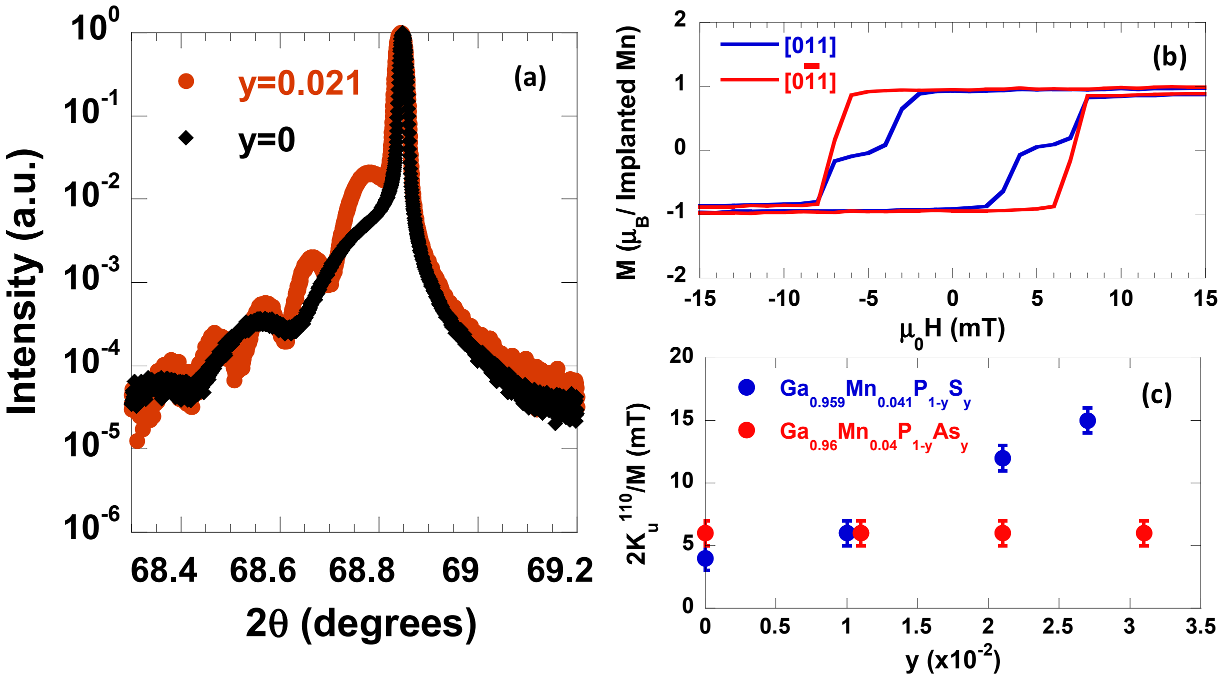

Figure 56: (a) X-ray diffraction measurements of $Ga_{1-x}Mn_xP_{1-y}S_y$ samples with and without sulfur. The addition of S clearly places the film under additional compression. (b) Field-dependence of the magnetization for $Ga_{0.96}Mn_{0.04}P_{1-y}S_y$ with $y \approx 0.02$ for the in-plane <011> directions. Note that the units of the magnetization are normalized per implanted Mn (not per Mn_{Ga}) since complete ion beam analysis was not performed on this sample. (c) Dependence of the in-plane uniaxial anisotropy field on anion sublattice composition for $Ga_{1-x}Mn_xP_{1-y}S_y$ and $Ga_{1-x}Mn_xP_{1-y}As_y$.

The changes in the magnetic anisotropy and magnetization reversal mechanism with increasing y have been attributed to compensation of ferromagnetism-mediating holes by S donors. Since the evidence for compensation is indirect (owing to complications of measuring the carrier concentration by the Hall effect in magnetic systems **[178]**), it is important to rule out other possible explanations. One possibility that can be ruled out is the effect of strain. The larger atomic radius of S compared to P causes the films to be placed under additional compressive strain [Figure 56(a)]. To test the effect of increasing the compressive strain on the in-plane magnetic anisotropy a parallel series of $Ga_{0.96}Mn_{0.04}P_{1-y}As_y$ films were synthesized. When isovalent As substitutes for P it adds compressive strain without intentional compensation. The addition of As to the anion sublattice does not cause the same changes in the magnetization reversal process as the addition of S. Figure 56(b) shows that the kinked lineshape is maintained for [011] magnetization reversal even for $y \approx 2\%$; no wasp-waisting occurs. FMR experiments support these observations; $2K_u^{011}/M$ does not change as y increases in $Ga_{0.96}Mn_{0.04}P_{1-y}As_y$ indicating that strain alone cannot cause the observed changes in the magnetic anisotropy of $Ga_{0.96}Mn_{0.04}P_{1-y}S_y$. The development of a paramagnetic resonance signal, and decrease in T_C and XMCD asymmetry with increasing y provide additional evidence that suggests that the results presented in this study are truly due to the modulation of p by compensating sulfur donors.

5.8. Summary and Implications of Results

Detailed knowledge of magnetic anisotropy in $Ga_{1-x}Mn_xP$ has important ramifications towards fundamental understanding of the exchange interactions in Mn-doped III-V semiconductors. The magnetic anisotropy of $Ga_{1-x}Mn_xP$ is substantially similar to both $Ga_{1-x}Mn_xAs$ and $In_{1-x}Mn_xAs$. This observation provides even more compelling evidence that we have synthesized the carrier-mediated phase of $Ga_{1-x}Mn_xP$ by II-PLM. If ferromagnetism resulted from, for example, 2nd phase impurities, one would not expect the magnetic anisotropy to exhibit the symmetry of the tetragonally-distorted zincblende structure.

Furthermore, strain and hole concentration dependence of the magnetic anisotropy of $Ga_{1-x}Mn_xP$ is similar to that observed in $Ga_{1-x}Mn_xAs$. In $Ga_{1-x}Mn_xAs$ the sign and magnitude of the in-plane uniaxial anisotropy field $2K_u^{011}/M$ is strongly dependent on the carrier concentration while that of $2K_{eff}^{100}/M$ depends on the epitaxial strain. As alluded to in Section 5.3 mean-field, valence-band theory reproduced this behavior by explicitly considering strain terms in the *p-d* exchange augmented **k·p** Hamiltonian. In these models the magnetic anisotropy arises due to the **k**-dependence of the hole dispersion, which through the *p-d* exchange interaction causes the energy of the entire Mn-hole system to depend on the orientation of the Mn moments relative to the crystallographic axes. The strain-dependence of the anisotropy then arises due to further splitting of the spin-split light-hole and heavy-hole valence bands, which causes a redistribution of the spin-polarized holes and therefore can change the orientation of the magnetic easy axis. In this formalism the *p*-dependence of the in-plane uniaxial anisotropy is consistent with a small shear ε_{xy} term while the out-of-plane anisotropy can be explained by biaxial strain terms. The evolution of the magnetic easy axis with doping**[159]**, compensation**[100]**, and strain has been observed in $Ga_{1-x}Mn_xP$ a system with *localized, impurity band* carriers. Therefore, we conclude that itinerant valence band holes are not essential for producing anisotropic carrier-mediated exchange interactions. An alternate and useful perspective can perhaps be found in multiband tight binding calculations**[28]** which have previously been shown to successfully describe STM experiments between Mn_{Ga} pairs as well as the behavior of *insulating, ferromagnetic* $Ga_{1-x}Mn_xAs$**[42, 179]**. Extension of this model would allow for the calculation of the anisotropy energy due to the relative orientation of the Mn_{Ga} spins and the crystallographic axes**[179]**.

6. Conclusions and Future Work

6.1 Summary of Findings

This work has focused on exploring the interplay of carrier localization, exchange strength, and ferromagnetism in Mn-doped $Ga_{1-x}Mn_x$-pnictide ferromagnetic semiconductors by the synthesis of the novel alloys $Ga_{1-x}Mn_xP$, $Ga_{1-x}Mn_xAs_{1-y}P_y$, and $Ga_{1-x}Mn_xAs_{1-y}N_y$ by II-PLM. One of the principal findings of this work is that changing the composition of the anion sublattice from GaAs to one with shorter bond length in order to enhance inter-Mn coupling is inhibited by carrier localization. In $Ga_{1-x}Mn_xP$ the deeper acceptor level causes significant localization of holes while in the quaternary materials $Ga_{1-x}Mn_xAs_{1-y}P_y$ and $Ga_{1-x}Mn_x As_{1-y}N_y$ scattering from the alloy-disorder potential decreases the mean free path of holes

Throughout this work great care was taken to demonstrate the ability of the II-PLM process to produce high-quality ferromagnetic semiconductors that exhibit the hallmarks of carrier-mediated ferromagnetism. This was achieved through detailed comparison of structural, magnetic and electrical measurements. Further evidence comes from the demonstrated equivalence of the static bulk magnetic and electrical properties of magnetic semiconductors grown by the conventional LT-MBE and II-PLM methods. The main findings of this work are intrinsic materials properties and are not artifacts of alternate materials synthesis.

Building upon previous research, the results of this dissertation have conclusively established the carrier-mediated nature of ferromagnetic exchange in $Ga_{1-x}Mn_xP$. Films of $Ga_{1-x}Mn_xP$ with systematically varying *x* and compensation (through S co-doping) exhibit the expected T_C scaling behavior; T_C increases (decreases) monotonically with increasing Mn_{Ga} (S) concentration. XMCD spectroscopy proves unambiguously that Mn_{Ga} atoms in a local environment similar to those in $Ga_{1-x}Mn_xAs$ are the source of ferromagnetism in $Ga_{1-x}Mn_xP$. Finally, the magnetic anisotropy of $Ga_{1-x}Mn_xP$ is dominated by contributions due to the anisotropic hole dispersion and can be modulated with strain, compensation, and doping. The results in combination with previous photoconductivity and electrical transport studies demonstrate that $Ga_{1-x}Mn_xP$ is a ferromagnetic semiconductor in which exchange is mediated by *localized*, *impurity-band* holes. This provides an important model system for testing models of ferromagnetism, band structure and localization beyond $Ga_{1-x}Mn_xAs$.

Localization effects are also prominent in Mn-doped $GaAs_{1-y}P_y$ and $GaAs_{1-y}N_y$ ternary hosts even in the dilute limit. The introduction of additional scattering mechanisms, in this case alloy disorder, can be detrimental to T_C depending of the Mn_{Ga} concentration. The proposed path of moving towards room temperature ferromagnetism by increasing *p-d* exchange by tailoring the composition of the semiconductor host seems unlikely to yield the desired result unless *x* is increased at the same time. Extension of models of ferromagnetism based on itinerant holes to Mn-doped GaP, $GaAs_{1-y}P_y$, and $GaAs_{1-y}N_y$ is, therefore, not valid in its present form. Localization effects must be taken into account explicitly in models of ferromagnetism in order to accurately predict T_C and other figures of merit in $III_{1-x}Mn_xV$ materials as well as to provide suitable guidance for exploring new materials.

6.2 Future Work

While the II-PLM process successfully overcomes equilibrium solubility limits in Mn-doped III-V semiconductors, there is still room for improving the process. The greatly reduced retained dose relative to the implanted dose of Mn implies that the effective segregation coefficient, k', is less than 1 (Section 2.6). To increase k' one must increase the velocity of the liquid-solid interface. This can be done by using a laser pulse with shorter temporal duration since $v \propto \tau^{1/2}$ (Equation 10). Currently a collaboration is in progress with the Bhamba Atomic Research Center in India where the 3rd harmonic of a Q-switched Nd-YAG laser (fundamental λ=1064 nm) can be used to produce laser pulses on the order of 1 ns. However, moving to even shorter pulse lengths will result in a saturation of the liquid-solid interfacial velocity at the point where the characteristic length scale for laser heating moves from heat transfer to optical absorption limited. In this case the characteristic length scale is $1/\alpha$, where α is the linear absorption coefficient, and the velocity is no longer proportional to the pulse length. Furthermore, faster interfacial velocities can promote constitutional supercooling during regrowth resulting in cellular dopant distributions, which places an upper limit on k' **[74]**.

Though the static electrical and magnetic properties are similar between II-PLM and LT-MBE synthesized magnetic semiconductors, there is still a question as to what effect the non-uniform Mn distribution has locally on the magnetic properties. This can be probed using polarized neutron reflectometry, which can depth-resolve the magnetic profile of a material. Comparing the magnetization profile measured by this method and the Mn distribution as measured by SIMS can elucidate whether or not the magnetization scales with Mn concentration throughout the thickness of the film. It will be interesting to see if the effective magnetic field due to the region of maximum Mn concentration enhances magnetic ordering in regions of the sample with lower Mn concentration that would be nominally paramagnetic in analogy to the exchange biasing of ferromagnetic thin films. Preliminary measurements performed in collaboration with the NIST Center for Neutron Research indicate that a gradient in magnetic properties is visible in the neutron reflectometry measurements.

There is also a need for future work to confirm several of the assumptions of the VBAC model of the MIT in quaternary ferromagnetic semiconductors. One of the major assumptions that has been made in attributing the transport behavior to alloy disorder scattering is that the concentration of ferromagnetism-mediating holes is not altered by alloying the anion sublattice. Accurate measurement of the carrier concentration in $Ga_{1-x}Mn_xAs$ has been carried out by measuring at milliKelvin temperature in magnetic fields of over 20 Tesla **[67]**. Though difficult, similar experiments on the $Ga_{1-x}Mn_xAs_{1-y}P_y$ films to test the assumption that the carrier concentration of these films remains constant upon alloying. Another assumption of the model is that carriers are localized in a detached, Mn-derived impurity band. In order to confirm the presence of a Mn impurity band, it is worthwhile to perform far-infrared photoconductivity spectroscopy on $Ga_{1-x}Mn_xAs_{1-y}P_y$. Such measurements have been previously used in order to establish the presence of a Mn impurity band in $Ga_{1-x}Mn_xP$ for $x \leq 0.042$ **[95, 99]**.

Finally, it would be useful to see if recently developed theoretical models of insulating $Ga_{1-x}Mn_xAs$ can improve the understanding of $Ga_{1-x}Mn_xP$. These models have been shown to explain the onset of ferromagnetism in low Mn doping **[42]** as well as the orientation of the magnetic easy axis **[179]**. Since this dissertation has presented these types of experiments for $Ga_{1-x}Mn_xP$, it will be interesting to see what information can be gleaned from more-detailed modeling of the experimental results.

References

1. D. D. Awschalom and M. E. Flatte, Nat Phys **3**, 153 (2007).
2. S. A. Wolf, D. D. Awschalom, R. A. Buhrman, J. M. Daughton, S. von Molnar, M. L. Roukes, A. Y. Chtchelkanova, and D. M. Treger, Science **294**, 1488 (2001).
3. M. N. Baibich, J. M. Broto, A. Fert, F. N. Van Dau, F. Petroff, P. Etienne, G. Creuzet, A. Friederich, and J. Chazelas, Phys. Rev. Lett. **61**, 2472 (1988).
4. J. Barnas, A. Fuss, R. E. Camley, P. Grünberg, and W. Zinn, Phys. Rev. B **42**, 8110 (1990).
5. M. E. Flatte, IEEE Transactions on Electronic Devices **54 (5)**, 907 (2007).
6. J. S. Moodera, L. R. Kinder, T. M. Wong, and R. Meservey, Phys. Rev. Lett. **74**, 3273 (1995).
7. I. Zutic, J. Fabian, and S. Das Sarma, Rev. Mod. Phys. **76**, 323 (2004).
8. S. Datta and B. Das, Appl. Phys. Lett. **56**, 665 (1990).
9. A. Fert and I. A. Campbell, Phys. Rev. Lett. **21**, 1190 (1968).
10. E. I. Rashba, Phys. Rev. B **62**, R16267 (2000).
11. P. C. van Son, H. van Kempen, and P. Wyder, Phys. Rev. Lett. **58**, 2271 (1987).
12. A. Fert and H. Jaffrès, Phys. Rev. B **64**, 184420 (2001).
13. H. Ohno, Science **281**, 951 (1998).
14. S. A. Chambers, Surf. Sci. Rep. **61**, 345 (2006).
15. J. K. Furdyna, J. Appl. Phys. **64**, R29 (1988).
16. D. Bougeard, S. Ahlers, A. Trampert, N. Sircar, and G. Abstreiter, Phys. Rev. Lett. **97** (2006).
17. T. Dietl, J. Konig, and A. H. MacDonald, Phys. Rev. B **64**, 241201(R) (2001).
18. T. Jungwirth, J. Sinova, J. Masek, J. Kucera, and A. H. MacDonald, Rev. Mod. Phys. **78**, 809 (2006).
19. T. Dietl, H. Ohno, and F. Matsukura, Phys. Rev. B **63**, 195205 (2001).
20. K. W. Edmonds, N. R. S. Farley, T. K. Johal, G. van der Laan, R. P. Campion, B. L. Gallagher, and C. T. Foxon, Phys. Rev. B **71**, 064418 (2005).
21. S. J. Potashnik, K. C. Ku, R. Mahendiran, S. H. Chun, R. F. Wang, N. Samarth, and P. Schiffer, Phys. Rev. B **66**, 012408 (2002).
22. D. Chiba, M. Yamanouchi, F. Matsukura, and H. Ohno, Science **301**, 943 (2003).
23. H. Ohno, D. Chiba, F. Matsukura, T. Omiya, E. Abe, T. Dietl, Y. Ohno, and K. Ohtani, Nature **408**, 944 (2000).
24. M. Yamanouchi, D. Chiba, F. Matsukura, and H. Ohno, Nature **428**, 539 (2004).
25. S. Koshihara, A. Oiwa, M. Hirasawa, S. Katsumoto, Y. Iye, C. Urano, H. Takagi, and H. Munekata, Phys. Rev. Lett. **78**, 4617 (1997).
26. T. Slupinski, H. Munekata, and A. Oiwa, Appl. Phys. Lett. **80**, 1592 (2002).
27. M. Sawicki, D. Chiba, A. Korbecka, Y. Nishitani, J. A. Majewski, F. Matsukura, T. Dietl, and H. Ohno, Nat Phys **6**, 22 (2010).
28. J.-M. Tang and M. E. Flatté, Phys. Rev. Lett. **92**, 047201 (2004).
29. A. Kaminski and S. Das Sarma, Phys. Rev. Lett. **88** (2002).
30. J. A. Gaj, J. Ginter, and R. R. Galazka, Phys. Status Solidi B. **89**, 655 (1978).
31. T. Jungwirth, K. Y. Wang, J. Masek, K. W. Edmonds, J. Konig, J. Sinova, M. Polini, N. A. Goncharuk, A. H. MacDonald, M. Sawicki, A. W. Rushforth, R. P. Campion, L. X. Zhao, C. T. Foxon, and B. L. Gallagher, Phys. Rev. B **72**, 165204 (2005).

32. J. Okabayashi, A. Kimura, T. Mizokawa, A. Fujimori, T. Hayashi, and M. Tanaka, Phys. Rev. B **59**, R2486 (1999).
33. J. Okabayashi, A. Kimura, O. Rader, T. Mizokawa, A. Fujimori, T. Hayashi, and M. Tanaka, Phys. Rev. B **58**, R4211 (1998).
34. T. Jungwirth, J. Sinova, A. H. MacDonald, B. L. Gallagher, V. Novak, K. W. Edmonds, A. W. Rushforth, R. P. Campion, C. T. Foxon, L. Eaves, E. Olejnik, J. Masek, S. R. E. Yang, J. Wunderlich, C. Gould, L. W. Molenkamp, T. Dietl, and H. Ohno, Phys. Rev. B **76**, 125206 (2007).
35. T. Dietl, H. Ohno, F. Matsukura, J. Cibert, and D. Ferrand, Science **287**, 1019 (2000).
36. M. Abolfath, T. Jungwirth, J. Brum, and A. H. MacDonald, Phys. Rev. B **63**, 054418 (2001).
37. M. Glunk, J. Daeubler, L. Dreher, S. Schwaiger, W. Schoch, R. Sauer, W. Limmer, A. Brandlmaier, S. T. B. Goennenwein, C. Bihler, and M. S. Brandt, Phys. Rev. B **79**, 195206 (2009).
38. M. Sawicki, K.-Y. Wang, K. W. Edmonds, R. P. Campion, C. R. Staddon, N. R. S. Farley, C. T. Foxon, E. Papis, E. Kaminska, A. Piotrowska, T. Dietl, and B. L. Gallagher, Phys. Rev. B **71**, 121302(R) (2005).
39. K. S. Burch, D. B. Shrekenhamer, E. J. Singley, J. Stephens, B. L. Sheu, R. K. Kawakami, P. Schiffer, N. Samarth, D. D. Awschalom, and D. N. Basov, Phys. Rev. Lett. **97**, 087208 (2006).
40. L. P. Rokhinson, Y. Lyanda-Gellar, Z. Ge, S. Shen, X. Liu, M. Dobrowolska, and J. Furdyna, Phys. Rev. B **76**, 161201(R) (2007).
41. K. Ando, H. Saito, K. C. Agarwal, M. C. Debnath, and V. Zayets, Phys. Rev. Lett. **100** (2008).
42. B. L. Sheu, R. C. Myers, J. M. Tang, N. Samarth, D. D. Awschalom, P. Schiffer, and M. E. Flatte, Phys. Rev. Lett. **99**, 227205 (2007).
43. J.-M. Tang and M. E. Flatte, Phys. Rev. Lett. **101**, 157203 (2008).
44. K. Alberi, K. M. Yu, P. R. Stone, O. D. Dubon, W. Walukiewicz, T. Wojtowicz, X. Liu, and J. Furdyna, Phys. Rev. B **78**, 075201 (2008).
45. M. A. Mayer, P. R. Stone, N. Miller, H. M. Smith, O. D. Dubon, E. E. Haller, K. M. Yu, W. Walukiewicz, X. Liu, and J. K. Furdyna, Phys. Rev. B **81**, 045205 (2010).
46. H. Munekata, H. Ohno, S. von Molnar, A. Segmüller, L. L. Chang, and L. Esaki, Phys. Rev. Lett. **63**, 1849 (1989).
47. H. Munekata, A. Zaslavsky, P. Fumagalli, and R. J. Gambino, Appl. Phys. Lett. **63**, 2929 (1993).
48. H. Ohno, H. Munekata, T. Penney, S. von Molnár, and L. L. Chang, Phys. Rev. Lett. **68**, 2664 (1992).
49. F. Matsukura, E. Abe, and H. Ohno, J. Appl. Phys. **87**, 6442 (2000).
50. T. Wojtowicz, G. Cywinski, W. L. Lim, X. Liu, M. Dobrowolska, J. K. Furdyna, K. M. Yu, W. Walukiewicz, G. B. Kim, M. Cheon, X. Chen, S. M. Wang, and H. Luo, Appl. Phys. Lett. **82**, 4310 (2003).
51. B. Clerjaud, J. Phys. C Solid State **18**, 3615 (1985).
52. M. Linnarsson, E. Janzen, B. Monemar, M. Kleverman, and A. Thilderkvist, Phys. Rev. B **55**, 6938 (1997).
53. T. Dietl, Semicond. Sci. Tech. **17**, 377 (2002).
54. J. Masek, J. Kudrnovsky, F. Maca, J. Sinova, A. H. MacDonald, R. P. Campion, B. L. Gallagher, and T. Jungwirth, Phys. Rev. B **75**, 045202 (2007).

55. L. Chen, S. Yan, P. F. Xu, J. Lu, W. Z. Wang, J. J. Deng, X. Qian, Y. Ji, and J. H. Zhao, Appl. Phys. Lett. **95**, 182505 (2009).
56. V. Novák, K. Olejník, J. Wunderlich, M. Cukr, K. Výborný, A. W. Rushforth, K. W. Edmonds, R. P. Campion, B. L. Gallagher, J. Sinova, and T. Jungwirth, Phys. Rev. Lett. **101**, 077201 (2008).
57. M. Wang, R. P. Campion, A. W. Rushforth, K. W. Edmonds, C. T. Foxon, and B. L. Gallagher, Appl. Phys. Lett. **93**, 132103 (2008).
58. K. Y. Wang, R. P. Campion, K. W. Edmonds, M. Sawicki, T. Dietl, and C. T. Foxon, in *Proceedings of the 27th International Conference on the Physics of Semiconductors*, edited by J. Menendez and C. G. V. d. Walle (Springer, New York, 2005), p. 333.
59. S. Mack, R. C. Myers, J. T. Heron, A. C. Gossard, and D. D. Awschalom, Appl. Phys. Lett. **92**, 192502 (2008).
60. O. Shinobu, O. Kenichi, and T. Masaaki, Appl. Phys. Lett. **90**, 112503 (2007).
61. D. Chiba, Y. Nishitani, F. Matsukura, and H. Ohno, Appl. Phys. Lett. **90**, 122503 (2007).
62. S. A. Abagyan, G. A. Ivanov, G. A. Koroleva, Y. N. Kuznetsov, and Y. A. Okunev, Sov. Phys. Semicond. **9**, 243 (1975).
63. O. Madelung, *Semiconductors - Basic Data, 2nd Ed.* (Springer, Berlin, 1996).
64. H. Ohno, A. Shen, F. Matsukura, A. Oiwa, A. Endo, S. Katsumoto, and Y. Iye, Appl. Phys. Lett. **69**, 363 (1996).
65. E. E. Haller, *Semiconductor Materials: Lecture Notes for MSE223* ((Berkeley, CA, 2005).
66. E. C. Larkins and J. S. Harris, in *Molecular Beam Epitaxy Applications to Key Materials*, edited by R. F. C. Farrow (Noyes, Park Ridge, NJ, 1995).
67. H. Ohno, J. Magn. Magn. Mater. **200**, 110 (1999).
68. R. P. Campion, K. W. Edmonds, L. X. Zhao, K. Y. Wang, C. T. Foxon, B. L. Gallagher, and C. R. Staddon, J. Cryst. Growth **247**, 42 (2003).
69. S. J. Potashnik, K. C. Ku, S. H. Chun, J. J. Berry, N. Samarth, and P. Schiffer, Appl. Phys. Lett. **79**, 1495 (2001).
70. K. M. Yu, W. Walukiewicz, T. Wojtowicz, I. Kuryliszyn, X. Liu, Y. Sasaki, and J. K. Furdyna, Phys. Rev. B **65**, 201303 (2002).
71. K. W. Edmonds, P. BogusÅ‚awski, K. Y. Wang, R. P. Campion, S. N. Novikov, N. R. S. Farley, B. L. Gallagher, C. T. Foxon, M. Sawicki, T. Dietl, M. Buongiorno Nardelli, and J. Bernholc, Phys. Rev. Lett. **92**, 037201 (2004).
72. D. E. Bliss, W. Walukiewicz, I. J. W. Ager, E. E. Haller, K. T. Chan, and S. Tanigawa, J. Appl. Phys. **71**, 1699 (1992).
73. M. A. Scarpulla, Ph.D. Thesis.University of California, Berkeley, (2006).
74. C. W. White, B. R. Appleton, and S. R. Wilson, in *Laser Annealing of Semiconductors*, edited by J. M. Poate and J. W. Mayer (Academic Press, New York, 1982).
75. O. D. Dubon, M. A. Scarpulla, R. Farshchi, and K. M. Yu, Physica B **376**, 630 (2006).
76. J. F. Ziegler, M. D. Ziegler, and J. P. Biersack, *SRIM-2008 v. 2008.04*. www.srim.org, 2008.
77. P. Baeri and S. U. Campisano, in *Laser Annealing of Semiconductors*, edited by J. M. Poate and J. W. Mayer (Academic Press, New York, 1982).
78. A. G. Cullis, in *Laser Annealing of Semiconductors*, edited by J. M. Poate and J. W. Mayer (Academic Press, New York, 1982).
79. J. M. Poate and J. W. Mayer, in *Laser Annealing of Semiconductors*, edited by J. M. Poate and J. W. Mayer (Academic Press, New York, 1982).
80. P. R. Stone, Masters Thesis.University of California, Berkeley, (2008).

81. *Landolt-Bornstein - Group III Condensed Matter* (Springer-Verlag, Berlin, 2002).
82. N. N. Sirota and A. A. Sidorov, Doklady Akademii Nauk SSSR **303**, 1123 (1988).
83. J. S. Blakemore, J. Appl. Phys. **53**, R123 (1982).
84. C. J. Glassbrenner and G. A. Slack, Phys. Rev. **134**, A1058 (1964).
85. A. S. Okhotin, A. S. Pushkarskii, and V. V. Gorbachev, *Thermophysical Properties of Semiconductors* ("Atom" Publ. House, Moscow, 1972).
86. J. A. Burton, R. C. Prim, and W. P. Slichter, J. Chem. Phys. **21**, 1987 (1953).
87. E. E. Haller, Personal Communication. March 22, 2007.
88. M. A. Scarpulla, U. Daud, K. M. Yu, O. Monteiro, Z. Liliental-Weber, D. Zakharov, W. Walukiewicz, and O. D. Dubon, Physica B **340**, 908 (2003).
89. M. A. Scarpulla, O. D. Dubon, O. Montiero, M. R. Pillai, M. J. Aziz, and M. C. Ridgway, Appl. Phys. Lett. **82**, 1251 (2003).
90. M. A. Scarpulla, R. Farshchi, P. R. Stone, R. V. Chopdekar, K. M. Yu, Y. Suzuki, and O. D. Dubon, J. Appl. Phys. **103**, 073913 (2008).
91. M. E. Overberg, B. P. Gila, C. R. Abernathy, S. J. Pearton, N. A. Theodoropoulou, K. T. McCarthy, S. B. Arnason, and A. F. Hebard, Appl. Phys. Lett. **79**, 3128 (2001).
92. M. E. Overberg, B. P. Gila, G. T. Thaler, C. R. Abernathy, S. J. Pearton, N. A. Theodoropoulou, K. T. McCarthy, S. B. Arnason, A. F. Hebard, S. N. G. Chu, R. G. Wilson, J. M. Zavada, and Y. D. Park, J. Vac. Sci. Technol. **20**, 969 (2002).
93. N. Theodoropoulou, A. F. Hebard, M. E. Overberg, C. R. Abernathy, S. J. Pearton, S. N. G. Chu, and R. G. Wilson, Phys. Rev. Lett. **89**, 107203 (2002).
94. N. Theodoropoulou, A. F. Hebard, S. N. G. Chu, M. E. Overberg, C. R. Abernathy, S. J. Pearton, R. G. Wilson, and J. M. Zavada, (AIP, 2002), Vol. 91, p. 7499.
95. R. Farshchi, M. A. Scarpulla, P. R. Stone, K. M. Yu, I. D. Sharp, J. W. Beeman, H. H. Silvestri, L. A. Reichert, E. E. Haller, and O. D. Dubon, Solid State Commun. **140**, 443 (2006).
96. J. Shi, J. M. Kikkawa, D. D. Awschalom, G. Medeiros-Ribeiro, P. M. Petroff, and K. Babcock, J. Appl. Phys. **79**, 5296 (1996).
97. E. E. Huber, Jr. and D. H. Ridgley, J. Appl. Phys. **34**, 1099 (1963).
98. I. Tsuboya and M. Sugihara, Journal of the Physical Society of Japan **18**, 143 (1963).
99. M. A. Scarpulla, B. L. Cardozo, R. Farshchi, W. M. Hlaing Oo, M. D. McCluskey, K. M. Yu, and O. D. Dubon, Phys. Rev. Lett. **95**, 207204 (2005).
100. P. R. Stone, C. Bihler, M. Kraus, M. A. Scarpulla, J. W. Beeman, K. M. Yu, M. S. Brandt, and O. D. Dubon, Phys. Rev. B **78**, 214421 (2008).
101. P. R. Stone, M. A. Scarpulla, R. Farshchi, I. D. Sharp, J. W. Beeman, K. M. Yu, E. Arenholz, J. Denlinger, E. E. Haller, and O. D. Dubon, in *Proceedings of the 28th International Conference on the Physics of Semiconductors*, edited by W. Jantsch and F. Schäffler (Springer, New York, 2007), p. 1177.
102. G. Vanderlaan and B. T. Thole, Phys. Rev. B **43**, 13401 (1991).
103. E. Arenholz and S. O. Prestemon, Rev. Sci. Instrum. **76** (2005).
104. Y. U. Idzerda, C. T. Chen, H. J. Lin, G. Meigs, G. H. Ho, and C. C. Kao, Nucl. Instrum. Meth. A **347**, 134 (1994).
105. Y. Ishiwata, M. Watanabe, R. Eguchi, T. Takeuchi, Y. Harada, A. Chainani, S. Shin, T. Hayashi, Y. Hashimoto, S. Katsumoto, and Y. Iye, Phys. Rev. B **65** (2002).
106. H. Ohldag, V. Solinus, F. U. Hillebrecht, J. B. Goedkoop, M. Finazzi, F. Matsukura, and H. Ohno, Appl. Phys. Lett. **76**, 2928 (2000).

107. K. W. Edmonds, N. R. S. Farley, R. P. Campion, C. T. Foxon, B. L. Gallagher, T. K. Johal, G. van der Laan, M. MacKenzie, J. N. Chapman, and E. Arenholz, Appl. Phys. Lett. **84**, 4065 (2004).
108. R. Nakajima, J. Stöhr, and Y. U. Idzerda, Phys. Rev. B **59**, 6421 (1999).
109. R. Nakajima, PhD Thesis.Stanford University, (1998).
110. P. Mahadevan and A. Zunger, Appl. Phys. Lett. **85**, 2860 (2004).
111. T. Graf, S. T. B. Goennenwein, and M. S. Brandt, Phys. Status Solidi B. **239**, 277 (2003).
112. T. C. Schulthess, W. M. Temmerman, Z. Szotek, W. H. Butler, and G. M. Stocks, Nat. Mater. **4**, 838 (2005).
113. E. Sarigiannidou, F. Wilhelm, E. Monroy, R. M. Galera, E. Bellet-Amalric, A. Rogalev, J. Goulon, J. Cibert, and H. Mariette, Phys. Rev. B **74**, 041306(R) (2006).
114. A. A. Freeman, K. W. Edmonds, N. R. S. Farley, S. V. Novikov, R. P. Campion, C. T. Foxon, B. L. Gallagher, E. Sarigiannidou, and G. van der Laan, Phys. Rev. B **76**, 081201 (2007).
115. B. I. Shklovskii and A. L. Efros, *Electronic Properties of Doped Semiconductors* (Springer, Berlin, 1984).
116. K. W. Edmonds, S. V. Novikov, M. Sawicki, R. P. Campion, C. R. Staddon, A. D. Giddings, L. X. Zhao, K. Y. Wang, T. Dietl, C. T. Foxon, and B. L. Gallagher, Appl. Phys. Lett. **86**, 152114 (2005).
117. S. Sonoda, S. Shimizu, T. Sasaki, Y. Yamamoto, and H. Hori, J. Cryst. Growth **237-239**, 1358 (2002).
118. A. H. Macdonald, P. Schiffer, and N. Samarth, Nat. Mater. **4**, 195 (2005).
119. C. Bihler, M. Kraus, H. Huebl, M. S. Brandt, S. T. B. Goennenwein, M. Opel, M. A. Scarpulla, P. R. Stone, R. Farshchi, and O. D. Dubon, Phys. Rev. B **75**, 214419 (2007).
120. W. Shan, W. Walukiewicz, J. W. Ager, E. E. Haller, J. F. Geisz, D. J. Friedman, J. M. Olson, and S. R. Kurtz, Phys. Rev. Lett. **82**, 1221 (1999).
121. K. M. Yu, W. Walukiewicz, M. A. Scarpulla, O. D. Dubon, J. Wu, J. Jasinski, Z. Liliental-Weber, J. W. Beeman, M. R. Pillai, and M. J. Aziz, J. Appl. Phys. **94**, 1043 (2003).
122. F. Matsukura, H. Ohno, A. Shen, and Y. Sugawara, Phys. Rev. B **57**, R2037 (1998).
123. R. Kling, A. Koder, W. Schoch, S. Frank, M. Oettinger, W. Limmer, R. Sauer, and A. Waag, Solid State Commun. **124**, 207 (2002).
124. G. Kobayashi, T. Mori, T. Kato, T. Hanada, H. Makino, and T. Yao, J. Cryst. Growth **301**, 642 (2007).
125. I. Oshiyama, T. Kondo, and H. Munekata, J. Appl. Phys. **98**, 093906 (2005).
126. W. Pacuski, P. Kossacki, D. Ferrand, A. Golnik, J. Cibert, M. Wegscheider, A. Navarro-Quezada, A. Bonanni, M. Kiecana, M. Sawicki, and T. Dietl, Phys. Rev. Lett. **100**, 037204 (2008).
127. K. Alberi, Ph.D. Thesis.University of California, Berkeley, (2008).
128. K. Alberi, J. Wu, W. Walukiewicz, K. M. Yu, O. D. Dubon, S. P. Watkins, C. X. Wang, X. Liu, Y. J. Cho, and J. Furdyna, Phys. Rev. B **75**, 045203 (2007).
129. J. W. Harrison and J. R. Hauser, Phys. Rev. B **13**, 5347 (1976).
130. T. Dietl, in *Handbook on Semiconductors*, edited by S. Mahajan (Elsevier, Amsterdam, 1994), Vol. 3.
131. J. Okabayashi, A. Kimura, O. Rader, T. Mizokawa, A. Fujimori, T. Hayashi, and M. Tanaka, Phys. Rev. B **64**, 125304 (2001).
132. P. R. Stone, J. W. Beeman, K. M. Yu, and O. D. Dubon, Physica B **401-402**, 454 (2007).

133. S. Das Sarma, E. H. Hwang, and D. J. Priour, Phys. Rev. B **70**, 161203(R) (2004).
134. A. Lemaître, A. Miard, L. Travers, O. Mauguin, L. Largeau, C. Gourdon, V. Jeudy, M. Tran, and J.-M. George, Appl. Phys. Lett. **93**, 021123 (2008).
135. A. W. Rushforth, M. Wang, N. R. S. Farley, R. P. Campion, K. W. Edmonds, C. R. Staddon, C. T. Foxon, and B. L. Gallagher, J. Appl. Phys. **104**, 073908 (2008).
136. M. Cubukcu, H. J. von Bardeleben, K. Khazen, J. L. Cantin, O. Mauguin, L. Largeau, and A. Lemaître, Phys. Rev. B **81**, 041202 (2010).
137. M. Cubukcu, H. J. Von Bardeleben, K. Khazen, J. L. Cantin, O. Mauguin, L. Largeau, and A. Lemaitre, in *11th Joint MMM-Intermag Conference*, Washington, DC, 2010).
138. S. Chikazumi, *Physics of Magnetism* (John Wiley and Sons, Inc., New York, 1964).
139. N. Spaldin, *Magnetic Materials: Fundamentals and Device Applications* (Cambridge University Press, Cambridge, 2003).
140. B. D. Cullity, *Introduction to Magnetic Materials* (John Wiley & Sons, Hoboken, NJ, 2009).
141. C. Gould, K. Pappert, G. Schmidt, and L. W. Molenkamp, Advanced Materials **19**, 323 (2007).
142. X. Liu, W. L. Lim, Z. Ge, S. Shen, M. Dobrowolska, J. K. Furdyna, T. Wojtowicz, K. M. Yu, and W. Walukiewicz, Appl. Phys. Lett. **86**, 112512 (2005).
143. X. Liu, Y. Sasaki, and J. K. Furdyna, Phys. Rev. B **67**, 205204 (2003).
144. A. Shen, H. Ohno, F. Matsukura, Y. Sugawara, N. Akiba, T. Kuroiwa, A. Oiwa, A. Endo, S. Katsumoto, and Y. Iye, J. Cryst. Growth **175/176**, 1069 (1997).
145. M. Sawicki, F. Matsukura, T. Dietl, G. M. Schott, C. Ruester, G. Schmidt, L. W. Molenkamp, and G. Karczewski, J. Supercond. **16**, 7 (2003).
146. M. Sawicki, F. Matsukura, A. Idziaszek, T. Dietl, G. M. Schott, C. Ruester, C. Gould, G. Karczewski, G. Schmidt, and L. W. Molenkamp, Phys. Rev. B **70**, 245325 (2004).
147. U. Welp, V. K. Vlasko-Vlasov, X. Liu, J. K. Furdyna, and T. Wojtowicz, Phys. Rev. Lett. **90**, 167206 (2003).
148. U. Welp, V. K. Vlasko-Vlasov, A. Menzel, H. D. You, X. Liu, J. K. Furdyna, and T. Wojtowicz, Appl. Phys. Lett. **85**, 260 (2004).
149. K. Y. Wang, M. Sawicki, K. W. Edmonds, R. P. Campion, S. Maat, C. T. Foxon, B. L. Gallagher, and T. Dietl, Phys. Rev. Lett. **95**, 217204 (2005).
150. P. T. Chiu, S. J. May, and B. W. Wessels, J. Appl. Phys. **99**, 083907 (2006).
151. L. V. Titova, M. Kutrowski, X. Liu, R. Chakarvorty, W. L. Lim, T. Wojtowicz, J. K. Furdyna, and M. Dobrowolska, Phys. Rev. B **72**, 165205 (2005).
152. O. M. Fedorych, E. M. Hankiewicz, Z. Wilamowski, and J. Sadowski, Phys. Rev. B **66**, 045201 (2002).
153. P. R. Stone, K. Alberi, S. K. Z. Tardif, J. W. Beeman, K. M. Yu, W. Walukiewicz, and O. D. Dubon, Phys. Rev. Lett. **101**, 087203 (2008).
154. Y. J. Cho, M. A. Scarpulla, Y. Y. Zhou, Z. Ge, X. Liu, M. Dobrowolska, K. M. Yu, O. D. Dubon, and J. K. Furdyna, J. Appl. Phys. **104** (2008).
155. Y. Y. Zhou, X. Liu, J. K. Furdyna, M. A. Scarpulla, and O. D. Dubon, Physical Review B (Condensed Matter and Materials Physics) **80**, 224403 (2009).
156. D. Hrabovsky, E. Vanelle, A. R. Fert, D. S. Yee, J. P. Redoules, J. Sadowski, J. Kanski, and L. Ilver, Appl. Phys. Lett. **81**, 2806 (2002).
157. C. Bihler, H. Huebl, M. S. Brandt, S. T. B. Goennenwein, M. Reinwald, U. Wurstbauer, M. Doppe, D. Weiss, and W. Wegscheider, Appl. Phys. Lett. **89**, 012507 (2006).

158. W. Limmer, M. Glunk, J. Daeubler, T. Hummel, W. Schoch, R. Sauer, C. Bihler, H. Huebl, M. S. Brandt, and S. T. B. Goennenwein, Phys. Rev. B **74**, 205205 (2006).
159. M. Kraus, Diploma Thesis.Technische Universität München, (2006).
160. S. T. B. Goennenwein, T. Graf, T. Wassner, M. S. Brandt, M. Stutzmann, J. B. Philipp, R. Gross, M. Krieger, K. Zurn, P. Ziemann, A. Koeder, S. Frank, W. Schoch, and A. Waag, Appl. Phys. Lett. **82**, 730 (2003).
161. S. Evans, Surf. Interface Anal. **17**, 85 (1991).
162. Y. K. Yogurtçu, A. J. Miller, and G. A. Saunders, Journal of Physics and Chemistry of Solids **42**, 49 (1981).
163. C. Bihler, W. Schoch, W. Limmer, S. T. B. Goennenwein, and M. S. Brandt, Phys. Rev. B **79**, 045205 (2009).
164. J. Kim, D. Y. Shin, S. Lee, X. Liu, and J. K. Furdyna, Phys. Rev. B **78**, 075309 (2008).
165. X. Liu, W. L. Lim, L. V. Titova, M. Dobrowolska, J. K. Furdyna, M. Kutrowski, and T. Wojtowicz, J. Appl. Phys. **98**, 063904 (2005).
166. C. Kittel, *Introduction to Solid State Physics* (John Wiley and Sons, Inc., Singapore, 2005).
167. C. Gourdon, A. Dourlat, V. Jeudy, K. Khazen, H. J. von Bardeleben, L. Thevenard, and A. Lemaître, Phys. Rev. B **76**, 241301 (2007).
168. A. Dourlat, V. Jeudy, A. Lemaître, and C. Gourdon, Phys. Rev. B **78**, 161303 (2008).
169. A. Dourlat, V. Jeudy, C. Testelin, F. Bernardot, K. Khazen, C. Gourdon, L. Thevenard, L. Largeau, O. Mauguin, and A. Lemaître, J. Appl. Phys. **102**, 023913 (2007).
170. M. A. Scarpulla, U. Daud, K. M. Yu, O. Montiero, Z. Liliental-Weber, D. Zakharov, W. Walukiewicz, and O. D. Dubon, Physica B **340**, 908 (2003).
171. V. Gottschalch, W. Heinig, E. Butter, H. Rosin, and G. Freydank, Krist. Tech. **14**, 563 (1979).
172. G. Nolze, V. Geist, G. Wagner, P. Paufler, and K. Jurkschat, Z. Kristallogr. **193**, 111 (1990).
173. R. S. Title, Appl. Phys. Lett. **14**, 76 (1969).
174. J. Szczytko, A. Twardowski, K. Swiatek, M. Palczewska, M. Tanaka, T. Hayashi, and K. Ando, Phys. Rev. B **60**, 8304 (1999).
175. N. M. Reinacher, M. S. Brandt, and M. Stutzmann, J. Appl. Phys. **80**, 4541 (1996).
176. R. S. Title, Phys. Rev. **154**, 668 (1967).
177. M. A. Scarpulla, P. R. Stone, I. D. Sharp, E. E. Haller, O. D. Dubon, J. W. Beeman, and K. M. Yu, J. Appl. Phys. **103**, 123906 (2008).
178. D. Ruzmetov, J. Scherschligt, D. V. Baxter, T. Wojtowicz, X. Liu, Y. Sasaki, J. K. Furdyna, K. M. Yu, and W. Walukiewicz, Phys. Rev. B **69**, 155207 (2004).
179. D. Kitchen, A. Richardella, J. M. Tang, M. E. Flatte, and A. Yazdani, Nature **442**, 436 (2006).
180. B. Schmid, R. Huber, and R. A. Kaindl, Personal Communication.
181. B. D. Cuillity, *Elements of X-ray Diffraction* (Addison-Wesley Publishing Co., Reading, Mass., 1978).
182. R. Feynman, R. B. Leighton, and M. L. Sands, (Addison-Wesley, Reading, Massachusetts, 1963).
183. J. Stohr, J. Electron Spectrosc. **75**, 253 (1995).
184. J. Stohr, J. Magn. Magn. Mater. **200**, 470 (1999).
185. J. Stohr and R. Nakajima, IBM J. Res. Dev. **42**, 73 (1998).

186. J. Stohr, H. A. Padmore, S. Anders, T. Stammler, and M. R. Scheinfein, Surf. Rev. Lett. **5**, 1297 (1998).
187. J. Stohr and Y. Wu, in *New Directions in Research with Third-Generation Soft X-ray Synchrotron Radiation Sources*, edited by A. S. Schlachter and F. J. Wuilleumier (Kluwer, London, 1994), Vol. 254.
188. J. Stohr, *NEXAFS Spectroscopy* (Springer, Heidelberg, 1992).
189. E. W. Weisstein, in *Mathworld -- A Wolfram Web Resource* (Wolfram Research, Vol. 2007.
190. H. A. Bethe and E. E. Salpeter, *Quantum Mechanics of One- and Two-Electron Atoms* (Academic Press, Inc., New York, 1957).

Appendix A: Ion Beam Analysis of $III_{1\text{-}x}Mn_xV$ Materials

The lattice location and total quantity of Mn atoms in $III_{1\text{-}x}Mn_xV$ materials can be determined by ion beam analysis techniques. In these measurements a sample is exposed to a 1.95 MeV $^4He^+$ ion beam. When the high energy $^4He^+$ ions encounter an atom in the sample the ion is elastically scattered. An energy detector can be placed in a backscattered geometry and detect those $^4He^+$ ions that are scattered through an angle of 180º, which is known as Rutherford backscattering spectrometry (RBS). The scattering event is modeled as a classic billiard ball, binary collision. The energy of the $^4He^+$ ion after the collision depends both on the mass of the other atom involved in the collision and the angle θ by which it is scattered. From conservation of energy and momentum one can derive the kinematic factor for the collision, which is the fraction of the original energy that the $^4He^+$ ion maintains after the scattering event

$$K = \left[\frac{\sqrt{m_2^2 - m_1^2 \sin^2\theta} + m_1 \cos\theta}{m_1 + m_2}\right]^2 \tag{A.1}$$

where m_1 is the mass of the incident projectile, and m_2 is the mass of the target atom. For the backscattered geometry θ=180º, and the kinematic factor depends only on the ratio of the mass of the target atom to that of the incident ion

$$K = \left[\frac{\frac{m_2}{m_1} - 1}{\frac{m_2}{m_1} + 1}\right]^2 . \tag{A.2}$$

Equation A.2 indicates that heavier atoms have larger K than lighter atoms for a given m_1. The kinematic factors for several elements relevant to this work are given in Table 9 for m_1=4. The energy of the detected ions also depends on the depth from which they are scattered. As the $^4He^+$ particles move through the solid they lose energy primarily due to electronic stopping. The deeper in the film that a nuclear collision occurs, the lower in energy the backscattered particle will appear since it will have lost energy due to electronic interactions over a length scale of approximately two times the depth at which the collision occurs. Therefore, it is possible for one to obtain depth-resolved, element specific information from an RBS measurement. The energy of a 1.95 MeV $^4He^+$ particle backscattered from a surface atom is shown in the last column of Table 9.

Further information can be obtained by orienting the ion beam such that it is incident ion is parallel to a channel in the target's crystal structure. If the material is a high-quality single crystal then the backscattered yield should be significantly reduced in channeled geometries since the channels are free of atoms. By comparing the channeled backscattered yield to the yield in a "random" geometry (one not intentionally aligned to open channels) one can quantify the quality of the sample by its χ_{min} value,

Table 9: Kinematic factors for several elements based on a binary collision with a $^4He^+$ ion. Masses are naturally occurring isotopic averages

Element	m_2 (amu)	K	*$^4He^+$ Energy From Surface Atom and Beam Energy of 1.95 MeV*
P	30.974	0.5948	1.160
Mn	54.938	0.7470	1.457
Ga	69.723	0.7947	1.550
As	74.922	0.8075	1.556

$$\chi_{min} = \frac{Y_{channeled}}{Y_{random}} \tag{A.3}$$

where Y stands for the total backscattered yield. A smaller value of χ_{min} reflects higher crystalline quality. The minimum value of χ_{min} is usually around 0.02-0.05 since there is a finite probability that the incident ions will collide with atoms at the sample surface due to their finite scattering radius.

With the basic theory and definitions defined, the rest of this appendix is devoted to an example of how one uses the ion-beam technique to determine the value of x for a $\mathrm{III}_{1-x}\mathrm{Mn}_x\mathrm{V}$ material. Here, the $\mathrm{Ga}_{1-x}\mathrm{Mn}_x\mathrm{P}$ system is used as an example, though similar principles apply to the analysis of $\mathrm{Ga}_{1-x}\mathrm{Mn}_x\mathrm{As}$ as well as the quaternary alloys discussed in Chapter 4. Figure 57 (a) shows RBS results for a representative $\mathrm{Ga}_{1-x}\mathrm{Mn}_x\mathrm{P}$ sample with an implant dose of $1.5\mathrm{x}10^{16}$ $\mathrm{Mn}^{+}/\mathrm{cm}^{2}$ and laser processed at 0.4 $\mathrm{J/cm}^{2}$ for <011> and random orientations. The energy corresponding to scattering events from the sample surface are indicated by the arrows. The RBS spectrum is dominated by contributions from the Ga and P atoms since these are the majority species present in the sample. To obtain the value of χ_{min} the channeled and random spectra are integrated over the energy interval 1.479-1.535 MeV which corresponding to particles backscattered from Ga atoms to a thickness of ~100 nm, the approximate depth of the film. For this sample $\chi_{min} \approx 0.04$ indicating that the material is of high crystalline quality.

To quantify the lattice location of the Mn atoms, it is necessary to determine χ_{min} due to scattering events exclusively from Mn atoms. If the scattering in channels is larger for Mn atoms relative to Ga and P then some of the Mn atoms are incommensurate with the lattice since they are not being shadowed from the incident ion beam. In cases where the solute atom is lighter than an element in the host, it is necessary to use a different technique to detect the atomic collisions since the solute atom's RBS signal is overwhelmed by the host. Simultaneous to the RBS measurement one can measure the characteristic radiation emitted from the target atom during the collision, which is known as particle-induced X-ray emission (PIXE). Like RBS, PIXE can also be performed in channeling geometries. However, it is slightly less powerful than RBS because one loses the depth resolution inherent in an RBS measurement. Figure 57 (b) shows PIXE measurements in the channeling mode, in particular along the <011> and <111> axial channels as well as in a random orientation, which were measured at the same time as the RBS measurements in Figure 57 (a). The detected radiation corresponds to the Mn K_{α} and K_{β} emission lines. A couple of conclusions regarding the lattice location of the Mn atoms can be made based on the PIXE results. The reduced Mn X-ray signals for the <011> -and <111>-aligned spectra in comparison to the random spectrum indicate that a large fraction of the Mn atoms occupies commensurate lattice sites in the zincblende structure. The <011> and <111> scans are nearly identical. Any atoms occupying the interstitial sites in the zincblende lattice would be exposed in the <011> channels but not the <111> channels. Therefore, if an appreciable fraction of Mn were present at this interstitial site (as is the case for as-grown LT-MBE $\mathrm{Ga}_{1-x}\mathrm{Mn}_x\mathrm{As}$), one would expect a larger Mn PIXE signal for the <011> spectrum than the <111> spectrum **[70]**. As this is *not* the case, the presence of Mn occupying interstitial positions can be excluded in II-PLM $\mathrm{Ga}_{1-x}\mathrm{Mn}_x\mathrm{P}$. As was done for the analysis of RBS measurements one can similarly define a χ_{min} for the Mn atoms. For the Mn impurities χ_{min} comes from the ratio of the integrated intensities of the channeled and non-aligned PIXE signals and is equal to ~0.23 for the sample in Figure 57 (b). The fraction of Mn occupying substitutional sites (f_{sub}) is then determined from the following approximate formula

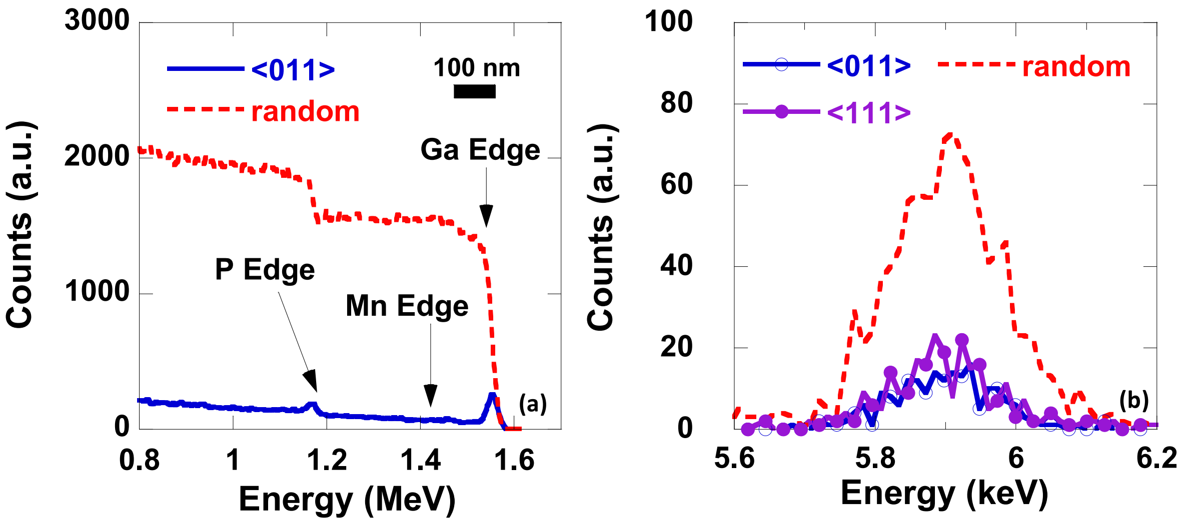

Figure 57: (a) Channeling RBS spectra for <110> channeling alignment and random alignment for a $Ga_{1-x}Mn_xP$ prepared by implanting $1.5x10^{16}$ 50 keV Mn^+ ions into GaP followed by PLM with a single 0.44 J/cm^2 laser pulse. (b) PIXE spectra of an identically prepared film with the ion beam in <110>, and <111> channeled alignment and random alignment.

$$f_{sub} = \frac{1-\chi_{min}^{impurity}}{1-\chi_{min}^{lattice}} \tag{A.4}$$

where the χ_{min} for the lattice has been determined above from the Ga RBS signals. Based on the χ_{min} values evaluated above f_{sub} for this sample is equal to ~0.8. This level of substitutional incorporation is similar to that observed in annealed $Ga_{1-x}Mn_xAs$ samples grown by LT-MBE. The location of the remaining ~20% of the Mn remains an open question. All that the ion channeling measurements can indicate is that they are incommensurate with the lattice- i.e. neither substitutional nor interstitial. One hypothesis is that they reside in small clusters too small to constitute a new phase since no evidence of 2nd phase formation is found in XRD, TEM or magnetic measurements **[73]**.

One final piece of information that can be obtained from the ion beam measurements is the concentration of Mn per unit area that is present in the film after processing, which is known as the retained dose, D_{Mn}. The retained dose is usually less than the implanted dose since not all of the implanted ions are incorporated during PLM (Section 2.6). The retained dose can be understood as the integrated concentration profile (see for example Figure 58). To obtain the retained dose the random PIXE yield at the Mn and Ga K_α edges for the sample of interest are measured and compared to a standard of known dose produced by ion implantation. The ratio of the integrated Mn K_α edge intensity to that of the Ga K_α edge provides a measure of the relative dose of the sample to that of the implant standard. The retained dose is used as the calibration standard for SIMS measurements.

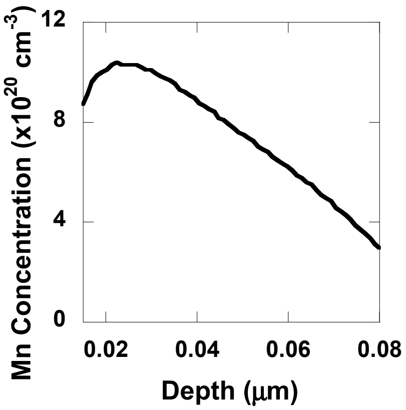

Figure 58: Total Mn concentration as a function of depth for a sample prepared identically to the one analyzed in Figure 57.

In order to calculate *x*, the peak Mn_{Ga} concentration, it is necessary to know the distribution of Mn atoms throughout the film, which is determined by secondary ion mass spectrometry (SIMS). Figure 58 shows a SIMS profile for a sample prepared identically to the one in which the ion beam analysis displayed in Figure 57 was done. The film is characterized by a Mn distribution that is approximately 100 nm in width and peaks ~20-30 nm from the film's surface, which is typical for most of the $Ga_{1-x}Mn_xP$ films that will be discussed. An inhomogeneous distribution of Mn is also present in $Ga_{1-x}Mn_xAs$ formed by II-PLM (Figure 10); nonetheless, good quantitative agreement is found between the ferromagnetic and transport properties of II-PLM grown $Ga_{1-x}Mn_xAs$ and LT-MBE formed materials (Section 2.6) **[73, 90]**. For the film in Figure 58 the maximum total Mn concentration is $1.04\text{x}10^{22}$ cm^{-3}, the Ga sublattice concentration in GaP is $2.47\text{x}10^{22}$ cm^{-3} and $f_{sub}\approx 80\%$ resulting in x=0.034 for this sample.

Appendix B: Supplemental Experimental Information for $Ga_{1-x}Mn_xP$

B.1. Materials Synthesis and Structural Properties of $Ga_{1-x}Mn_xP$

50 keV $^{55}Mn^+$ ions were implanted into (100)-oriented, *n*-type GaP substrates to doses ranging from $1.0\text{x}10^{15} - 2.0\text{x}10^{16}$ cm^{-2}. The wafers have sulfur background doping of 10^{16}-10^{17} cm^{-3} which is essential to junction isolate the *p*-type $Ga_{1-x}Mn_xP$ film for electrical transport measurements. After implantation, samples were irradiated with a single pulse from a KrF (λ=248 nm) excimer laser at a fluence of 0.44±0.05 J/cm^2. TEM analysis has shown that after the pulsed-laser melting step the $Ga_{1-x}Mn_xP$ films are single crystalline though the first ~25 nm from the surface are highly defective **[88]**. This poorly regrown layer is readily removed by etching in concentrated HCl for ~24 hours **[88, 99]**, resulting in epitaxial $Ga_{1-x}Mn_xP$ grown on GaP. The parameter x is defined as the peak Mn_{Ga} concentration and is determined from the combination of secondary ion mass spectrometry and ion-beam analysis (Appendix A).

Several parameters characterizing the distribution of Mn in a $Ga_{1-x}Mn_xP$ thin film are shown in Table 10 as a function of the nominal implanted Mn^+ dose. The data in Table 10 show that increasing the implantation dose results in an increase in x for Mn^+ implantation. The trend, however, is not linear. As the implant dose increases both the retained fraction of the implanted Mn dose and the Mn f_{sub} generally decrease. The combined effect of these two trends is to decrease the marginal utility of increasing the Mn^+ implant dose. The limiting step in increasing x in films formed by II-PLM is the ability of the growing film to incorporate increasing concentrations of Mn from the melt during PLM, not the Mn concentration in the melt itself. Further details of the interplay of Mn implantation dose, laser processing parameters, and the final Mn compositional parameters can be found in Chapter 2 and Ref. **[73]**.

Table 10: Dependence of the Mn retained dose, substitutional fraction and peak concentration on the implanted Mn dose.

Implanted Mn^+ Dose [cm^{-2}]	Retained Mn^+ Dose [cm^{-2}]	Retained Fraction	Mn f_{sub}	Peak in Mn Profile by SIMS[cm^{-3}]	x
$1.0\text{x}10^{15}$	$9.0\text{x}10^{14}$	0.90	0.80	$1.36\text{x}10^{20}$	0.0042
$2.5\text{x}10^{15}$	$1.6\text{x}10^{15}$	0.64	0.84	$2.59\text{x}10^{20}$	0.0088
$5.0\text{x}10^{15}$	$3.2\text{x}10^{15}$	0.64	0.84	$5.29\text{x}10^{20}$	0.018
$7.5\text{x}10^{15}$	$4.2\text{x}10^{15}$	0.56	0.88	$5.61\text{x}10^{20}$	0.020
$1.0\text{x}10^{15}$	$5.0\text{x}10^{15}$	0.50	0.85	$8.43\text{x}10^{20}$	0.029
$1.5\text{x}10^{16}$	$6.0\text{x}10^{15}$	0.40	0.80	$1.05\text{x}10^{21}$	0.034
$1.7\text{x}10^{16}$	$7.2\text{x}10^{15}$	0.42	0.71	$1.32\text{x}10^{21}$	0.038
$2.0\text{x}10^{16}$	$8.3\text{x}10^{15}$	0.42	0.70	$1.48\text{x}10^{21}$	0.042

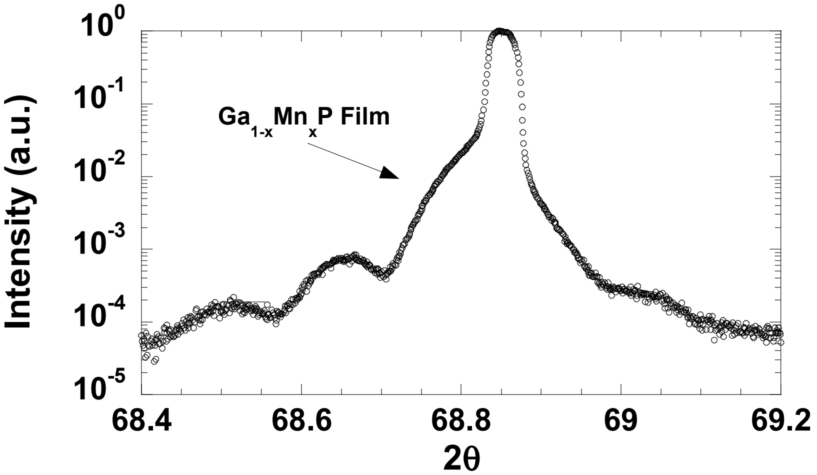

Figure 59: X-ray diffraction measurement about the (400) peak for $Ga_{0.966}Mn_{0.034}P$. The measurement was performed with Cu K_α radiation (λ=1.5405 Å).

Figure 59 shows an X-ray diffraction measurement on a $Ga_{1-x}Mn_xP$ film with x=0.034 around the (400) diffraction peak. The $Ga_{0.966}Mn_{0.034}P$ thin film gives rise to a broad feature at lower 2θ than the GaP substrate peak at 2θ=68.847°. This indicates that the film is under slight compressive strain, which is expected since the substitution of 3.4% Mn for the slightly smaller Ga atoms leads to an expansion of the lattice perpendicular to the growth direction. Asymmetric reciprocal space maps around the (511) peak indicate the $Ga_{0.966}Mn_{0.034}P$ thin film is pseudomorphic with respect to the underlying substrate (Section 5.6.1). The $Ga_{0.966}Mn_{0.034}P$ film gives rise to a shoulder in the diffraction pattern and not a distinct, well-resolved peak due in part to the non-uniform Mn distribution throughout the film thickness, which is inherent to II-PLM processing (Chapter 2 and Appendix A). The inhomogeneous Mn concentration as a function of depth causes a distribution of interplanar spacing parallel to the growth direction, which in turn affects the range of 2θ for which the diffraction condition is satisfied for a given X-ray wavelength. This hinders quantitative analysis of the X-ray diffraction pattern. In order to extract structural parameters such as the epitaxial strain, it is necessary to numerically fit a two-peak model to the X-ray diffraction measurement (Appendix C). Based on this model the strain in the growth direction $\varepsilon_\perp$=0.02201±0.01889%.

B.2. The Character of Holes in $Ga_{1-x}Mn_xP$

In Section 1.5 the effective ***k·p*** Hamiltonian theory adapted from the Zener kinetic-exchange model was discussed. Two major assumptions implicit in this mean-field approach are that the holes are itinerant and are well-described by the parameters of the host valence band, i.e. the carriers responsible for ferromagnetic exchange and charge transport are of valence band character. In this section, it will be shown that neither assumption is met by $Ga_{1-x}Mn_xP$, at least for $x\leq0.042$. Instead the carriers in $Ga_{1-x}Mn_xP$ are *localized* in a Mn-derived *impurity band.*

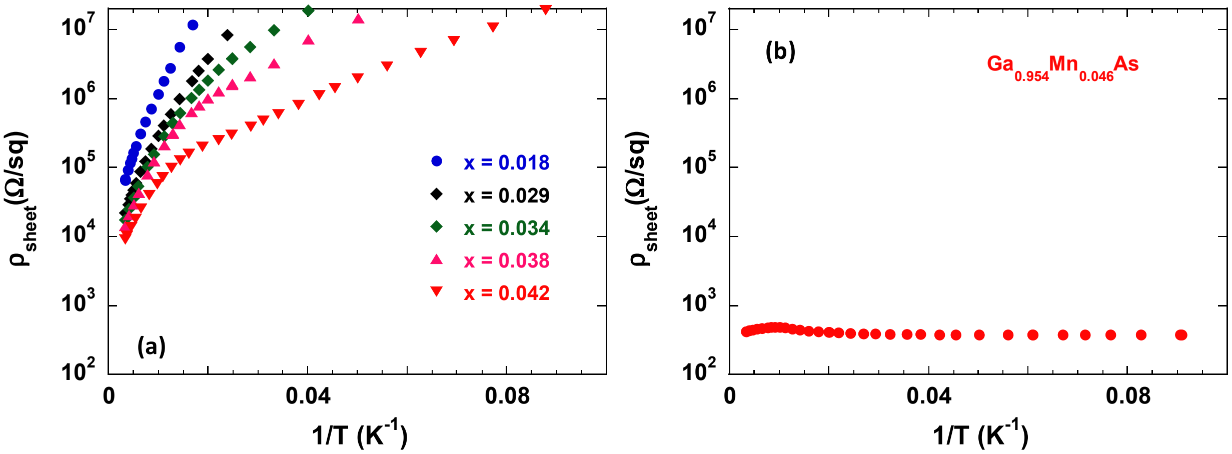

Figure 60: Sheet resistivity as a function of inverse temperature for (a) several $Ga_{1-x}Mn_xP$ films with varying Mn_{Ga} concentration. After [95]. (b) Temperature dependence of the sheet resistivity of $Ga_{0.954}Mn_{0.046}As$.

Figure 60(a) shows the temperature dependence of the sheet resistivity (ρ_{sheet}) for several $Ga_{1-x}Mn_xP$ samples with varying Mn_{Ga} concentration, x. $Ga_{1-x}Mn_xP$ is an electrical insulator up to at least x=0.042, which is the most heavily doped material produced to date. For comparison, the temperature-dependent sheet resistivity is shown on the same scale in Figure 60(b) for a $Ga_{1-x}Mn_xAs$ sample with similar Mn_{Ga} content (x=0.046). The magnitude of ρ_{sheet} is lower at all temperatures in the GaAs-based film. Furthermore, the low temperature resistivity tends towards a constant value, which is indicative of metallic transport by delocalized carriers. The slight peak observed at $1/T \approx 0.009K^{-1}$ ($T \approx 110K$) is due to critical behavior of the resistivity at T_C in metallic $Ga_{1-x}Mn_xAs$ (see also Section 4.3) **[56]**. The compositional change in the anion sublattice from GaAs to GaP causes a metal-to-insulator transition for near constant Mn doping. This behavior originates from the deeper Mn acceptor level in $Ga_{1-x}Mn_xP$ (400 meV **[51]**) in relation to $Ga_{1-x}Mn_xAs$ (110 meV **[52]**). Carrier localization will therefore play a significant role in the magnetic properties of the $Ga_{1-x}Mn_xP$ system since the carriers are non-itinerant.

The holes which mediate ferromagnetic exchange in $Ga_{1-x}Mn_xP$ reside in a Mn-derived impurity band which remains unmerged with the valence band for $x \leq 0.042$ **[95, 99]**. The presence of this gap has been indicated by three experimental techniques: variable temperature resistivity, low-temperature far-infrared photoconductive spectroscopy, and THz spectroscopy. Figure 61 shows the temperature dependent sheet resistivity for $Ga_{0.958}Mn_{0.042}P$. The high-temperature behavior indicates a thermally-activated process with activation energy near 30 meV. This activation energy differs from the 400 meV acceptor binding energy; however, at the $\sim 10^{21}$ cm^{-3} doping levels realized in $Ga_{0.958}Mn_{0.042}P$ even very compact wavefunctions will have significant overlap leading to the formation of an impurity band. Thus it is reasonable to hypothesize that the observed activation energy may be due to thermal excitation from a broadened impurity band to valence band. Furthermore, samples with lower Mn_{Ga} concentration have larger values for this activation energy (see Figure 60), which is consistent with a picture of a broadening of the impurity band with increasing x **[95, 99]**. An increase in the activation energy is also observed by compensating the Mn acceptors by Te donors **[99]**, which is consistent with the impurity band model.

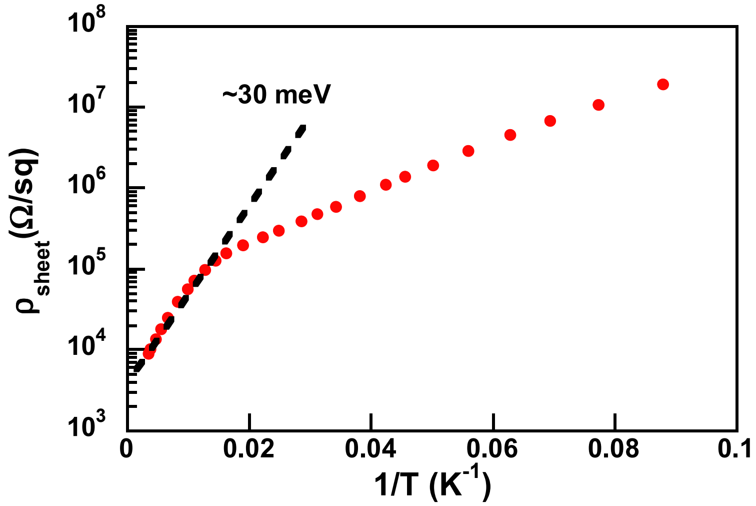

Figure 61: Sheet resistivity vs. 1/T for $Ga_{0.958}Mn_{0.042}P$. The dashed line emphasizes the ~30 meV slope of the high temperature data. After [73].

Figure 62 (a) shows the results of far-infrared photoconductivity experiments on $Ga_{0.958}Mn_{0.042}P$. In these measurements a bias is applied across a highly resistive sample which is illuminated. If photon absorption results in the transition of carriers from bound states to extended, current-carrying states, an increase in conductivity is detected. The dashed line in Figure 62 (a) shows the instrument response function of the spectrometer. The solid line in Figure 62 (a) reproduces this spectrum except in two regions. The dip at ~45 meV is due to absorption by optical phonon modes. The region below 26 meV, where the sample shows no photoconductivity yet where there is significant spectral weight in the incident spectrum is clear evidence of an excitation gap for transitions between bound impurity states and delocalized valence band states for holes. The magnitude of the excitation gap determined by the onset of the photoconductive response is in good agreement with that determined from variable temperature transport. Figure 62 (b) compares the photoconductive response for $Ga_{1-x}Mn_xP$ samples with x=0.042 and x=0.032. The decrease in the Mn_{Ga} concentration causes the photoexcitation edge to increase to ~65 meV. This observation is consistent with the hypothesis of an unmerged impurity band, and variable temperature transport measurements. Additionally, in Te-compensated samples the photoconductive response begins to shift to lower energies as the temperature is increased, which is consistent with increased thermal population of states closer to the edge of the partially-emptied impurity band **[99]**.

Finally, THz spectroscopy measurements on $Ga_{0.958}Mn_{0.042}P$ (T_C=60 K) show that the Drude free carrier response of valence band holes is strongly suppressed with decreasing temperature **[180]**. The activation energy of this carrier freeze-out process is ~44 meV, which is in reasonable agreement with the gap between the impurity band and valence band extracted from variable temperature transport and photoconductivity results. Furthermore, the Drude free carrier response decreased to undetectable levels near T=80 K, which is *greater* than T_C. The negligible concentration of valence band holes at the onset of ferromagnetism provides strong evidence for ferromagnetism mediated by impurity band carriers.

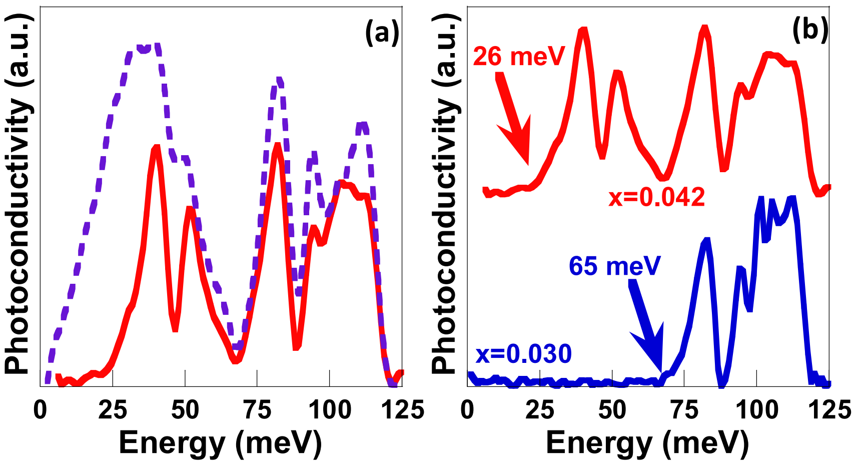

Figure 62: (a) The solid red line is the far-infrared photoconductivity spectrum from $Ga_{0.958}Mn_{0.042}P$. The instrument response, which is a measure of the spectrum incident on the sample, is indicated by the dashed purple line. (b) Far-infrared photoconductivity spectra from samples with x=0.032 and x=0.042 showing the increase in the activation energy for ionization of holes to the valence back with decreasing Mn_{Ga} composition. All spectra were measured at T=4.2 K. After [95]and [99].

Appendix C: X-ray Diffraction Measurements of II-PLM-formed Materials

X-ray diffraction is a powerful technique commonly used to determine the arrangement of atoms within a material. A simple understanding of this phenomenon in crystals is provided by the Bragg construction, which is drawn in Figure 63. A regular array of atoms is exposed to monochromatic electromagnetic radiation of wavelength λ. The direction of propagation of the photons makes an angle θ with the planes of atoms in the crystal. The planes of atoms partially reflect some of this radiation also at an angle θ to the atomic planes. Consider the reflection of electromagnetic waves from two successive plans of atoms separated by a distance d, which are indicated by the blue and red wavefronts in Figure 63. Since the scattering process is elastic the wavelength of the reflected wave is equal to that of the incident wave. The scattered wavefronts will interfere constructively if their path difference is equal to an integer multiple of the wavelength. From Figure 63 it is clear that the path difference between the blue and red waves is equal to $2d\sin(\theta)$, which results in Bragg's Law

$$n\lambda = 2d\sin(\theta) \tag{C.1}$$

where n is an integer. Therefore, if one measures the intensity of the scattered X-rays with a detector peaks will be observed only when the Bragg condition Equation C.1 is met; in other cases the scattered waves will deconstructively interfere. Since λ and θ are typically known in a standard diffraction experiment d is readily determined. Since the sine function can only return values up to magnitude 1, $n\lambda \leq 2d$, which places an upper bound on the wavelength that can be used to observe diffraction in crystals with interplanar spacing d. Typically d is on the order of a few Angstroms, which necessitates using radiation with λ of similar magnitude, i.e. X-rays. All diffraction studies presented in this dissertation were performed using Cu $K_{\alpha 1}$ X-rays with λ=1.5405 Å.

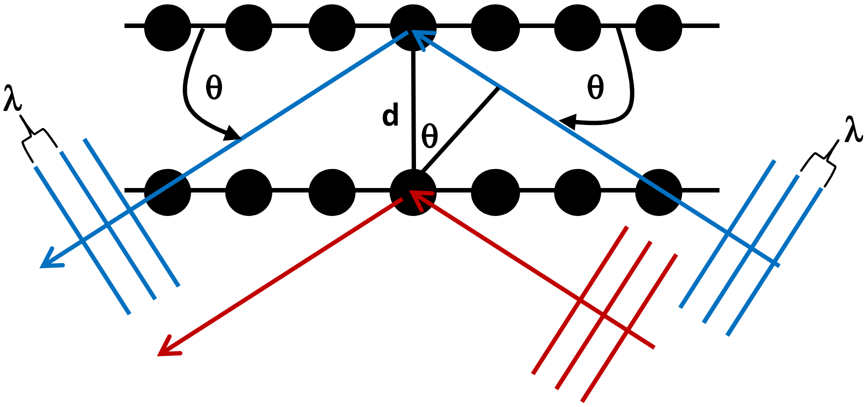

Figure 63: Bragg construction illustrating the diffraction of X-rays by a regular array of atoms with interplanar spacing *d*.

An alternative and more general view of X-ray diffraction is derived from consideration of the reciprocal lattice. The reciprocal lattice is the Fourier transform of the crystal lattice. The primitive reciprocal lattice vectors $\boldsymbol{b}_j$ are defined in relation to the primitive real space lattice vectors $\boldsymbol{a}_i$ by the relation

$$\boldsymbol{a_i} \cdot \boldsymbol{b_j} = 2\pi\delta_{ij} \tag{C.2}$$

where δ_{ij} is the Kronecker delta function and equal to 1 for i=j and 0 for $i \neq j$. The reciprocal lattice vectors $\boldsymbol{G}$ are written as linear combination of the basis vectors $\boldsymbol{b}_j$

$$\boldsymbol{G} = v_1\boldsymbol{b_1} + v_2\boldsymbol{b_2} + v_3\boldsymbol{b_3} \tag{C.3}$$

where v_1, v_2, and v_3 are integers. Following Kittel it is shown that the set of **G** determine all possible X-ray reflections from a material**[166]**. Consider an incident wave of the form $\exp(i\boldsymbol{k}\cdot\boldsymbol{r})$ scattered by a volume element dV separated by the origin by vector $\boldsymbol{r}$, which results in a scattered wave $\exp(i\boldsymbol{k}'\cdot\boldsymbol{r})$. Since the scattering is elastic, $\boldsymbol{k}$ and $\boldsymbol{k}'$ have the same magnitude but may differ in their direction of propagation. This results in a phase difference between the wave scattered at the origin and at $\boldsymbol{r}$ of $\exp[i(\boldsymbol{k}-\boldsymbol{k}')\cdot\boldsymbol{r}]$. The total amplitude of the scattered wave can be written as

$$F = \int dV \cdot n(\boldsymbol{r}) \cdot \exp\,[-i\boldsymbol{Q}\cdot\boldsymbol{r}] \tag{C.4}$$

where $\boldsymbol{Q}=\boldsymbol{k}'-\boldsymbol{k}$ is the scattering vector and $n(\boldsymbol{r})$ is the electronic density responsible for scattering the incident photons, and is periodic in crystals. Since $n(\boldsymbol{r})$ is periodic we can write its Fourier series

$$n(\boldsymbol{r}) = \sum_{\boldsymbol{G}} n_{\boldsymbol{G}} exp\,(i\boldsymbol{G}\cdot\boldsymbol{r}) \tag{C.5}$$

where $\boldsymbol{G}$ are the set of reciprocal lattice vectors defined in Equation C.3. Combining Equations C.4 and C.5 reveals that the scattered intensity is maximized when the argument of the exponential is zero:

$$\boldsymbol{Q} = \boldsymbol{G}. \tag{C.6}$$

Diffraction occurs whenever the scattering vector is equal to a reciprocal lattice vector of the crystal. Therefore, an X-ray diffraction measurement provides a map of a material's reciprocal lattice, which can then provide information about the material's lattice parameters through Equation C.2.

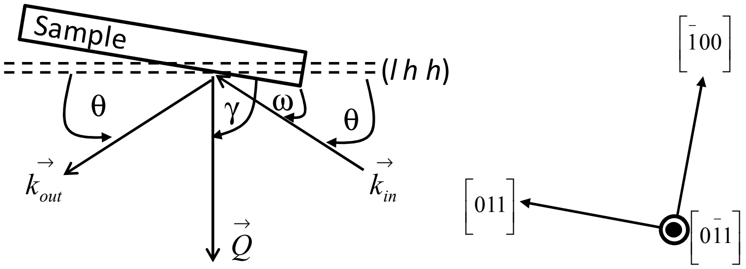

Figure 64: Schematic illustration of the diffraction geometry used throughout this work. The sample is a rectangular prism with long edges parallel to <011> type directions and the short direction parallel to the out-of-plane [100] direction. The scattering vector $\boldsymbol{Q}$ is defined as k_{out}-k_{in} and must be equal to a reciprocal lattice vector for diffraction to be observed.

The experimental geometry used for all X-ray diffraction measurements in this work is illustrated in Figure 64. Here, discussion is limited to diffraction from $\{l\ h\ h\}$ type planes. This is sufficient for determining the structural parameters of materials of tetragonal symmetry or higher, which is the case for the materials studied in this dissertation. In general the momentum transfer vector $\boldsymbol{Q}$ that satisfies the diffraction condition contains components both parallel and normal to the film surface. If γ is the angle between the sample surface and $\boldsymbol{Q}$ then the parallel and perpendicular components of the scattering vector are

$$q_{||} = \boldsymbol{Q}\cos\gamma \tag{C.7}$$

$$q_{\perp} = \boldsymbol{Q}\sin\gamma \tag{C.8}$$

where $q_{||}$ is parallel to the $[0\ h\ h]$ direction of reciprocal space and $q_{\perp}$ is parallel to $[l\ 0\ 0]$ according the coordinate system defined in Figure 64. In a typical diffraction measurement the sample and detector are rotated such that one measures the intensity as a function of ω and 2θ. Thus, it is desirable to express $\boldsymbol{Q}$ and γ in terms of ω and θ. Inspection of Figure 64 reveals

$$\gamma = 90° + \omega - \theta \tag{C.9}$$

where the angles are measured in degrees. From the diffraction condition C.6 one can write

$$\boldsymbol{Q} = \frac{4\pi}{\lambda}\sin\theta \tag{C.10}$$

as the magnitude of the scattering vector. Finally, the in-plane and out of-plane lattice constants are determined by the parallel and perpendicular components of the reciprocal lattice vector

$$a_{||} = \sqrt{2}h\frac{2\pi}{q_{||}} \tag{C.11}$$

$$a_{\perp} = l\frac{2\pi}{q_{\perp}}. \tag{C.12}$$

The relaxed lattice constant, a,- i.e. the lattice constant that the film material would have if it was allowed to be free standing and relaxed to its cubic symmetry- is related to $a_{||}$ and $a_{\perp}$ by

$$a = \frac{a_{\perp} + 2a_{||}\nu - a_{\perp}\nu}{1+\nu} \tag{C.13}$$

where ν is Poisson's ratio. Evaluation of Equation C.13 requires knowledge of both $a_{||}$ and $a_{\perp}$, which makes it is necessary to choose a diffraction geometry such that a region of reciprocal space with non-zero $q_{||}$ and $q_{\perp}$ components is probed. This condition is met as long as $\gamma \neq 90°$, which implies that $h \neq 0$. One can also evaluate Equation C.13 for an (l 0 0) scan and measuring $a_{\perp}$ only if one independently knows that the film is pseudomorphic ($a_{||}=a_{\text{substrate}}$) or fully relaxed ($a_{||}= a_{\perp}$).

The specific diffraction peak that one chooses must be allowed by the symmetry of the crystal system. The set of allowed diffractions can be determined by the structure factor

$$F_{str} = \sum_{n} f_n\, e^{2\pi i(hu_n + kv_n + lw_n)} \tag{C.14}$$

where the sum is taken over the n atoms of the unit cell and the coordinates u_n, v_n, w_n, refer to the position of atom n within the unit cell and f_n is the atomic scattering factor of atom n. The absolute magnitude of F_{str} gives the amplitude of the scattered waves in terms of the scattering factors of the individual atoms that make up a material. The zincblende crystal system consists of a face-centered cubic (fcc) lattice with a two atom basis. From Equation C.14 one can derive the diffraction selection rules for the zincblende crystal system composed of A and B atoms**[181]**:

$$\begin{aligned} |F_{str}|^2 &= 16(f_A^2 - f_B^2), (h+k+l) \text{ is an odd multiple of 2} \\ |F_{str}|^2 &= 16(f_A^2 + f_B^2),\ (h+k+l) \text{ is an even multiple of 2} \\ |F_{str}|^2 &= 16(f_A^2 + f_B^2),\ (h+k+l) \text{ is odd} \end{aligned} \tag{C.15}$$

and the individual indices h,k, and l are unmixed- i.e. all odd or all even. All diffractions normally allowed in the fcc structure are seen, however some will be reduced in intensity due to the deconstructive interference between scattering events from planes of different atomic species.

The diffraction peak must be accessible to the diffractometer. The angular range of the ω and 2θ motors is 90° and 180 ° respectively. For a specific set of ω, 2θ and λ not all reflections may be accessible. This is illustrated in Figure 65 where the accessible region of reciprocal space is plotted for GaP measured with Cu $K_{\alpha 1}$ radiation for reflections of the type (l h h). Numerous reflections that are allowed by symmetry are inaccessible due to the experimental geometry. Therefore, the reflections used for mapping out reciprocal space in this work were chosen to be (5 1 1) since it meets all of the criteria set forward so far, namely it scans both parallel and perpendicular components of reciprocal space, has maximum intensity from the structure factor, and is easily accessible in the diffractometer.

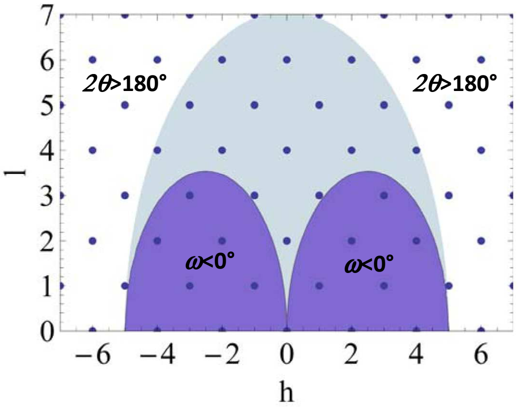

Figure 65: Contour plot of ω as a function of h and l for (l h h) diffraction peaks. All allowed reflections for fcc lattices are plotted as the blue circles, though the intensity of those spots is determined by Equation C.15. Only reflections within the light blue shaded area are accessible in diffractometer. The dark blue area is prohibited by the range of ω while the white area is prohibited by the range of the 2θ arm.

The analysis of reciprocal space maps and individual ω-2θ scans for films grown by II-PLM is sometimes not straightforward. As was discussed in Chapter 2 the II-PLM process can give rise to an impurity distribution that is non-uniform in the growth direction of the film. A non-uniform distribution of impurities implies that the interplanar spacing normal to the film growth direction will also vary as a function of depth. Peaks are broadened significantly since the diffraction condition is met for a greater range of angles. For small lattice mismatches and strong non-uniformity of the impurity concentration the film peak cannot be resolved from the substrate peak. The film signal instead appears as a broad shoulder to one side of the substrate peak. In these cases it is necessary to fit the diffraction data to a numerical model in order to extract the lattice parameters of the film. The substrate peak is modeled by a combined Lorentzian-Gaussian function**[161]**

$$I_{sub} = \frac{m}{1 + \frac{(x - x_0)^2}{w^2}} + (1 - m) exp\left(-\frac{(x - x_0)}{w^2} ln(2)\right). \tag{C.16}$$

The substrate peak is centered around x_0 with a width parameter w that is equal to the half width at half maximum (HWHM). The degree of Lorentzian-Gaussian mixing is parameterized by m which is equal to 0 for a pure Gaussian and 1 for a pure Lorentzian. The film peak is modeled by a Gaussian of variance σ^2 with its peak center shifted by δ from the substrate peak:

$$I_{film} = A exp\left(\frac{-\left(x - (x_0 + \delta)\right)^2}{2\sigma^2}\right) \tag{C.17}$$

with A the amplitude of the film peak. The total intensity $I_t = I_{sub} + I_{film}$ is fit to the experimental data using a least squares routine written in Mathematica. The results of the fitting routine are illustrated in Figure 66 for a $Ga_{0.966}Mn_{0.034}P$ film grown on GaP where the $q_\perp$ values were determined from a (400) ω-2θ scan. This sample is nominally identical to the one for which the (511) reciprocal space map was presented in Section 5.6.1 and assumed to be pseudomorphic with the substrate. The simple two peak model fits the experimental data quite well, with the exception of the thickness fringes which are not considered in the model. For this film the best fit is achieved for δ=-0.0022 Å^{-1} and σ^2=3.6×10^{-6} Å^{-2}. Therefore the mean vale for $a_\perp$ is 5.4531

Å, and the relaxed lattice constant a=5.4519 Å. Taking into account σ^2 and the lattice constant of the GaP substrate the strain in the growth direction for this film is $\varepsilon_\perp$=0.02201±0.01889%.

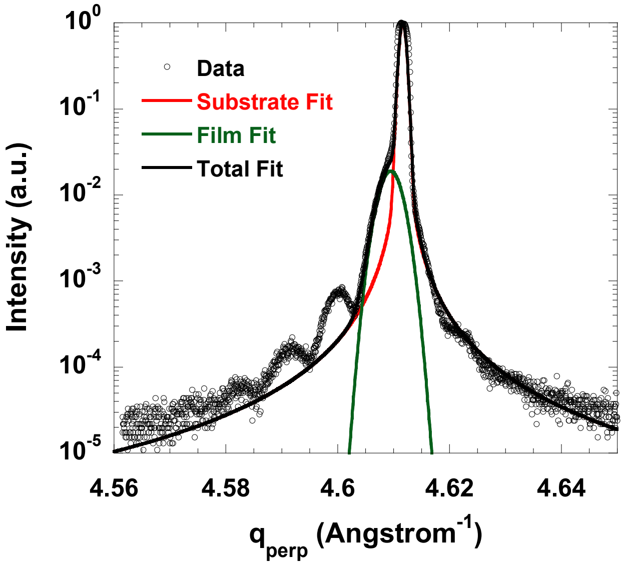

Figure 66: Diffracted intensity as a function of perpendicular scattering vector for a $Ga_{0.966}Mn_{0.034}P$/GaP film. The $q_\perp$ values were derived from an ω-2θ scan about the (400) reflection. The solid lines represent fits to the model described in the text.

In some cases a (400) scan was not available because only the (511) reciprocal space maps were measured. In these cases it is not possible to obtain data akin to Figure 66 since the ω-2θ scans that constitute the (511) reciprocal space map produce $q_\perp$ values that that are a function of $q_\parallel$. This is illustrated in Figure 67 for $Ga_{0.966}Mn_{0.034}P$ which shows the mesh of points used to construct the reciprocal lattice map. Ideally, one would construct a plot similar to Figure 66 using the mesh points with $q_\parallel$≈1.6303 Å, but not enough of the points satisfy this criterion to perform a useful data analysis. Instead, the following procedure was used to determine the film strain:

1. Analyze the asymmetric ω-2θ scan using the two peak model to determine ε and σ^2.
2. Assume that the substrate peak lies at $q_\perp$=5.7639 Å^{-1}, and $q_\parallel$=1.6303 Å^{-1}.
3. Generate a "virtual" (400) ω-2θ scan using the values of ε and σ^2, but confining $q_\parallel$ to a value of 1.6303 Å^{-1}.
4. Calculate the strain as above from the (400) scan.

The basic concept of this method is to generate a symmetric (400) scan using information from the (511) ω-2θ scan, which is indicated by the red points in Figure 67. While not perfect, this method provides a reasonable estimate of the film strain. The error introduced by the scan asymmetry should be on the order of Sin(γ), which is equal to ~25% for the (511) geometry. This error is less than the error bar introduced by the film Gaussian half-widths. For a $Ga_{0.966}Mn_{0.034}P$ sample the strain was determined by both methods: a (400) scan and the adaptation of parameters extracted from a (511) scan. The former yielded mean values of $\varepsilon_\perp$=0.02201% while the latter produced $\varepsilon_\perp$=0.02458%, which is well within the intrinsic error of the measurement. The modified (511) procedure outlined above was used to determine the strain in the $Ga_{0.966}Mn_{0.034}P_{1-y}N_y$ film with y≈0.004 (Section 5.6.1).

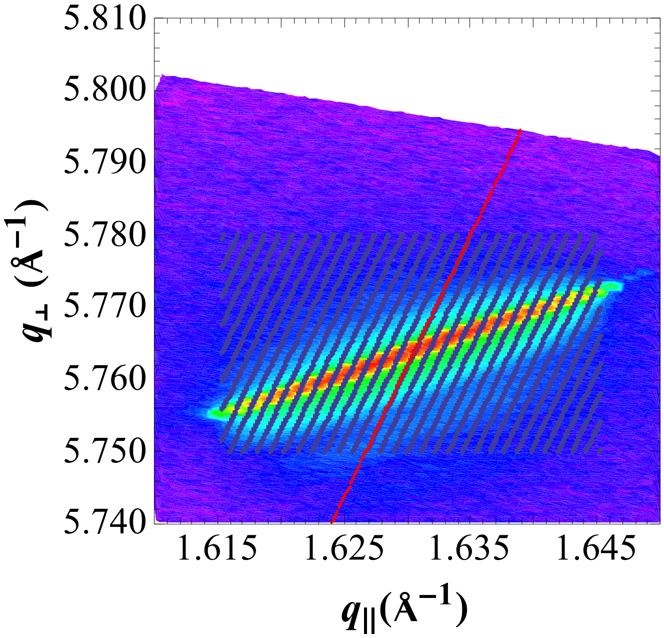

Figure 67: Reciprocal space map for $Ga_{0.966}Mn_{0.034}P$ around the (511) reflection. The blue dots indicate the points in reciprocal space where the data were measured. Red points are from the ω-2θ scan analyzed using the two peak model described in the text.

Annotated versions of the *Mathematica* routines used to process the reciprocal space maps and fit the data to the two peak model are presented below. The programs were compiled using Version 7.0; some syntax may not be compatible with previous versions.

This notebook takes the raw ω - 2 θ data acquired from an X-ray diffraction measurement and converts it to a offset-corrected reciprocal space map.

```
In[117]:= SetDirectory ["C:\Documents and Settings\Peter\My
              Documents\Lab Work\GaMnPN\XRD\Reciprocal Lattice Maps\MS712"];
```

```
In[118]:= r115 = Import["MS712_115_rsm_3_2_09.csv"];
```

The first lines of the data file contain the measurement conditions. This puts them in a separate array and then deletes them from the array to be processed.

```
In[119]:= MeasurementConditions = {};
          For[i = 1, i < 37,
            AppendTo [MeasurementConditions , r115[[i]]];
            i++]
```

```
In[121]:= For[i = 1, i < 36,
            r115 = Delete [r115, 1];
            i++]
          r115[[1]]
```

```
Out[122]= {2Theta position, Omega position, Intensity}
```

```
In[123]:= rplot115 = Delete[r115, 1];
```

To deal with the log scaling of the intensity plot I remove all of the "0" s from the data file and replace them with "1"s. The data file right now is in counts. The peak count intensity is of the order 10^5 so replacing a 0 with a 1 does not pose a problem.

```
In[124]:= For[i = 1, i < Length [rplot115] + 1,
            If[rplot115[[i]][[3]] == 0,
              rplot115 = ReplacePart[rplot115, 1, {i, 3}];];
            i++]
```

Wavelength of radiation was Cu K_α. The number of points per ω-2θ scan is obtained in the preliminary information in the datafile.

```
In[125]:= λ = 1.5405;
```

```
In[126]:= PointsPerScan = MeasurementConditions [[27]][[2]];
```

The following lines generate an array which contains the intensity as a function of perpendicular and parallel components of the Q vector. The intensity goes first into the array 'recip' for ease of sorting. The array 'recipscan' contains the scan number as well for ease of pulling out individual ω-2θ scans if desired for the data processing.

```
In[127]:= recipscan = {};
          mincounts = Sort[rplot115, #1[[3]] < #2[[3]] &][[1]][[3]];
          maxcounts = Sort[rplot115, #1[[3]] < #2[[3]] &][[Length [rplot115]]][[3]];
          recip = {};
          For[i = 1, i < Length [rplot115] + 1,
            Q = (4 * π / λ) * Sin[π / 180 * rplot115[[i]][[1]] / 2];
            γ = π / 180 * rplot115[[i]][[2]] + (π − π / 180 * rplot115[[i]][[1]]) / 2;
            AppendTo [recip, {Q * Cos[γ], Q * Sin[γ], rplot115[[i]][[3]] / maxcounts }];
            AppendTo [recipscan,
              {Q * Cos[γ], Q * Sin[γ], rplot115[[i]][[3]] / maxcounts, IntegerPart[(i − 1) / PointsPerScan ] + 1}];
            i++]
          intmin = 10^-5;
          intmax = Sort[recip, #1[[3]] < #2[[3]] &][[Length[recip]]][[3]];
```

The following finds the "center of mass" of the substrate peak. After finding the maximum intensity an array is generating of all mesh points that have intensity greater than 10 % of the maximum intensity. These contributions are due entirely to the substrate. This method is more accurate than simply using the maximum intensity to find the center of the substrate peak which suffers from errors due to the finite spacing of the reciprocal lattice point mesh. The offests are then calcuated by taking the difference of the measured substrate peak with its theoretical value determined from the lattice constant of GaP.

```
In[134]:= qparsubs = {};
          qperpsubs = {};
          For[i = 1, i < Length [recip] + 1,
            If[recip [[i]][[3]] == intmax,
              Print[recip [[i]][[1]]];
              Print[recip [[i]][[2]]];];
            If[recip [[i]][[3]] > intmax / 10,
              AppendTo [qparsubs, recip [[i]][[1]]];
              AppendTo [qperpsubs, recip [[i]][[2]]];];
            i++]
          qpartrue = 1.6303;
          qperptrue = 5.7639;
          paroffset= qpartrue − Mean [qparsubs]
          perpoffset= qperptrue − Mean[qperpsubs]
```

```
1.59676

5.77525

Out[139]= 0.0364902

Out[140]= −0.00952215
```

For ease of computation (especially for the contour plots) I define some smaller arrays that contain all the relevant information but exclude the regions of near zero intensity.

```
In[141]:= recip2 = {};
          recipscan2 = {};
          For[i = 1, i < Length[recip] + 1,
            qparcorrected = recip[[i]][[1]] + paroffset;
            qperpcorrected = recip[[i]][[2]] + perpoffset;
            If[qparcorrected > 1.60999,
              If[qparcorrected < 1.650001,
                  If[qperpcorrected > 5.73999,
                      If[qperpcorrected < 5.810001,
                          AppendTo[recip2, {qparcorrected, qperpcorrected, recip[[i]][[3]]}];
                          AppendTo[recipscan2,
                            {qparcorrected, qperpcorrected, recip[[i]][[3]], recipscan[[i]][[4]]}];];];];];
            i++]
```

The following creates the color scheme and contour scaling for the contour plot.

```
scaling = 10;
scalefactor = N[Log[scaling, intmin]];
conts = {};
Legend1 = {};
Legend2 = {};
max = N[Log[scaling, intmax]];
min = N[Log[scaling, intmin]];
numconts = 40;
spacing = (max − min) / numconts;
For[i = 1, i < numconts + 2,
  AppendTo[conts, N[scaling^(min + (i − 1) ∗ spacing)]];
  AppendTo[Legend1, (min + (i − 1) ∗ spacing) / scalefactor ∗ .9];
  i++]
q = 1;
For[i = 1, i < Length[Legend1] + 1,
  AppendTo[Legend2, Hue[Legend1[[i]]]];
  AppendTo[Legend2, Rectangle[{1, q − 1}, {0, q}]];
  If[FractionalPart[Round[Log[10, conts[[i]]], .0001]] == 0,
    AppendTo[Legend2, Black];
    AppendTo[Legend2,
      Text[Style[ScientificForm[conts[[i]]], {FontWeight → Bold, FontSize → 16}], {5, q}]]];
  q = q + 1;
  i++]
```

Finally, the reciprocal space map is generated. Most of this code simply defines the tick marks, and plot characteristics.

```
In[157]:= frameticksx = {};
          frameticksxtop = {};
          s = 0;
          For[i = 1.61, i < 1.66,
            If[Mod[s, 10] == 0, AppendTo [frameticksx, {i, , {.02, 0}}];, If[Mod[s, 5] == 0,
                  AppendTo [frameticksx, {i, ToString[i], {.02, 0}}], AppendTo [frameticksx, {i, , {.01, 0}}]];];
            If[Mod[s, 10] == 0, AppendTo [frameticksxtop, {i, , {.02, 0}}];, If[Mod[s, 5] == 0,
                  AppendTo [frameticksxtop, {i, , {.02, 0}}], AppendTo [frameticksxtop, {i, , {.01, 0}}]];];
            s++;
            i = i + .001]
          frameticksy = {};
          frameticksyright = {};
          s = 0;
          For[i = 5.74, i < 5.810001,
            If[i == 5.80, AppendTo [frameticksy, {i, StringJoin[ToString[i], "00"], {.02, 0}}];,
                If[Mod[s, 5] == 0, AppendTo [frameticksy, {i, StringJoin[ToString[i], "0"], {.02, 0}}];,
                    AppendTo [frameticksy, {i, , {.01, 0}}]];]
              If[Mod[s, 5] == 0, AppendTo [frameticksyright, {i, , {.02, 0}}];,
                AppendTo [frameticksyright, {i, , {.01, 0}}]];
            s++;
            i = i + .002]
```

```
In[165]:= Show[ListContourPlot[recip2,
              PlotRange → {{1.61, 1.65}, {5.74, 5.81}, {intmin, intmax}}, FrameLabel →
                {Style["q||(Å^-1)", {Bold, FontSize → 22}], Style["q⊥ (Å^-1)", {Bold, FontSize → 22}]},
              FrameTicks → {{frameticksy, frameticksyright}, {frameticksx, frameticksxtop}},
              LabelStyle → {FontSize → 20}, ColorFunction → (Hue[Log[10, #] / scalefactor * .9] &),
              ContourLines → False, ColorFunctionScaling → False, Contours → conts],
            ListPlot[{{1.6303, 0}, {1.6303, 100}}, Joined → True , PlotStyle → {Thickness[.01], GrayLevel [0]}]]
```

Out[165]=

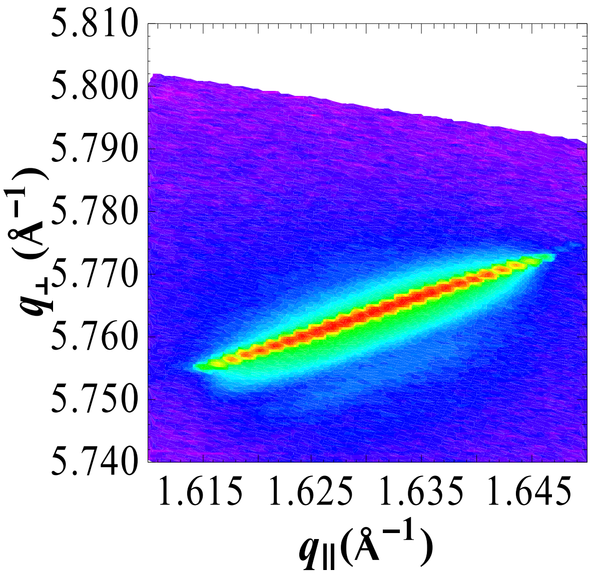

The following routine fits an experimental ω - 2 θ curve to the two peak model. The example shown here is for the 511 reciprocal lattice map of a GaMnP sample with x=0.034. While the specific case shown here is a 511 scan the notebool is easily generalized to other diffraction peaks. First the scan is identified in the data. Then the appropriate functions are defined. The center of the substrate peak is set to the variable 'mean'

```
MS712finalscans = {};
MS712usefulmesh = {};
scannumber = 29;
For[i = 1, i < Length[recipscan2] + 1,
   If[recipscan2[[i]][[4]] == scannumber,
     AppendTo [MS712finalscans, {recipscan2 [[i]][[2]], recipscan2 [[i]][[3]]}];
     AppendTo [MS712usefulmesh, {recipscan2[[i]][[1]], recipscan2 [[i]][[2]]}];
   ];
   i++];
```

```
In[219]:= Gauss[x_, x0_, σ_] := E^(-(x - x0)^2 / (2 * σ))
          substratefit[x_, F_, e_, m_] := (1 - m) * E^(-Log[2] * (x - e)^2 / F^2) + m / (1 + (x - e)^2 / F^2)
          peak = {};
          For[i = 1, i < Length [MS712finalscans] + 1,
            If[MS712finalscans[[i]][[2]] ≥ .3,
              AppendTo[peak, MS712finalscans[[i]][[1]]];
            ];
            i++]
          mean = Mean [peak];
```

First perform a fit only to the substrate contribution. In this case the fit is done for the substrate peak and larger values of q_perp since the film only contributes to the left-hand side of q_perp. The fitting is done using a least-squares method. The least squares sum is formed by the relative difference of the model and data, not the absolute difference; this was found to best describe the data as a whole and not overemphasize the contribution of the substrate peak.

```
mgap = .01;
mmin = 0;
mmax = 1;
ggap = .00001;
gmin = 0.0001;
gmax = 0.001;
δ = 10^-11;
```

```
scrit = 1 000 000;
n = 0;
For[m = mmin, m < mmax + δ,
    For[g = gmin,  g < gmax + δ,
      s = 0;
      For[i = 85, i < Length[MS712finalscans] + 1,
        n++;
        dum = ((substratefit[MS712finalscans[[i]][[1]], g, mean, m] - MS712finalscans[[i]][[2]]) /
                MS712finalscans[[i]][[2]])^2;
        s = s + dum;
        i++];
      If[s < scrit,
        scrit = s;
        mguess = m;
        gguess = g;
      ];
      g = g + ggap];
    m = m + mgap];
Print["The critical value of m is ",  mguess];
Print["The critical value of Γ is ",  gguess];
Show[LogPlot[{substratefit[x, gguess, mean,  mguess]}, {x, 5.74, 5.81},  PlotRange → {10^-5, 1}],
  ListLogPlot[{MS712finalscans},  PlotRange → {10^-5, 1}]]
```

The critical value of m is 0.13

The critical value of Γ is 0.00047

Out[237]=

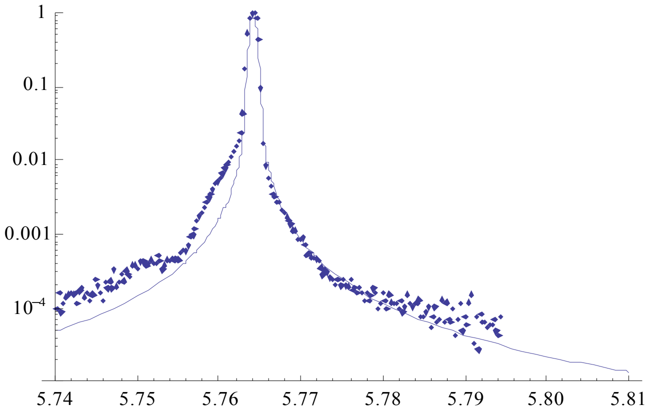

Now the fit is done for the entire set of data. The substrate parameters are taken as those determined in the previc step. Again a modified least squares method is used to fit the data.

```
In[238]:= shifgap= .0002;
          shifmin= −0.05;
          shifmax= 0.005;
          Ggap = .2 ∗ 10^-6;
          Gmin = 1 ∗ 10^-6;
          Gmax = 1 ∗ 10^-5;
          Agap = .001;
          Amin = 0.001;
          Amax = 0.03;
          m = mguess;
          g = gguess; δ = 10^-11;
```

```
scrit = 1 000 000;
n = 0;
For[shif = shifmin, shif < shifmax + δ,
    For[G = Gmin, G < Gmax + δ,
      For[A = Amin, A < Amax + δ,
        s = 0;
        For[i = 1, i < Length[MS712finalscans] + 1,
          n++;
          dum =
            ((substratefit[MS712finalscans[[i]][[1]], g, mean, m] + A * Gauss[MS712finalscans[[i]][[1]],
                          mean + shif, G] - MS712finalscans[[i]][[2]]) / MS712finalscans[[i]][[2]])^2;
          s = s + dum;
          i++];
        If[s < scrit,
          scrit = s;
          Gcrit = G;
          mcrit = m;
          gcrit = g;
          shifcrit = shif;
          Acrit = A;];
        progress = n / steps;
        A = A + Agap];
      G = G + Ggap];
    shif = shif + shifgap];
Print["The critical value for the shift is ", shifcrit];
Print["The critical value of A is ", Acrit];
Print["The critical value of G is ", Gcrit];
Print["The critical value of m is ", mcrit];
Print["The critical value of Γ is ", gcrit];
Show[LogPlot[{substratefit[x, gcrit, mean, mcrit] + Acrit * Gauss[x, mean + shifcrit, Gcrit]},
    {x, 5.74, 5.81}, PlotRange → {10^-5, 1}], ListLogPlot[{MS712finalscans}, PlotRange → {10^-5, 1}]]
```

```
The critical value for the shift is -0.003

The critical value of A is 0.005

The critical value of G is 4.2×10^-6

The critical value of m is 0.13

The critical value of Γ is 0.00047
```

Appendix D: X-ray Magnetic Circular Dichroism of 3*d* Transition Metals

Circular dichroism (CD) refers to a difference in the absorption of right- and left-hand circularly polarized light by a material. Magnetic circular dichroism (MCD) is a specific case of the CD effect in which the asymmetric absorption of circularly polarized light occurs due to broken degeneracy of the ground state, excited state, or both due to a magnetic field. The even more specific X-ray magnetic circular dichroism (XMCD) effect simply refers to an MCD experiment in which the photons have energy in the X-ray regime. This appendix explores the physical origins of the XMCD effect. Specific emphasis is placed on circular dichroism in 3*d* transition metals since it is excitations involving the 3*d* states of Mn that provide information about ferromagnetic exchange in Mn-doped III-V materials.

Right-hand circularly polarized (RCP) and left-hand circularly polarized (LCP) photons have equal and opposite projections of their angular momentum. This work will use the Feynman convention for defining the chirality of circularly polarized photons **[182]**. According to the Feynman definition, one's thumb points in the direction of the photon's ***k*** vector. If the helicity is described by wrapping the fingers of the right hand about the ***k*** axis then the photon has right-handed circular polarization. A similar definition is used for left-handed circular polarization [Figure 68 (a)].

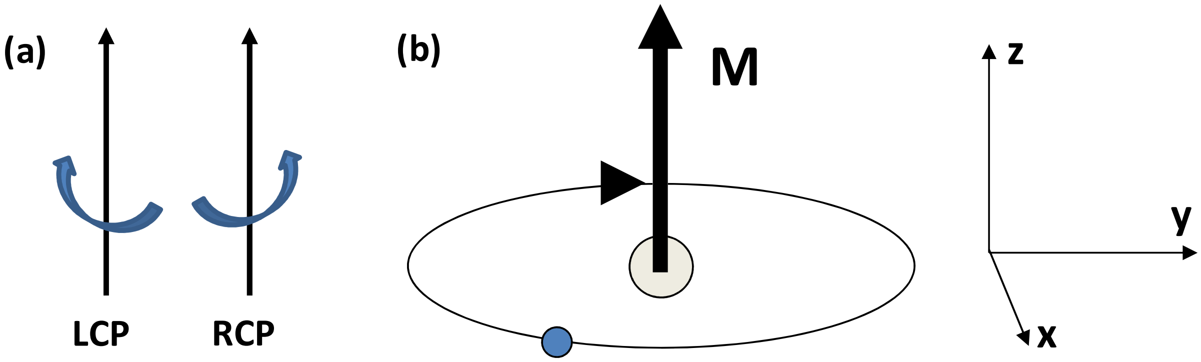

Figure 68: (a) Illustration of left- and right-hand circularly polarized light according to the Feynman definition. (b) Origin of the electronic orbital angular momentum.

When a circularly polarized photon is absorbed by an atom its angular momentum is transferred to the excited photoelectron. In the absence of spin-orbit coupling the angular momentum of the photon can be transferred only to the orbital angular momentum of the electron. Taking a simple, classical view of atomic physics one can gain an intuitive understanding of how the angular momentum of the photon affects the orbital angular momentum of the electron. The orbital moment originates from the electronic orbit about the nucleus, as illustrated in Figure 68(b). The orbiting electron will feel an equal and opposite torque from an RCP or LCP photon since the electric field rotates in opposite directions about the ***k***-vector for the opposite circular polarizations. As an example, the electron in Figure 68(b) has its moment parallel to the +*z*-axis. Consider that the photons are incident such that ***k*** is parallel to the +*z* direction. Looking head-on down the +*z*-axis the electron is orbiting clockwise and the electric field vector for RCP is rotating in an anti-clockwise manner. Due to the negative charge of the electron, the torque felt by the electron due to the rotating electric field is in the opposite direction, i.e. in the same direction as the electron's motion. Therefore RCP photons increase the z-component of the electron's angular momentum. Analogously, LCP photons apply a torque that decreases the z-component of the electron's angular momentum.

The manifestations of the qualitative arguments above are best illustrated using a simple, contrived example of the MCD effect. Let a sample be placed in a magnetic field parallel to its z-axis. The applied magnetic field splits the energy levels characterized by azimuthal quantum number l into $2l+1$ sublevels ordered energetically by the magnetic quantum number m_l. For simplicity it is assumed that the initial state has $l=l_i=0$, which is not split by the magnetic field since m_l must be 0 for $l=0$. According to the dipole selection rules $\Delta l = \pm 1$, resulting in $l_f=1$ for this specific transition, which will be split according to the 3 unique values of m_l as shown in (a). Now let the sample be illuminated with circularly polarized photons which have $\boldsymbol{k}$ parallel to the z-axis. Circularly polarized photons carry an angular momentum of magnitude $\hbar$, which is transferred to the excited electron. Recall from above that in this geometry right (left) circularly polarized photons increase (decrease) the orbital angular momentum of an electron. Therefore, right (left) circularly polarized photons possess an angular momentum of $+\hbar$ ($-\hbar$), which simplifies the dipole selection rule $\Delta m_l = 0, \pm 1$ to $\Delta m_l = 1$ ($\Delta m_l = -1$) for right (left) circularly polarized light. Consequently, RCP light can result only in transitions to the $m_l = 1$ state and left circularly polarized light only in transitions to the $m_l = -1$ state.

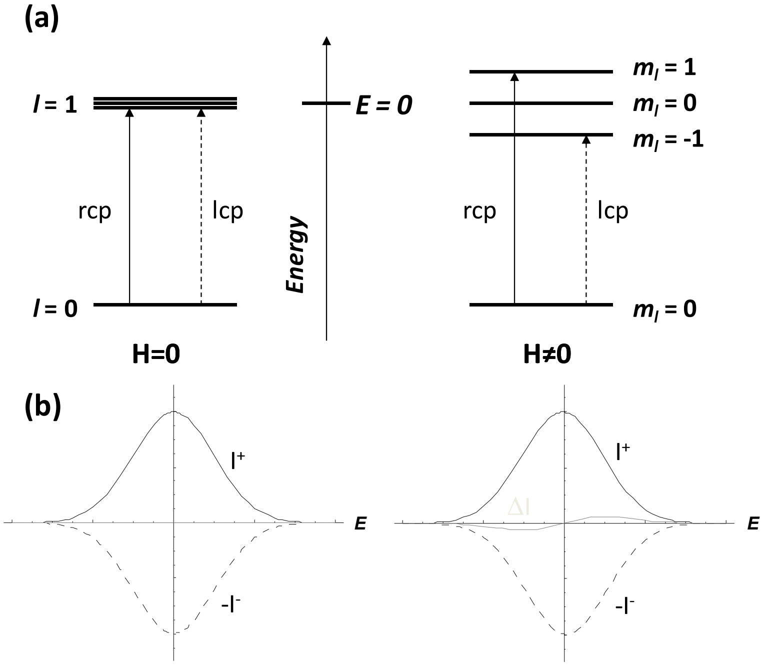

Figure 69: (a) Simple example of MCD Effect. (b) Schematic absorption profiles for cases illustrated in (a). See text for details.

Figure 69(b) schematically shows what the absorption of RCP, I^+, and LCP, I^-, might look like for the two scenarios illustrated in Figure 69(a). The I^- absorption data has been reflected over the y-axis for clarity. For $H=0$, I^+ (solid black line) and I^- (dashed black line) are equal for all energies since the final states ($m_l = \pm 1$) are degenerate in energy. On the other hand when $H \neq 0$ the RCP absorption will be shifted to higher energy than that for LCP absorption. The differential absorption is quantified by the dichroism intensity

$$\Delta I = I^+ - I^-. \tag{D.1}$$

Taking the zero of the energy scale to be at the energy of the l=0, m_l =0 level, the dichroism spectrum (gray line) will be less than zero for E<0 since LCP photons are preferentially absorbed with respect to RCP photons-i.e. $\Gamma^{-}>\Gamma^{+}$. An equal and opposite effect is observed for E>0 since $\Gamma^{+}>\Gamma^{-}$.

The above examples have shown that it is possible to preferentially excite carriers to states based on their orbital angular momentum by utilizing circularly polarized photons. As the orbital contribution to the magnetic moment of 3*d* transition metals is typically 10% or less of the total magnetic moment **[183]** it would be more useful to use circular dichroism to probe the spin polarization of the 3*d* density of states, which is the dominant contributor to the magnetic moment. Probing the spin asymmetry of the 3*d* states requires the ability to preferentially excite electrons according to their spin, which, as will be shown in more detail below, is possible if the initial states are strongly spin-orbit coupled. In the presence of spin-orbit coupling, the electronic wavefunctions are no longer pure spin or orbital states. A circularly-polarized photon's angular momentum is now transferred to both the orbital and spin degrees of freedom of the electron, thus providing a means to achieve preferential excitations of electrons according to their spin. For the 3*d* magnetic elements an appropriate set of wavefunctions comes from the $2p_{3/2}$ and $2p_{1/2}$ energy levels. The relevant X-ray absorption edges for XMCD of Mn are, therefore, L_2 ($2p_{1/2} \rightarrow 3d$) and L_3 ($2p_{3/2} \rightarrow 3d$) since the final states in these transitions are spin-polarized.

A fairly simple way to understand the origin of the XMCD effect is to use the two step model pioneered by Stöhr and Wu **[183-187]**. In the first step electrons of a specific spin orientation are preferentially excited from spin-orbit-split core energy levels. For a given initial state, *i*, and final state, *f*, the absorption matrix element can be written as **[187, 188]**:

$$I = \frac{2m}{\hbar^2}\frac{\left(E_f - E_i\right)^2}{\hbar\omega}|\langle f|\boldsymbol{e}\cdot\boldsymbol{r}|i\rangle|^2 \tag{D.2}$$

where E_f and E_i are the energy of the initial and final states, w is the photon frequency and ***e*** and ***r*** are unit vectors describing the orientation of the electric-field of the incident photon and the position of the electron respectively. Taking the +*z*-direction as parallel to the direction of photon propagation, the electric field vector ***e*** for an RCP photon is

$$\boldsymbol{e}\cdot\boldsymbol{r} = -\frac{1}{\sqrt{2}}\left(\boldsymbol{e}_x + i\boldsymbol{e}_y\right) \tag{D.3}$$

while for LCP it is

$$\boldsymbol{e}\cdot\boldsymbol{r} = \frac{1}{\sqrt{2}}\left(\boldsymbol{e}_x - i\boldsymbol{e}_y\right). \tag{D.4}$$

The dot product in Equation D.2 is then

$$\boldsymbol{e}\cdot\boldsymbol{r} = P^{(1)}_{\pm 1} = \mp\frac{1}{\sqrt{2}}(x \pm iy) \tag{D.5}$$

in Cartesian coordinates. The operator $P^{(l)}_{m_l}$ contains the relevant information regarding the interaction of a circularly polarized photon with an electronic wavefunction. $P^{(l)}_{m_l}$ can be written in terms of the spherical harmonics, $Y_l^{m_l}$. For l=1, and m_l=±1 **[189]**

$$Y_1^{\pm 1} = -\frac{1}{2}\sqrt{\frac{3}{2\pi}}\frac{x \pm iy}{\sqrt{x^2+y^2+z^2}}. \tag{D.6}$$

Comparing Equations D.5 and D.6 it is observed that

$$P_{\pm 1}^{(1)} = r\sqrt{\frac{4\pi}{3}}Y_1^{\pm 1} \tag{D.7}$$

with $r=(x^2+y^2+z^2)^{1/2}$. Bethe and Salpeter **[190]** have evaluated the matrix elements in Equation D.2 using the form of the dipole operators in the right hand side of Equation D.7. For an initial state with quantum numbers *n, l, m_l* the appropriate matrix element for absorption of RCP photons ($m_l \rightarrow m_l+1$) is

$$\left\langle n', l+1, m_l+1 \middle| P_1^{(1)} \middle| n, l, m_l \right\rangle = \sqrt{\frac{(l+m_l+2)(l+m_l+1)}{2(2l+3)(2l+1)}}R \tag{D.8}$$

While for LCP

$$\left\langle n', l+1, m_l-1 \middle| P_{-1}^{(1)} \middle| n, l, m_l \right\rangle = \sqrt{\frac{(l-m_l+2)(l-m_l+1)}{2(2l+3)(2l+1)}}R \tag{D.9}$$

where *R* is the radial matrix element, which are assumed to be the same for all initial states **[187]**.

Table 11: Spin-orbit coupled *p* wavefunctions written in both the one-electron label and the |*lsm$_l$m$_s$*> basis.

One-electron Label	$\left\vert lsm_l m_s \right\rangle$ Basis
$p_{1/2}$	$\frac{1}{\sqrt{3}}\left(Y_1^0\left\vert\uparrow\right\rangle - \sqrt{2}Y_1^1\left\vert\downarrow\right\rangle\right)$
	$\frac{1}{\sqrt{3}}\left(\sqrt{2}Y_1^{-1}\left\vert\uparrow\right\rangle - Y_1^1\left\vert\downarrow\right\rangle\right)$
$p_{3/2}$	$Y_1^1\left\vert\uparrow\right\rangle$
	$\frac{1}{\sqrt{3}}\left(\sqrt{2}Y_1^0\left\vert\uparrow\right\rangle + Y_1^1\left\vert\downarrow\right\rangle\right)$
	$\frac{1}{\sqrt{3}}\left(Y_1^{-1}\left\vert\uparrow\right\rangle - \sqrt{2}Y_1^0\left\vert\downarrow\right\rangle\right)$
	$Y_1^{-1}\left\vert\downarrow\right\rangle$

The first step of the two step model is concerned only with the spin polarization of the excited carriers. Therefore, it is assumed for these calculations that all final 3*d* states are available for the photo-excited electrons. As will be discussed below, the occupation of the final 3*d* states enters only into the second step of this model. Equations D.8 and D.9 are inserted into Equation D.2 and evaluated for all initial states at the L_3 and L_2 absorption edges. The wavefunctions for the $2p_{3/2}$ and $2p_{1/2}$ states are listed in Table 11, and are determined by solving the relativistic Dirac wave equation, which is beyond the scope of this work. The angular parts of the resultant *p* wavefunctions are listed in Table 11 in the |*lsm$_l$m$_s$*> basis as the product of a spherical harmonic and a spin state. This form is the most useful for evaluating Equations D.8 and D.9 since the dependence on *l* and m_l is obvious. The spin component of the wavefunction,

$\left|\uparrow\right\rangle$ or $\left|\downarrow\right\rangle$, do not directly enter the calculations since the photons cannot interact directly with spin angular momentum. However, the spherical harmonic coefficients of the spin-dependent functions differ within given spin-orbit split wavefunction. This is a mathematical representation of the coupling of the spin and orbital angular momenta.

To calculate the spin-polarization of the excited carriers the following summation must be evaluated

$$I^{\pm} \propto \sum_{i,f} \left|\left\langle f \middle| P^{(1)}_{\pm 1} \middle| i \right\rangle\right|^2 \quad \Delta I = I^{+} - I^{-} \qquad \text{(D.10)}$$

where the summation runs over all dipole allowed transitions and the subscript of the operator P is determined by the chirality of the circularly polarized light. The prefactors in Equation D.2 are neglected since they will be the same for all absorption elements and this derivation is concerned only with the relative spin polarization. Since there are two wavefunctions corresponding to $2p_{1/2}$ states, the L_2 absorption intensity will have two terms in the summation. For RCP photons

$$\begin{aligned}
I^{+}_{L_2} = &\left\{ \left| \left\langle l = 2, m_l + 1 \middle| P^{(1)}_{1} \middle| \frac{1}{\sqrt{3}}\left(Y^{0}_{1}|\uparrow\rangle - \sqrt{2}Y^{1}_{1}|\downarrow\rangle\right) \right\rangle \right|^2 \right. \\
&\left. + \left| \left\langle l = 2, m_l + 1 \middle| P^{(1)}_{1} \middle| \frac{1}{\sqrt{3}}\left(-Y^{0}_{1}|\downarrow\rangle + \sqrt{2}Y^{-1}_{1}|\uparrow\rangle\right) \right\rangle \right|^2 \right\} \\
= &\left\{ \left| \frac{1}{\sqrt{3}} \left\langle l = 2, m_l = 1 \middle| P^{(1)}_{1} \middle| l = 1, m_l = 0 \right\rangle \right|^2 |\uparrow\rangle \right. \\
&+ \left| \frac{-\sqrt{2}}{\sqrt{3}} \left\langle l = 2, m_l = 2 \middle| P^{(1)}_{1} \middle| l = 1, m_l = 1 \right\rangle \right|^2 |\downarrow\rangle \\
&+ \left| \frac{-1}{\sqrt{3}} \left\langle l = 2, m_l = 1 \middle| P^{(1)}_{1} \middle| l = 1, m_l = 0 \right\rangle \right|^2 |\downarrow\rangle \\
&\left. + \left| \frac{\sqrt{2}}{\sqrt{3}} \left\langle l = 2, m_l = 0 \middle| P^{(1)}_{1} \middle| l = 1, m_l = -1 \right\rangle \right|^2 |\uparrow\rangle \right\}.
\end{aligned} \qquad \text{(D.11)}$$

The index n has been omitted in Equation D.11 because it does not enter the calculation of the matrix elements; all transitions have n=2 for the initial state and n=3 for the final state. Each of the four terms in Equation D.11 is evaluated according to Equation D.8

$$\begin{aligned}
I^{+}_{L_2} = &\frac{1}{3}\frac{(1+0+2)(1+0+1)}{2(2\times 1+3)(2\times 1+1)}R^2|\uparrow\rangle + \frac{2}{3}\frac{(1+1+2)(1+1+1)}{2(2\times 1+3)(2\times 1+1)}R^2|\downarrow\rangle \\
&+ \frac{1}{3}\frac{(1+0+2)(1+0+1)}{2(2\times 1+3)(2\times 1+1)}R^2|\downarrow\rangle \\
&+ \frac{2}{3}\frac{(1-1+2)(1-1+1)}{2(2\times 1+3)(2\times 1+1)}R^2\left|\uparrow\right\rangle = \frac{1}{9}R^2(|\uparrow\rangle + 3|\downarrow\rangle).
\end{aligned} \qquad \text{(D.12)}$$

Equation D.12 demonstrates that when RCP light is used at the L_2 absorption edge spin down electrons are excited 75% of the time. For LCP light the operator P^{I}_{I} is replaced by P^{I}_{-I},

$$\begin{aligned} I_{L_2}^{-} = \Bigg\{ & \left|\left\langle l = 2, m_l - 1 \middle| P_{-1}^{(1)} \middle| \frac{1}{\sqrt{3}}\left(Y_1^0|\uparrow\rangle - \sqrt{2}Y_1^1|\downarrow\rangle\right)\right\rangle\right|^2 \\ & + \left|\left\langle l = 2, m_l - 1 \middle| P_{-1}^{(1)} \middle| \frac{1}{\sqrt{3}}\left(-Y_1^0|\downarrow\rangle + \sqrt{2}Y_1^{-1}|\uparrow\rangle\right)\right\rangle\right|^2 \Bigg\} \\ = \Bigg\{ & \left|\frac{1}{\sqrt{3}}\left\langle l = 2, m_l = -1 \middle| P_{-1}^{(1)} \middle| l = 1, m_l = 0\right\rangle\right|^2 |\uparrow\rangle \\ & + \left|\frac{-\sqrt{2}}{\sqrt{3}}\left\langle l = 2, m_l = 0 \middle| P_{-1}^{(1)} \middle| l = 1, m_l = 1\right\rangle\right|^2 |\downarrow\rangle \\ & + \left|\frac{-1}{\sqrt{3}}\left\langle l = 2, m_l = -1 \middle| P_{-1}^{(1)} \middle| l = 1, m_l = 0\right\rangle\right|^2 \Big|\downarrow\rangle \\ & + \left|\frac{\sqrt{2}}{\sqrt{3}}\left\langle l = 2, m_l = -2 \middle| P_{-1}^{(1)} \middle| l = 1, m_l = -1\right\rangle\right|^2 |\uparrow\rangle \Bigg\} \end{aligned} \tag{D.13}$$

which is evaluated using Equation D.9 as

$$\begin{aligned} I_{L_2}^{-} = & \frac{1}{3}\frac{(1-0+2)(1-0+1)}{2(2\times 1+3)(2\times 1+1)}R^2|\uparrow\rangle + \frac{2}{3}\frac{(1-1+2)(1-1+1)}{2(2\times 1+3)(2\times 1+1)}R^2|\downarrow\rangle \\ & + \frac{1}{3}\frac{(1-0+2)(1-0+1)}{2(2\times 1+3)(2\times 1+1)}R^2|\downarrow\rangle \\ & + \frac{2}{3}\frac{(1+1+2)(1+1+1)}{2(2\times 1+3)(2\times 1+1)}R^2\Big|\uparrow\rangle = \frac{1}{9}R^2(3|\uparrow\rangle + |\downarrow\rangle). \end{aligned} \tag{D.14}$$

At the L_2 edge LCP photons excite spin down electrons 75% of the time.

Table 12: Probability of electronic transition at $L_{3,2}$ absorption edges as a function of electron spin and orientation of circularly polarized light.

Absorption Edge	*Spin up, rcp*	*Spin down, rcp*	*Spin up, lcp*	*Spin down, lcp*
L_3	62.5%	37.5%	37.5%	62.5%
L_2	25%	75%	75%	25%

Table 12 summarizes the results of calculating all L_3 and L_2 matrix elements sorted by the spin polarization of the electrons. Details of the L_3 calculations were not shown here but can be performed in a similar manner to the L_2 calculations. For the L_3 edge the summation has four terms corresponding to the four $2p_{3/2}$ wavefunctions in Table 11. The calculations demonstrate that excitations are spin-polarized at both the L_3 and L_2 edges when circularly polarized light is used. The spin polarization is opposite at the L_3 and L_2 edges due to the opposite spin-orbit coupling of the $p_{1/2}$ (***l*** parallel to ***s***) and $p_{3/2}$ (***l*** antiparallel to ***s***) states.

In the second step of the two step model, the “spin rich” baths of electrons serve as a probe for the spin-polarized 3*d* contribution to the density of states at E_F as illustrated in Figure 70. Figure 70 is artificially divided by a dotted line, which separates steps one and two of the two step model. The left and right hand sides of Figure 70 represent illumination with RCP and LCP photons respectively. The thick green arrows represent strong excitations, while the dotted red arrows represent weak excitations (*c.f.* Table 12). The 3*d* density of states is drawn in Figure 70 according to the rigid band model in which an asymmetric distribution of spins exists due to a reduction in the exchange energy **[139]**. At E_F there is a difference in the number of available states for spin up and spin down electrons. When circularly polarized light is used to preferentially excite carriers, the number of final states is different depending on the spin of the preferentially excited carrier. Therefore, one would expect the matrix elements from to be different for spin up and spin down carriers. In other words, the matrix elements would be different for right-hand circularly polarized light and left-hand circularly polarized light. Therefore, $\Gamma^{+}\neq\Gamma^{-}$ and the XMCD$\neq$0. If there is no asymmetry at the density of states at E_F then the dichroism signal will be zero. Circularly polarized light of opposite handedness will still excite carriers preferentially, but they now have the same number of final states to go to. The XMCD signal thus contains information about the magnitude of the spin polarization of the 3*d* density of states at E_F and, therefore, the magnetic properties of a sample.

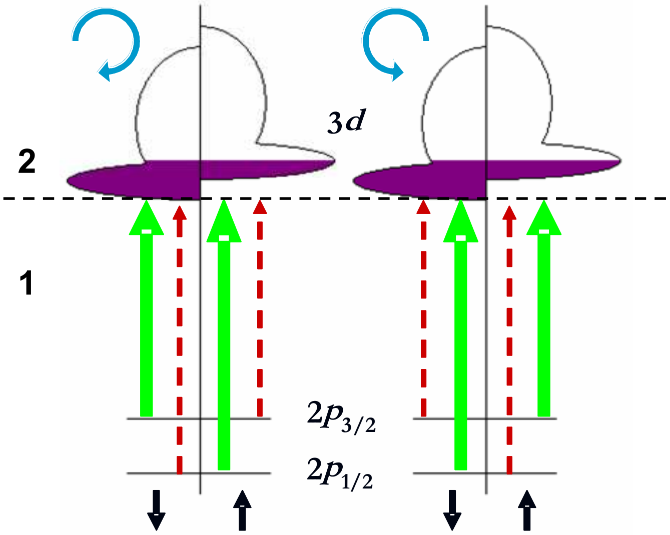

Figure 70: Illustration of the two step model of XMCD. Blue arrows represent photon helicity. k is assumed to be out of the page such that the left hand side represents LCP light and the right hand side RCP light. The dotted line artificially separates the two steps in the process. See text for further discussion.

Appendix E: Supplemental Experimental Results in $Ga_{1-x}Mn_xAs_{1-y}P_y$

Selected electrical, magnetic, and electrical properties of several other $Ga_{1-x}Mn_xAs_{1-y}P_y$ films are presented here in order to further emphasize the trends in electrical and magnetic properties discussed in Sections 4.2 through 4.5. These samples have different cation sublattice compositions (i.e. different x) than those discussed in and should therefore be viewed as distinct sample series. One series was produced under nominally identical conditions but resulted in $x\approx0.04$ for all samples, which was determined by SIMS and ion beam analysis. Again, no significant change in either the Mn concentration profile or the substitutional fraction of Mn was observed with P alloying. The difference in x is likely due to laser calibration differences, as a different KrF laser was used to synthesize this series. The incorporation of 3% P into the As sublattice induces an MIT in $Ga_{0.96}Mn_{0.04}As$ [Figure 71 (a)]. In parallel, T_C drops from 100 K to 70 K [Figure 71 (b)], which is in agreement with the trends in magnetic properties discussed in Section 4.5.

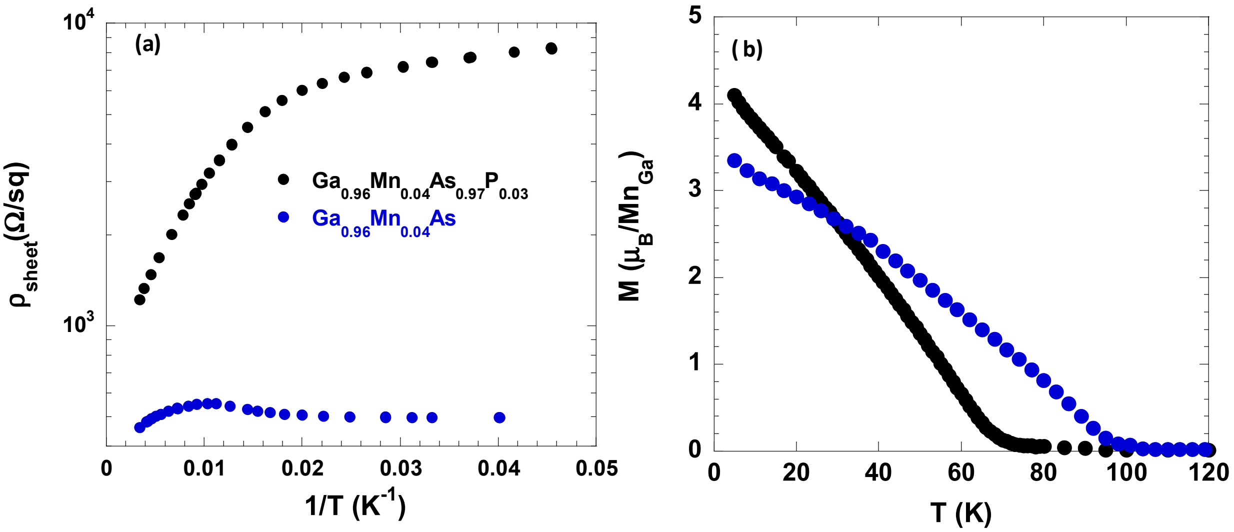

Figure 71: (a) Sheet resistivity vs. inverse temperature and (b) magnetization as a function of temperature for $Ga_{0.96}Mn_{0.04}P$ and $Ga_{0.96}Mn_{0.04}As_{0.97}P_{0.03}$. The magnetization data were taken with $H||[100]$ for y=0.03 and H||<011> for y=0 in an applied field μ_0H=5 mT after field cooling.

A series of $Ga_{1-x}Mn_xAs_{1-y}P_y$ films with lower x were also examined. These samples were produced by using a lower Mn implant dose of $5.0x10^{15}$ cm^{-2} while the other processing parameters were held the same. SIMS and ion beam analysis indicate that $x\approx0.018$ for the P-free reference sample, which is assumed to hold for samples in this series that contain P. This series of samples provides an interesting contrast to the others that have been presented thus far because the P-free reference sample is already on the cusp of the metal-insulator transition due to its smaller Mn concentration. A decrease in T_C from 55 to 40 K is observed with 1.6% P alloying of the anion sublattice in $Ga_{0.982}Mn_{0.018}As$.

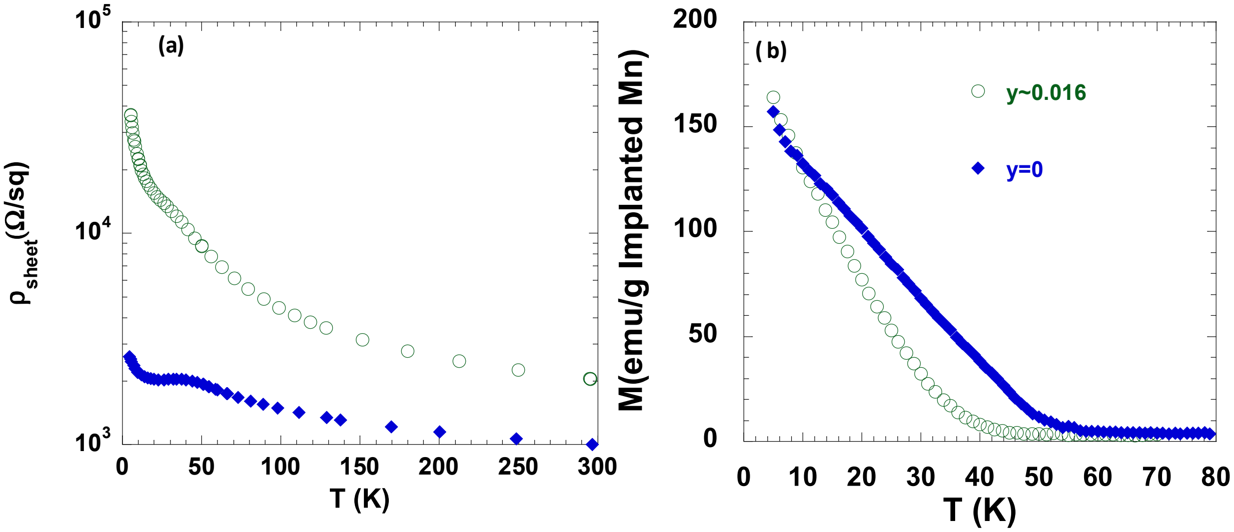

Figure 72: (a) Sheet resistivity and (b) magnetization as a function of temperature for $Ga_{1-x}Mn_xAs_{1-y}P_y$ with x=0.018. The magnetization data were taken with H||[100] for y≈0.016 and H||<011> for y=0 in an applied field μ_0H=5 mT after field cooling.

Appendix F: Simulation of *M(H)* Curves

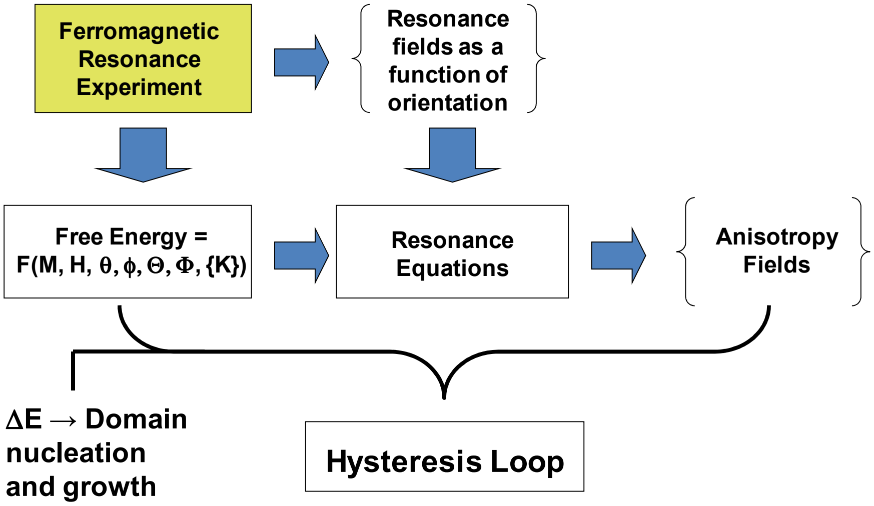

Figure 73: Flow chart illustrating the process by which *M(H)* curves are calculated by the free energy approach.

The steps involved in calculating the field-dependence of the magnetization are outlined in Figure 73. The FMR experiment yields the resonance field as a function of crystallographic orientation. From the FMR data, as well as basic knowledge of the material's crystal structure, one can infer the form of the free energy from symmetry considerations. The free energy is then combined with the resonance equations 31 and 33 to fit the experimental FMR data, which yields the magnetic anisotropy fields as fitting parameters. Once the anisotropy fields are known Equation 38 can be used to map out the dependence of the free energy on the orientation and strength of the magnetization and magnetic field.

To calculate the field-dependence of the magnetization from Equation 38 the orientation of the magnetic field is fixed by setting the values of θ and ϕ (Figure 37). The magnitude of the magnetization vector is determined from SQUID magnetometry measurements and also used as an input. Once the strength of the magnetic field is specified, Equation 38 is minimized with respect to the orientation of the magnetization vector (Θ,Φ). The projection of the magnetization on the field direction is then calculated, which determines the value of the magnetization that would be measured for the particular orientation and magnitude of the applied magnetic field. The magnetic field is then stepped to its next value and the minimization procedure is repeated. There are several possible outcomes:

1. The global energy minimum occurs at the same magnetization orientation. No change in the magnetization occurs due to the field change.
2. A new global minimum appears in the free energy landscape. The energy difference between the new global minimum and old local minimum is compared. If the energy gained by switching to the global minimum is greater than the free parameter ΔE then the magnetization switches (noncoherent spin switching). If the energy gained is less than ΔE the magnetization remains pinned in the local minimum.
3. The global minimum has shifted slightly in angular space with no energy barrier separating it from the previous orientation of the magnetization vector. The magnetization is free to rotate to the new orientation (coherent rotation).

4. The previous minimum has completely disappeared. The magnetization is free to switch to the nearest local minimum. This case is rarely encountered.

In this manner the *M(H)* curve is produced as the field is swept from large positive to large negative fields and then back to large positive fields with the minimization procedure performed at each magnetic field point. The *M(H)* model relies on a single free parameter, ΔE, which takes into account the hysteretic losses due to domain wall nucleation and growth.

The model described above assumes that the material is well-described by single-valued parameters for the magnetic anisotropy and hysteretic losses. As a result the calculations predict sharp noncoherent switches, which are generally not seen in experiment. The experimental *M(H)* loops are characterized by smoother features which suggest that non-uniformity plays a role in determining the *M(H)* lineshape. To account for this non-uniformity the free parameter ΔE is assumed to take on a distribution of values. Normal, log-normal, and uniform distributions were explored. The best agreement was found using a normal distribution of ΔE values in agreement with magnetic anisotropy experiments that were performed around the same time in $Ga_{1-x}Mn_xAs$ **[164]**. Identifying the calculated curve with a single-value of ΔE as $M(H,\Delta E)$ the calculated loop using the normal distribution is

$$M^*(H,\overline{\Delta E},\sigma) = \sum_{\Delta E} \frac{1}{\sqrt{2\pi}\sigma} exp\left(\frac{-(\Delta E - \overline{\Delta E})^2}{2\sigma^2}\right) M(H,\Delta E) \tag{F.1}$$

where the normal distribution is centered at $\overline{\Delta E}$ with standard deviation, σ.

The following are Mathematica notebooks that were used for the *M(H)* simulations. The first notebook is the *M(H)* calculation for the single-valued model. The second notebook takes numerous *M(H)* curves for different values of ΔE and combines them using the normal distribution function (Equation F.1). Both notebooks use the wasp-waisted *M(H)* loop measured for $Ga_{0.959}Mn_{0.041}P_{0.989}S_{0.011}$ with $H\|[011]$ as the model system.

```
Clear["Global`*"];
```

Input the magnetization in units of A/m. The anisotropy parameters are the anisotropy field in Tesla multiplied by the magnetization.

```
In[360]:= M = 20.988`10^3;
          KC1 = 0.` M;
          KC1ip = -0.014` M;
          KC1oop = -0.02` M;
          KuniaxZ = 0.` M;
          KuniaxX = 0.034` M;
          KuniaxY = 0.` M;
          Kuniax01m1 = -0.00385` M;
```

Define the various terms that enter the free energy (Zeeman and anisotropy terms). Here captial letters refer to the angles of tl magnetization and lower case to the magnetic field. T and t refer to thetas in the coordinate system defined in the main text an G and g refer to phi.

```
In[368]:= Fzeemann[M_, B_, T_, G_, t_, g_] :=
            -M B (Sin[T] Sin[G] Sin[t] Sin[g] + Cos[T] Cos[t] + Sin[T] Cos[G] Sin[t] Cos[g]);
          Fcubic[M_, B_, T_, G_, t_, g_] := 1/4 KC1 (Sin[2 T]^2 + Sin[T]^4 Sin[2 G]^2);
          Fcubicip[M_, B_, T_, G_, t_, g_] := KC1ip (1/2 - 1/2 (Cos[T]^4 + Sin[T]^4 Cos[G]^4));
          Fcubicoop[M_, B_, T_, G_, t_, g_] := -1/2 KC1oop Sin[T]^4 Sin[G]^4;
          FuniaxAlongZ[M_, B_, T_, G_, t_, g_] :=
            KuniaxZ (0 Sin[T] Sin[G] + 0 Cos[T] + Sin[T] Cos[G])^2;
          FuniaxAlongY[M_, B_, T_, G_, t_, g_] :=
            KuniaxY (0 Sin[T] Sin[G] + 1 Cos[T] + 0 Sin[T] Cos[G])^2;
          FuniaxAlongX[M_, B_, T_, G_, t_, g_] :=
            KuniaxX (Sin[T] Sin[G] + 0 Cos[T] + 0 Sin[T] Cos[G])^2;
          Funiax01m1[M_, B_, T_, G_, t_, g_] :=
            1/2 Kuniax01m1 (0 Sin[T] Sin[G] + 1 Cos[T] - Sin[T] Cos[G])^2;

In[376]:= FreieEnergCubic[M_, B_, T_, G_, t_, g_] :=
            1.` Fzeemann[M, B, T, G, t, g] + 0.` Fcubic[M, B, T, G, t, g] +
             1.` Fcubicip[M, B, T, G, t, g] + 1.` Fcubicoop[M, B, T, G, t, g] +
             0.` FuniaxAlongZ[M, B, T, G, t, g] + 1.` FuniaxAlongX[M, B, T, G, t, g] +
             0.` FuniaxAlongY[M, B, T, G, t, g] + 1.` Funiax01m1[M, B, T, G, t, g];
```

Define the free parameter DeltaE in units of J/m^3. If a new energy minimum exists in the free energy landscape then it must be at least this much lower in energy in order for a magnetization switch to occur.

```
In[377]:= DeltaE = -20;

In[378]:= Loop011 = {};
          LMatrix011 = {};
          rawMatrix011 = {};
```

Define the magnetic field parameters in Tesla and the angular parameters in radians. Bstart is the maximum magnitude of the magnetic fiel that is used. Bgap is the stepsize. The angular parameters determine the density of the mesh that is used to find all of the local minima in the free energy landscape.

```
In[381]:= Bstart = 0.015`;
          Bgap = 0.0002`;
          phigap = 2;
          thetagap = 2;
```

Lists that the local minima of the free energy are written in

```
Hys = {};
Hys1 = {};
```

Orientation of the external magnetic field. The x direction is normal to the thin film plane.

```
x = 10^-8;
y = 1;
z = 1;
```

Transformation of the x, y, z coordinates of the external magnetic field into speherical coordinates.

```
t0 = ArcTan[Sqrt[z^2 + x^2] / y];
g0 = ArcTan[x / z];
If[y < 0, t0 = t0 + Pi];
If[z < 0, g0 = g0 + Pi, If[x < 0, g0 = g0 + 2 Pi]];
If[g0 > 2 Pi, g0 = g0 - 2 Pi];
```

The starting value for the first minimization.

```
xm = -x;
ym = -y;
zm = -z;
```

This for loop compiles half of the M (H) loop. It starts by converting our best guess of the magnetization orientation from Cartesian coordinates to spherical coordinates. Then the energy is calculated for this orientation of the magnetization and magnetic field (Evg1). Then the program looks for the nearest minimum in free energy in {T,G} space and records its coordinates {xm,ym,zm} and computes it magnetization Mr. We then write the {B, Mr} values into the Hys1 matrix and the details in the rawMatrix.

The program then looks to see if any other minima are present in the free energy landscape that are lower in energy than the one that we found. If a minimum is found that is lower in energy by at least the "DeltaE" value then we overwrite the magnetization coordinates. If n such minimum is present then the original coordinates are maintained.
After scanning all of the angular space the final {B, Mr} values are written to the Loop01 lmatrix. This is the matrix that is compared t experiment.

When the loop goes to the next field value the first location from which it searches for a new minimum is from the previous orientation o the magnetization. In this way the program successfully captures coherent rotation of the magnetic moment since the first minimum that i will find will be nearby the old orientation of the magnetization provided that the magnetic field stepsize is not too large.

```
For[B = Bstart, B > -Bstart,

 L = {};
 L1 = {};
 t0m = ArcTan[Sqrt[zm^2 + xm^2] / ym];
 g0m = ArcTan[xm / zm];
 If[ym < 0, t0m = t0m + Pi];
 If[zm < 0, g0m = g0m + Pi, If[xm < 0, g0m = g0m + 2 Pi]];
 If[g0m > 2 Pi, g0m = g0m - 2 Pi];
 Evgl = FreieEnergCubic[M, B, t0m, g0m, t0, g0];
 lsg1 =
  N[FindMinimum[FreieEnergCubic[M, B, T, G, t0, g0], {T, t0m + 0.01}, {G, g0m + .01}], 10];
     xm = Sin[T] Sin[G] /. Last[lsg1];
     ym = Cos[T] /. Last[lsg1];
     zm = Sin[T] Cos[G] /. Last[lsg1];
     Mr = M (x * xm + y * ym + z * zm) / Sqrt[x^2 + y^2 + z^2];
     lsglist1 = {B, Mr};
     Hys1 = Append[Hys1, lsglist1];
     En = lsg1[[1]];
     AppendTo[rawMatrix011, {B, Mr, xm, ym, zm, En, t0m + 0.01, g0m + 0.01}];
 L = {B, Mr, xm, ym, zm};
 L1 = {B, Mr};
 Encomp = En;


 For[i = -π, i < π,
  For[j = -π, j < π,
   cand = N[FindMinimum[FreieEnergCubic[M, B, T, G, t0, g0], {T, i}, {G, j}]];
       xm = Sin[T] Sin[G] /. Last[cand];
       ym = Cos[T] /. Last[cand];
       zm = Sin[T] Cos[G] /. Last[cand];
       Mr = M (x * xm + y * ym + z * zm) / Sqrt[x^2 + y^2 + z^2];
       AppendTo[rawMatrix011, {B, Mr, xm, ym, zm, cand[[1]], N[i], N[j]}];

   If[cand[[1]] - En < DeltaE, If[cand[[1]] < Encomp,   L = {B, Mr, xm, ym, zm}; L1 = {B, Mr};
                        Encomp = cand[[1]];
             (* Print["Emin"]*);];];
   j = j + phigap];
  i = i + thetagap];
 xm = L[[3]];
 ym = L[[4]];
 zm = L[[5]];
 AppendTo[LMatrix011, L];
 AppendTo[Loop011, L1];
 (*Print["MinE:      B: ", L[[1]], " Mr: ", L[[2]],  " xm: ", L[[3]],
   " ym: ", L[[4]], " zm: ", L[[5]], " Energy: ",En/(1.4 10^(15))];*)
 B = B - Bgap]
```

Here the second half of the M (H) loop is generated.

```
In[397]:= For[B = -Bstart, B < Bstart,

    L = {};
    L1 = {};
    t0m = ArcTan[Sqrt[zm^2 + xm^2] / ym];
    g0m = ArcTan[xm / zm];
    If[ym < 0, t0m = t0m + Pi];
    If[zm < 0, g0m = g0m + Pi, If[xm < 0, g0m = g0m + 2 Pi]];
    If[g0m > 2 Pi, g0m = g0m - 2 Pi];
    Evgl = FreieEnergCubic[M, B, t0m, g0m, t0, g0];
    lsg1 =
     N[FindMinimum[FreieEnergCubic[M, B, T, G, t0, g0], {T, t0m + 0.01}, {G, g0m + .01}], 10];
        xm = Sin[T] Sin[G] /. Last[lsg1];
        ym = Cos[T] /. Last[lsg1];
        zm = Sin[T] Cos[G] /. Last[lsg1];
        Mr = M (x * xm + y * ym + z * zm) / Sqrt[x^2 + y^2 + z^2];
        lsglist1 = {B, Mr};
        Hys1 = Append[Hys1, lsglist1];
        En = lsg1[[1]];
        AppendTo[rawMatrix011, {B, Mr, xm, ym, zm, En, t0m + 0.01, g0m + 0.01}];
    L = {B, Mr, xm, ym, zm};
    L1 = {B, Mr};
    Encomp = En;

    For[i = -π, i < π,
     For[j = -π, j < π,
      cand = N[FindMinimum[FreieEnergCubic[M, B, T, G, t0, g0], {T, i}, {G, j}]];
          xm = Sin[T] Sin[G] /. Last[cand];
          ym = Cos[T] /. Last[cand];
          zm = Sin[T] Cos[G] /. Last[cand];
          Mr = M (x * xm + y * ym + z * zm) / Sqrt[x^2 + y^2 + z^2];
          AppendTo[rawMatrix011, {B, Mr, xm, ym, zm, cand[[1]], N[i], N[j]}];

      If[cand[[1]] - En < DeltaE, If[cand[[1]] < Encomp,   L = {B, Mr, xm, ym, zm}; L1 = {B, Mr};
                            Encomp = cand[[1]];
                (*Print["Emin"]*);];];
      j = j + phigap];
     i = i + thetagap];
    xm = L[[3]];
    ym = L[[4]];
    zm = L[[5]];
    AppendTo[LMatrix011, L];
    AppendTo[Loop011, L1];
    (*Print["MinE:      B: ", L[[1]], " Mr: ", L[[2]], " xm: ", L[[3]],
      " ym: ", L[[4]], " zm: ", L[[5]], " Energy: ",En/(1.4 10^(15))];*)
    B =
     B +
      Bgap]
```

```
In[398]:= Exploop = Import [
            "C:\Documents and Settings\Peter\My Documents\Lab Work\SQUID Simulation\WSI Model
              (with Christoph)\Simulations for Paper\Final Simulations\PS24_WaspWaist.csv"];
```

Comparison is made between the model and experiment.

```
In[399]:= ListPlot [{Loop011, Exploop}, Joined → {True, False},
           PlotStyle → {{Hue[0], Thickness[0.01`]}, {GrayLevel[0], PointSize[.02]}},
           PlotRange → {{-0.015`, 0.015`}, {-22000, 22000}},
           AxesLabel → {Style["μ0H (T)", {Bold, FontSize → 22}],
             Style["M (A/m)", Bold, FontSize -> 22]}, LabelStyle → {FontSize → 20}]
```

Out[399]=

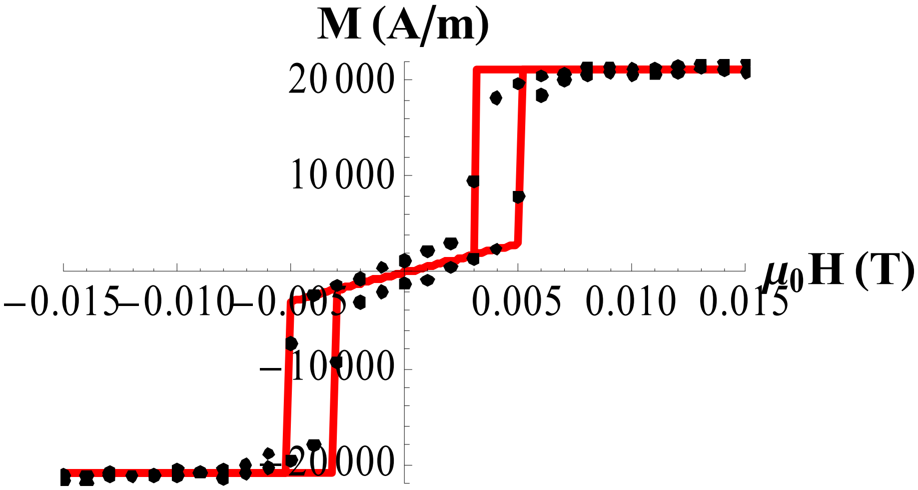

This notebook produces a calucated M (H) curve based on a normal distributionof domain energies. Here "Exploop" is the experimental data imported into *Mathematica* and "Hysloop" is an array of fields and magnetizations produced from the single-valued model. The single-valued loops were done sequentially from ΔE=-60 J/m^3 to ΔE = −1 J/m^3. Each loop had 200 point and a loop was done every 1 J/m^3 in between the endpoint ΔE values. These values must be modified if different ranges of ΔE were used in the single-valued simulations. The program produces the *M(H)* loop based on the inputs for the mean value of ΔE and its standard deviation. The distribtuion function is also generated.

```
In[568]:= SetDirectory[
            "C:\Documents and Settings\Peter\My Documents\Lab Work\SQUID Simulation\WSI
              Model (with Christoph)\Simulations for Paper\Final Simulations"];

In[569]:= Exploop = Import["PS24_WaspWaist.csv"];

In[570]:= Hysloop = Import["DeltaETest_ParameterSetPS245K_011_Gaussian.csv"];

In[571]:= Hysloop = Delete[Hysloop, 1];

In[573]:= PointsPerLoop = 200;
          ΔEMesh = 1;
          ΔEMax = -60;

In[576]:= DelE = ΔEMax;
          For[j = 1, j < Length[Hysloop],
            counter = 0;
            While[counter < PointsPerLoop,
             AppendTo[Hysloop[[j + counter]], DelE];
             counter++];
            DelE = DelE + ΔEMesh;
            j = j + PointsPerLoop];

In[578]:= meanΔE = -20;
          stddev = 8;

In[580]:= ndist = NormalDistribution[meanΔE, stddev];
          pdf = PDF[ndist, x];

In[582]:= EDist1 = {};
          EDist2 = {};
          For[i = ΔEMax, i < ΔEMax + Length[Hysloop] / PointsPerLoop,
           AppendTo[EDist1, {i, N[PDF[ndist, i]]}];
           i = i + ΔEMesh]
          s = 0;
          For[j = 1, j < Length[EDist1] + 1,
            s = s + EDist1[[j]][[2]];
            j++];
          For[k = 1, k < Length[EDist1] + 1,
            AppendTo[EDist2, {EDist1[[k]][[1]], EDist1[[k]][[2]] / s}];
            k++];
          s2 = 0;
          For[l = 1, l < Length[EDist2] + 1,
            s2 = s2 + EDist2[[l]][[2]];
            l++];
          s
          s2
```

```
In[593]:= FinalLoop= {};
          For[i = 1, i < 201,
            c = 1;
            s = 0;
            For[j = 1, j < Length[Hysloop] + 1,
             s = s + Hysloop[[j + i - 1]][[2]] * EDist2[[c]][[2]];
             c++;
             j = j + 200];
            AppendTo[FinalLoop, {Hysloop[[i]][[1]], s}];
            i++];
          ListPlot[{FinalLoop, Exploop}, Joined -> {True, False},
           PlotStyle→ {{Hue[0], Thickness[0.01`]}, {GrayLevel[0], PointSize[.02]}},
           PlotRange -> {{-.01, .01}, {-25 000, 25 000}},
           AxesLabel → {Style["μ0H (T)", {Bold, FontSize → 22}],
             Style["M (A/m)", Bold, FontSize -> 22]}, LabelStyle→ {FontSize→ 20}]
```

Out[595]=

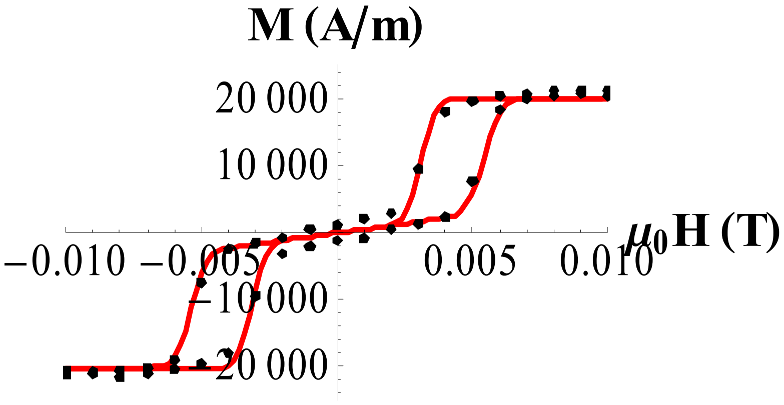

```
In[596]:=
          ListPlot[EDist2, Joined → True,
           AxesLabel → {Style["ΔE (J/cm3)", {Bold, FontSize → 22}],
             Style["Weight of ΔE (a.u.)", Bold, FontSize -> 22]},
           LabelStyle→ {FontSize→ 20}, PlotStyle → Thickness[.01]]
```

Out[596]=